Title
Fundamental Study of Nanoparticles Enabled High Performance Copper

Author
Yao, Gongcheng

Publication Date
2020

Peer reviewed|Thesis/dissertation

UNIVERSITY OF CALIFORNIA

Los Angeles

Fundamental Study of Nanoparticles Enabled High Performance Copper

A dissertation submitted in partial satisfaction of the

requirements for the degree Doctor of Philosophy

in Materials Science and Engineering

by

Gongcheng Yao

2020

ABSTRACT OF THE DISSERTATION

Fundamental Study of Nanoparticles Enabled High Performance Copper

by

Gongcheng Yao

Doctor of Philosophy in Materials Science and Engineering

University of California, Los Angeles, 2020

Professor Xiaochun Li, Chair

High performance (hardness, strength, electrical/thermal conductivity, ductility, Young's modulus, and corrosion resistance, etc.) copper (Cu) based materials are in strong demand in industry for numerous applications. However, it has been a long-standing challenge to achieve high performance Cu by scalable and cost-effective fabrication due to the limits of traditional metallurgy. Pure Cu is very soft and improving the mechanical properties of Cu comes at great expense of electrical and thermal conductivity. The properties of traditional Cu alloys have reached certain limits. Nanotechnology enabled metallurgy provides a new pathway to achieve significant performance enhancement of Cu. The overarching goal of this dissertation is to advance the fundamental understanding of nanoparticle effects on micro/nano-structures and properties of

Cu/Cu alloys, thereby overcoming the existing limits of Cu/Cu alloys. The specific research objectives are to develop effective processing methods to synthesize and disperse suitable nanoparticles in Cu/Cu alloys and to break the limits of grain refinement, phase modification, and property enhancement in Cu/Cu alloys by nanoparticles.

Two ex-situ processing methods were utilized to fabricate Cu matrix nanocomposites with a wide volume fraction range of well-dispersed nanoparticles. To enable the size control of the nanoparticles and expand the choices of nanoparticles for Cu/Cu alloys, novel in-situ synthesis of nanoparticles and Cu matrix nanocomposites were developed. In-situ TiB_2 nanoparticles with an average size of 65 nm in the Cu matrix were synthesized using fluoride salts as precursors and Al as the reduction agent via casting. It was also discovered that Al in molten Cu can stabilize TiB_2 nanoparticles. This finding overcame the challenge of incorporating TiB_2 nanoparticles into molten Cu. In addition, Cu with in-situ W nanoparticles (average size as small as 132.7 nm) was cast using tungsten oxide microparticles as the precursor.

Cu/WC nanocomposites can exhibit simultaneously enhanced microhardness, strength, and Young's modulus without significant degradation of the electrical/thermal conductivity. The as-solidified Cu/40 vol.% WC showed a yield strength over 1000 MPa, a Young's modulus over 250 GPa, and still maintained reasonable electrical and thermal conductivity. In addition, a CuAlMg/TiB_2 nanocomposite was designed and fabricated by casting. Results showed that TiB_2 nanoparticles effectively increased the hardness while causing less deterioration of the electrical conductivity compared to alloying of Al and Mg.

Nanoparticle-enabled grain modification was investigated. Bimodal grain structure has been demonstrated effective to overcome the strength-ductility tradeoff in nanostructured materials. We report a new and scalable method to fabricate bimodal grained metals, *i.e.*, casting

followed by regular hot rolling, when the metals are loaded with nanoparticles. After hot rolling, as WC nanoparticles restricted grain growth, the nanoparticle-rich zones retained ultrafine grains, while the grains in the nanoparticle-sparse zones grew to microscale. This new pathway has great potential to advance the scalable manufacturing of bimodal grained metals for various applications.

In addition, it was discovered that microparticles (CrB and CrB_2) with surface nanofeatures can enable ultrafine/nanograined Cu via slow cooling. CrB/CrB_2 microparticles, formed by coalescence of nanoparticles in Cu matrix, displayed surface nanofeatures, which induced substantial grain refinement and stabilization down to the ultrafine/nanoscale. The UFG Cu/CrB and Cu/CrB_2 samples exhibit exceptional thermal stability, comparable to UFG Cu induced by nanoparticles, without coarsening after annealing at 600 ℃ for 1 h.

The nanoparticle enabled phase modification in Cu alloys was studied targeting the intermetallic phase, the solid solution, and the precipitates, which potentially offers a profound impact on alloy design. High-Al bronze (Cu-14Al) has high hardness, wear resistance, but extremely low ductility, resulted from the brittle intermetallic phases especially at the grain boundaries. Nanoparticles tuned the morphology and distribution of the intermetallic phases, effectively increasing ductility. In addition, Cu-4Al is a corrosion-resistant alloy, comprised of Al solid solution in Cu. Dispersed TiB_2 nanoparticles not only significantly increased its hardness and modulus, but also mitigated the intergranular corrosion, which is anticipated to arise from the reduced grain boundary energy of serrated grain boundaries in the nanocomposite sample and the partially blocked dealumination by nanoparticles at the grain boundaries.

For many alloys, bulky and brittle intermetallic phases are detrimental to their properties, and the refinement of those phases is considered a long-time challenge. Here, we show that nanoparticles can modify and refine such intermetallics to the ultrafine/nanoscale during

solidification. Cu-ZrCuSi pseudo-binary alloy was nano-treated by WC nanoparticles. Significant morphology transformation and refinement of ZrCuSi down to the ultrafine/nanoscale was achieved upon the addition of 4 vol.% WC nanoparticles, which arose from the nanoparticle-enabled phase control during solidification. The CuZrSi alloy with 4 vol.% WC nanoparticles exhibit simultaneously enhanced hardness, strength, and plasticity over pure CuZrSi.

Cu-Cr alloys are a class of high-strength high-conductivity Cu alloys. However, the strength of Cu-Cr alloys by precipitation-hardening has reached a certain limit. Cu-Cr alloy containing W nanoparticles was fabricated. W nanoparticles accelerated the precipitation, leading to a significant reduction in the peak-aging time. Moreover, the nano-treated sample exhibit increased peak microhardness and improved thermal stability. Thus, nano-treating the Cu-Cr alloys is promising to break the limits of current Cu-Cr alloys.

In summary, this dissertation has demonstrated the effectiveness of dispersing nanoparticles into Cu/Cu alloys to achieve high performance Cu. First, nanoparticles with suitable volume fractions can effectively enhance the mechanical properties without significantly deteriorating the electrical/thermal properties of pure Cu. Second, nanoparticles can modify the grain structures of Cu during solidification, enabling bimodal grained and ultrafine grained Cu. Third, nanoparticles can enable Cu alloys with much improved properties by refining intermetallics to ultrafine/nanoscale (CuZrSi alloy), enhancing aging behavior (Cu-Cr alloy), mitigating intergranular corrosion (Cu-4Al), and modifying the morphology and distribution of the brittle phases to improve ductility (Cu-14Al). This approach breaks the limits of traditional liquid metallurgy and lays a foundation for the rational design of high performance metals with dispersed nanoparticles for widespread applications.

The dissertation of Gongcheng Yao is approved.

Dwight C. Streit

Jaime Marian

Yongjie Hu

Xiaochun Li, Committee Chair

University of California, Los Angeles

2020

TABLE OF CONTENTS

ACKNOWLEDGMENTS

First, I would like to express my sincere appreciation and gratitude to my advisor, Prof. Xiaochun Li, for his guidance and support during my Ph.D. study. His expertise, kindness, professionalism, dedication, and motivation have and will continue to inspire me.

I am thankful to other doctoral committee members, *i.e.*, Prof. Jaime Marian, Prof. Dwight C. Streit, and Prof. Yongjie Hu. Their advice has been precious to my research.

I thank my collaborators, *i.e.*, Chezheng Cao, Shuaihang Pan, Zeyi Guan, Jie Yuan, Maximilian Sokoluk, Ting Chiang Lin, Igor De Rosa, and Abdolreza Javadi, for their help with my research.

I would like to acknowledge my colleagues in the SciFacturing Lab. I learned a lot from them through collaborations, discussions, and everyday life. I would also like to thank the lab and department staff that have helped me at UCLA.

I would like to thank my family for their unconditional love and support. Without them, I would never have been who I am today.

Last but not least, I would like to say thank you to all the healthcare workers battling COVID-19 and the essential workers providing support to us.

VITA

- Ph.D., Materials Science and Engineering — UCLA, 2016-2020
- M.S., Materials Processing Engineering — Wuhan University, 2013-2016
- B.S., Metallic Material Engineering — Wuhan University, 2009-2013

Journal Papers

- **G. Yao**, C. Cao, S. Pan, T.-C. Lin, M. Sokoluk, X. Li, High-performance copper reinforced with dispersed nanoparticles, J Mater Sci. 54 (2019) 4423–4432.
- **G. Yao**, C. Cao, S. Pan, J. Yuan, I. De Rosa, X. Li, Thermally stable ultrafine grained copper induced by CrB/CrB2 microparticles with surface nanofeatures via regular casting, Journal of Materials Science & Technology. 58 (2020) 55–62.
- **G. Yao**, C. Cao, S. Pan, X. Li, Facile manufacturing of bimodal grained copper with nanoparticles, Materials Letters. 281 (2020) 128606.
- **G. Yao**, S. Pan, C. Cao, M. Sokoluk, X. Li, Nanoparticle-enabled phase modification (nano-treating) of CuZrSi pseudo-binary alloy, Materialia. 14 (2020) 100897.
- **G. Yao**, J. Yuan, S. Pan, Z. Guan, C. Cao, X. Li, Casting In-Situ Cu/CrBx Composites via Aluminum-Assisted Reduction, Procedia Manufacturing. 48 (2020) 320–324.
- C. Cao, G. Yao, L. Jiang, M. Sokoluk, X. Wang, J. Ciston, A. Javadi, Z. Guan, I.D. Rosa, W. Xie, E.J. Lavernia, J.M. Schoenung, X. Li, Bulk ultrafine grained/nanocrystalline metals via slow cooling, Science Advances. 5 (2019) eaaw2398.
- S. Pan, T. Saso, N. Yu, M. Sokoluk, G. Yao, N. Umehara, X. Li, New study on tribological performance of AA7075-TiB2 nanocomposites, Tribology International. 152 (2020) 106565.
- J. Li, J. Liu, Z. Guan, G. Yao, C. Linsley, B.M. Wu, J.-M. Yang, Fabrication and characterization of bioresorbable zinc/WC nanocomposite springs for short bowel syndrome treatment, Materials Letters. 280 (2020) 128577.
- S. Pan, G. Yao, Z. Guan, N. Yu, M. Sokoluk, X. Li, Kinetics and dynamics of surface thermal oxidation in Al-ZrB2 nanocomposites, Corrosion Science. 176 (2020) 108890.
- C. Cao, G. Yao, M. Sokoluk, X. Li, Molten salt-assisted processing of nanoparticle-reinforced Cu, Materials Science and Engineering: A. 785 (2020) 139345.
- Z. Guan, C.S. Linsley, I. Hwang, G. Yao, B.M. Wu, X. Li, Novel zinc/tungsten carbide nanocomposite as bioabsorbable implant, Materials Letters. 263 (2020) 127282.
- S. Pan, J. Yuan, P. Zhang, M. Sokoluk, G. Yao, X. Li, Effect of electron concentration on electrical conductivity in in situ Al-TiB2 nanocomposites, Appl. Phys. Lett. 116 (2020) 014102.
- S. Pan, G. Yao, J. Yuan, M. Sokoluk, X. Li, Manufacturing of Bulk Al-12Zn-3.7Mg-1Cu Alloy with TiC Nanoparticles, Procedia Manufacturing. 48 (2020) 325–331.
- Z. Guan, G. Yao, Y. Zeng, X. Li, Fabrication and Characterization of In Situ Zn-TiB2 Nanocomposite, Procedia Manufacturing. 48 (2020) 332–337.

- J. Yuan, M. Zuo, M. Sokoluk, G. Yao, S. Pan, X. Li, Nanotreating High-Zinc Al–Zn–Mg–Cu Alloy by TiC Nanoparticles, in: A. Tomsett (Ed.), Light Metals 2020, Springer International Publishing, Cham, 2020: pp. 318–323.
- M. Sokoluk, G. Yao, S. Pan, C. Cao, X. Li, High Strength Nanotreated Filler Material for TIG Welding of AA6061, in: A. Tomsett (Ed.), Light Metals 2020, Springer International Publishing, Cham, 2020: pp. 380–385.
- S. Pan, G. Yao, M. Sokoluk, Z. Guan, X. Li, Enhanced thermal stability in Cu-40 wt% Zn/WC nanocomposite, Materials & Design. 180 (2019) 107964.
- S. Pan, Z. Guan, G. Yao, C. Cao, X. Li, Study on electrical behaviour of copper and its alloys containing dispersed nanoparticles, Current Applied Physics. 19 (2019) 452–457.
- S. Pan, G. Yao, J. Liu, X. Li, Effect of Hot Rolling on Naval Brass/WC Nanocomposite, Procedia Manufacturing. 34 (2019) 193–196.
- S. Zheng, M. Sokoluk, G. Yao, I. de Rosa, X. Li, Fe–Ni Invar alloy reinforced by WC nanoparticles with high strength and low thermal expansion, SN Applied Sciences. 1 (2019) 172.
- S. Pan, G. Yao, J. Yuan, X. Li, Electrical Performance of Bulk Al–ZrB2 Nanocomposites from 2 K to 300 K, in: T.S. Srivatsan, M. Gupta (Eds.), Nanocomposites VI: Nanoscience and Nanotechnology in Advanced Composites, Springer International Publishing, Cham, 2019: pp. 63–70.
- A. Javadi, S. Pan, C. Cao, G. Yao, X. Li, Facile synthesis of 10 nm surface clean TiB2 nanoparticles, Materials Letters. 229 (2018) 107–110.
- G. Yao, Q.S. Mei, J.Y. Li, C.L. Li, Y. Ma, F. Chen, M. Liu, Cu/C composites with a good combination of hardness and electrical conductivity fabricated from Cu and graphite by accumulative roll-bonding, Materials & Design. 110 (2016) 124–129.
- G. Yao, Q. Mei, J. Li, C. Li, Y. Ma, F. Chen, G. Zhang, B. Yang, G. Yao, Q. Mei, J. Li, C. Li, Y. Ma, F. Chen, G. Zhang, B. Yang, Hard Copper with Good Electrical Conductivity Fabricated by Accumulative Roll-Bonding to Ultrahigh Strains, Metals. 6 (2016) 115.
- Y. Li, J.Y. Li, M. Liu, Y.Y. Ren, F. Chen, G. Yao, Q.S. Mei, Evolution of microstructure and property of NiTi alloy induced by cold rolling, Journal of Alloys and Compounds. 653 (2015) 156–161.

Patents

- X. Li, C. Cao, G. Yao, S. Pan, Scalable Manufacturing of Cu Nanocomposites with Unusual Properties, 2020.
- X. Li, J. Yuan, G. Yao, S. Zheng, Interface-controlled In-situ Synthesis of Nanostructures in Molten Metals for Mass Manufacturing, 2020.

Chapter 1 Introduction

1.1 Motivation

High performance materials are one of the keys to the pursuit of higher system performance and energy efficiency, among which, copper and its many varieties are of interest due to their high electrical and thermal conductivities, malleability, and resistance to corrosion. Pure copper has good electrical conductivity, but it is too soft for many applications. High performance copper-based materials are in strong demand in industry for numerous applications, e.g., high-speed railway contact wires [1], electric resistance welding electrodes [2], lead frames [3], rotors for electric motors [4], and propellers. Two categories of high performance copper are pursued: (1) high strength high conductivity copper; (2) high performance copper alloys with enhanced ductility, corrosion resistance, strength, Young's modulus, etc. For instance, in electric motors, the achievable revolutions per minute and the rotor diameter are limited by the centrifugal forces and the low strength of the die cast pure copper. Developing high strength high conductivity copper will help increase its the energy efficiency. It was reported that even a 1% increase in motor efficiency can save $1.1 billion in energy costs annually, according to the U.S. Department of Energy [4].

Cu alloys have not achieved the desired high performance due to the restrictions by traditional metallurgy. Solid solution strengthening will deteriorate electrical conductivity significantly due to the severe electron scattering by solute atoms. Precipitation strengthening is strictly limited by the phase diagram causing alloy properties to reach limits. Other inherent issues of alloying are that Young's modulus not improved; softening at elevated temperatures; brittleness caused by intermetallics. Apart from alloying, severe plastic deformation (SPD) was utilized to increase the strength of copper/copper alloys, but it also significantly decreases the ductility. While

nano-twinned copper was proved to have high strength and high electrical conductivity, the fabrication method, i.e., electrodeposition, limits its application. In addition, rapid cooling was adopted to obtain in-situ nanophase. However, rapid cooling also increases the manufacturing cost. Therefore, it still remains a dilemma.

Here we introduce nanoparticles to copper/copper alloys, thereby utilizing nanoparticles to break the barriers of traditional liquid metallurgy and achieve significant performance enhancement that cannot be achieved by conventional methods. First, it is expected that nanoparticles can strengthen copper while not severely affecting electrical conductivity. Moreover, nanoparticles can modify the micro/nano-structures: tune grain structures and modify the phases to impart superior properties to copper/copper alloys.

1.2 Research Objectives

The overarching goal of the proposed research is to advance the fundamental understanding of nanoparticle effects on tuning micro/nano-structure and enhancing properties of copper/copper alloys in order to enable a rational design of high performance copper/copper alloys. Specific research objectives are to develop effective processing routes to synthesize and disperse suitable nanoparticles in copper/copper alloys; understand nanoparticle effects on copper/copper alloys including nanoparticle interaction with micro/nano-structure and the resultant property evolution; break the limits of grain refinement, phase modification, and property enhancement in Cu/Cu alloys by nanoparticles.

1.3 Work Summary

The following chapters of this dissertation will be organized as follows.

- Chapter 2 presents the literature review related to this study.
- Chapter 3 introduces the molten-salt assisted ex-situ and in-situ fabrication of Cu matrix nanocomposites and the resultant property enhancement.
- Chapter 4 studies the grain modification in Cu enabled by nanoparticles.
- Chapter 5 investigates the phase modification in Cu alloys enabled by nanoparticles.
- Chapter 6 makes conclusions of this study.
- Chapter 7 recommends research directions for future work.

Chapter 2 Literature Review

2.1 Basics about Copper

Copper is the oldest engineering metal in human history, first used by mankind more than 10,000 years ago [5]. Decorative pendants, hammered to shape from nuggets of "native copper," i.e., pure copper together with copper-bearing ores, were found in the Middle East, dating back to 8700 B.C. [5]. The first metal objects were fabricated from smelted copper. Artifacts made from smelted copper were found in Turkey, dating back to 7000 B.C. [5]. Copper is also the first metal being cast, i.e., 4000 B.C., and the first being alloyed with another metal, tin, to create bronze, i.e., 3500 B.C., leading to the famous Bronze Age [6]. Interestingly, the iron materials, which are common today started in human history much after the ending of the Bronze Age [5].

The Industrial Revolution and especially the discovery and development of electricity dramatically changed the applications of copper and its alloys. Nowadays, copper is a major group of materials that are essential to our lives, ranking third in consumption only after iron and aluminum in the US. Their popularity can be attributed to the facts that copper has excellent electrical/thermal conductivities, high corrosion resistance, ease fabrication, antimicrobial property, color for decorative purposes, and good strength and fatigue resistance. Interestingly, it was reported that copper base alloys containing more than 65% copper can effectively kill several bacteria [4]. Using copper in hospitals, heating, ventilation, air conditioning systems can be very beneficial for human health. It was reported that electrical applications account for more than 60% of the copper and its alloys consumed in the U.S [5]. They are widely used in building construction (plumbing goods, building wires, etc.), electrical applications (electrical contacts, resistors, etc.), electronics (printed circuit boards, connectors, lead frames, etc.), communications (cables), transportation (motor vehicles, marine applications, etc.), industrial machinery and equipment

(heat exchangers and condensers, bearings, plastic injection molds, container for nuclear wastes, etc.), consumer products (coinage, musical instruments, etc.), health related purposes (nutrients, antimicrobial materials) and arts (pigments, statues, etc.). Copper materials are also becoming more and more important for superconductors, photovoltaic (PV) systems, solar heating, desalination of water, etc [5].

It was estimated by the U.S. Geological Survey that every American born in 2008 will use 1,309 pounds of copper during their lifetime. It was also reported that in an average single-family home, 439 pounds of copper will be found, including 195 pounds for building wire, 151 pounds for plumbing tube, fittings, valves, 24 pounds for plumbers' brass goods, 47 pounds for built-in appliances, 12 pounds for builders' hardware, and 10 pounds for other wire and tube [4]. On the other hand, copper is also a very abundant natural resource. The total deposits of copper on earth is about 8.1 trillion pounds. Only 1.1 trillion of them have been mined [4]. More importantly, as copper has the highest recycling rate among metals, a lot of the mined copper is still in circulation. Each year in the USA., nearly 45% as much copper is recovered from recycled material as is derived from newly mined ore [4].

Other elements are added to copper to improve certain properties. Currently, there are more than 570 copper alloys listed with the American Society for Testing and Materials International [4]. They are identified by numbers preceded by a "C" and are assigned and reviewed by the Copper Development Association for ASTM, more than 350 of which have been acknowledged by the U.S. Environmental Protection Agency as antimicrobial [4]. The main alloying elements are zinc, tin, lead, and nickel following descending order.

The elements most commonly alloyed with copper are aluminum, nickel, silicon, tin, and zinc [5]. Other elements and metals are alloyed in small quantities to improve certain material

characteristics, such as strength, corrosion resistance or machinability. Copper and its alloys are divided into nine major groups, as shown in Table 2-1 [5].

Table 2-1. Major nine groups of copper alloys [5]

Groups	Composition
Coppers	a minimum of 99.3% Cu
High-copper alloys	up to 5% alloying elements
Copper-zinc alloys (brasses)	up to 40% Zn
Copper-tin alloys (phosphor bronzes)	up to 10% Sn and 0.2% P
Copper-aluminum alloys (aluminum bronzes)	up to 10% Al
Copper-silicon alloys (silicon bronzes)	up to 3% Si
Copper-nickel alloys	up to 30% Ni
Copper-zinc-nickel alloys (nickel silvers)	up to 27% Zn and 18% Ni
Special alloys	contain alloying elements to enhance a specific property or characteristics

The more detailed classification of coppers and copper alloys with UNS number and composition is shown in Table 2-2 [5].

Table 2-2 General classification of coppers and copper alloys with UNS number and composition [5]

Generic name	UNS No.	Composition
Wrought alloys		
Coppers(a)	C10100–C15815	>99% Cu
High-copper alloys(b)	C16200–C19900	>96% Cu
Brasses	C20100–C28000	Cu-Zn
Leaded brasses	C31200–C38500	Cu-Zn-Pb
Tin brasses	C40400–C48600	Cu-Zn-Sn-Pb
Phosphor bronzes	C50100–C52480	Cu-Sn-P
Leaded phosphor bronzes	C53400–C54400	Cu-Sn-Pb-P
Copper-phosphorus and copper-silver-phosphorus alloys(c)	C55180–C55284	Cu-P-Ag
Aluminum bronzes	C60800–C64210	Cu-Al-Ni-Fe-Si-Sn
Silicon bronzes	C64700–C66100	Cu-Si-Sn
Other copper-zinc alloys	C66300–C69710	Cu-Zn-Mn-Fe-Sn-Al-Si-Co
Copper nickels	C70100–C72950	Cu-Ni-Fe
Nickel silvers	C73500–C79830	Cu-Ni-Zn
Cast alloys		
Coppers(a)	C80100–C81200	>99% Cu
High-copper alloys(d)	C81400–C82800	>94% Cu
Red and leaded red brasses	C83300–C83810	Cu-Sn-Zn-Pb (82–94% Cu)
Semi-red and leaded semi-red brasses	C84200–C84800	Cu-Sn-Zn-Pb (75–82% Cu)
Yellow and leaded yellow brasses	C85200–C85800	Cu-Zn-Pb
Manganese bronzes and leaded manganese bronzes(e)	C86100–C86800	Cu-Zn-Mn-Fe-Pb
Silicon brasses/bronzes	C87300–C87800	Cu-Zn-Si
Copper-bismuth and copper-bismuth-selenium alloys	C89320–C89940	Cu-Sn-Zn-Bi-Se
Tin bronzes	C90200–C91700	Cu-Sn-Zn
Leaded tin bronzes	C92200–C94500	Cu-Sn-Zn-Pb
Nickel-tin bronzes	C94700–C94900	Cu-Ni-Sn-Zn-Pb
Aluminum bronzes	C95200–C95900	Cu-Al-Fe-Ni
Copper nickels	C96200–C96950	Cu-Ni-Fe
Nickel silvers	C97300–C97800	Cu-Ni-Zn-Pb-Sn
Leaded coppers	C98200–C98840	Cu-Pb
Special alloys	C99300–C99750	Cu-Zn-Mn-Al-Fe-Co-Sn-Pb

2.2 Copper Alloys and Their Limits

In alloy system, the material can be strengthened by solid solution strengthening, precipitate strengthening, spinodal strengthening, and strain hardening.

2.2.1 Solid Solution Strengthening

For solid solution strengthening, as solute atoms distort the lattice of copper, the electrical conductivity will be significantly decreased due to the increased scattering of electrons. Effects of alloying elements on the conductivity of pure copper are further illustrated in Figure 2-1 [5]. As

shown in Figure 2-1, Ti, P, and Fe show very detrimental effects while Cd, Ag, and Zn have milder effects on conductivity.

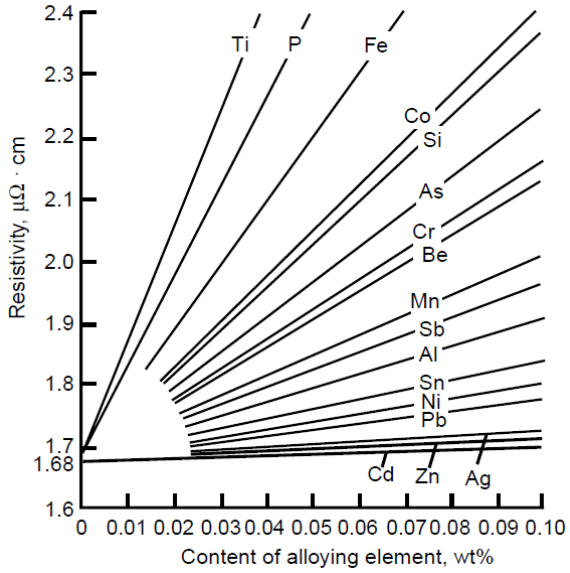

Figure 2-1 Effect of alloying element contents on the electrical conductivity of copper [5]

2.2.2 Precipitation Strengthening

Elements that have a low room temperature solubility to copper and forms a solid solution at high temperature are added to the metal matrix. After it is subjected to solution heat treatment and an aging treatment, the material is hardened and electrical conductivity is increased. The principles of precipitation hardening processing are shown in Figure 2-2 [7].

The major precipitate hardened copper alloy systems include: Cu-Cr, Cu-Be, Cu-Fe-P, Cu-Ni-Si, Cu-Zr, Cu-Cr-Zr, Cu-Cr-Nb.

The disadvantages of precipitates hardened alloys should also be considered. Firstly, at high temperatures, the Cu alloys will soften due to the dealloying or coarsening of the strengthening precipitates [8]. Secondly, the amount of precipitates is dictated by phase diagrams (e.g., not to exceed point M in Figure 2-2a), which puts a limit on achieving a sufficient volume

fraction of the strengthening phase. Moreover, it is hard to precipitate all the alloying elements out of the solid solution, which will be detrimental to the electrical/thermal conductivity. Thirdly, in order to produce the well-dispersed fine precipitates, several steps of thermomechanical processing are often needed.

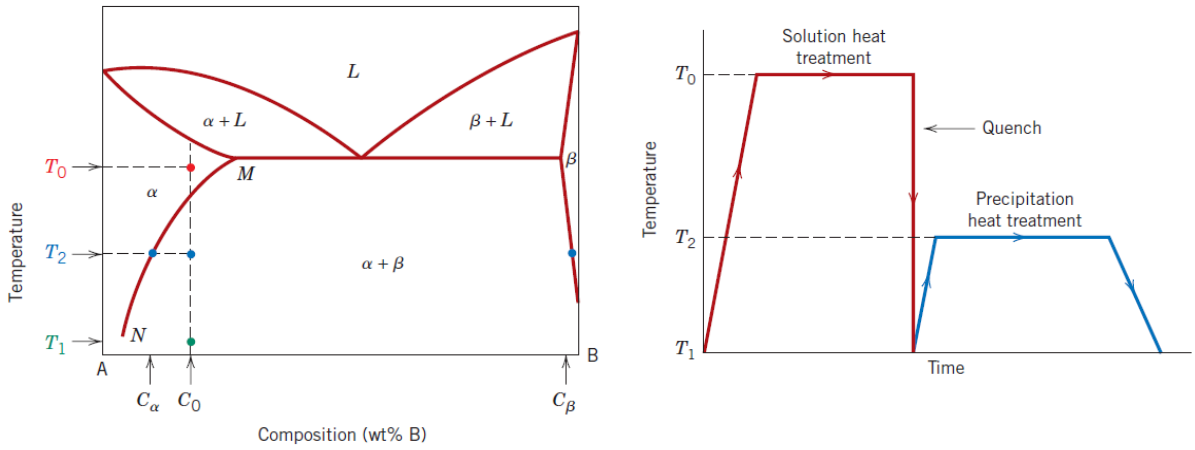

Figure 2-2 Principles of precipitation hardening processing: (a) phase diagram; (b) heat treatment routes

2.2.3 Spinodal Hardening

Alloys in the Cu-Ni-Sn system in the range of Cu-4Ni-4Sn to Cu-15Ni-8Sn exhibit spinodal decomposition [5]. Spinodal hardening is similar to precipitation hardening except that one phase decomposes into two coherent phases without a nucleation barrier.

2.2.4 Currently Available High-strength High-conductivity Cu Alloys

Currently available high strength high-conductivity copper alloys are shown in Table 2-3 [9]. The desired property such as 600 MPa in tensile strength, 80% IACS in electrical conductivity, and 10% in elongation is not achieved yet.

Table 2-3 Compositions and properties of high-strength high-conductivity Cu alloys

Materials	Composition	Ultimate Tensile strength (MPa)	Electrical conductivity (IACS, %)	Thermal conductivity ($W*m^{-1}K^{-1}$)	Elongation (%)
Cu-Fe	Cu-2.35Fe-0.12Zn-0.03P	362-568	55-65	262	4-5
	Cu-1.5Fe-0.8Co-0.6Sn-0.05P	360-670	50	197	3-13
	Cu-0.6Fe-0.2P-0.04Mg	380-500	80	173	2-10
	Cu-0.1Fe-0.034P	294-412	90	364	5-10
Cu-Cr	Cu-0.3Cr-0.1Zr-0.05Mg	590	82	301	8
	Cu-0.3Cr-0.25Sn-0.2Zn	560	75	301	13
Cu-Ni-Si	Cu-3.2Ni-0.7Si-0.3Zn	490-588	40	220	8-15
	Cu-3.2Ni-0.7Si-1.25Sn-0.3Zn	667	35	N/A	9
	Cu-3.0Ni-0.6Si-0.1Mg	585-690	35-40	147-190	2-6
Cu-Sn	Cu-2Sn-0.2Ni-0.05P	490-588	35	155	9
Others	Cu-0.1Zr	294-490	95	360	3-21
	Cu-0.11Ag-0.06P	275-550	86	345	3-40

2.3 Approaches for Copper to Achieve High-strength High-conductivity

2.3.1 Severe Plastic Deformation

Severe plastic deformation (SPD) has been conducted on copper to induce an ultrafine grain structure and lead to a significant strengthening without decreasing its electrical/thermal conductivity much. It was reported that a deoxidized low phosphorous (DLP) processed by accumulative roll-bonding (ARB) can have a yield strength of 472 MPa while possessing an electrical conductivity larger than 74% IACS [10]. Cu/Nb composites fabricated by bounding and drawing showed that the ultimate tensile strength reached 1 GPa while the electrical conductivity was higher than 70%IACS at room temperature [11]. Cu/Nb nanostructured multilayers were also fabricated by accumulative roll-bonding (ARB) [12]. The microstructure is shown in Figure 2-3 [12]. However, after SPD processing, the ductility of the samples also dropped significantly, and the anisotropy of properties remains an issue. Besides, the SPD processing is hard to scale up.

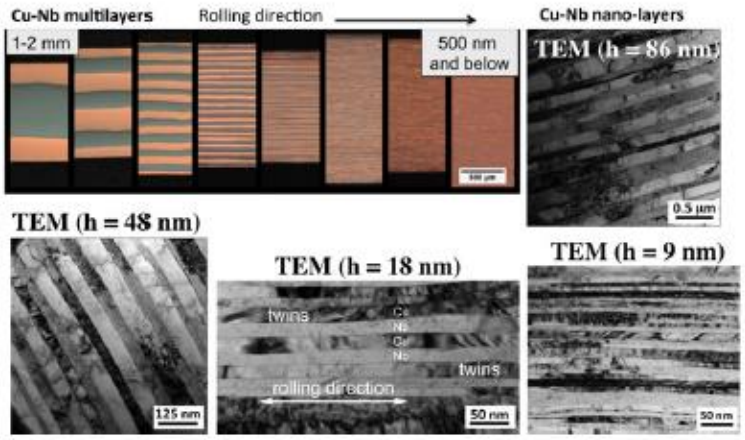

Figure 2-3 Micorstructure of Cu/Nb multilayers fabricated by accumulative roll-bonding

For Cu-Ag alloys, drawing (although not to the amount of deformation compared to SPD) was applied to refine the microstructure, The intermediate-heat-treated Cu-16 at%Ag with 99% reduction in area had an ultimate tensile strength of 1000 MPa and an electrical conductivity of 80% IACS at room temperature [13]

2.3.2 Rapid Cooling

(1) Rapid cooling to form in situ nanoparticles through reaction in molten metal

A copper matrix composite reinforced by turbulent in situ TiB_2 nanoparticle was prepared through the reactions of boron and titanium under rapid cooling [14]. By doing so, the size of TiB_2 particles was reduced to ~50 nm, as shown in Figure 2-4 [14]. This composite showed a very high performance: 5.2 GPa hardness and 78% IACS when the wheel speed of the cooling system was 4000 rpm.

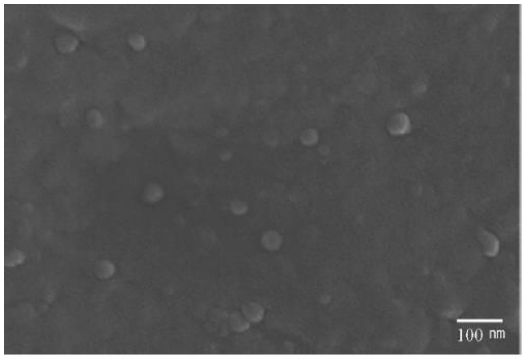

Figure 2-4 Micorstructure of Cu/TiB_2 nanocomposites fabricated by turbulent in situ mixing

(2) Rapid cooling to form fine second phase directly from molten alloy through phase transformation

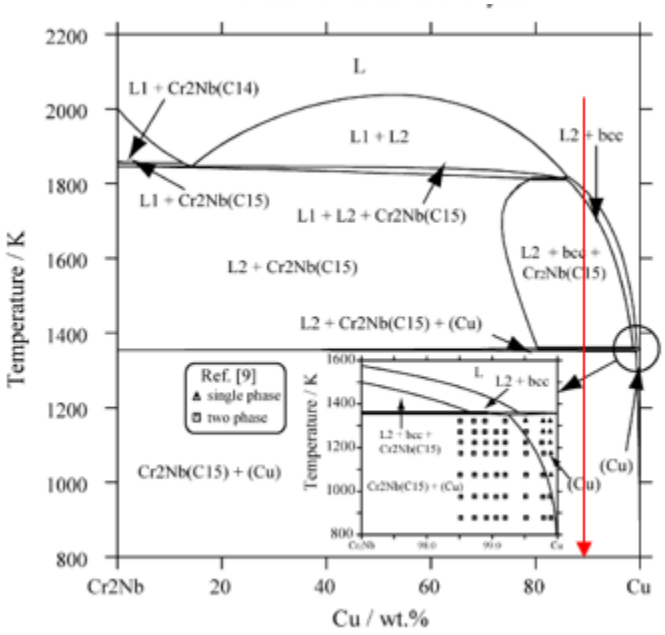

Figure 2-5 Pseudo-binary Phase diagram of Cu-Cr_2Nb

During manufacturing of the Cu-8 at.% Cr-4 at.% Nb alloy, chill block melt spinning (CBMS) had to be used to allow the formation of fine Cr_2Nb particles directly from the melt, as shown in Figure 2-5 [15] by the red arrow in the phase diagram. By rapid solidification, Cr_2Nb particle size was reduced to submicron compared to hundreds of microns for a regularly cooled sample, as shown in Figure 2-6.

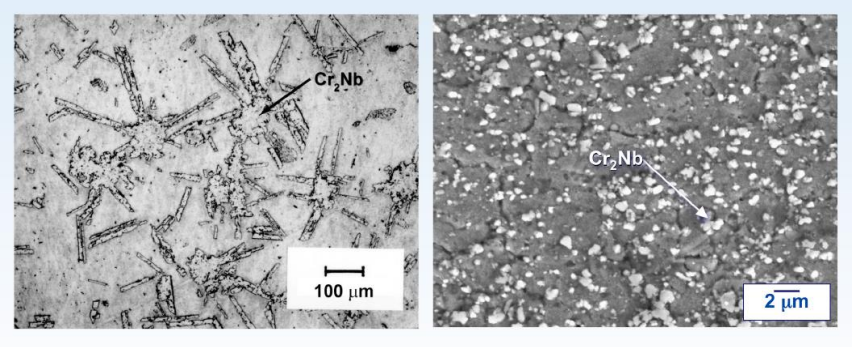

Figure 2-6 Micorstructure of Cu-Cr-Nb alloy: (a) regularly cast; (b) P/M from rapidly cooled powders

2.3.3 Nano-twinned Copper

Ultrahigh strength and high electrical conductivity copper was achieved by inducing a high density of nanoscale growth twins [16]. They showed a tensile strength about 10 times higher than that of conventional coarse-grained copper, while retaining an electrical conductivity comparable to that of pure copper, as shown in Figure 2-7. The ultrahigh strength originates from the effective blockage of dislocation motion by numerous coherent twin boundaries that possess an extremely low electrical resistivity, which is not the case for other types of grain boundaries. However, the fabrication method, i.e., electrodeposition, severely limits the sample size.

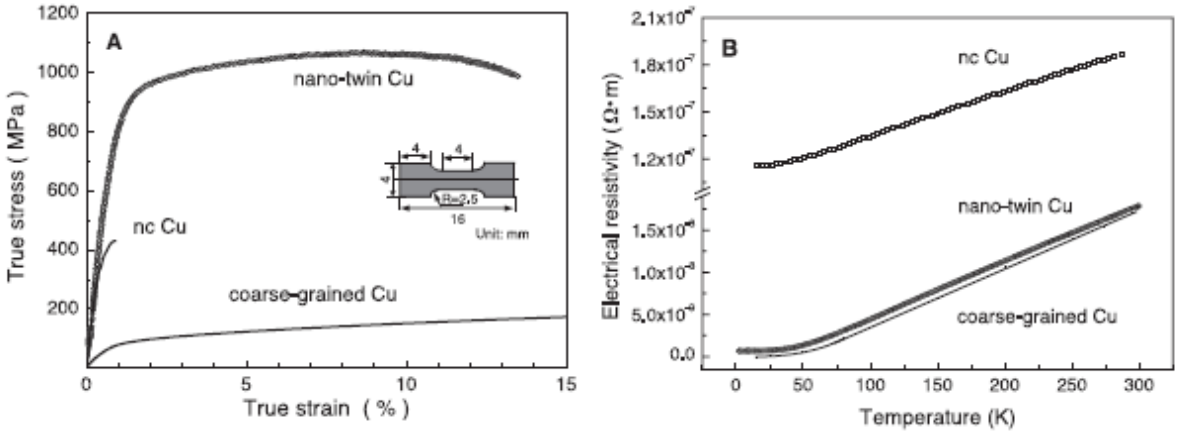

Figure 2-7 Tensile and electrical properties of nano-twin Cu, nc Cu, and coarse-grained Cu

2.4 Nanoparticles Self-dispersion and Stabilization Theory in Molten Metals

In 2015, a breakthrough in discovering a thermally-activated nanoparticle self-dispersion and stabilization mechanism in molten metals, which was published in Nature [17], was made to enable a major advance in solidification processing of Super Metals, defined as metals with populous dispersed nanoparticles offering unprecedented mechanical properties/performance (e.g., strength, ductility, stiffness, wear resistance, and creep resistance), thermophysical properties, and so on.

In this theory, three interactions between nanoparticles were considered, i.e., interfacial energy (short-range), Van der Waals potential (long-range), Brownian motion energy. Nanoparticles can be self-dispersed and stabilized by a synergy of reduced Van der Waals forces between nanoparticles to reduce attraction, high thermal energy of the nanoparticles for them to disperse, and a high energy barrier preventing them from sintering, as shown in Figure 2-8.

The Van der Waals attractions between two nanoparticles can be estimated by Equation 2-1.

$$W_{vdw} = -\frac{(\sqrt{A_{NP}}-\sqrt{A_{liquid}})^2}{6}\frac{R}{D} \qquad \text{Equation 2-1}$$

where D is the distance in nm between nanoparticles, A is the Hamaker constant, R is the nanoparticle radius. As shown in Eq. 2.1, when the Hamaker constants of the nanoparticles and the molten metal are close, W_{vdw} can be reduced. Also, reducing R will also reduce Vander Waals attraction. Eq. is only effective when D is larger than two atomic layers of molten metal.

The thermal energy for Brownian motion of nanoparticles can be estimated by Equation 2-2.

$$E_b = kT \qquad \text{Equation 2-2}$$

where k is Boltzmann constant, T is absolute temperature. At high temperature, it is possible for the Brownian motion energy to be larger than Van der Waals potential, so that nanoparticles can break away from the attraction and thus disperse.

At high temperatures, nanoparticles may contact and sinter together, driven by the reduction of interfacial energy. When the separation between two nanoparticles is smaller than one atomic layer of molten metal, the molten metal will be squeezed out. Therefore, the nanoparticle–molten metal interface will be replaced by the nanoparticle surfaces. The interfacial energy increase will be given by Equation 2-3.

$$W_{barrier} = S\left(\sigma_{NP} - \sigma_{NP-liquid}\right) = S\sigma_{liquid}\cos\theta \quad \text{Equation 2-3}$$

where S is the effective area, σ_{NP} is the surface energy of the nanoparticles, $\sigma_{NP-liquid}$ is the interfacial energy between the nanoparticle and molten metal, θ is the contact angle of molten metal on the nanoparticle surface. It suggests that the smaller the wetting angle (θ), the larger the energy barrier preventing the nanoparticles from sintering together.

What can be learned from this theory is that to achieve good dispersion and distribution of nanoparticles in molten metals, nanoparticle size and the wetting angle between nanoparticle and the molten metal should be small. This provides a solid theoretical foundation to guide us on the matrix metal–reinforcement nanoparticle selection for further experimental studies.

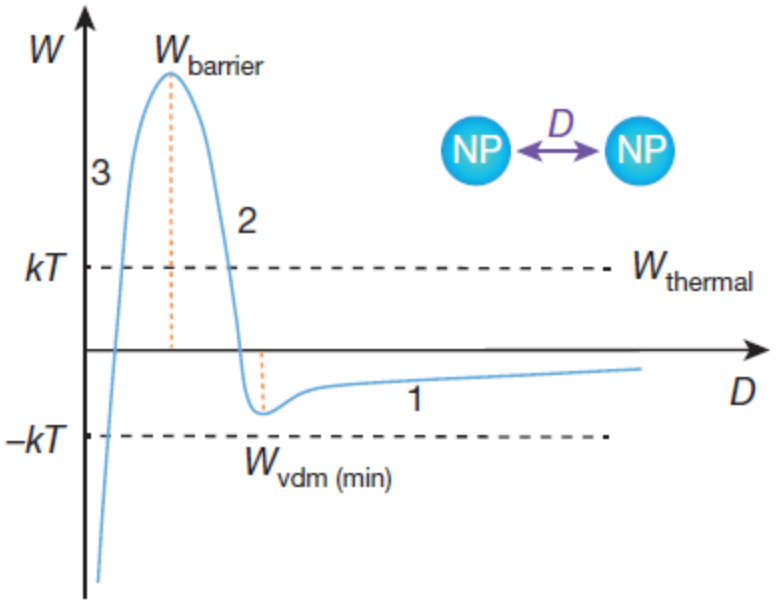

Figure 2-8 The principle of self-dispersion and stabilization of nanoparticles in molten metals

2.5 Nanoparticles Enabled Enhancement of Mechanical Properties

2.5.1 Orowan Strengthening

The strength of material relies on to what degree it resists the movement of dislocation. Nanoparticles can impede dislocation motion, thereby increasing the strength of the material. There are two ways that dislocations can bypass the nanoparticle obstacles, i.e., cutting through them or bowing/looping around them. As for nanocomposites, where nanoparticles often have different crystal structure from the matrix and also the size of nanoparticles exceeds 5-30 nm, the nanoparticles are more likely to be non-deformable. Therefore, dislocations usually bypass nanoparticles by the Orowan looping mechanism. The increase in yield strength caused by Orowan strengthening of dispersed nanoparticles is given by Equation 2-4.

$$\Delta\sigma_{Orowan} = \frac{\varphi G_m b}{d_p}\left(\frac{6V_p}{\pi}\right)^{1/3} \qquad \text{Equation 2-4}$$

where G_m, b, V_p, and d_p are the shear modulus of the matrix, the Burgers vector, the volume fraction, and the size of the nanoparticles. φ is constant. As shown in Eq. 1, the more prominent Orowan strengthening effect arises from smaller nanoparticle size and larger nanoparticle volume fraction.

2.5.2 Load Bearing

When the composite is loaded, the load can be transferred from the matrix through the matrix-reinforcement interface to the harder and stiffer reinforcements, meaning the reinforcements can bear more load. While particles can be different from fibers in terms of bearing load, a modified shear-lag model was proposed by Nardone and Prewo to address the particulate materiasl. When the reinforcement particles are equiaxed, the strengthening can be estimated by Equation 2-5 [18].

$$\Delta\sigma_{LB} = \frac{1}{2} V_p \sigma_i \quad \text{Equation 2-5}$$

where V_p is particle volume fraction, σ_i is the strength of the interfacial bonding. A strong interfacial bonding is essential to achieve the load bearing effect.

2.5.3 Hall-Petch Effect

Grain boundaries can be effective barriers to dislocation motion. The efficacy of the strengthening effect induced by grain boundaries increases with the angle of misorientation. As grain size becomes smaller, there will be more grain boundaries to impede dislocation slips, resulting in greater strengthening, which is known as the famous Hall-Petch effect. The increase in yield strength due to Hall-Petch effect can be calculated by Equation 2-6 [19].

$$\Delta\sigma_y = \frac{k}{\sqrt{d}} - \frac{k}{\sqrt{d_0}} \qquad \text{Equation 2-6}$$

where k is a constant, d is grain size of the matrix after nanoparticle addition, d_0 is the original grain size of the matrix.

It should be noted that Eq. 2.6 may not be valid when the grain size goes under 10s nm as grain boundary rotation becomes the major mechanism for deformation, causing the reverse Hall-Petch effect.

2.5.4 Sum of the Strengthening Effects

The total strength of the composite can be calculated by simply adding all the strengthening effects together as shown in Equation 2-7 [20].

$$\sigma_C = \sigma_m + \sum_i \Delta\sigma_i \qquad \text{Equation 2-7}$$

where σ_C is the yield strength of the composite, σ_m is the yield strength of the unreinforced matrix, $\Delta\sigma_i$ is the individual strengthening effect.

Some other studies suggested other approaches to calculate σ_C considering the superposition of the strengthening effects. One example is shown in Equation 2-8 [20].

$$\sigma_C = \sigma_m + \sqrt{\sum_i \Delta\sigma_i{}^2} \qquad \text{Equation 2-8}$$

2.6 Nanoparticles Enabled Grain Refinement

The importance of grain refining has long been recognized in casting. Among the benefits of a fine-grain microstructure are enhanced mechanical properties, reduced anisotropy, improved distribution of the second phase, and shorten homogenization time for alloys.

The main mechanisms of nanoparticle enabled grain refinement include nanoparticle enabled effective nucleation and growth restriction.

In addition, in the solid state, the dispersed nanoparticles can impede the grain growth due to the Zener pinning effect. Maximum mean grain size can be theoretically estimated by Equation 2-9.

$$D_{max} = \frac{4r}{3f_v} \qquad \text{Equation 2-9}$$

where r is the nanoparticle radius and f_v is the volume fraction of the nanoparticles.

During solidification, it is known that heterogeneous sites, e.g., inclusions and mold wall, can decrease the nucleation energy barrier, thereby increasing the nucleation rate. The volume rate of heterogeneous nucleation can be calculated as Equation 2-10.

$$N_{het} = fC\exp\left(-\frac{\Delta G^*_{hom} S(\theta)}{kT}\right) \qquad \text{Equation 2-10}$$

where f denotes the rate that each nucleus can be made supercritical, C is the number of atoms in contact with heterogeneous nucleation sites per unit volume, ΔG^*_{hom} is the activation energy barrier against homogeneous nucleation, k is Boltzmann's constant, T is absolute temperature, θ is given by the condition that the interfacial tensions balance as shown in Figure 2-9, $S(\theta)$ is a function of θ, which increases with increasing θ. It can be seen from Equation 2-10 that nanoparticles that have large surface areas and wet the metal well will have a larger C value and smaller $S(\theta)$ value. Therefore, nanoparticles will promote the nucleation of the metals.

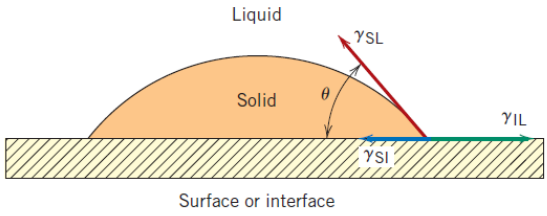

Figure 2-9 Heterogeneous nucleation of a solid from a liquid

According to the theory of heterogeneous nucleation mentioned above, the grain refinement potency of inoculant nanoparticles depends on the wetting angle. Low values of θ are favored by a low energy interface between the inoculant and solid nucleus. Thus, in general, a better lattice matching between the particle and the solid suggests higher grain refinement potency. However, other factors, e.g., surface roughness and surface segregation, also contribute to the effectiveness. In addition, the nanoparticles should not agglomerate or float. To achieve a fine grain size, the concentration of the nucleating agents is also important.

Al-5Ti-1B master alloy is widely used in the aluminum industry as inoculants. The adsorption of Al_3Ti on the TiB_2 particle promotes the heterogeneous nucleation of Al grain on the TiB_2 particle and thereby enhances the grain refinement potency of the TiB_2 particle [21,22]. The grain size achievable by inoculation can only be down to tens of micrometers in common solidification practice [23].

Grain refining via peritectic reaction is another well-known technique employed especially for aluminum alloys. The grain refining effects on copper by the addition of iron and electromagnetic stirring was studied [24]. It was found that in the hypoperitectic region, the refinement mechanism was due to the solute build-up ahead of the interface. In the hyperperitectic region, the mechanism can be attributed to either the growth restrictive nature of the peritectic reaction or the presence of iron primaries.

It was reported that trace amount modified SiC nanoparticles (0.05 wt.%) coupled with electromagnetic stirring (EMS) remarkably refined $CuNi_{10}Fe_1Mn$ alloy grain from 2.15mm to 0.52mm [25]. The original inhomogeneous coarse equiaxed and columnar crystal macrostructure developed into homogeneous refined equiaxed crystal macrostructure. However, as they directly

wrap the nanoparticles and put them in the mold, the amount of nanoparticles that could be loaded into the alloy was small, which limited the refining effect.

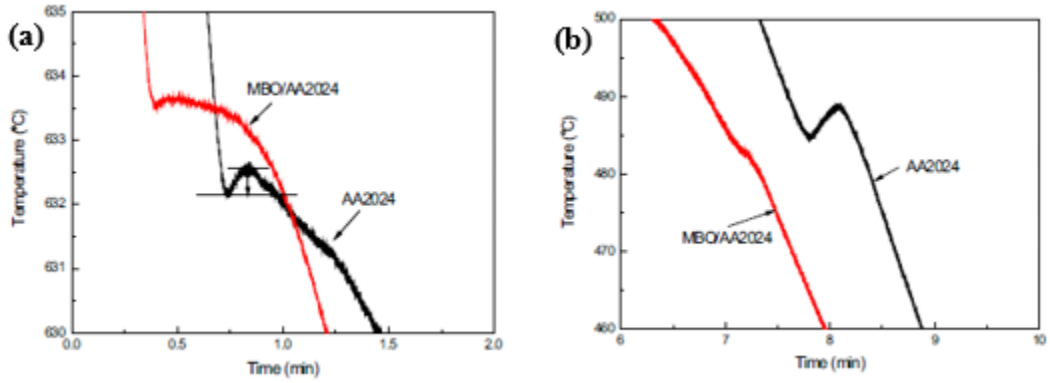

Figure 2-10 Cooling curves of the AA2024 and AA2024 MBO from (a) 635-630 °C; (b) 500-460 °C

The grain refinement in the MBO whisker ($Mg_2B_2O_5$) reinforced AA2024 matrix composite and the solidification behavior was studied. MBO reduced the primary α-Al phase grain size from 116 μm to 82 μm by restricting its growth. MBO also served as heterogeneous nucleation sites for the eutectic phase due to the good lattice match although no obvious refinement of the eutectic phase was found. As shown in Figure 2-10, the nucleation behavior was indicated by the cooling curves. While both AA2024 and MBO/AA2024 exhibited a clear supercooling (4.2 °C) as the nucleation of the primary phase happened (Figure 2-10a), there was no supercooling observed for the solidification of the eutectic phase in MBO/AA2024 composite (Figure 2-10b).

2.7 Nanoparticles Enabled Phase Modification

Incorporating nanoparticles can modify the phases in alloys. With proper phase morphology control, the properties of the materials can be enhanced. However, in literature, the

amount of nanoparticles that can be incorporated into the alloys were very low, which resulted in very limited modification of the phases.

In eutectic systems where one phase solidifies in a faceted manner and the other nonfaceted, e.g., Fe-C system and Al-Si system, the morphology of the faceted growing phase will be isolated flakes or needles embedded in the matrix of the other phase, which will have detrimental effects on mechanical properties. Therefore, the modification of this type of microstructure has drawn much attention. Two ways were proposed to change the originally faceted growing phase from a flake morphology to a fibrous morphology: 1) rapid cooling; 2) minor additions of a chemical agent, e.g., sodium, sodium salts, strontium. Although the underlying mechanisms of how impurity additions change the microstructure is still controversial, it has been discussed based on: 1) phase equilibria; 2) different nucleation or growth kinetics [26]. For example, it was suggested that the modification of Si phase in the Al-Si eutectic by the addition of sodium or sodium salts was due to the increased supercooling, which led to a higher nucleation rate. It was also suggested that sodium induced a high density of growth twins which would not found in the pure Al-Si alloy [26].

The nanoparticle-induced nucleation of eutectic silicon in hypoeutectic Al-Si alloy was investigated [27]. $TiC_{0.5}N_{0.5}$ ceramic nanoparticle has a favorable crystallographic matching with Si, and thus can act as a desirable nucleating particle. The addition of 1.5 vol.% $TiC_{0.5}N_{0.5}$ nanoparticles reduced the eutectic grain size from 1416 μm to 328 μm and also reduced the cellular substructure of the eutectic grains from ~28 μm to 8.5 μm. As shown in Figure 2-11 [27], eutectic Si particles in the nanocomposites also had smaller fiber spacings and were denser within each eutectic cell. Besides, the morphology of the Si particles also evolved into more granular with a smaller aspect ratio.

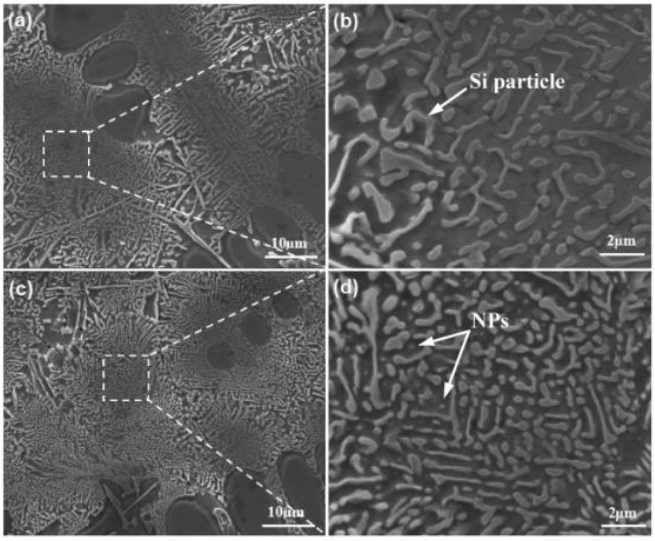

Figure 2-11 SEM pictures of eutectic phase in (a-b) matrix alloy; (c-d) alloy with 1.5 vol.% nanoparticles

The heterogeneous nucleation of primary Si and eutectic Si by AlP addition in hypereutectic Al-Si alloys were studied [28]. AlP particles significantly decreased the size of primary Si as shown in Figure 2-12 [28]. While the direct nucleation of eutectic Si on Al does not occur in the alloy without nanoparticle addition, it was found that the AlP nanoparticles formed on the surface of Al matrix, and subsequently acted as an efficient heterogeneous nucleation site for eutectic Si.

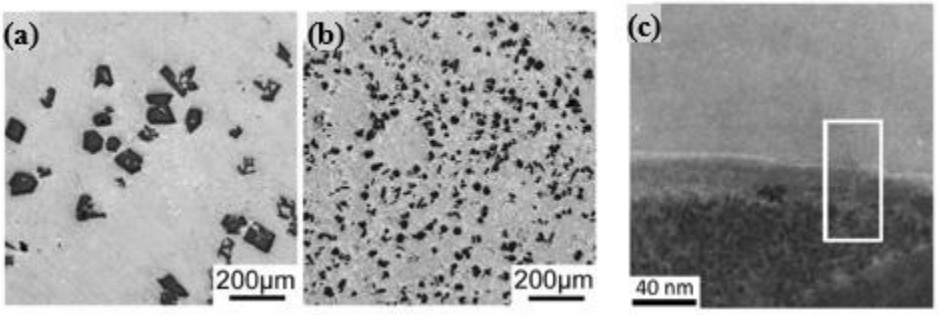

Figure 2-12 Optical images of Al-18Si (a) without and (b) with 0.03 P; (c) High resolution HAADF STEM image of the Al-Si interface in (b)

The effects of mischmetal additions on the microstructure of an in situ Al-15 wt.% Mg_2Si composite were investigated [29]. The pseudo-binary phase diagram of the Al-Mg_2Si is shown in Figure 2-13a [29]. The in situ composite without mischmetal addition had a low ductility because of the large Mg_2Si particle size and the brittle eutectic matrix. It was concluded that with mischmetal addition, the size of the primary Mg_2Si particles was considerably reduced, and that the pseudo-eutectic Mg2Si was changed from a fibrous morphology to a flake-like morphology, showing a divorced character, as shown in Figure 2-13b.

The microstructural modification effects of SiC nanoparticles (0.7 wt.%) on Sn-3.0Ag-0.5Cu (SAC305) solder alloys were studied [30]. The purpose of adding nanoparticles to this solder alloy is to refine the primary β-Sn dendrites and increase the fraction of fine eutectic in the as-solidified alloy. The results clearly showed that the microstructure was significantly refined.

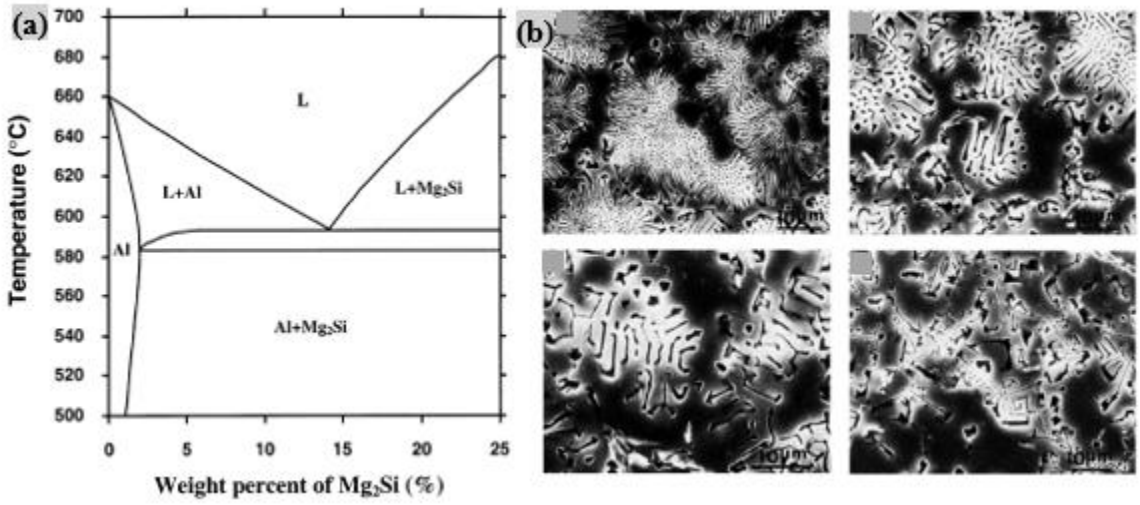

Figure 2-13. (a) Phase diagram of Al-Mg_2Si; (b) pseudo-eutectic matrix in Al–Mg_2Si composites with increasing mischmetal additions

2.8 Effects of Nanoparticles on Electrical/Thermal Properties and Others

Most metals are extremely good conductors, because of the large number of free electrons. The total resistivity of a metal is the sum of the contributions from thermal vibrations, impurities, and plastic deformation, which act independently of one another. The incorporation of nanoparticles into metals can increase the scattering of the electrons at the nanoparticle-metal interfaces, decreasing the electrical conductivity. Different nanoparticles will play a different role in determining the electrical property. Yang et al. [31] reported that with up to 10 wt. % SWCNT addition, the electrical resistivity of Cu-CNT composites remains the same as that of pure Cu. When Cu-Al_2O_3 (of 10~150 nm) nanocomposite was obtained by thermochemical process, the electrical conductivity sees a clear drop of 5~10%, even only 1~4 vol.% Al_2O_3 nanoparticle is incorporated [32,33].

Heat is conducted by electrons and phonons in materials. The presence of nanoparticles in metals results in the scattering of electrons and phonons. This scattering of electrons and phonon results in a reduction of the thermal conductivity. On the other hand, the nanoparticle structure and interaction with the metal matrix may tune the heat transport modes. If the directional thermal transport is achieved, the thermal conductivity can be escalated, due to the reduction of scattering. Moreover, it was also shown that the nanoparticles can increase the thermal conductivity of the matrix if the nanoparticles themselves have higher carrier (electrons and holes) concentration than the base matrix. This higher carrier concentration enhances the electronic thermal conductivity and aids in improving the effective thermal conductivity of the matrix [34]. Therefore, the change of thermal conductivity in nanocomposites is a function of not just the concentration of the nanoparticles, but also the type and properties of the nanoparticles. It was reported that phase-

change Bi nanoparticles embedded in an Ag matrix showed tunable melting temperature and high thermal conductivity for phase-change thermal storage [35].

Nanoparticles could also work as interfacial energy modifier. Basic mechanism is nanoparticles assemble at the interface boundary and thereby modify the interfacial energy between the two phases. Surfactants are frequently used in nanostructure synthesis for phase control, as the surfactants effectively tune the interfacial energy between different phases. With suitable nanoparticles, they could also self-assemble to the interface and modify the interfacial energy. Viscosity is a crucial parameter during material processing and nanoparticles could increase viscosity significantly. Therefore, nanoparticles could work as a powerful tool for material properties improvement.

Nanocomposites are also very useful for magnetic applications such as magnetic recording. Typically, these nanocomposites are composed of nanoscale hard magnetic particles, embedded in a soft magnetic nanocrystalline phase, such as ferrite and Fe_3Pt. These hard and soft magnetic phases interact magnetically, combining the best properties of a soft magnetic phase as the high saturation magnetization and that of a hard phase for the high coercive field. For the interaction to occur and exert its coupling effect, the two phases must be at the nanoscale. Nanocomposites materials exhibit high remanence (magnetization that is left behind after the magnetic field has been removed) and high magnetic energy (as high as 200 kJ/m^3). This effect is strongly dependent on the size of particles as well as the volume fraction and distribution of each phase.

2.9 Processing of Metals with Nanoparticles

As mentioned above, nanoparticles have several positive effects that can be utilized to achieve unprecedented properties of metals. However, to realize that, proper processing techniques

to incorporate and disperse nanoparticles in metal matrices is very important., as well as the capability to control the particle size and volume fraction. Due to their high surface area, nanoparticles tend to agglomerate and form clusters, which to a certain degree will deteriorate the properties of the composites. For this reason, the incorporation and dispersion of nanoparticles are both challenging, since the former faces nanoparticle ignition or reaction and the latter faces nanoparticle agglomeration and growth.

In general, the nanoparticles in metals can be formed in situ or ex situ. For the in situ methods, reinforcement nanoparticles are formed in metals through phase transformation, or by chemical reactions. For the ex situ methods, reinforcement nanoparticles are directly added to powdered metal or into molten metal.

Typically powder metallurgy, deformation processing, vapor phase processing, and in some cases solidification processing is used to process metal matrix composites. Powder metallurgy is the process of blending fine powdered materials, pressing them into a desired shape or form (compacting), and then heating the compressed material in a controlled atmosphere to bond the material (sintering). Deformation process such as Severe Plastic Deformation (SPD) applies high rate deformation in metal matrix to produce nanosized grains and in some cases to obtain the nanoparticles into the metal matrix. Vapor phase processing methods such as chemical vapor deposition (CVD) can be used to deposit thin films creating dispersed multiphase microstructures, multilayered microstructures, or homogeneous nanostructured coatings. Notably, each of these methods can fabricate desirable metal matrix nanocomposites under certain circumstances, but the cost is too high and it's hard to manufacture bulk materials on a large scale.

Rapid solidification through methods such as melt spinning (a liquid metal stream is impinged on a spinning cold copper drum), or spray atomization (a superheated liquid metal is

atomized with gas jets and impinged on a cold substrate) can lead to nanosized grains as well as nanosized second phase particles.

Mixing techniques involve adding particulate reinforcements and mechanically dispersing them in the matrix. Mixing methods that have been applied to synthesize metal matrix nanocomposites include stir mixing, where a high-temperature impeller is used to stir a melt that contains reinforcements, and ultrasonic mixing, where an ultrasonic horn is used to create cavitation in the melt that disperses the particulate reinforcements by an acoustic streaming effect that occurs through the cavitation of bubbles within the melt. During solidification, some nanoparticles are pushed to grain boundaries. Chen et al. [36] used a solid-state stirring to further incorporate nanoparticles into grains.

Infiltration techniques entail infiltrating a preform or partial matrix containing the reinforcements with a liquid metal. The preform consists of particles formed in a particular shape with some binding agent. Infiltration methods include ultra-high pressure, where the pressure used to infiltrate a high-density preform of nanoparticles is over 1 Gpa, and pressureless infiltration, where a block of metal is melted on top of a lower density preform of nanoparticles and allowed to seep into the preform [37].

For Cu/WC system, Wang et al. [38] reported that by powder metallurgy WC particles agglomerated obviously in Cu matrix even when WC volume percentage is only 2%, making its hardness smaller than the Cu/1.6 vol.% counterpart. Other methods were adopted to fabricated Cu/WC composites, too. Khosravi et al. [39] reported that Cu/WC composites were prepared by friction stir processing. However, this method requires several mechanical processing steps and confines the shape complexity of the samples. Besides, Yang et al. [40] reported that W-Cu alloy reinforced by WC particles were fabricated by the infiltration method. Similar to powder

metallurgy, excess addition (larger than 1.5 vol.% WC) leads to an obvious decrease in hardness. Gu et al. [41] reported that WC–Co particulate reinforced Cu matrix composites can be prepared by direct laser sintering, for which, however, using a high reinforcement content of 40 wt.% leads to a heterogeneous microstructure with a significant aggregation of the reinforcing particulates because of a limited liquid formation and the resultant high liquid viscosity and reduced Marangoni effect.

Among these processing methods, the least expensive method for the production of bulk metals with nanoparticles is solidification processing under regular cooling.

2.10 Synthesis of Nano-scaled Metal Borides

Various methods have been proposed aiming to fabricate nanoscaled metal borides. They can be divided into two categories: top-down method and bottom-up method.

For the top-down method, for example, superconductive MgB_2 nanowires were fabricated from MgB_2 thin film by means of standard electron beam lithography (EBL) coupled with Ar milling and standard photolithography [42]. However, the top-down method is expensive and has a very small yield, which may be suitable for applications like electronic devices, but not suitable for mass production such as metal matrix nanocomposites.

More researches have been conducted aiming to fabricate nanoscaled metal borides using the bottom-up method, i.e., reactions between boron and metal precursors. Several methods have been proposed and various boron precursors can be used, which will be discussed in detail below [43].

2.10.1 Boron Sources

There is a vast variety of boron precursors for metal boride synthesis. Classified by composition, there are: boron-metal alloys, elemental boron, boranes, borohydrides, boron halide, boron-oxygen compounds, and molecular single source.

2.10.2 Methods

(1) Deposition from a reactive vapor phase

Deposition from a reactive vapor phase, e.g., CVD, HPCVD, PLD, is one of the bottom-up methods. It wasn't until recently that CVD was the only efficient way to fabricate nanoscaled metal borides. This method has been extensively used to fabricate nanowires of metal borides and MgB_2 superconducting nanostructures.

(2) Solid state synthesis

Solid state synthesis can also generate nanoscaled metal borides. It can further be classified into three methods, which include reduction of nanostructured metal oxides, solid state reactions under autogenous pressure (SRAPET), and mechanosynthesis.

(3) Preceramic routes

The reduction of metal and boron oxides by C or B_4C has been known for a long time for the production of bulk metal borides. To reduce the particle size, the methods were modified. For example, using nanosized metal oxide particles combined with ball milling. The preceramic routes can be further classified into 3 categories: 1): carboreduction in physical mixtures of metal oxide, boron oxide or boric acid, and carbon; 2) carboreduction in mixtures of metal oxides and Boron-containing polymers; 3) carboreduction in metal and boron hybrid oxo-gels. These methods were

named preceramic routes because they involve the preliminary formation of a ground oxidation state metal-boron mixture at the solid state or as a gel.

(4) Liquid phase synthesis in high temperature flux (> 1000 °C)

Molten metal has been used for the fabrication of metal borides. 20 nm TiB_2 nanoparticles were precipitated in molten copper through in situ reaction and rapid solidification [44]. Copper can be further removed to produce pure metal borides.

(5) Liquid phase synthesis under autogenous pressure

Liquid phase synthesis refers to using liquid solvents (molten salts or organic solvents), or liquid reactants for the synthesis of metal borides. Liquid phase synthesis usually relies on elevated temperatures. However, the liquid solvent or reactants will also have a high vapor pressure under these conditions. Using closed vessels can help in terms of reducing evaporation, triggering reaction, improving yield, and crystallinity.

Molten salts for liquid-phase synthesis:

Bulk metal borides were fabricated by electrochemical synthesis from molten salts [45]. For example, electrolysis was performed on a fused mixture of magnesium chloride, potassium chloride, and magnesium borate at 600 °C under Ar atmosphere using a graphite anode and a Pt cathode, resulting in MgB_2 deposit on the cathode [42].

Recently, molten salts have been mused as a flux for the synthesis of nanoscaled metal borides in an autoclave. It was also reported that molten salt can mediate magnesiothermic reduction in order to fabricate nanoscaled metal borides at a low temperature [46]. For example, molten $NaCl/MgCl_2$ mixture was used for fabrication of 30-nm NbB2 with niobium pentoxide and boric acid as precursors and magnesium as a reductant at 650 °C for 10 h [46].

Organic solvents for liquid-phase synthesis:

In addition to molten salts, organic solvents have been used for boride synthesis. Benzene was used as the medium to fabricate TiB_2 nanoparticles by reaction of metallic sodium with titanium tetrachloride and amorphous boron at 400 ℃ in an autoclave [47]. However, partial carbonization of benzene and incorporation of carbon in the final product can be an issue for this method.

Liquid reactants:

The reactants can be in a liquid phase. Liquid $TiCl_4$ and solid $NaBH_4$ were heated up to above 500 ℃ in an autoclave for reaction into TiB_2 nanoparticles [48]. Except for the physical state of the reactants, the experimental procedure is similar to that of solid state reactions under autogenic pressure.

(6) Low temperature and atmospheric pressure colloidal synthesis

Although liquid phase synthesis of metal borides in molten salts have shown success, it requires sealed containers. Recent researches have shown success to fabricate nanoscaled metal borides under atmospheric pressure with special salt melts as solvents, which will produce metal borides in the range of 5-10 nm, or with an organic solvent, which will produce metal borides of around 100 nm.

Eutectic LiCl/KCl is water-soluble and has a low melting point of 355 ℃. More importantly, its vaporization rate is low up to 900 ℃ [49], which makes it suitable as solvents for atmospheric pressure synthesis for which the reaction temperature is below 900 ℃. With solid metal chlorides as metal precursors and sodium borohydride as the boron source and reductant in LiCl/KCl eutectic molten salt, various metal borides (HfB_2, CeB_6, MoB_4, FeB, Mn_2B, etc.) were synthesized at temperatures between 700–900 ℃ [50]. For NbB_2, by increasing the Boron precursor content, NbB_2 particle size decreased from 10 nm to 5 nm.

Figure 2-14 illustrates the typical processing temperature and the resultant metal borides particle size of different bottom-up synthesis techniques [43]. Only one method, namely colloidal synthesis in salt melts can achieve the goal of sub 10 nm nanoparticles. Besides, Also, to subjectively tune particle size, only CVD, precipitation of amorphous nanoparticles, and colloidal synthesis in molten salts can achieve size control.

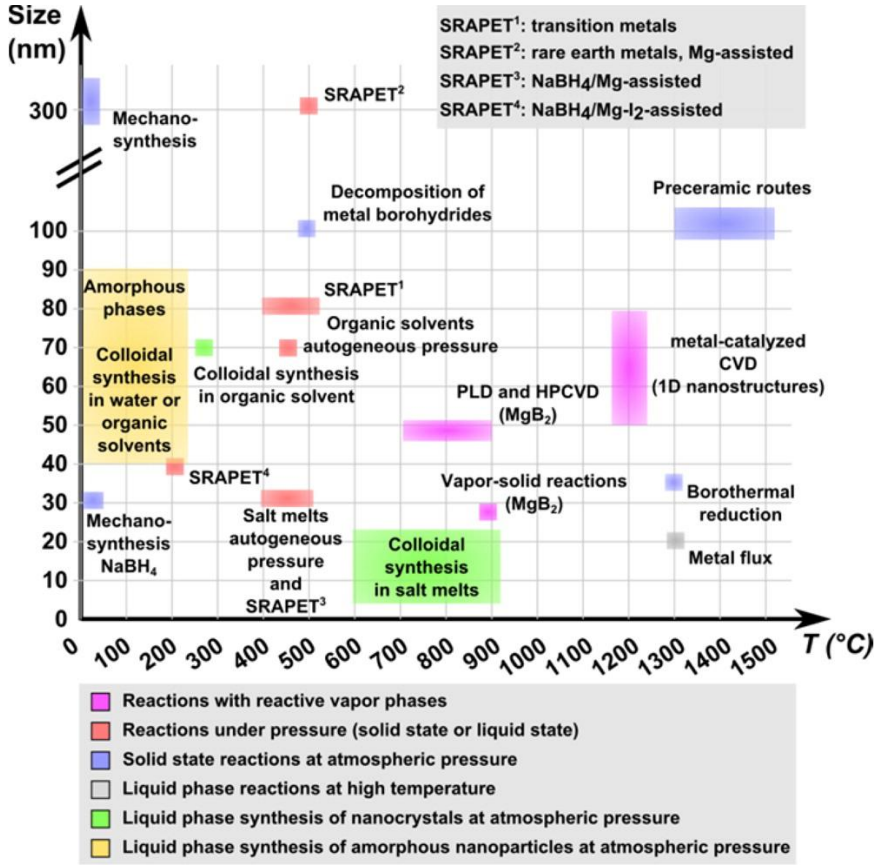

Figure 2-14 Comparison in aspects of processing temperature and nanoparticle size for different metal boride synthesis methods

Chapter 3 Fabrication of Cu Containing Dispersed Nanoparticles and the Property Enhancement

The incorporation and dispersion of nanoparticles into metals is crucial to study the nanotechnology enabled metallurgy in Cu. Ex-situ processing methods were utilized to fabricate Cu matrix nanocomposites containing a wide volume fraction range of well dispersed nanoparticles [51,52]. The advantages of the ex-situ processing methods are the effective nanoparticle incorporation, the good nanoparticle dispersion, and the versatility of nanoparticle volume fractions. Cu/WC nanocomposites with a series of WC loadings were fabricated by the ex-situ methods. Cu/WC nanocomposites with suitable WC contents can exhibit simultaneously enhanced microhardness, strength, and Young's modulus without significant degradation of the electrical/thermal conductivity.

To enable the size control of the nanoparticles, novel in-situ synthesis of nanoparticles and Cu matrix nanocomposites were also developed. In-situ Cu/W and Cu/TiB_2 nanocomposites were fabricated. The in-situ synthesis method can be utilized to fabricate metals reinforced by nanoparticles through conventional casting using inexpensive raw materials, which also decreases the nanoparticle size and expand the choices of nanoparticles for Cu/Cu alloys. Moreover, in-situ fabrication of Cu/CrB_x composites [53] and the synthesis of CrB_x nanoparticles by magnesiothermic reductions in molten salts and the subsequent incorporation into Cu [54] were developed.

3.1 High-performance Copper Reinforced with Dispersed WC Nanoparticles

3.1.1 Introduction

High performance copper (Cu)-based materials are needed for various industrial applications [1], including high-speed railway contact wires [2], electric resistance welding electrodes [3], lead frames [4], and rotors for electric motors [5]. Since pure Cu is very soft, it is frequently alloyed with other elements for strengthening. However, it is difficult, if not impossible, for Cu alloys to obtain a tensile strength higher than 600 MPa with a good ductility while maintaining reasonable electrical and thermal conductivity [6]. Additionally, alloying does not alter the Young's modulus from pure Cu [7]. Furthermore, Cu alloys soften at elevated temperatures due to dealloying or coarsening of the strengthening precipitates [8, 9].

Numerous efforts have been made to tackle these problems. For instance, severe plastic deformation (SPD) has been used to increase the strength of Cu and its alloys [10]. However, this approach also significantly decreased the ductility [11]. While nano-twinned copper shows high strength and high electrical conductivity, the fabrication method (electrodeposition) remains an obstacle for scale up production [12]. Rapid cooling (e.g. gas atomization, melt spinning, etc.) was used to achieve high-strength Cu with high conductivity by obtaining a nanosized second phase from molten Cu alloys through phase transformation [13], as well as by obtaining *in situ* nanoparticles through reactions in molten Cu [14]. However, the rapid cooling method is limited in the sample size and volume.

Incorporating a strengthening phase, e.g. ceramic nanoparticles, into copper to form a metal matrix nanocomposite (MMNC) is one way to create high performance Cu-based materials [15]. One promising candidate of ceramic nanoparticles is tungsten carbide (WC). WC has a high hardness (22 GPa) and high Young's modulus (620-720 GPa) [16]. Additionally, the wetting

between molten Cu and WC is very good with a low wetting angle less than 10° at 1200°C [17], beneficial for a good interfacial bonding between Cu and WC. Furthermore, there is no reaction between Cu and WC, making it thermally stable in molten Cu [18].

Powder metallurgy was often used to fabricate MMNCs. However, the distribution and dispersion of the nanofillers in MMNCs is highly dependent on the mechanical mixing. It is hard to obtain a uniform dispersion of the fillers in the matrices [19], as the particles tend to form clusters due to their large surface area, which can negatively impact the properties of the resulting nanocomposites. For instance, it was reported that the WC nanoparticles in Cu/WC nanocomposites prepared by powder metallurgy agglomerated so severely in the Cu matrix that the strength of the Cu/3 wt.% WC nanocomposite was even less than its Cu/2 wt.% WC counterpart [20]. Consequently, the powder metallurgy method cannot be used to fabricate nanocomposites with a high percentage of the strengthening phase for favorable properties.

Other methods have also been used to fabricate Cu/WC nanocomposites with limited success. Cu/WC/graphene nanocomposites were produced by electrophoretic deposition [21]. However, this method is more suitable for producing films rather than bulk materials. Additionally, Cu matrix composites with 40 wt.% WC–Co submicron particles was processed by direct laser sintering, but there were significant particulate aggregations due to a limited liquid formation and high viscosity as well as a reduced Marangoni effect [22].

In this study, Cu matrix nanocomposite with dispersed WC nanoparticles was successfully fabricated. Microstructure and properties including microhardness, yield strength, Young's modulus, electrical conductivity and thermal conductivity of the samples were investigated. Our results showed that a uniform dispersion of dense WC nanoparticles in the Cu matrix is achieved. A significant enhancement of hardness/strength and Young's modulus is achieved while the

conductivities are maintained at reasonable levels. The new Cu/WC nanocomposites can offer high performance for widespread applications. Moreover, the scalable manufacturing method can be easily extended to fabricate Cu matrix nanocomposites with other suitable nanoparticles and various nanoparticle loadings for industrial production.

3.1.2 Materials and Methods

(1) Molten-salt assisted self-incorporation

A scalable fabrication method, i.e., molten-salt assisted self-incorporation was utilized to fabricate bulk Cu/WC nanocomposites. The schematic is shown in Figure 3-1. Pure copper was first melted at 1200 °C and a mixture of WC nanoparticles (US Research Nanomaterials, 200 nm) and $KAlF_4$ powders by volume ratio of 1:9 mechanically mixed by a shaker (SK-O330-Pro) for 20 min was added to the top of the molten Cu with argon protection, which then stayed at 1200 °C for 30 min before cooling to room temperature in furnace.

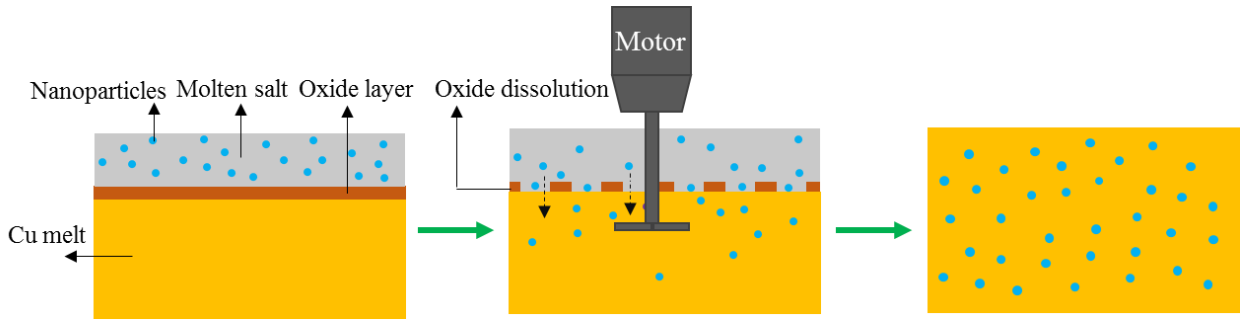

Figure 3-1 Schematic of molten-salt assisted self-incorporation method for fabrication of Cu/WC nanocomposites

(2) Melting of nanocomposite micro-powders

As the WC volume fraction increases, the viscosity of molten Cu with WC also increases, which inevitably would trap some salt inside. When salt inclusion in the first method becomes an

issue, the second method will be used, which is melting of nanocomposite micro-powders. Cu/WC nanocomposites with high WC content (40 vol.% and 46 vol.%) were fabricated by a two-step method as shown in Figure 3-2: (1) Cu micro-powders with dispersed WC nanoparticles were fabricated by molten-salt-assisted self-incorporation of the nanoparticles; and (2) bulk nanocomposites were produced by melting the powders under pressure after salt dissolving. More specifically, to fabricate the designed Cu/40 vol.% WC micro-powders, pure Cu powders (Sigma-Aldrich, <10 μm, 99%), WC nanoparticles (US Research Nanomaterials, average particle size 150–200 nm, 99.9%) and NaCl particles (Fisher Chemical, 99.5%) were mechanically mixed (1 : $\frac{2}{3}$: 6 by volume ratio) via shaking (SK-O330-Pro) for 20 mins. The mixed powders were heated to 1200 °C at a heating rate of 80 °C/min in an induction heater under argon protection and held for 30 min before cooling in the furnace. Manual mixing using a graphite rod with applied. Then the material underwent 3 rounds of soaking in DI water to fully dissolve NaCl before drying in a vacuum drying oven. Bulk Cu/40 vol.% WC nanocomposite samples were fabricated by melting the micro-powders at 1500 °C for 30 mins with a pressure of 7.5 MPa under argon protection.

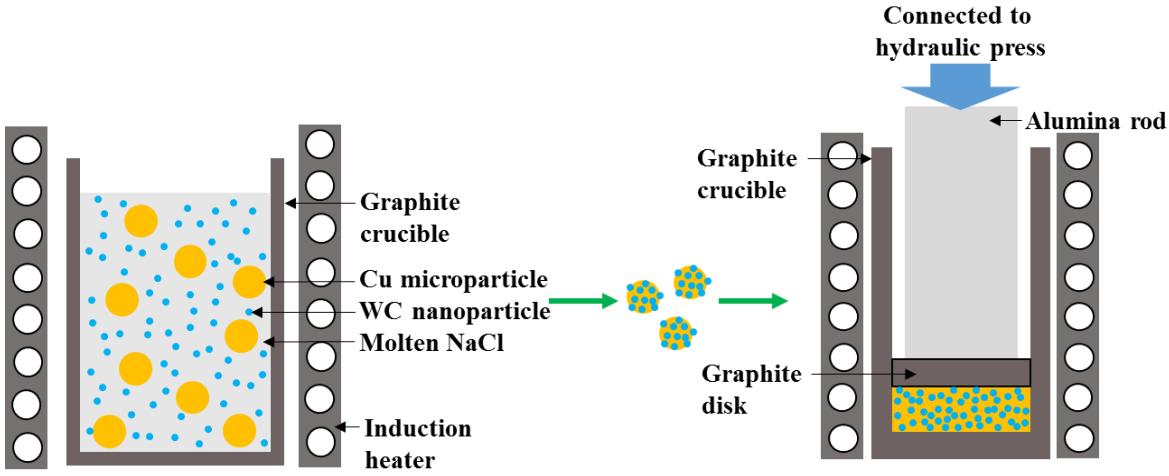

Figure 3-2 Schematic of the two-step method for fabrication of Cu/WC nanocomposites

The microstructure of both Cu micro-powders and bulk nanocomposites were examined by scanning electron microscopy (SEM, ZEISS Supra 40VP). To reveal the WC nanoparticles, the SEM samples for the bulk nanocomposite were cleaned by low-angle ion milling at 4° and 4.5 kV for 3.5 h (Model PIPS 691, Gatan) following manual grinding and polishing. The SEM sample for observing cross-sections of micro-powders was prepared by encapsulating a piece of solidified NaCl and micro-powders using graphite-based conductive mounting powders (Allied, #155-20015), followed by grinding and polishing. The micropillars for mechanical testing were observed by dual-beam FIB-SEM (FEI Nova 600) with a tilted angle of 52°.

Compression tests using an MTS nanoindenter with a strain rate of $5 \times 10^{-2}\ s^{-1}$ and a 3 μm compression depth limit at room temperature were conducted on micropillars (3-4 μm in diameter and 9-12 μm in length), which were machined by focused ion beam (FIB, FEI Nova 600) from the bulk nanocomposites. The yield strength was obtained by an average of at least three measurements. The Young's modulus was measured by the same nanoindenter machine with a Berkovich tip under the Young's modulus measuring mode with an indent depth of 2 μm. The microhardness was determined by a LM 800AT microhardness tester using a load of 200 gf with a 10 s dwell time. Each Young's modulus and microhardness data represents 10 measurements at random spots at room temperature.

Thermal conductivity of the sample was measured by the laser flash method [23] at room temperature. First, thermal diffusivity was calculated by Equation 3-1 based on the classic one-dimensional heat diffusion.

$$\alpha = \frac{0.139 L^2}{t_{0.5}} \qquad \text{Equation 3-1}$$

where α is the thermal diffusivity, L is the sample length, and $t_{0.5}$ is the time required for the backside temperature of the sample to rise by half of the maximum temperature change. In this

experiment, the sample length was set to be 2 cm with a cross-section of 2 mm × 2 mm. Finally, the thermal conductivity was calculated by Equation 3-2.

$$k = \alpha \rho c_p \qquad \text{Equation 3-2}$$

where k is the thermal conductivity, ρ is the density, and c_p is the specific heat. To obtain the specific heat capacity value of the nanocomposite, the differential scanning calorimetry (DSC, Perkin Elmer DSC 8000) was used to experimentally measure the heat capacity at a temperature scan rate of 10 °C/min. Electrical conductivity of the sample was measured on Prometrix Omnimap RS-35 4 point probe at room temperature. Each conductivity data represents at least three measurements.

3.1.3 Results and Discussion

(1) Molten-salt assisted self-incorporation

The microstructure of a Cu/WC nanocomposite fabricated by the molten-salt assisted self-incorporation method is shown in Figure 3-3. It is shown that WC particles are also incorporated into Cu matrices. The incorporation of WC particles into Cu is driven by the minimization of Gibbs free energy. Figure 3-3b also demonstrates the well-dispersion of WC particles in the Cu matrix. This fabrication method of nanocomposites via casting can meet the requirements of scalable manufacturing of bulk metals with dispersed nanoparticles.

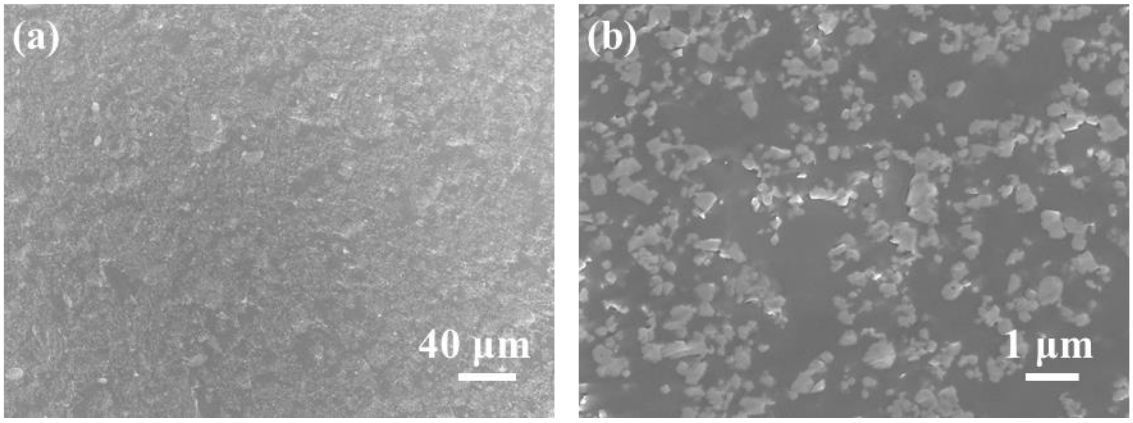

Figure 3-3 Microstructure of Cu/14.7 vol.% WC fabricated by molten-salt assisted self-incorporation at different magnifications

(2) Melting of nanocomposite micro-powders

The morphologies of as-received WC nanoparticles and Cu powders are shown in Figure 3-4. As shown in Figure 3-5, the Cu/WC nanocomposite micro-powders were created by the molten-salt-assisted self-incorporation process. Cross-sections of the Cu/40 vol.% WC micro-powders (Figures 3-5b) before NaCl dissolution show a dense and uniform distribution of WC nanoparticles in the Cu matrix. The incorporation mechanism of WC nanoparticles into Cu is discussed below. Qualitatively, WC is a metallic ceramic, which will tend to wet metals (metallic bond) more than the salt (ionic bond) [24]. The good wettability between WC and molten Cu is indicated by the low contact angle [17]. The interfacial energy of WC/molten Cu should be lower than WC/molten NaCl. We have previously shown that nanoparticles preferentially stay at the molten salt/metal interface, but when the nanoparticle volume percentage is high, the nanoparticles are forced to migrate into the molten metal [24]. Moreover, molten salt acts as a protection layer to reduce the oxidation of both WC nanoparticles and molten Cu. Molten salt can also partially

dissolve metal oxides to enable direct contact between WC nanoparticles and molten Cu and consequent incorporation of WC nanoparticles into Cu.

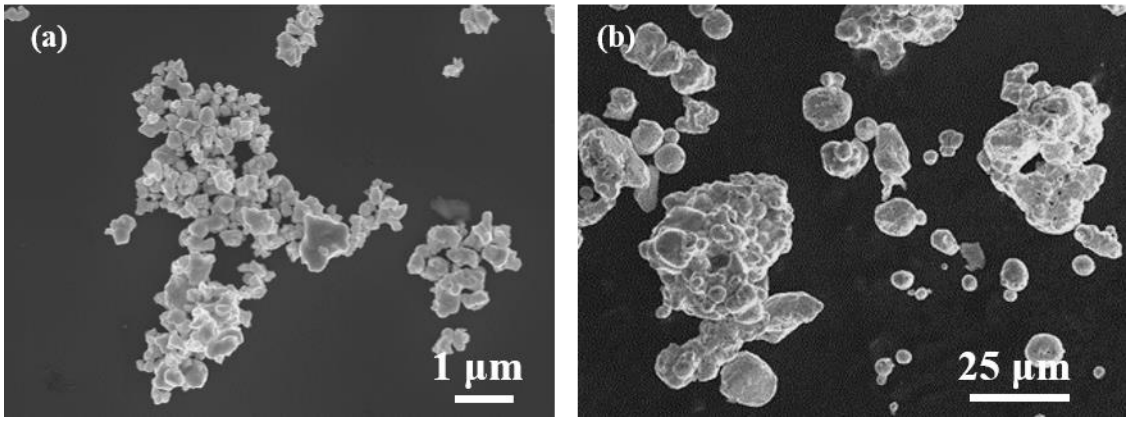

Figure 3-4 SEM images of (a) as-received WC nanoparticles; (b) as-received Cu powders

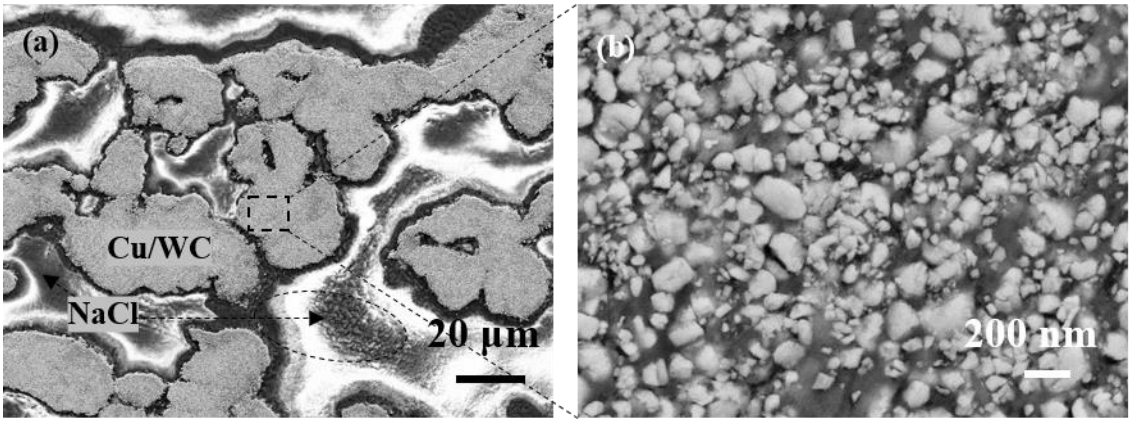

Figure 3-5 SEM images of micro Cu/WC powders before NaCl dissolution: (a) cross-sections of Cu/40 vol.% WC micro-powders in NaCl; (b) magnified image of boxed area in (a)

Microstructures of the bulk Cu/40 vol.% WC nanocomposite are shown in Figure 3-6. The dense WC nanoparticles are uniformly distributed and well-dispersed/separated in the Cu matrix instead of clustering even though the WC content is very high. Additionally, the bulk nanocomposite is free of porosity, demonstrating the feasibility of producing bulk samples by simply melting the nanocomposite micro-powders under low pressure. Histograms representing the size distribution of WC nanoparticles (by image processing of Figure 3-6b) in Cu matrix are

shown in Figure 3-7. The average WC diameter in Cu matrix is 197.5 nm, which is close to the original WC size (average particle size 150–200 nm). The mechanism for bulk material formation from the initial nanocomposite micro-powders is inferred to be that, under the high temperature, Cu from each powder diffuses to the powder's surface and the applied pressure binds the powders together. The reason the Cu/40 vol.% WC melt can sustain the pressure instead of being squeezed out is that the viscosity of molten metals can be dramatically increased when nanoparticles are incorporated, which is beneficial for the current method to form bulk nanocomposites. It was reported that the dynamic viscosity f Ni/6.6 vol.% Al_2O_3 nanoparticles was ~4 times that of pure Ni [25].

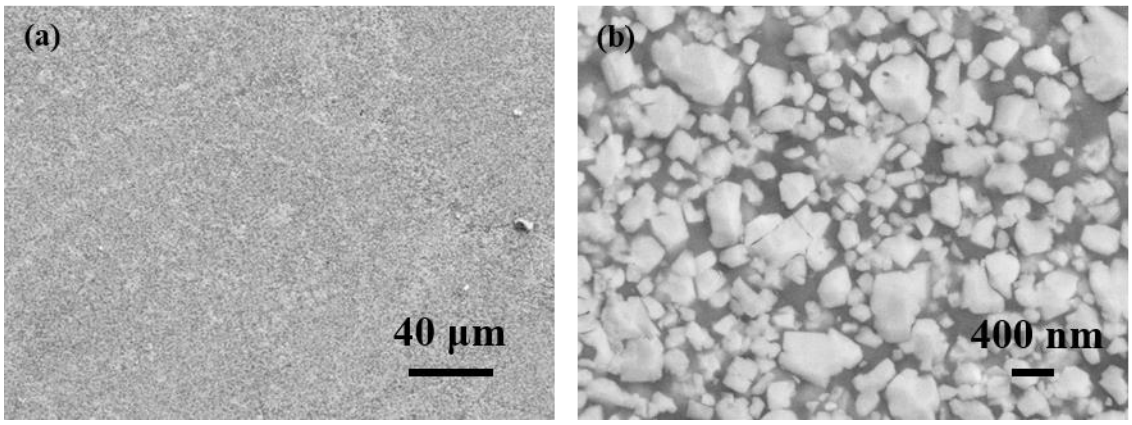

Figure 3-6 SEM images of the bulk Cu/40 vol.% WC nanocomposite at different magnifications

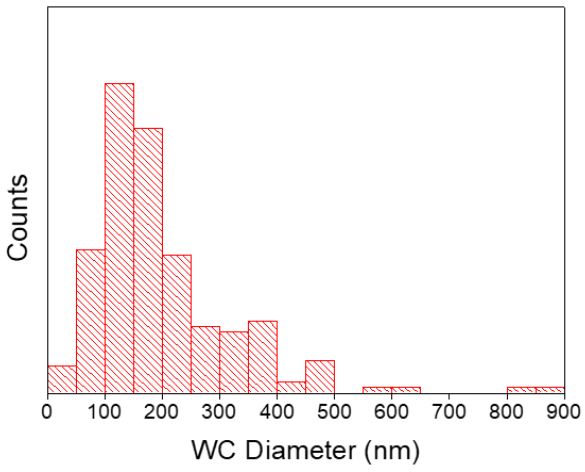

Figure 3-7 Size distribution of WC nanoparticles in Cu matrix

The Cu/40 vol.% WC nanocomposite is expected to have excellent mechanical properties due to the dense well-dispersed WC nanoparticles. To investigate the strength of the nanocomposite, micropillar compression tests were conducted. A SEM image of one micropillar is shown in Figure 6a. Whereas Figure 4 showed the microstructure of one plane, Figure 3-8a shows that WC nanoparticles are globally well dispersed and distributed in the pillar. Corresponding engineering stress-strain curve of the compression test is shown in Figure 3-8b. The strain became discontinuous after 8.6%, indicating failure. The typical post-deformed pillar is shown as the inset of Figure 3-8b. The average yield strength of the nanocomposite was 1020.7±244.3 MPa with a uniform plasticity of more than 8%. The yield strength of the Cu/40 vol.% WC nanocomposite is much higher than most previously reported Cu alloys [6].

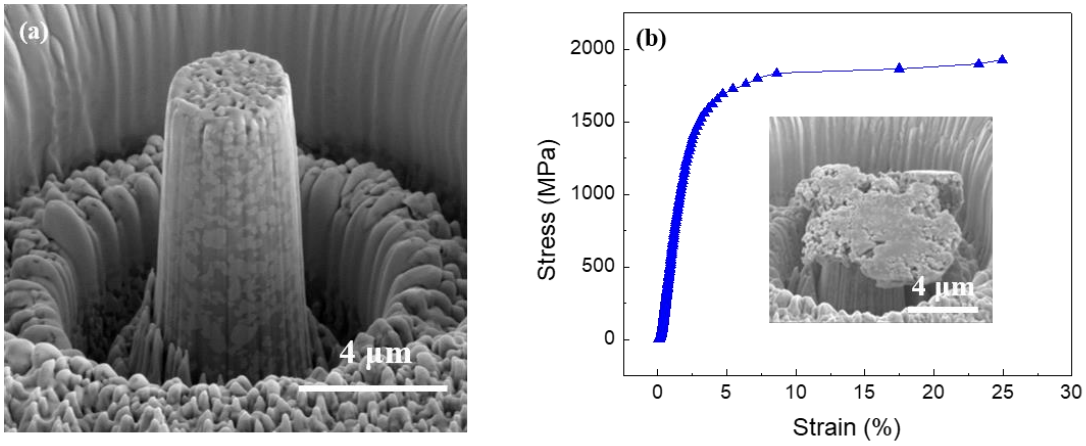

Figure 3-8 Micropillar compression tests for Cu/40 vol.% WC nanocomposite sample: (a) SEM image of one micropillar from Cu/40 vol.% WC nanocomposite; (b) engineering stress-strain curve of the micropillar compression test with SEM image showing the post-deformed micropillar as the inset

The average microhardness of the bulk Cu/40 vol.% WC nanocomposite was 426.0±47.2 HV. Considering the microhardness of pure Cu was ~50 HV [11, 26], a significant strengthening effect was achieved. Strengthening efficiency (R) [26, 27] of reinforcements in MMNCs is defined as:

$$R = (H_C - H_m)/(x \cdot H_m) \quad \text{Equation 3-3}$$

where H_c is microhardness (HV) of the nanocomposite, H_m is the microhardness of the matrix (the microhardness of pure Cu was used for H_m), and x is the volume percentage of the strengthening phase. The strengthening efficiency for Cu/40 vol.% WC nanocomposite was 18.8. The superior strengthening can be attributed to the Orowan strengthening, load bearing resulting from populous well-dispersed WC nanoparticles and the Hall-Petch effect resulting from refined grains of Cu matrix as nanoparticles can refine grains of the matrix in MMNCs [28].

The Young's modulus of the nanocomposite was 254.4±11.2 GPa, which is significantly enhanced compared to pure Cu. The enhancement is attributed to the high Young's modulus of WC, the effective load bearing by WC, and its uniform dispersion in the nanocomposite. The dramatically increased Young's modulus achieved with nanocomposites shows the advantage this strategy has over alloying, which does not effectively increase Cu's Young's modulus (115 GPa [29]).

The electrical and thermal conductivity of the Cu/WC nanocomposite was decreased compared to pure Cu, but comparable to many commonly used Cu alloys. The thermal conductivity was 155.7±19.5 $W \cdot m^{-1} \cdot K^{-1}$ for Cu/40 vol.% WC and the specific heat capacity at 25 °C was measured to be 0.239±0.002 J/(g·°C). Its electrical conductivity was 21.0±0.3% IACS. There are a couple reasons for the decreased thermal and electrical conductivities of the nanocomposite compared to pure Cu. First, WC has lower thermal and electrical conductivity

values than pure Cu. Moreover, the addition of WC to the Cu matrix introduces imperfections in the Cu lattice, such as interfaces and grain boundaries (from the refining of Cu grains), which act as scattering centers and lower electron motion efficiency.

The underlying mechanism for the dispersion of WC nanoparticles in Cu as shown in Figure 6a can be explained by the thermally-activated nanoparticle dispersion and self-stabilization theory in molten metals [15]. Three interactions between nanoparticles are considered: interfacial energy, van der Waals potential, and Brownian motion energy. Good wetting between molten metal and nanoparticles creates an energy barrier to prevent nanoparticles from contacting with each other. Thermal energy makes nanoparticles to disperse by Brownian motion. Nanoparticles are dispersed and stabilized in molten metals by synergistically reducing attractive van der Waals forces between the nanoparticles, providing high thermal energy for the nanoparticles to disperse, and creating a high energy barrier to prevent clustering [15]. In this system, the small WC particle size and their conductive nature result in small van der Waals attraction. Additionally, the high processing temperature provides the nanoparticles with high thermal energy. Finally, the good wetting between Cu and WC produces the high energy barrier.

The energy barrier ($W_{barrier}$), thermal energy (E_b), and van de Waals interaction (W_{vdw}) can be calculated by Equation 3-4 to Equation 3-6, respectively [15].

$$W_{barrier} = S\left(\sigma_{NP} - \sigma_{NP-liquid}\right) = S\sigma_{liquid}cos\theta \quad \text{Equation 3-4}$$

$$E_b = kT \quad \text{Equation 3-5}$$

$$W_{vdw} = -\frac{\left(\sqrt{A_{NP}}-\sqrt{A_{liquid}}\right)^2}{6D}\frac{R}{2} \quad \text{Equation 3-6}$$

where S: effective area ($S = \pi R D_0$, $D_0 = 0.2$ nm); σ_{NP}: surface energy of nanoparticles; $\sigma_{NP-liquid}$: interfacial energy between nanoparticles and molten metal; σ_{liquid}: molten metal surface tension; θ: contact angle of molten metal on nanoparticle surface. k: Boltzmann constant;

T: absolute temperature; *A*: Hamaker constant; *R*: nanoparticle radius; *D*: distance between two nanoparticles; Equation (6) is only effective when two nanoparticles interact in molten Cu with *D* approximately larger than two atomic layers (~ 0.4 nm).

In this study, to estimate $W_{barrier}$, using R = 98.75 nm, θ = 10°, σ_{liquid} = 1.2 J/m^2 at 1500 °C [30], $W_{barrier}$ is 73324 zJ. At 1500 °C, E_b is 24.5 zJ. The energy barrier is much higher than the thermal energy. To estimate W_{vdw}, A_{Cu} is 410 ZJ [31] and A_{WC} is not available. Since WC is conductive ceramic, Awc could range from 200 to 500 zJ [32]. $W_{barrier}$ would always be much higher than E_b and W_{vdw} for stabilization of dispersed WC nanoparticles in Cu melt.

As mentioned above. the wettability between molten metal and nanoparticles is very crucial to the successful incorporation and dispersion of nanoparticles into molten metal. It has been reported that adding other elements can improve the wettability in some cases [33]. Therefore, it is of interest to apply the current method to fabricating Cu MMNCs reinforced by nanoparticles that have good properties (such as lightweight, highly conductive, etc.) but originally don't have a good wettability with Cu with the aid of adding other alloying elements.

The Orowan strengthening can be estimated by Equation 3-7 [34]:

$$\Delta\sigma_{Orowan} = \frac{0.13Gb}{d_p[\sqrt[3]{(\frac{1}{2}V_p)}-1]} ln\frac{d_p}{2b} \qquad \text{Equation 3-7}$$

where *G* and *b* are the shear modulus and Burger's vector of the matrix, d_p and V_p are the diameter and volume fraction of nanoparticles. In this study, *G* = 47.7 GPa [35], *b* = 0.256 nm [35], V_p = 0.4, and d_p = 197.5 nm, the calculated $\Delta\sigma_{Orowan}$ is 620 MPa. The total strengthening in the as-solidified Cu/40 vol.% WC nanocomposite is about 944 MPa using yield strength of annealed pure Cu as 76 MPa as a counterpart for simplicity. It has been reported that the increase of dislocation density in the as-solidified nanocomposite is not obvious [15]. Thus, the strengthening from the

formation of geometrically necessary dislocations may be neglected. It is inferred that the rest increase of yield strength (324 MPa) comes from load bearing effect of WC nanoparticles and the Hall-Petch effect resulting from refined grains of Cu matrix compared with pure Cu [28].

According to the Maxwell model, the electrical resistivity of composites can be estimated by Equation 3-8:

$$\rho_c = \rho_m \left(\frac{1+2\frac{\rho_m}{\rho_p}-2V_p\left(\frac{\rho_m}{\rho_p}-1\right)}{1+2\frac{\rho_m}{\rho_p}+2V_p\left(\frac{\rho_m}{\rho_p}-1\right)} \right) \qquad \text{Equation 3-8}$$

where ρ_c, ρ_m, and ρ_p are the electrical resistivity of the nanocomposite, matrix, and nanoparticles. V_p is the volume fraction of nanoparticles. Electrical resistivity values of Cu and WC at 20 ℃ are 1.7241 μΩ·cm [29]and 22 μΩ·cm [16]. The electrical resistivity of the nanocomposites in this work is estimated to be 7.8 μΩ·cm (22.1% IACS). The experimental value (21% IACS) is close to the calculated value.

This method for fabricating MMNCs has several advantages over other existing methods. First, this method produces a metal matrix with a high content of uniformly dispersed nanoparticles, solving the problem of incorporation and dispersion of nanoparticles into metal matrices. Additionally, the pressure employed to fabricate MMNCs in this study was much lower than the pressures required for cold compaction in traditional powder metallurgy (several hundreds of MPa) [36]. In traditional powder metallurgy methods, WC particles and Cu powders are mixed mechanically by ball milling before compaction [34, 37] which can bring impurities such as iron into the system.

(3) Effects of Nanoparticles on Properties of Cu

By the above-mentioned two ex-situ fabrication methods, the fabrication of Cu/WC nanocomposites with a wide range of WC volume fractions was achieved, which enabled the study of effects of nanoparticles on properties of Cu. To understand how the properties of the Cu/WC nanocomposites evolve with the WC volume percentage (x), different properties including microhardness, Young's modulus, electrical conductivity, and thermal conductivity of a series Cu/WC composites were measured and analyzed.

Microhardness and Young's modulus

Figure 3-9 illustrates the microhardness of the nanocomposites as a function of WC volume percentage. As shown in Figure 3-9, the microhardness of the nanocomposites almost keeps increasing linearly with x. The relationship can be summarized as:

$$H_c = 74 + 6.35x \quad \text{Equation 3-9}$$

where H_c is microhardness (HV) of the nanocomposite. On the other hand, in previous studies, the microhardness versus WC vol.% curves for Cu/WC nanocomposites usually had a peak pattem showing no continuous enhancement of microhardness since the WC particles were not well dispersed. The average microhardness of the bulk Cu/40 vol.% WC sample is ~426 HV. Strengthening efficiency (R) [24,25] of reinforcements in MMCs is defined as:

$$R = (H_C - H_m)/(x \cdot H_m) \quad \text{Equation 3-10}$$

where H_m is the microhardness of the matrix (microhardness of the pure Cu, i.e., 74 HV, is taken as H_m here). The strengthening efficiency for Cu/40 vol.% WC is 12. The superior strengthening effect here can be attributed to the Orowan strengthening, load bearing and Hall-Petch effect resulted from well-dispersed WC particles and refined Cu matrix.

Figure 3-10 shows the Young's modulus of Cu/WC nanocomposites versus WC volume percentage. The Yong's modulus of the nanocomposite is enhanced dramatically with the addition

of WC particles, which can be attributed to the high Young's modulus of WC and its uniform dispersion. On the contrary, alloying doesn't effectively increase the Young's modulus of Cu, which renders nanocomposites advantageous in this aspect. If we apply the mixture rule, considering the Young's modulus of WC and Cu as 620 GPa [57] and 115 GPa [58], respectively, the ideal Young's modulus of Cu/40 vol.% WC would be 317 GPa. Therefore, our experimental data is roughly consistent with the theoretical data.

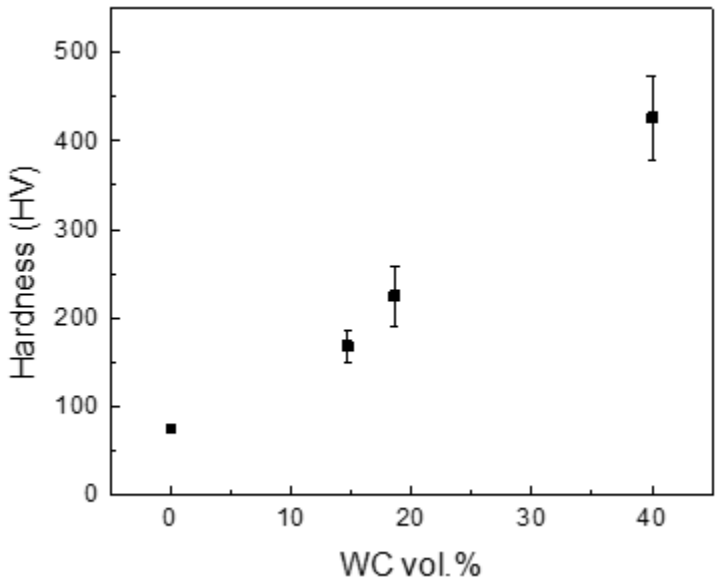

Figure 3-9 Microhardness of the Cu/WC nanocomposites as a function of WC volume percentage

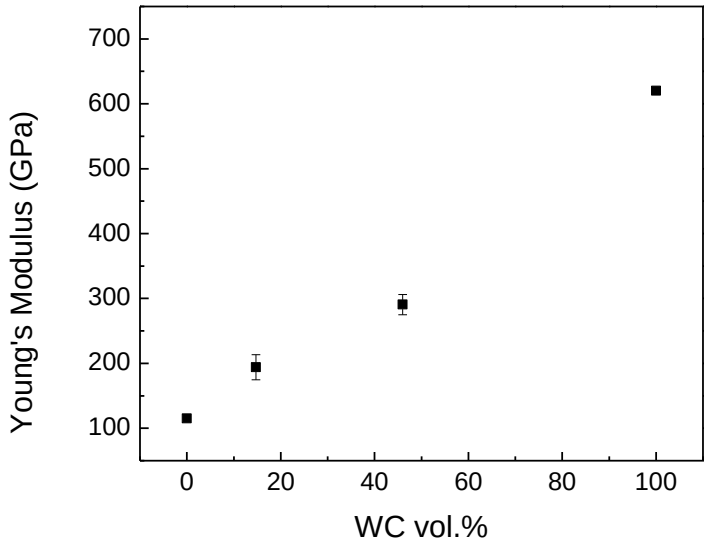

Figure 3-10 Young's modulus of Cu/WC nanocomposites versus WC volume percentage

Electrical and Thermal Conductivity

As for thermal conductivity, Figure 3-11 shows the variation of thermal conductivity of the Cu/WC nanocomposites with different WC concentrations at room temperature. The thermal conductivity decreases as WC volume percentage increases. For Cu/40 vol.% WC, its thermal conductivity is still ~156 W/(m·K). Figure 3-12 shows the curve of electrical conductivity of the Cu/WC nanocomposites versus WC volume percentage at room temperature. The electrical conductivity decreases with increasing WC addition. For Cu/40 vol.% WC, its electrical conductivity is still ~20% IACS. Compared to alloying especially that forms a solid solution, where less than 1 wt.% solutes can sometimes decrease the electrical conductivity to below 50% IACS, there is less deterioration of the conductivity caused by nanoparticles.

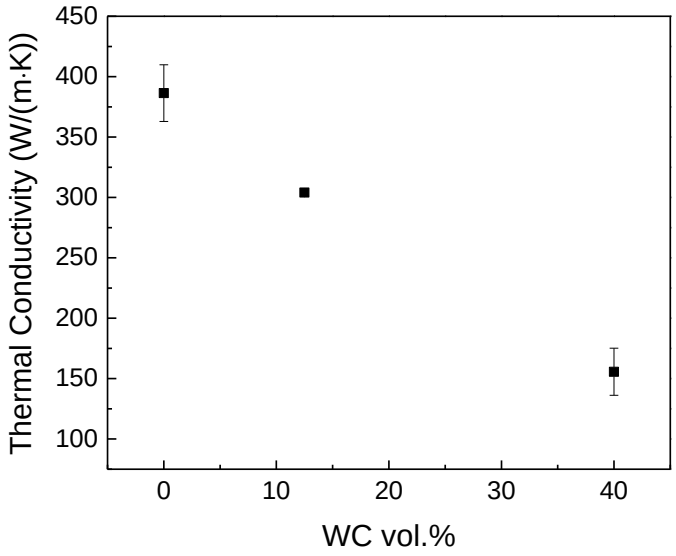

Figure 3-11 Variation of thermal conductivity of the Cu/WC nanocomposites with different WC contents at room temperature

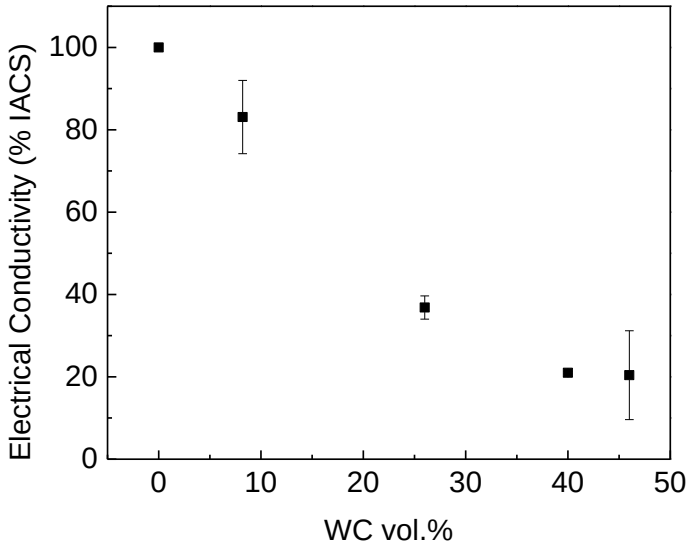

Figure 3-12 Electrical conductivity of the Cu/WC nanocomposites versus WC volume percentage at room temperature

The reasons that thermal and electrical conductivities of the composites decrease with the increase of WC contents are as follows. Firstly, WC itself, as a constituent of the composite, has lower thermal and electrical conductivity values than pure Cu. The introduction of WC into Cu matrix creates interfaces, dislocations, and grain boundaries (from the refining of Cu grains) in the Cu lattice, which will act as scattering centers, lowering the electron motion efficiency. However, nanoparticles do not introduce impurities into pure Cu lattice, unlike alloying that forms a solid solution causing severe degradation of electrical and thermal conductivity.

Theoretical study to analyze and estimate the electrical resistivity of pure metals has been reported [7]. The decrease of electrical resistivity arises from crystalline defects, which act as scattering centers of conducting electrons [7]. The more the defects are, the lower the electrical conductivity will be. According to Matthiesen's rule, the resistivity of a metal is the sum of contributions from thermal vibrations, impurities, and plastic deformation (increasing dislocation density) as shown in Equation 3-11 [7]. The scattering mechanisms are independent of each other [7].

$$\rho_{total} = \rho_t + \rho_i + \rho_d \qquad \text{Equation 3-11}$$

where ρ_t, ρ_i, and ρ_d represents thermal, impurity, and formation resistivity contributions.

Moreover, the electrical resistivity increase caused by specific defects such as grain boundaries and dislocations can be estimated by Equation 3-12 to 3-14 [59].

$$\Delta\rho_{Gb} = \frac{2}{3}\alpha_T \times \Omega_{GB} \times \frac{2.37}{D} \qquad \text{Equation 3-12}$$

$$\Delta\rho_{dis} = \frac{2\sqrt{3}\Omega_{dis} \times \frac{\beta \times \cos\theta - \frac{0.9\lambda}{D}}{\sin\theta}}{Db} \qquad \text{Equation 3-13}$$

$$\Delta\rho_{dis} = 6\Omega_{dis} \times \frac{f \times \Delta CTE \times \Delta T}{rb(1-f)} \qquad \text{Equation 3-14}$$

where Ω_{GB} and Ω_{dis} are grain boundary and dislocation resistance; D is grain size; r is nanoparticle radius; b is Burgers vector of the matrix; α_T compensates for the temperature dependence of electron mean free path; β is peak broadening of a certain peak θ in XRD patterns with X-ray wavelength of λ; f is nanoparticle volume fraction; ΔCTE is the CTE mismatch between matrix and nanoparticle; ΔT is temperature difference.

However, the theoretical study of the electrical conductivity of metals with dispersed nanoparticles has not been established. Pan et al. built a theoretical model to study the electrical behavior of Cu and its alloys with dispersed nanoparticles, which is described as follows [60]. In the metallic systems, electrons with high energy near the Fermi surface greatly affects the electron transport. A thermostatic environment is appropriate near the Fermi level. The electron transport is governed by interfacial scattering. Whether an electron will be blocked or transport through the nanoparticle follows the probability of its partition functions, as shown in Equation 3-15. The probability of electron transmission through the interface is governed by the energy of the system and the energy barrier, as shown in Equation 3-16. The nanoparticle volume fraction (x) will conjugate with the pure energy state probability, which yields a diffusion free energy of activation, as shown in Equation 3-17. Electron scattering probability at the nanoparticle/matrix interface is proportional to the nanoparticle percentage. Thus, the theoretical electrical conductivity of the nanocomposite must obey the Arrhenius Relationship, as shown in Equation 3-18. This model suggests that the electrical conductivity of nanocomposites decays exponentially with increasing nanoparticle volume fraction. The experimental study shown in Figure 3-12 roughly agrees with this theoretical analysis. Thus, by properly selecting the nanoparticle volume fraction, the desired high electrical conductivity of the Cu matrix nanocomposite can be achieved.

$$P(E) = \frac{\exp\left(-\frac{E}{k_B T}\right)}{\sum \zeta_{(\varepsilon)}} \qquad \text{Equation 3-15}$$

$$P(E) = \frac{\exp\left(-\frac{\varepsilon_{WC}}{k_B T}\right)}{\exp\left(-\frac{\varepsilon_{WC}}{k_B T}\right) + \exp\left(-\frac{\varepsilon_{metal}}{k_B T}\right)} \approx \exp\left(-\frac{\varepsilon_{WC} - \varepsilon_{metal}}{k_B T}\right) \quad \text{Equation 3-16}$$

$$\Delta E \approx x \cdot (\varepsilon_{WC} - \varepsilon_{metal}) \quad \text{Equation 3-17}$$

$$\sigma = \sigma_0(T)\left[\exp\left(-\frac{\varepsilon_{F-WC} - \varepsilon_{F-metal}}{k_B T_F}\right)\right]^x = \sigma_0(T)\exp\left(-\frac{\varepsilon_{F-WC} - \varepsilon_{F-metal}}{k_B T_F} \cdot x\right) \quad \text{Equation 3-18}$$

where $P(E)$ is the possibility for electrons to be in a certain energy state E; T is temperature; ε_{WC} is Fermi energy of WC nanoparticles; ε_{metal} is Fermi energy of the matrix; x is nanoparticle volume percentage; T_F is the Fermi temperature of free electrons in metals.

The electrical conductivity of Cu/WC nanocomposites remains higher than 80% when the nanoparticle percentage is approximately below 8 vol.%, which can also be understood in aspects of the electron mean free path [52]. The mean free path of electrons in Cu at room temperature is approximately 38 nm [52]. When the spacing between WC nanoparticles in the Cu matrix is larger than 38 nm, the scattering of electrons by the nanoparticle-matrix interfaces can be less effective [52].

Based on the established material property vs. WC vol.% relationships, it was found that Cu with suitable WC contents can achieve the goal of high strength and high conductivity. Cu/7.6 vol.% WC cold rolled with 70% thickness reduction exhibits an ultimate tensile strength of 614±15 MPa, tensile elongation of 2-3%, and an electrical conductivity of 85% IACS [52]. It is also expected that the Cu/WC nanocomposites will offer excellent thermal stability due to the high stability of WC nanoparticles in the Cu matrix, which would be an advantage over Cu and its alloys. Moreover, dispersed WC nanoparticles are expected to improve the wear resistance of Cu. The nanocomposite was compared with common Cu alloys, as shown in Figure 3-13. Cu/WC shows a better combination of strength and electrical conductivity than common Cu alloys.

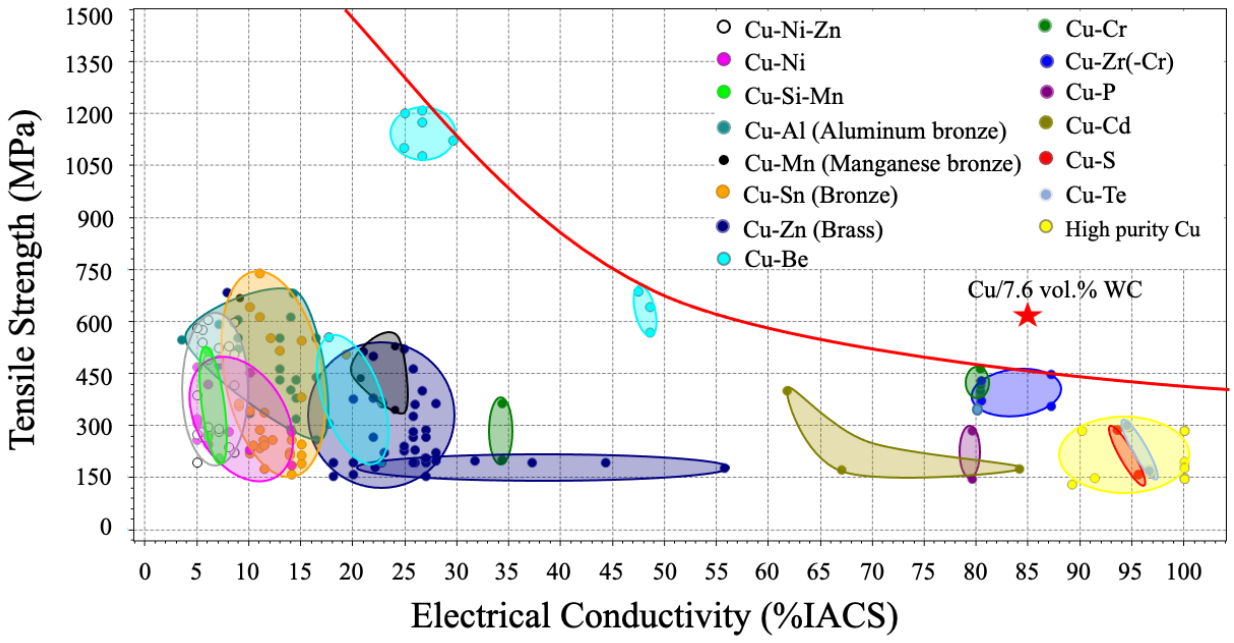

Figure 3-13 Tensile strength versus electrical conductivity of Cu/WC nanocomposite in comparison with common Cu alloys

3.1.4 Conclusions

We reported the ex-situ fabrication of Cu/WC nanocomposites with a wide range of WC contents, in which WC particles are well-dispersed. The hardness/strength of the Cu/WC nanocomposites can be significantly enhanced while maintaining reasonable electrical and thermal conductivity. Our study created a system of Cu/WC nanocomposites with different properties, which provided a feasible way to achieve the goal of fabricating high performance Cu based composites. By tuning the WC volume percentage, different combinations of properties can be achieved for specific applications.

3.2 In-situ Fabrication of Cu/TiB_2 Nanocomposites via Casting

3.2.1 Introduction

TiB_2 nanoparticles have attracted much attention as reinforcing elements in metal matrix nanocomposites since they exhibit excellent properties, such as high hardness, modulus, corrosion resistance, thermal stability. Besides, TiB_2 has good electrical and thermal conductivities among ceramics [61].

Molten Cu and TiB_2 have poor wettability (158° at 1100 °C), which has been a major obstacle to fabricating Cu/TiB_2 nanocomposites by regular casting. Attempts to fabricate Cu/TiB_2 nanocomposites have only resulted in limited success. Cu/TiB_2 nanocomposites were fabricated by powder metallurgy [62,63]. TiB_2 with sizes of 100-500 nm in Cu were fabricated by melting a ball-milled mixture of Ti, B, and Cu powders for 10 min [61]. It was also reported that TiB_2 nanoparticles in the range of 50-200 nm were formed in molten Cu by turbulent in-situ mixing of Cu-Ti and Cu-B masters under rapid cooling [14].

In this study, a new and scalable method to manufacture bulk TiB_2-nanoparticle-reinforced Cu via casting was developed. With titanium and boron bearing fluoride salts as precursors and aluminum as the reductant, dispersed TiB_2 nanoparticles with an average size of 65.1 nm were in-situ synthesized in molten copper. The microstructure of the as-solidified samples and the reaction mechanism of the synthesis were investigated.

3.2.2 Materials and Methods

Synthesis of Cu/TiB_2 Nanocomposites

Copper (99.99%, Rotometals) was heated to 1130 °C with argon protection in a graphite crucible by an induction heater. Al shots were added to molten Cu, followed by mixed KBF_4

(Spectrum), K_2TiF_6 (Spectrum), and $KAlF_4$ (AMG Aluminum) powders. The weight of raw materials was calculated according to Reaction 3-1 for desired volume fractions of TiB_2 in copper, with KBF_4 50% in excess. The volume of $KAlF_4$ (buffer salt) was 5 times of Cu. After holding for 1.5 h, the melt was cooled naturally in the furnace. After solidification, the salt on top of the metal was removed. As-synthesized sample was re-melted at 1100 ℃ for 5 min. The schematic is shown in Figure 3-14.

$$10Al + 6KBF_4 + 3K_2TiF_6 \rightarrow 3TiB_2 + 9KAlF_4 + K_3AlF_6 \qquad \text{Reaction 3-1}$$

The residual Al in the as-solidified samples can be removed by $CuCl_2$ according to Reaction 3-2. The as-solidified sample was heated to 1100 ℃ with Ar protection. $CuCl_2$ powders were loaded on top of the molten metal. The melt was held at 1100 ℃ for 20 min before cooling to room temperature.

$$3CuCl_2 + 2Al \rightarrow 2AlCl_3 + 3Cu \qquad \text{Reaction 3-2}$$

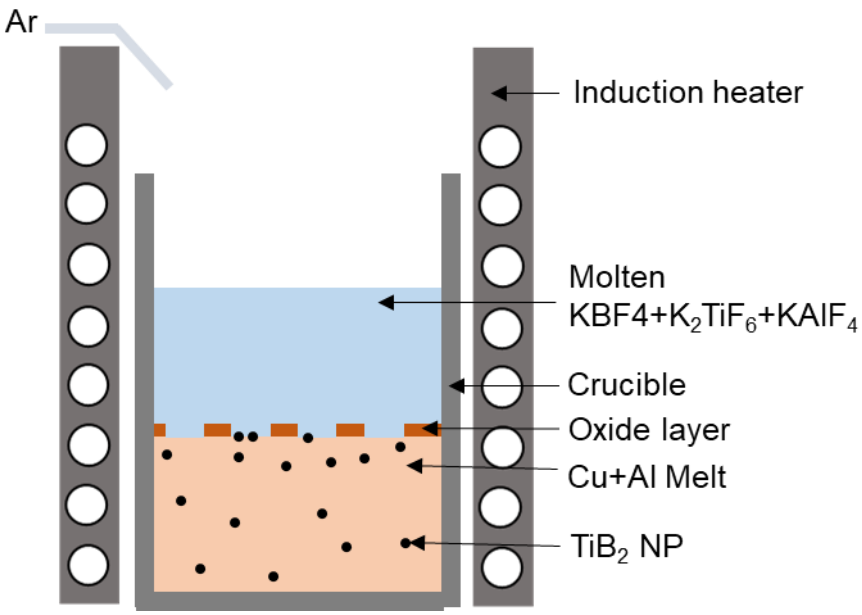

Figure 3-14 Schematic of in-situ fabrication of Cu/TiB_2 nanocomposites

Characterizations

Specimens cut from bulk samples were ground, polished, and ion milled at 4° and 4.5 kV for 1 h by Precision Ion Polishing System (Model PIPS 691, Gatan) to clean the surfaces. The microstructures were observed by scanning electron microscopy (SEM, ZEISS Supra 40VP) equipped with energy-dispersive X-ray spectroscopy (EDS). X-ray diffraction (XRD) analysis was conducted on the samples to identify the phases using Bruker D8 at a step size of 0.05° and a speed of 4°/min. The particle sizes were measured by image processing using Image-Pro software.

3.2.3 Results and Discussion

The XRD patterns of the as-synthesized Cu/TiB_2 sample are shown in Figure 3-15. The peaks are clearly indexed as the TiB_2 phase and the Cu phase. Thus, the successful synthesis of TiB_2 in Cu is confirmed. It should be noted that Cu peaks are shifted towards the lower angle side, which indicates the residual Al in Cu.

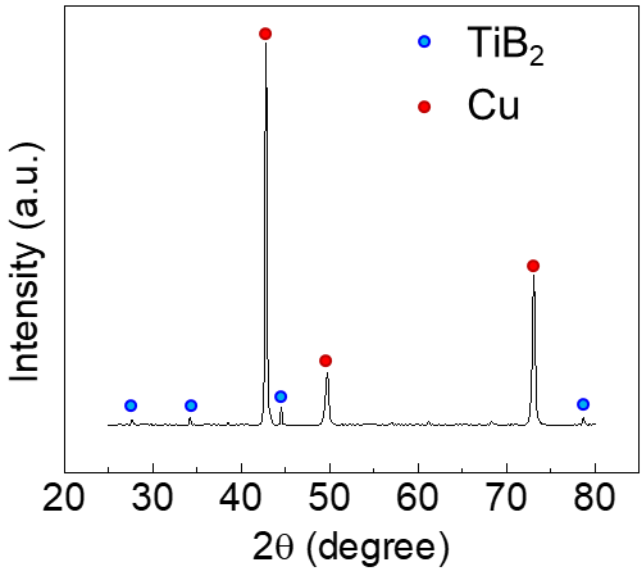

Figure 3-15 XRD patterns of as-synthesized in-situ Cu/TiB_2

The microstructural characterizations of the as-synthesized Cu/TiB_2 nanocomposite are shown in Figure 3-16. As shown in Figure 3-16a, the TiB_2 nanoparticles are uniformly distributed in the matrix. The corresponding EDS mappings of Cu, Al, and Ti are presented in Figure 3-16b, 3-16c, and 3-16d. The spatial distribution of Ti in Figure 3-16d coincides with the TiB_2 nanoparticles. The uniform distribution of TiB_2 nanoparticles is also demonstrated by the uniform mapping result of Ti in Figure 3-16d.

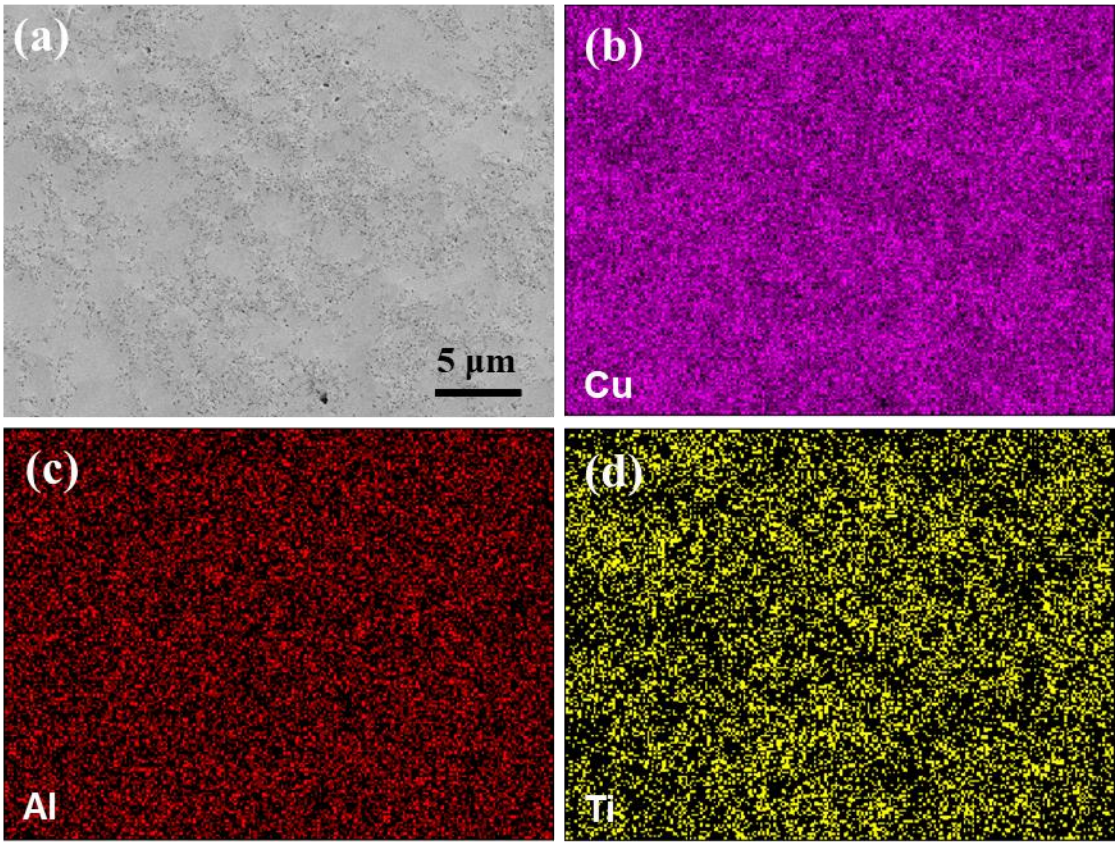

Figure 3-16 (a) Microstructure of as-synthesized in-situ Cu/TiB_2; (b)-(d) spatial distributions of Cu, Al, and Ti in (a) by EDS mapping

The mechanism of forming TiB_2 nanoparticles by the in-situ reactions in molten Cu was investigated. Figure 3-17 shows SEM images of locations close to the salt-metal interface in the as-solidified samples. String-like features in the micrometer scale are observed, as shown in Figure

3-17a. More importantly, nanoparticles are disintegrated from the string-like features. EDS point scan in the string-like feature only shows Ti peaks. A similar phenomenon is observed in other samples, as shown in Figure 3-17b. It should be noted that boron cannot be detected by EDS. Thus, the TiB_2 formation mechanism is anticipated as follows. Ti is reduced by Al from the molten salt at the interface and diffuses into molten Cu. Due to the high concentration of Ti in Cu close to the salt-metal interface, the Ti-rich phase grow laterally, which forms the string-like feature. As B diffuses into the Ti-rich phase, TiB_2 nanoparticles are formed and disintegrate from the string-like phase at the boundaries. KBF_4 is more volatile than K_2TiF_6. Besides, it was reported that the transfer efficiency of Ti from the molten salt to molten Al was higher than B in the Al-Ti-B system due to the strong heat evolution when Al reacts with K_2TiF_6 [64,65]. Hence, in this study, KBF_4 is 50% in excess in raw materials to maintain the stoichiometry.

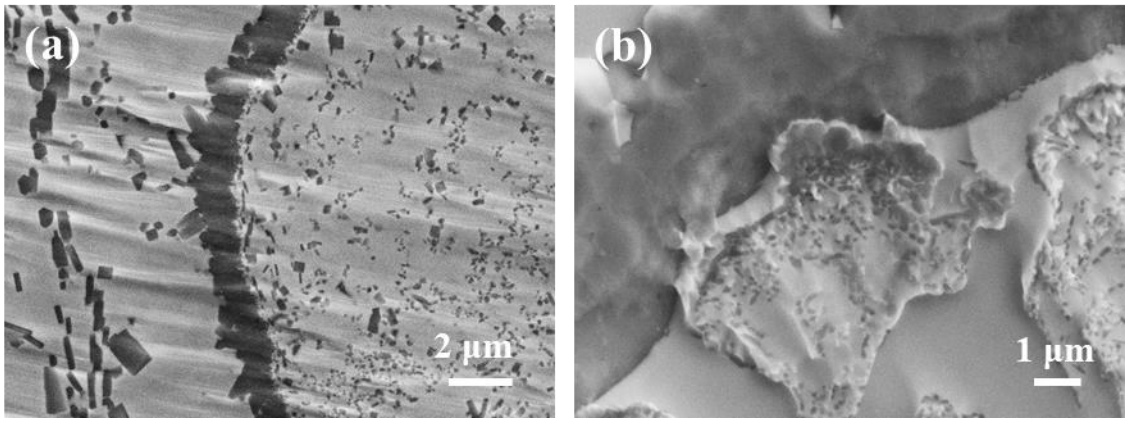

Figure 3-17 SEM images of the string-like features in the in-situ Cu/TiB_2 samples

Synthesis of TiB_2 particulates in Al by two fluoride salts has been reported. Al reacts with KBF_4 and K_2TiF_6 at the molten salt/molten metal interface, reducing B and Ti from KBF_4 and K_2TiF_6, respectively. According to the phase diagram, B and Ti form AlB_2 and $TiAl_3$ in molten Al. TiB_2 nanoparticles are formed by the reaction of AlB_2 and $TiAl_3$. Meanwhile, Cu can form

different intermetallic phases with Al, Ti, and B in molten Cu. In future studies, more studies need to be conducted to identify the phase evolutions in the Cu-Al-Ti-B system.

The microstructure of the sample after re-melting is shown in Figure 3-18. Re-melting the as-synthesized sample improves the microstructure. As shown in Figure 3-18a, no microscale phases such as the string-like features are present in the sample anymore. TiB_2 nanoparticles with uniform sizes are uniformly distributed in the matrix, as shown in Figure 3-18b. It is anticipated that microscale features float to the top due to buoyance during re-melting while TiB_2 nanoparticles are dispersed in the molten metal due to Brownian motion. The average size of TiB_2 nanoparticles is 65.1 ± 22.8 nm. The size distribution of TiB_2 nanoparticles in the matrix is shown in Figure 3-18c.

The in-situ TiB_2 nanoparticles are mostly in hexagonal platelet or cuboid shape, as shown in Figure 3-18b, which agrees well with the literature. Effects of compositions on the morphology of as-synthesized nanoparticles such as TiB_2 and TiC have been reported [66–68]. The morphology of TiB_2 particles was converted from hexagonal plates into rod-like structures by increasing Ti contents [67]. By increasing the Sc content in Al, TiB_2 transformed from hexagonal platelets to polyhedral or near-spherical morphology with decreasing particle sizes [68], which can be attributed to the preferential lattice plane adsorption of Sc by TiB_2. Morphological evolution of TiC from octahedron to cube induced by elemental nickel was reported owing to modified surface energy and crystal growth kinetics [66]. In future studies, it is of interest to study the effects of alloying elements on the growth mechanism of TiB_2 nanoparticles, in order to achieve synthesis of TiB_2 nanoparticles with desired shape and size in different Cu alloys.

Residual Al in Cu will severely deteriorate the conductivity. The removal of Al by $CuCl_2$ was studied. The microstructure of the sample after $CuCl_2$ processing is shown in Figure 3-19.

Severe coarsening of TiB_2 occurred, as indicated by the TiB_2 microparticles in Figure 3-19a. Coarsening of TiB_2 was to reduce the interfacial energy. It suggests molten pure Cu and TiB_2 have poor wetting, and that Al in the Cu melt can significantly increase the wettability. Some TiB_2 nanoparticles growing to larger sizes than before can be found in the sample, as shown in Figure 3-19b. It is expected that the coarsening of TiB_2 nanoparticles can kinetically be mitigated by reducing the duration of the TiB_2 nanoparticles in molten Cu.

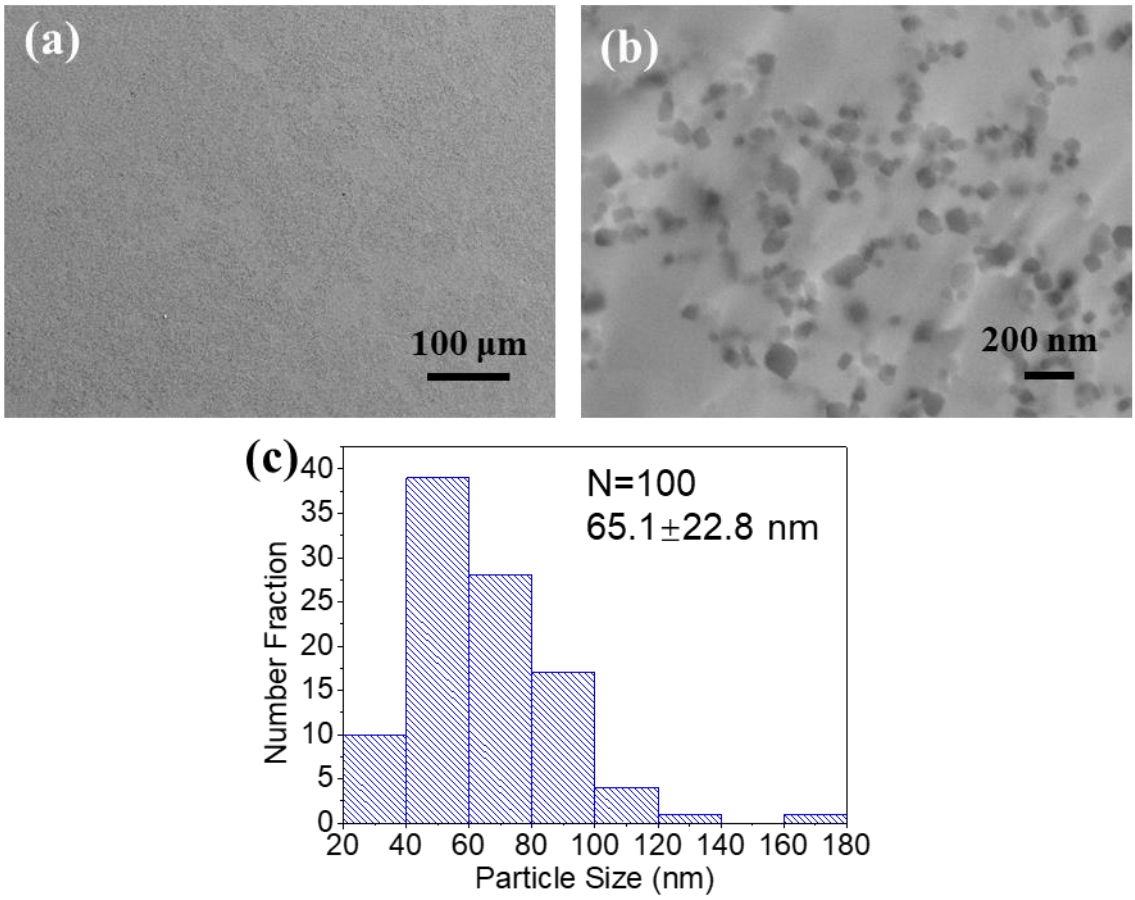

Figure 3-18 (a) Microstructure of Cu/TiB_2 after re-melting; (b) magnified image of an area in (a); (c) size distribution of TiB_2 nanoparticles in (b)

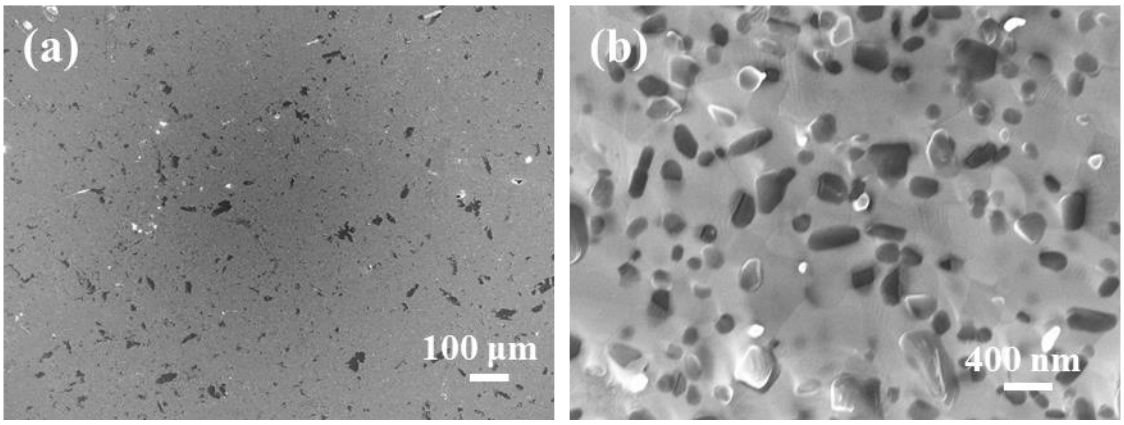

Figure 3-19 Microstructure of Cu/TiB_2 after $CuCl_2$ processing

3.2.4 Conclusions

A novel method to cast Cu containing dispersed in-situ TiB_2 nanoparticles using inexpensive fluoride salts as raw materials was developed. Aluminum not only acted as the reduction agent but also stabilized TiB_2 nanoparticles in molten Cu. The nanoparticle forming mechanism was discussed. TiB_2 nanoparticles with an average size of 65.1 nm uniformly distributed in the Cu matrix was achieved.

3.3 High performance Cu-0.1Al-0.1Mg/TiB_2 Nanocomposite

3.3.1. Introduction

TiB_2 nanoparticles have been attractive for strengthening metals. TiB_2 exhibits a relatively higher electrical conductivity (19% IACS at 20 °C) and microhardness (33 GPa) among borides and carbides of transition metals. However, molten pure Cu and TiB_2 have poor wettability, with a contact angle of 158° at 1100 °C. Thus, it has been a great challenge to fabricate Cu/TiB_2 nanocomposites via regular casting since TiB_2 nanoparticles cannot be stabilized in molten Cu.

Alloying has been reported to improve the wettability between molten metals and ceramics. Increasing Ti contents in Cu-Ti melts can effectively decrease the contact angles and increase the

work of adhesion on Y_2O_3 and Al_2O_3 at 1423 K [69]. In our previous study, we developed in-situ fabrication of CuAl/TiB_2 nanocomposites by casting, which can effectively incorporate and control the size of TiB_2 nanoparticles in Cu. We used two fluoride salts as Ti and B sources and Al as the reduction agent to form TiB_2 nanoparticles in molten Cu. The residual Al in Cu melt helped stabilize TiB_2 in molten Cu.

Cold rolling is an effective strategy to enhance the hardness/strength of metallic materials. Cu-Mg alloys are usually used in strain hardened conditions due to the high strain hardening exponent. The content of Mg is usually kept below 0.5 wt.% to maintain electrical conductivity.

Although alloying can modify the microstructure and enhance the properties of the nanocomposites, it will also substantially decrease the electrical conductivity of Cu. Thus, the alloying contents must be appropriately selected to ensure the desired stabilization of TiB_2 nanoparticles in Cu, the prominent strain hardening effect, while maintaining high electrical conductivity.

In this study, we designed and fabricated Cu-0.1Al-0.1Mg/3 vol.% TiB_2 nanocomposite. The microstructure, microhardness, and electrical conductivity of the nanocomposite were evaluated. Results showed that 0.1 wt.% Al stabilized TiB_2 nanoparticles in Cu. The addition of 0.1 wt.% Mg led to higher hardness after cold rolling by the same thickness reduction. TiB_2 nanoparticles effectively increased the hardness over Cu-0.1Al-0.1Mg while causing less deterioration of the electrical conductivity compared to alloying of Al and Mg. The nanocomposite sample with cold rolling by 37% thickness reduction can achieve a microhardness of 156.8 HV with an electrical conductivity of 65% IACS.

3.3.2. Materials and Methods

Cu-0.1Al-0.1Mg/3 vol.% TiB_2 nanocomposite was fabricated by a two-step process. First, Cu-0.1Al/3 vol.% TiB_2 was fabricated by diluting in-situ Cu-3.3Al/15 vol.% TiB_2 nanocomposite master with pure Cu at 1130 °C. Second, Cu-0.1Al-0.1Mg/3 vol.% TiB_2 was fabricated by alloying Cu-0.1Al/3 vol.% TiB_2 with Mg using a Cu-9.5 Mg master at 1130 °C. It should be noted that the ingot was not homogeneous due to the extensive dilution. The Cu-0.1Al-0.1Mg/3 vol.% TiB_2 was taken from the top of the ingot for theoretical study.

Specimens cut from the as-solidified bulk samples were ground, polished. The microstructure of the samples was observed by optical microscopy and scanning electron microscopy (SEM, Zeiss Supra 40VP). The samples are cold rolled with a 37% thickness reduction. The microhardness of samples was measured using an LM 800AT microhardness tester with a load of 200 g and a dwell time of 10 s. Electrical conductivity was measured by 4-point probe at room temperature.

3.3.3. Results and Discussion

The microstructure of Cu-0.1Al-0.1Mg/3 vol.% TiB_2 is shown in Figure 3-20. As shown in Figure 3-20, TiB_2 nanoparticles are dispersed and stabilized in the Cu matrix. It is believed that the addition of 0.1 wt.% Al decreases the interfacial energy between TiB_2 and the melt, inhibiting the sintering of the TiB_2 nanoparticles while not sacrificing electrical conductivity severely. No reaction was observed in the nanocomposite sample. However, it should also be noted that increasing the contents of the alloying elements might also lead to possible reactions between the alloy elements and the nanoparticles.

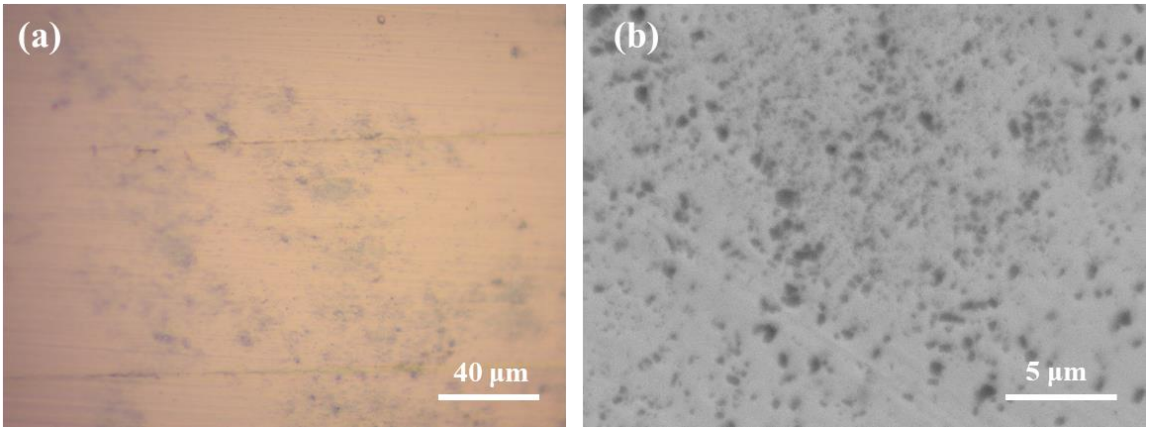

Figure 3-20 (a) optical image; (b) SEM image of the microstructure Cu-0.1Al-0.1Mg/3 vol.% TiB_2

It is anticipated that the stabilization of TiB_2 nanoparticles in Cu can be attributed to the segregation of aluminum at the interface and the resultant improved adhesion of the interfaces. The contact angle of molten metal on a solid surface is given by Equation 3-19 to 3-21 [70].

$$\cos\theta = \frac{\sigma_{SV}-\sigma_{SL}}{\sigma_{LV}} \qquad \text{Equation 3-19}$$

$$W_a = \sigma_{SV} + \sigma_{LV} - \sigma_{SL} \qquad \text{Equation 3-20}$$

$$\cos\theta = \frac{W_a}{\sigma_{LV}} - 1 \qquad \text{Equation 3-21}$$

where θ is contact angle. σ_{SV}, σ_{LV}, σ_{SL} are the surface energy of the solid, surface energy of the liquid, and the interfacial energy of the solid/liquid interface. W_a is the adhesion energy of the system that is required to separate a solid and a liquid.

According to Equation 3-21, the contact angle depends on two competing factors: the adhesion forces decided by the adhesion energy which promotes wetting; the cohesion forces (equal to $2\sigma_{LV}$) of a liquid in the opposite direction [70]. Molten metals have high surface energy and high cohesion. Good wettability can be achieved when W_a increases, possible when interfacial bonding is strong [70]. In this study, we suspect that Al segregated at the nanoparticle/molten metal

interfaces bonds with Ti on the surface of the nanoparticles, forming strong interfacial bonding. Thus, the TiB_2/molten Cu interfacial energy is decreased and stabilization of TiB_2 nanoparticles in molten Cu is achieved.

The microhardness of Cu-0.1Al, Cu-0.1Al-0.1Mg, Cu-0.1Al-0.1Mg/3 vol.% TiB_2 before and after cold rolling (37% thickness reduction) are summarized in Figure 3-21. After cold rolling, the hardness of Cu-0.1Al-0.1Mg is increased by 19.8 HV, while that of Cu-0.1Al-0.1Mg is increased by 53.9 HV. Thus, the addition of 0.1 wt.% Mg contributes to stronger strain hardening effects. We suspect that the addition of Mg can change lattice parameters of Cu and enhance the ability to store dislocations. In addition, it is possible that Mg, as foreign atoms in Cu lattice, can pin segments of dislocations to increase the ability for dislocation multiplication during cold rolling. The microhardness of Cu-0.1Al-0.1Mg/3 vol.% TiB_2 is further increased to 156.8±14.9 HV after cold rolling.

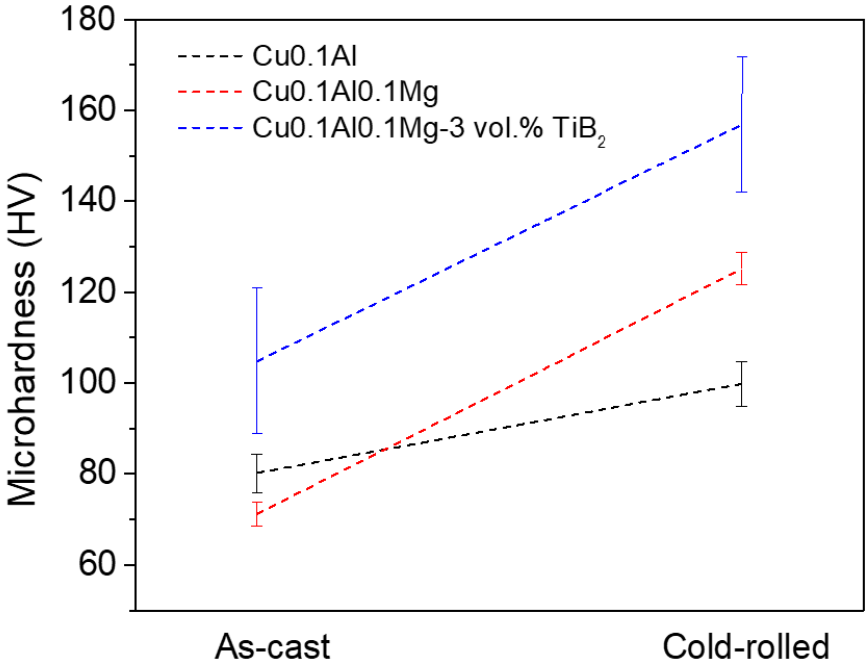

Figure 3-21 Microhardness evolution of Cu-0.1Al, Cu-0.1Al-0.1Mg, and Cu-0.1Al-0.1Mg/3 vol.% TiB_2

The electrical conductivity of Cu-0.1Al-0.1Mg/3 vol.% TiB_2 was measured to be 65.0±6.3% IACS. The breakdowns of the electrical conductivity drop in the nanocomposite sample compared to pure Cu are shown in Table 3-1. The addition of 0.1 wt.% Al roughly leads to a decrease of 15% IACS [5]. Besides, the addition of 0.1 wt.% Mg combined with cold rolling (37% thickness reduction) results in another decrease of approximately 15% [71]. Accordingly, the incorporation of 3 vol.% TiB_2 nanoparticles only caused an electrical conductivity drop of roughly 5% IACS. The cold-rolled Cu-0.1Al-0.1Mg/3 vol.% TiB_2 exhibits a good combination of hardness and electrical conductivity.

Table 3-1 Breakdown of the electrical conductivity drop in cold rolled Cu-0.1Al-0.1Mg/3 vol.% TiB_2 compared to pure Cu.

Condition	Electrical Conductivity Decrease
0.1 wt.% Al	~15% IACS
0.1 wt.% Mg+37% thickness reduction	~15% IACS
3 vol.% TiB_2	~5% IACS

3.3.4. Conclusions

In summary, a new Cu alloy matrix nanocomposite, Cu-0.1Al-0.1Mg/3 vol.% TiB_2 was designed and fabricated by casting. Results showed that Al stabilizes TiB_2 nanoparticles in Cu. Mg contributes to higher hardness after cold rolling under the same thickness reduction. TiB_2 nanoparticles effectively increase the hardness while causing much less deterioration of the electrical conductivity compared to alloying. The nanocomposite sample with cold rolling (37%

thickness reduction) can achieve a microhardness of 156.8 HV with an electrical conductivity of 65% IACS.

3.4 Salt Melt Assisted In-Situ Synthesis of Tungsten Nanoparticles in Copper

Copper (Cu)/tungsten (W) nanocomposites exhibit novel properties, thus widely used in industry. However, fabrication of bulk Cu/W nanocomposites by casting has not been demonstrated. Moreover, it is very difficult to control the severe coarsening of W nanoparticles in Cu during processing. In this study, a scalable molten-salt-assisted in-situ synthesis method was developed to cast Cu containing uniformly distributed W nanoparticles using tungsten oxide (WO_3) microparticles as the precursor. With WO_3 microparticles dissolved by molten $KAlF_4$ and reduced by molten aluminum, W nanoparticles were formed in the Cu matrix. Effects of the synthesis parameters on the W nanoparticle size were studied theoretically and experimentally. An average size of the W nanoparticles as small as 132.7 nm in the Cu matrix was achieved. The in-situ Cu/W nanocomposites exhibit enhanced mechanical properties due to the effective nanoparticle size control. For in-situ Cu/5.6 vol.% W, it exhibits a Young's modulus of 137.2 GPa and a microhardness of 100.9 HV, 20.4% and 50.6% higher than Cu respectively. This work paves a new way to fabricate metals reinforced by uniformly distributed nanoparticles through conventional casting using inexpensive microparticles.

3.4.1 Introduction

Copper (Cu) and tungsten (W) are immiscible in both liquid and solid states due to a high positive heat of mixing, making them a good pair for nanocomposites to exhibit novel material properties [72–74]. Cu/W nanocomposites combine the high electrical and thermal conductivities

of Cu and the high hardness/strength, wear resistance, modulus, and thermal stability of W. Cu/W nanocomposites are strongly demanded in industry especially for heavy-duty applications, e.g., electrical contacts, electric resistance welding electrodes, high-current circuit breakers, heat sinks [75–77].

Currently, Cu/W nanocomposites are mainly prepared by powder metallurgy (PM) [78–81]. However, issues including porosity, inhomogeneity, and especially coarsening of W nanoparticles due to the large lattice mismatch between Cu and W are inevitable. More importantly, it encounters difficulties to produce large parts with complex structures by PM. Casting, a widely used technique in manufacturing, is of significance for the production of high-performance and complex parts. Fabrication of Cu/W nanocomposites by casting has not been demonstrated so far, due to the hardship to incorporate and disperse W nanoparticles and also the severe coarsening and sintering of W nanoparticles during processing.

The size of nanoparticles in metal matrices strongly affects the properties of the nanocomposites. Smaller W nanoparticles are desired to induce higher Orowan strengthening, improve microstructural homogeneity and ductility, and potentially increase the arc erosion resistance. It was reported that although the starting W nanoparticles were 40-60 nm in size, W nanoparticles in Cu grew to 3-5 μm after vacuum sintering at 1200 °C for 1 h [82]. While spark plasma sintering (SPS) can reduce the processing time, the growth of W nanoparticles to 200-300 nm and the formation of dense W clusters were still reported [82]. By dynamic consolidation, which utilized a shock wave to enable an ultra-fast consolidation of powders into bulk samples to prevent grain growth, the W crystalline size (by the Scherrer-equation) retained almost the same as the as-milled one [83]. However, dynamic consolidation is difficult to meet the requirements of mass production. Additionally, infiltration was used to fabricate W/Cu nanocomposites. Despite

the short processing time (5s), the W nanoparticle size increased from 100 nm to 300nm [84], let alone inhomogeneity caused by infiltration. Besides, Cu/W nanocomposites were fabricated by annealing Cu/W nano-multilayers prepared by sputtering [85]. These methods are difficult to achieve mass production of bulk Cu/W nanocomposite samples with desired microstructures and properties.

Besides, the high cost of W nanoparticles is limiting the application of Cu/W nanocomposites. Several attempts have been made to synthesize W nanoparticles via chemical reactions using inexpensive raw materials [86,87]. Cu/W nanocomposite powders were prepared by joint reduction of CuO and WO_3 micropowders by a Mg-C reducer through self-propagation high-temperature synthesis [81]. Cu/W nanocomposite powders were also prepared by a sol-gel method using copper nitride and ammonium tungstate as precursors. These powders were subsequently consolidated by PM to fabricate bulk samples [88]. However, direct in-situ synthesis of W nanoparticles from microparticle precursors into bulk Cu matrix has not yet been reported.

In this study, a scalable manufacturing method of bulk Cu containing uniformly distributed W nanoparticles by casting via molten-salt-assisted in-situ reactions was developed. The underlying mechanism of synthesizing W nanoparticles from inexpensive WO_3 microparticles into the Cu matrix is elucidated. The effects of the synthesis parameters including temperature, reaction time, and the WO_3 concentration in the molten salt on the size of in-situ W nanoparticles in the Cu matrix were investigated. The relationships between microhardness and Young's modulus of in-situ Cu/W nanocomposites with the W nanoparticle contents were studied.

3.4.2 Materials and Methods

The schematic of the in-situ fabrication of Cu/W nanocomposites is shown in Figure 3-22, with WO_3 microparticles (labeled 50 μm) as the W source. Additionally, the chemical reaction is shown in Reaction 3-3. For a certain designed volume percentage of W nanoparticles in Cu, the amount of initial Al and WO_3 is calculated according to Reaction 3-3. Firstly, mixed WO_3 and $KAlF_4$ powders were melted at 700 ℃ in a graphite crucible by induction heating and held for 20 min before being cast out. Then, Cu was heated to 1100 ℃ under Ar protection in a graphite crucible by induction heating. Aluminum (Al) beads were added into the melt. A spoonful of $KAlF_4$ was loaded on top of the melt to form a molten salt pool. The cast WO_3-$KAlF_4$ mixtures were added into the salt pool and held for different times (0.5 h or 1 h) to allow the reaction to happen. The overall concentration of WO_3 in $KAlF_4$ was controlled at 3 wt.% or 6 wt.%.

$$2Al + WO_3 \rightarrow Al_2O_3 + W \qquad \text{Reaction 3-3}$$

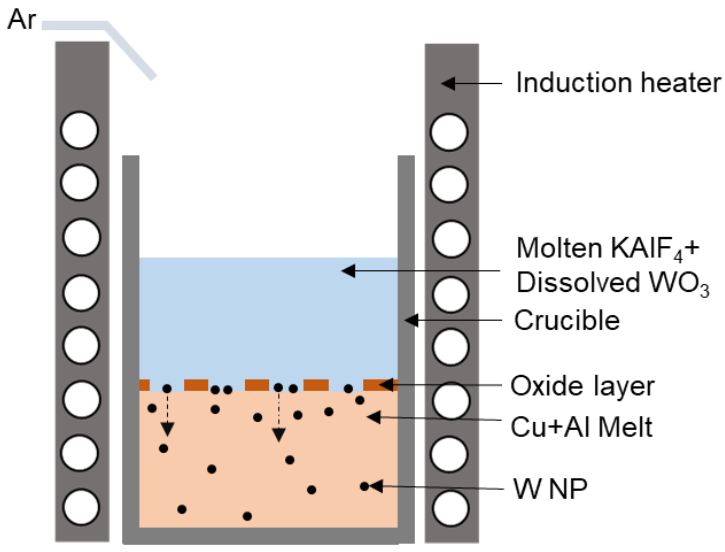

Figure 3-22. Schematic of the salt-melt assisted in-situ fabrication of Cu distributed with W nanoparticles from WO_3 microparticles

In comparison, ex-situ Cu/W nanocomposites were fabricated with commercial W nanoparticles (40-60 nm, US Research Nanomaterials) via the molten-salt assisted self-incorporation method (see experimental procedures in [89–91]) using $KAlF_4$ as the flux. The melt was held at 1130 ℃ for 0.5 h.

To remove the residual Al, the in-situ Cu/W samples were heated to 1100 ℃ with Ar protection, and $CuCl_2$ powders were loaded on top of the molten metal. The melt was held at 1100 ℃ for 5 mins with mechanical mixing at 400 rpm by a graphite blade before cooling to room temperature in the furnace.

To extract W nanoparticles from the in-situ Cu/W, the nanocomposite samples were immersed in a $FeCl_3$/DI water solution until the Cu matrix was fully dissolved. Then, the W nanoparticles were washed by DI water and collected in a centrifuge.

The initial WO_3 microparticles and bulk nanocomposites (in-situ and ex-situ) were examined by scanning electron microscopy (SEM, ZEISS Supra 40VP) equipped with energy-dispersive X-ray spectroscopy (EDS). To reveal the W nanoparticles in the Cu matrix, the SEM samples of the bulk nanocomposites were prepared by grinding, polishing, and ion milling at 4° and 4.5 kV for 1 h (Model PIPS 691, Gatan). The phases of the bulk Cu/W nanocomposites were analyzed by X-ray diffraction (XRD, Bruker D8) using Cu Kα radiation with a step size of 0.05° at a speed of 4°/min. Initial WO_3 microparticles, simply mixed WO_3-$KAlF_4$, and solidified WO_3-$KAlF_4$ (held at 700℃ for 20 min) were analyzed by XRD with the same parameters mentioned above. For XRD analysis samples, the WO_3 was 3 wt.% in $KAlF_4$. The Young's modulus of the nanocomposites was measured by the MTS nanoindenter with a Berkovich tip with an indent depth of 2 μm. The microhardness of Cu/W nanocomposites was tested by the LM 800AT microhardness

tester using a 200 g load with a 10 s dwell time. Each Young's modulus and microhardness data represents 10 measurements at room temperature.

The size analysis of the W phase in the Cu matrix was conducted via image processing. The actual volume percentages of W nanoparticles in the Cu matrix were calculated based on the weight percentages of Cu and W from EDS mappings.

3.4.3 Results and Discussion

The morphology of the as-received WO_3 microparticles is shown in Figure 3-23. The representative microstructure of the as-solidified in-situ Cu/5.6 vol.% W nanocomposite is shown in Figure 3-24a, where W nanoparticles are uniformly distributed in the Cu matrix. Unlike Cu/W nanocomposites prepared by PM, no porosities are observed in this sample. The XRD patterns of the as-solidified Cu/5.6 vol.% W sample are illustrated in Figure 3-24b. The peaks are clearly indexed as Cu and W phases. Therefore, the synthesis of in-situ W nanoparticles in the Cu matrix from WO_3 microparticles is confirmed.

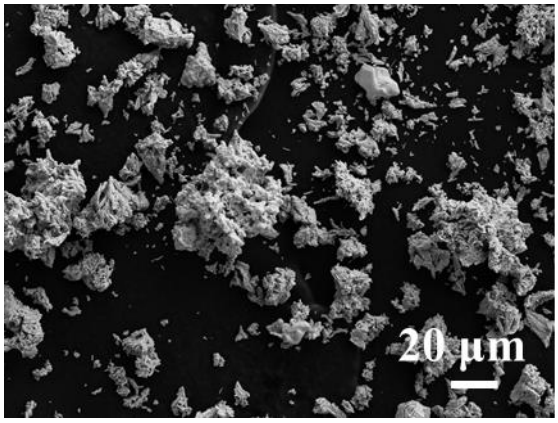

Figure 3-23. SEM image of initial WO_3 microparticles.

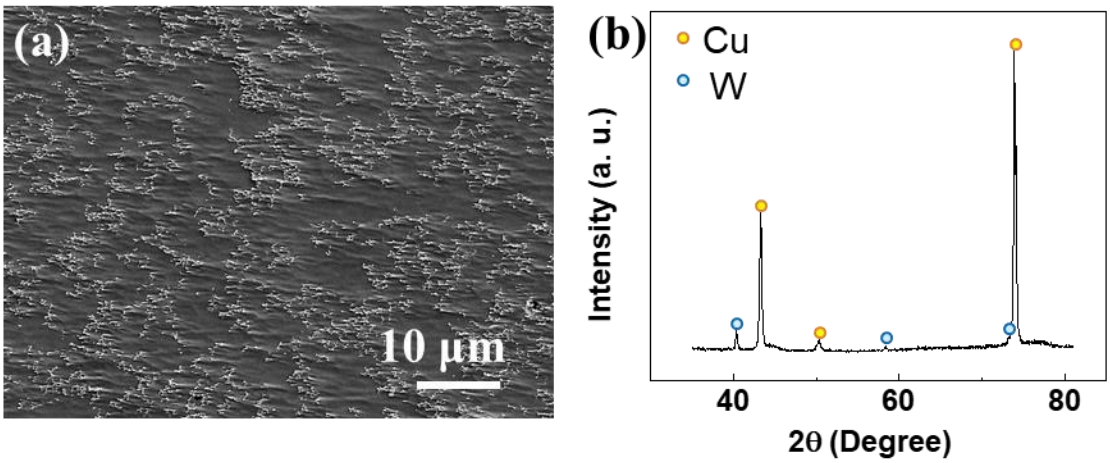

Figure 3-24 (a) SEM image of as-solidified Cu/5.6 vol.% W nanocomposite; (b) XRD patterns of (a)

To understand the underlying mechanisms of obtaining W nanoparticles from WO_3 microparticles despite the large size differences, XRD analysis of the raw materials at different conditions was conducted, with the results shown in Figure 3-25. Firstly, the XRD patterns of as-received WO_3 microparticles are indicated by the black line. The phase integrity of the as-received WO_3 is confirmed as all the peaks are indexed as WO_3. Secondly, for WO_3 and $KAlF_4$ that were simply mixed, the XRD patterns are indicated by the red line, which can still be indexed as two phases, i.e., WO_3 and $KAlF_4$. However, only $KAlF_4$ peaks are shown in the XRD patterns of the solidified WO_3-$KAlF_4$ (blue line) after melting the mixture at 700 °C for 20 min. Moreover, the $KAlF_4$ peaks are shifted towards lower angles, indicating an increase in the lattice parameters of the resolidified $KAlF_4$. The understanding of oxide interactions with molten salts is not thorough yet in literature, especially at the molecular scale. It suggests that $KAlF_4$ dissolved some WO_3 microparticles, causing its lattice parameters to increase. As a result, the synthesis of W nanoparticles from the initial WO_3 microparticles despite the large size difference is enabled. In future studies, detailed investigation of WO_3 interaction with molten $KAlF_4$ will be conducted.

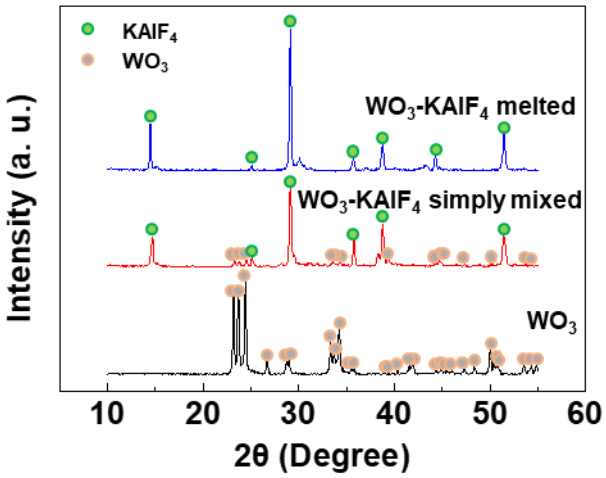

Figure 3-25 XRD patterns of WO_3, mixed WO_3-$KAlF_4$, and as-solidified WO_3-$KAlF_4$ after melting

The reaction mechanism to generate W nanoparticles is discussed as follows. The salt melt can dissolve metal oxides, with the dissolution reaction of oxide being basic dissolution or acidic dissolution [92]. For simplicity, it is assumed that molten $KAlF_4$ dissolved WO_3 microparticles up to the solubility, forming W^{6+}, according to Reaction 3-4 (acidic dissolution). At the molten metal-molten slat interface, molten Al reacts with W^{6+}, generating W atoms according to Reaction 3-5. The resultant W atoms will nucleate and grow to W nanoparticles. The incorporation of W nanoparticles into molten Cu is driven by the minimization of the system's Gibbs energy. W has a better wettability with molten Cu (despite the semi-coherent interface [93]) than with molten salt. Thus, W migrating into molten Cu reduces the interfacial energy, thereby decreasing Gibbs energy ($\Delta G < 0$, according to Equation 3-22). The molten salt can also inhibit the oxidation of the molten metal and dissolve the oxide layer on the surface of the molten metal.

$$WO_3 \rightarrow W^{6+} + 3O^{2-} \qquad \text{Reaction 3-4}$$

$$W^{6+} + 2Al \rightarrow W + 2Al^{3+} \qquad \text{Reaction 3-5}$$

$$\Delta G = 4\pi R^2(\gamma_{NM} - \gamma_{NS}) \qquad \text{Equation 3-22}$$

where R is the radius of the W nanoparticle, γ_{NM} is the interfacial energy between the nanoparticle and the molten metal, and γ_{NS} is the interfacial energy between the nanoparticle and the molten salt.

It is vital to dissolve WO_3 microparticles in the salt melt to achieve the synthesis of W nanoparticles, which is limited by the solubility of WO_3 in the salt melt. Thus, increasing the solubility of oxides in molten salt can enable an increased reaction rate and yield. However, there is no data available on the solubility of WO_3 in molten $KAlF_4$. The hard-soft acid-base (HSAB) theory was recommended to predict the solubility of metal oxides in salt melts [94]. Manipulating the compositions of the salt melt can potentially increase the solubility of oxide. It was reported that the solubility of metal oxides increased significantly with the Na_2O content in the B_2O_3 solvent [95]. It was also reported that the solubility of CaO in the $CaCl_2$ melt is more than 15% [94].

Chen *et al.* investigated the diffusional growth of Bi in an immisible Al-Bi alloy with theoretical models to describe the growth of Bi nanoparticles [96]. Thus, assuming W nanoparticles in Cu melt grow by diffusional transport of W atoms. The diameter of W nanoparticles is estimated by Equation 3-23 and 3-24 [96].

$$d = 2\sqrt{2DSt} \qquad \text{Equation 3-23}$$

$$S = \frac{C_0 - C_1}{C_2 - C_0} \qquad \text{Equation 3-24}$$

where d is the diameter of W nanoparticle, D is the diffusion coefficient, t is the time, S is the supersaturation, C_0 is the overall average W concentration, C_1 is the W concentration at the interface between the growing W nanoparticle and the Cu melt, and C_2 is W concentration in the W nanoparticle. Thus, the sizes of W nanoparticles can be controlled by the synthesis temperature, time, and the WO_3 concentration in the molten salt.

Since the size of the W nanoparticles increases with increasing D, which increases with the temperature, the synthesis temperature should be maintained as low as possible such as slightly above the melting point of Cu. Thus, the synthesis temperature was set at 1100 °C. To minimize the size of synthesized W nanoparticles as much as possible, the effects of reaction time and the WO_3 concentrations in the salt melt on the sizes of the W nanoparticles were studied experimentally. Figure 3-26 shows the SEM images of the microstructures of the in-situ Cu/designed 5 vol.% W samples and the corresponding nanoparticle size distributions under different experimental conditions. The effect of the reaction time is revealed by the comparison of Figure 3-26a and 3-26c. With the concentration of WO_3 in $KAlF_4$ at 6 wt.%, and the reaction time of 1 h, the microstructure of the resultant Cu/W is depicted in Figure 3-26a. The average size of W nanoparticles is 420.1 ± 278.3 nm. For a reaction time of 0.5 h, the microstructure of the resultant Cu/W is shown in Figure 3-26c, where the average W nanoparticle size is reduced to 170.5 ± 101.2 nm. Hence, the average nanoparticle size decreases when reducing the reaction time. Furthermore, the effect of the WO_3 concentration is revealed by comparing Figure 3-26c and 3-26e. With the reaction time fixed at 0.5 h, while the concentration of WO_3 in $KAlF_4$ decreased from 6 wt.% (Figure 3-26c) to 3 wt.% (Figure 3-26e), the nanoparticle size decreased from 170.5 nm to 132.7 nm. Moreover, Fig. 5f shows that the number fraction of W nanoparticles below 100 nm in the Cu/W sample (Figure 3-26e) also increased to more than 30%. Thus, the size of the nanoparticles decreases with decreasing the WO_3 concentration in the molten salt. It is expected that by furthering optimizing the experimental parameters, the size of the W nanoparticles in Cu can be reduced to below 100 nm.

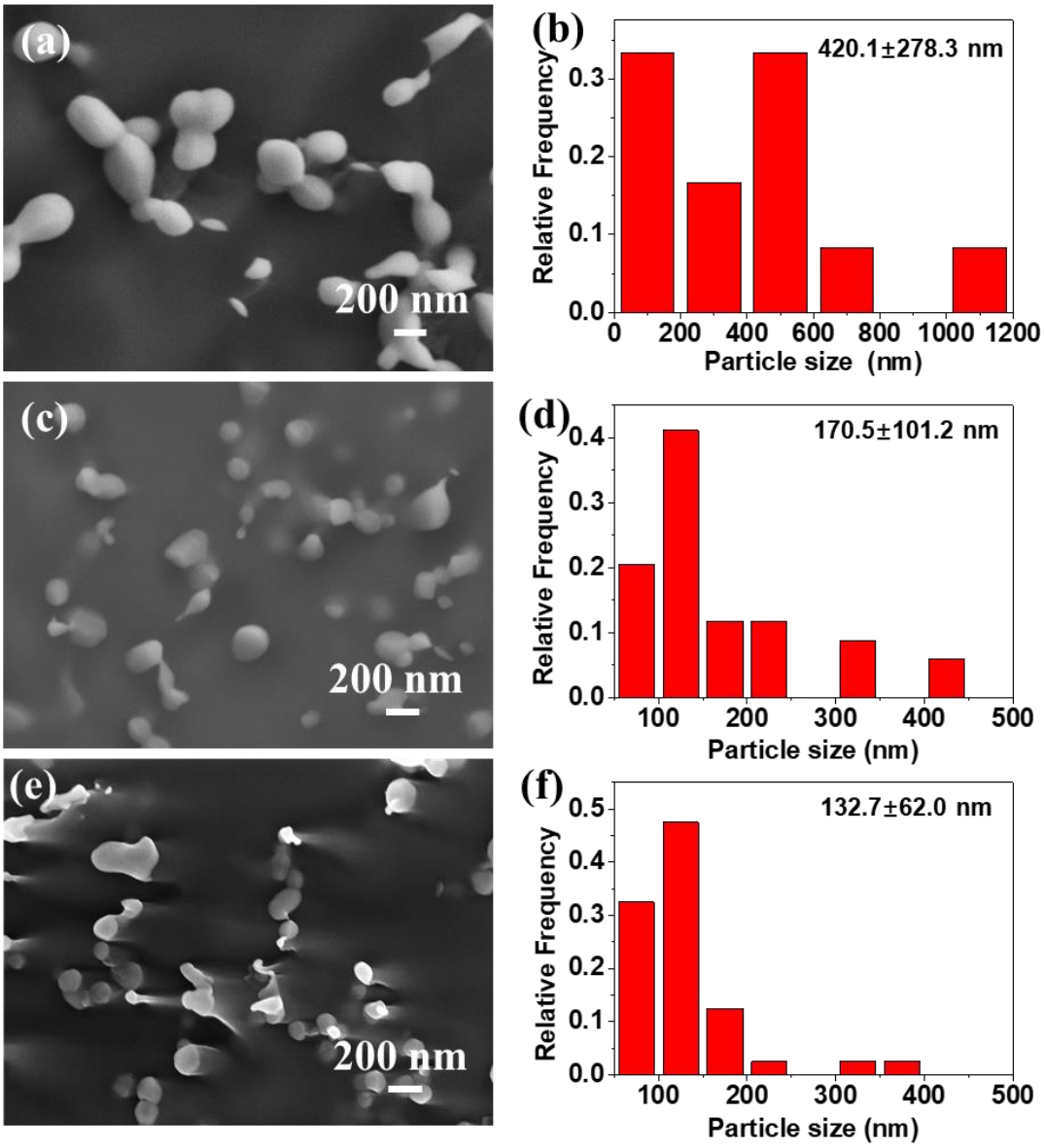

Figure 3-26 Microstructure of in-situ Cu/designed 5 vol.% W by different experimental parameters: (a) WO_3 is 6 wt.% in $KAlF_4$ and reaction time is 1 h; (b) Size distributions of W in (a); (c) WO_3 is 6 wt.% in $KAlF_4$ and reaction time is 0.5 h; (d) Size distributions of W in (c); (e) WO_3 is 3 wt.% in $KAlF_4$ and reaction time is 0.5 h; (f) Size distributions of W in (e)

While smaller crystalline sizes of W nanoparticles by XRD analysis were reported in some studies, it should be noted that the crystalline size calculated from XRD can be much smaller than the actual particle size [97]. For example, the crystalline size of W particles in bulk Cu/5 vol.% W

was calculated to be 30.5 nm according to the Scherrer equation, but the actual average W particle size under SEM was 1127 nm [93]. In addition, W nanoparticles with an average size of 14.5 nm were observed in TEM samples of Cu-13.4 vol.% W fabricated by cryomilling of Cu and W microparticles and subsequent annealing of the compacted powders [97]. However, it was also clarified that the actual W particle size ranged from 5-5000 nm from SEM observation, with only half of the W particles reduced to nanoscale [97]. Lu *et al.* reported that the size of W nanoparticles increased to 199 nm in bulk Cu-10W (4.9 vol.%) fabricated by a sol-gel method with ball-milling and SPS [88]. Due to the dissolution of WO_3 microparticles in molten salt, the W nanoparticles in the present study were generated from W ions by the nucleation and the following grain growth. Therefore, starting with WO_3 microparticles, small in-situ W nanoparticles in the Cu matrix were achieved via casting, with no ball milling or other powder techniques needed.

The mechanical properties of the as-solidified Cu containing different volume percentages of in-situ W nanoparticles (using the optimal experimental parameters discussed above) were evaluated. The actual volume percentages of in-situ W nanoparticles in Cu were estimated by EDS mapping data and used to establish the relationships. Young's modulus of the Cu/W nanocomposites versus the volume percentage of W is shown in Figure 3-27. For Cu/5.6 vol.% W, its Young's modulus is 137.2 ± 10.6 GPa, which is 20.4% higher than that of pure Cu. The theoretical upper limit and lower limit of the Young's modulus of nanocomposites can be estimated by Equation 3-25 and 3-26, respectively [98].

$$E_U = (1 - f_r)E_m + f_r E_r \qquad \text{Equation 3-25}$$

$$E_L = \frac{E_m E_r}{(1-f_r)E_r + f_r E_m} \qquad \text{Equation 3-26}$$

Considering the Young's moduli of Cu and W are 110-128 GPa and 411 GPa respectively, the theoretical Young's modulus of Cu/5.6 vol.% W is estimated to be between 115 GPa and 144

GPa. It should be noted that residual Al (1.21 wt.%) in the Cu matrix can slightly modify the Young's modulus of the Cu matrix. Overall, the experimental value agrees with the theoretical calculation.

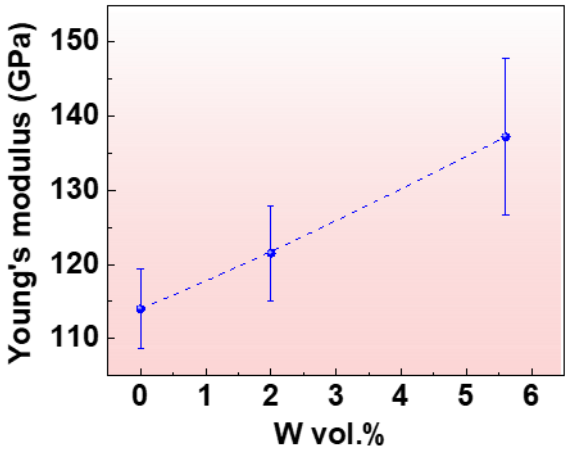

Figure 3-27 Variations of the Young's modulus of the in-situ Cu/W samples with the volume percentages of W nanoparticles

The microhardness of the in-situ Cu/W nanocomposites as a function of the W nanoparticle volume percentage is presented in Figure 3-28. It exhibits a roughly linear trend between the microhardness and the W content. For Cu/5.6 vol.% W, the microhardness is 100.9 ± 6.8 HV. Possible mechanisms contributing to the strengthening of the Cu/W nanocomposites are the Orowan strengthening and load bearing of W nanoparticles [17,51], grain refinement, dislocation density increment by the thermal expansion coefficient mismatch between Cu and W, and the solid solution strengthening from residual Al (1.21 wt.%). Meanwhile, the Cu/5 vol.% W sample prepared by powder metallurgy was reported to exhibit a maximum microhardness of approximately 625 MPa (about 64 HV) when sintering at 1090 °C, with an average W particle size of 1.127 μm although starting with W nanoparticles before sintering [93]. The significantly enhanced microhardness of the in-situ Cu/W nanocomposite in this study can be mainly attributed

to the effective size control of in-situ W nanoparticles and the increased densification by casting compared to powder metallurgy. By further increasing the volume percentages of in-situ W nanoparticles, higher mechanical performances of the Cu/W nanocomposites are expected to be achieved.

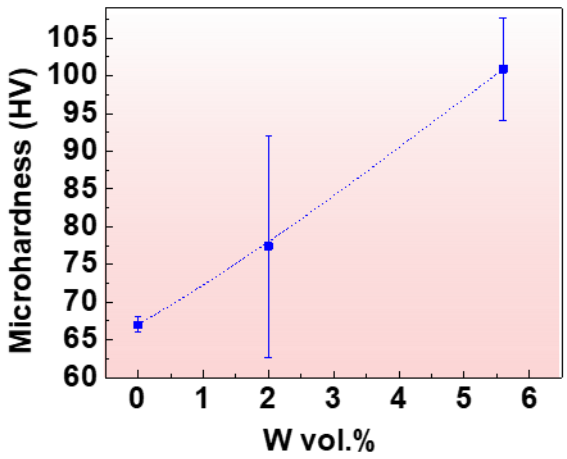

Figure 3-28 Variations of the microhardness of the in-situ Cu/W samples with the volume percentages of W nanoparticles

Besides, it is anticipated that the wear resistance and breakdown strength of the in-situ Cu/W nanocomposites will be improved due to the uniform distribution of small W nanoparticles in the Cu matrix. Due to the small sizes of W nanoparticles and the larger interfacial areas, this nanocomposite is also expected to have extraordinary radiation tolerance since interfaces can be sinks for point defects generated by radiation.

Residual Al in Cu from the in-situ synthesis has two effects on the properties of Cu/W nanocomposites. Al can give rise to an effective solid solution strengthening in Cu, which will enhance the mechanical properties of the nanocomposite. On the other hand, it can deteriorate the electrical/thermal properties due to the increased lattice scattering. Residual Al in the Cu matrix can be removed by copper chloride in the molten state, according to Reaction 3-6. Molten $CuCl_2$

will react with Al at the molten-salt/molten-Cu interface, depleting Al from the molten Cu gradually. The representative EDS patterns acquired by EDS point scan in the Cu matrix of the in-situ Cu/5.6 vol.% W before (Figure 3-29a, 1.21 wt.% Al) and after being treated by molten $CuCl_2$ (Figure 3-29b, 0 wt.% Al) are shown in Figure 3-29. No Al peaks are identified in Figure 3-29b, confirming the removal of the residual Al in the Cu matrix. It is worth mentioning that the resolution of EDS is about 0.1 wt.%. In future studies, analyses with higher precision will be conducted to more precisely analyze the residual Al content.

$$3CuCl_2 + 2Al \rightarrow 2AlCl_3 + 3Cu \qquad \text{Reaction 3-6}$$

The study can also be readily applied to obtain pure W nanoparticles for other applications. With the matrix of the in-situ Cu/designed 5 vol.% W sample dissolved by a $FeCl_3$ solution (Reaction 3-7), the synthesized small W nanoparticles can be extracted by centrifuging. The SEM image of the W nanoparticles is shown in Figure 3-30. The agglomeration of W nanoparticles in air is due to Van der Waals attraction of the W nanoparticles with large surface areas.

$$2Fe^{3+} + Cu \rightarrow Cu^{2+} + 2Fe^{2+} \qquad \text{Reaction 3-7}$$

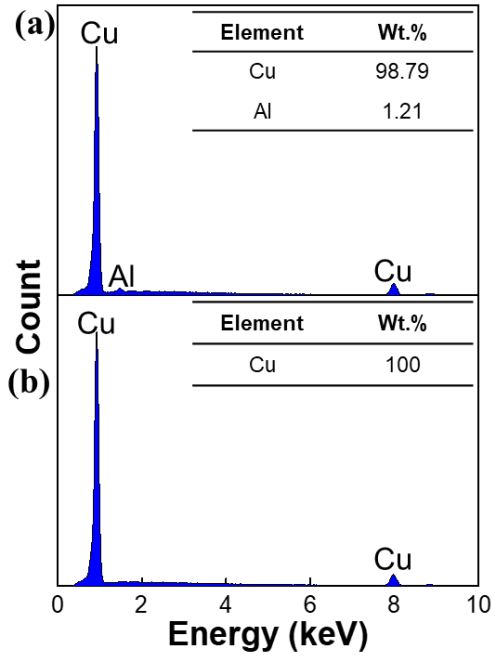

Figure 3-29 EDS point scan patterns of the in-situ Cu/5.6 vol.% W (a) before and (b) after being treated by molten $CuCl_2$ to remove Al

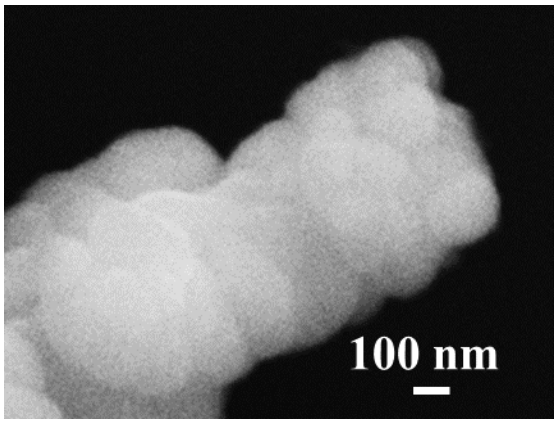

Figure 3-30 SEM image of extracted W nanoparticles from in-situ Cu/designed 5 vol.% W

On the other hand, Figure 3-31 displays the results of Cu/designed 5 vol.% W particles fabricated by the ex-situ incorporation method using commercial W nanoparticles. The morphology of the as-received W nanoparticles (labeled as 40-60 nm) is shown in Figure 3-31a. The SEM image of the W particles in the ex-situ Cu/designed 5 vol.% W is shown in Figure 3-31b. The EDS mappings of Figure 3-31b are shown in Figure 3-31c (for W) and Figure 3-31d (for Cu). The particles are the W phase and the darker areas are the Cu matrix, as indicated by the arrows in Figure 3-31b. Thus, the incorporation of ex-situ W nanoparticles into Cu is confirmed. However, there is severe coalescence of the W particles, leading to the formation of W microparticles. The size distribution of the W particles in the as-solidified ex-situ Cu/W is shown in Figure 3-31e. Their average size (2.3 ± 1.7 μm) in the Cu matrix is much larger than their initial size. The lattice mismatch between Cu and W is about 15% [99], so the Cu/W interface is expected to be semi-coherent with a relatively large interfacial energy. Hence, severe coalescence/coarsening of the W nanoparticles forming W microparticles in molten Cu occurred

in this ex-situ method. Thus, the in-situ synthesis method proposed in this study is advantageous to form small W nanoparticles in the Cu matrix by casting.

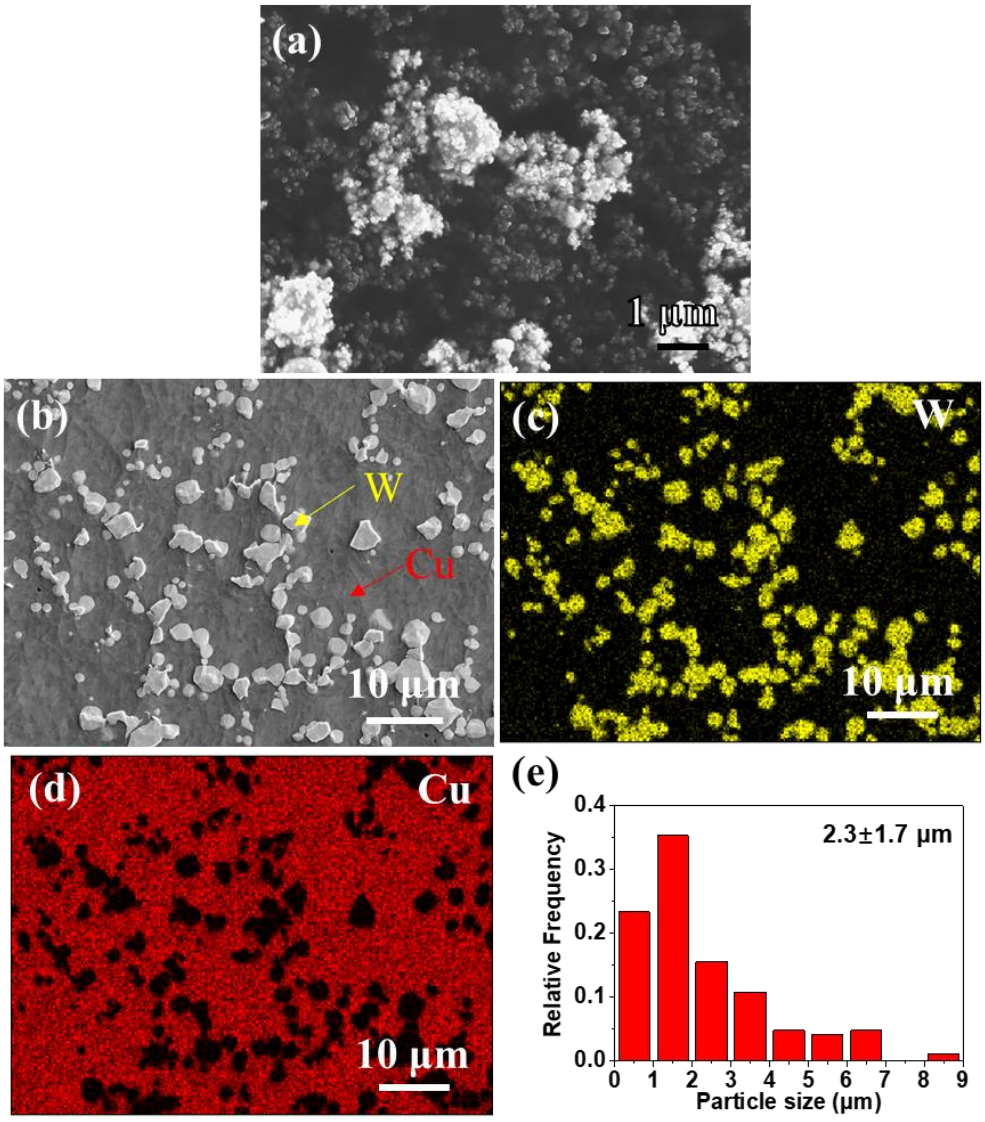

Figure 3-31 Ex-situ Cu/designed 5 vol.% W: (a) SEM image of as-received commercial W nanoparticles; (b) SEM image of W particles in as-solidified ex-situ Cu/designed 5 vol.% W; (c) EDS mapping of W in (b); (d) EDS mapping of Cu in (b); (e) Size distributions of ex-situ W particles in (b)

3.4.4 Summary

In summary, a novel and scalable method to fabricate Cu/W nanocomposites by casting using inexpensive WO_3 microparticles as the W precursor with salt-melt assisted in-situ reactions was developed. The size of the in-situ W nanoparticles in Cu was reduced by decreasing the reaction time and the concentration of WO_3 dissolved in the molten salt. An average size of the in-situ W nanoparticles as small as 132.7 nm was achieved. Roughly linear relationships between the Young's modulus and the microhardness of the in-situ Cu/W nanocomposites with the content of W nanoparticles were discovered.

3.5 Casting In-Situ Cu/CrB_x Composites via Aluminum-Assisted Reduction

Chromium borides (CrB_x) have been considered as promising strengthening phases for copper (Cu). However, traditional manufacturing methods such as powder metallurgy greatly restrict the sample size and part complexity. Here, we report that bulk Cu containing high volume percentages of uniformly distributed CrB_x were fabricated by casting via in-situ reduction assisted by aluminum (Al). Two sets of precursors, i.e., borax-CuCr and KBF_4-CrF_3, were used and the respective reaction mechanisms were illustrated. In addition, the resultant in-situ particle morphologies and sizes from the precursors were studied. The use of KBF_4-CrF_3 generated smaller in-situ particles due to the less severe coalescence of particles. The microhardness of in-situ Cu/CrB_x was significantly enhanced over pure Cu.

3.5.1 Introduction

Pure copper (Cu) is soft. Incorporating a ceramic phase into Cu is effective to improve its performance [17,51]. Cu matrix composites with strong mechanical properties and high

electrical/thermal conductivities are strongly desired for applications such as rotors for electric motors, circuit breakers, electric resistance welding electrodes, heat exchangers, etc. Transition metal borides exhibit novel properties such as high hardness, high wear resistance, high thermal stability, and good electrical/thermal conductivity [100–102]. Chromium (Cr) and boron (B) can form solid-state compounds with seven different stoichiometries (CrB_x) depending on their relative contents, exhibiting different properties [103]. Among them, CrB and CrB_2 are the most stable phases [103]. Borides of chromium have been considered promising strengthening phases for Cu.

Traditionally, Cu containing CrB_x was fabricated by powder metallurgy. Cu containing CrB_2 (44 μm) was produced by powder metallurgy as electrodes for electrical discharge machining [104]. Extrusion of mechanically alloyed Cu/CrB_2 powders at 500 °C to produce bulk samples was also reported. As-extruded Cu-1.5 vol.% CrB_2 showed a yield strength of 476 MPa [105]. However, the sample size and complexity were restricted by powder metallurgy. Casting is a scalable and facile method that is widely used in metal fabrication. Attempts to cast Cu composites have been made. Cu-25.7%Zn-3.58%Al with 0.64% CrB_2 microparticles was fabricated by simply melting the alloy together with CrB_2 [106]. However, the feasible volume percentage of boride particles by this method was very low.

The wettability between the molten metal and the particles is vital to the successful incorporation and stabilization of particles during solidification processing. The wetting angle between CrB_2 and Cu is 26°–15° when the temperature is 1100°C–1300°C [107]. Taking advantage of the good wettability, a layer of CrB_2, formed by the reaction of B_4C and Cr (addition of 1 at.%) at the interface, promoted the wetting of B_4C and Cu [108].

In this study, a new scalable method to manufacture bulk in-situ Cu/CrB_x via casting was developed. Aluminum was introduced as the reductant to assist the in-situ reactions, as Cu is

relatively inert. Two sets of inexpensive raw materials as B and Cr precursors, i.e., borax-CuCr and KBF_4-CrF_3, were experimented. The respective reaction mechanisms were elucidated. High loadings of uniformly distributed CrB_x particles were achieved in the Cu matrix by both sets of precursors. Using the two fluoride salts, smaller particle sizes were achieved than using the borax-CuCr, possibly due to the less severe coalescence of particles. The microhardness of in-situ Cu/CrB_x is significantly enhanced over pure Cu.

3.5.2 Materials and Methods

(1) $Na_2B_4O_7$ and CuCr Alloy as Precursors

Cu-6.5wt.% Cr (in-house alloyed, 200g) was heated to 1300℃ (temperature measured by a K-type thermocouple) with argon protection in a graphite crucible by an induction heater. Cu-6.5Cr will provide sufficient Cr source to generate 10-15 vol.% CrB_x while maintaining a melting point that is still processible. Al shots (99.99%, Alfa Aesar, 13.5g) were added to molten Cu. Mixed $KAlF_4$ (AMG Aluminum) and $Na_2B_4O_7$ (99.5%, Alfa Aesar) were added on top of the melt. $KAlF_4$, as a buffer salt, was 5 times the volume of the CuCr alloy. The ratio of Al, $Na_2B_4O_7$, and Cr (in CuCr) in raw materials was decided by Reaction 3-8, with $Na_2B_4O_7$ 4 times in excess to compensate for the loss of salt evaporation during synthesis. The melt was held at 1300 ℃ for 1.5 h. It was then cooled to 900 ℃ naturally in the furnace to allow Cu to solidify, and the molten salt was poured out. In addition, instead of adding $KAlF_4$ and $Na_2B_4O_7$, pure $Na_2B_4O_7$ 5 times the volume of CuCr was added, with other procedures unchanged. Assuming all Cr in CuCr alloy was transformed to boride particles, Cu-6.5wt.% Cr would be converted to Cu/14 vol.% CrB_2, or Cu/11 vol.% CrB.

$$4Al + Na_2B_4O_7 + 2Cr \rightarrow 2CrB_2 + Na_2O + 2Al_2O_3 \quad \text{Reaction 3-8}$$

(2) KBF_4 and CrF_3 as Precursors

Copper (99.99%, Rotometals, 200g) was heated to 1130 ℃ with argon protection in a graphite crucible by an induction heater. Al shots (11.2g) were added to molten Cu. KBF_4 (Spectrum), CrF_3 (Sigma-Aldrich, $CrF_3 \cdot 4H_2O$, 97%), and $KAlF_4$ (AMG Aluminum) were mixed by a mechanical shaker (SK-O330-Pro). The KBF_4-CrF_3-$KAlF_4$ powder mixture was added on top of the melt. The designed volume percentage of CrB_2 in Cu was 8 vol.%, with the amounts of reactants calculated according to Reaction 3-9. The volume of $KAlF_4$ (buffer salt) was 5 times of Cu. The melt was held at 1130℃ for 1.5 h. Then, the melt was cooled to 900 ℃ naturally in the furnace to allow Cu to solidify, and the molten salt was poured out. The as-cast sample was characterized to be Cu/7.6 vol.% CrB by image processing.

$$3Al + 2KBF_4 + CrF_3 \rightarrow CrB_2 + 2KAlF_4 + AlF_3 \qquad \text{Reaction 3-9}$$

(3) Characterizations

As-cast Cu/CrB_x samples were ground, polished, and ion milled at 4° and 4.5 kV for 1 h by Precision Ion Polishing System (Model PIPS 691, Gatan) to reveal the microstructures. These samples were observed via scanning electron microscopy (SEM, ZEISS Supra 40VP) equipped with energy-dispersive X-ray spectroscopy (EDS). X-ray diffraction (XRD) analysis was conducted on the samples to identify the phase compositions using Bruker D8 with Cu Kα radiation ($\lambda = 0.1542$ nm) at a step size of 0.05° and a speed of 4°/min. The microhardness of the Cu/CrB_x samples was measured using an LM 800AT microhardness tester with a load of 100 g and a dwell time of 10 s. Each hardness data represents 10 tests at randomly selected points across the sample at room temperature. The particle sizes and aspect ratios were measured by image processing using Image-Pro software. The average diameters of the particles were decided by the average length of

diameters measured at 2-degree intervals and passing through the particle's centroid. The aspect ratio of a particle is the ratio between major axis and minor axis of ellipse equivalent to the particle.

3.5.3 Results and Discussion

(1) Phase Compositions and Reaction Mechanisms of In-Situ Synthesis

$Na_2B_4O_7$ and CuCr as Precursors

The XRD patterns of in-situ Cu/CrB_x samples using borax and CuCr alloy as B and Cr sources are shown in Figure 3-32a and Figure 3-32b. The XRD patterns in Figure 3-32a were indexed as Cu and CrB_2 phases, while patterns in Figure 3-32b were indexed as Cu and CrB. Hence, by adjusting the ratio between borax and CuCr in the reactants, the in-situ particles can form as CrB_2 or CrB. It should be noted that borax was more than the theoretically needed amount to compensate for the evaporation loss during synthesis ($Na_2B_4O_7$ melting point 743°C). The in-situ reactions are shown in Reaction 3-10 and 3-11. At 1300°C, Cu-6.5wt.% Cr is in the single-phase liquid zone according to the Cu-Cr phase diagram. Al, acting as reductant, reduces B from borax to ground state (Reaction 3-10 [109]). The high activity B atoms will diffuse into molten CuCr and react with Cr atoms in the CuCr solution (Reaction 3-11), forming chromium borides with different stoichiometries depending on the relative Cr and B contents.

$$4Al + Na_2B_4O_7 \rightarrow 4B + Na_2O + 2Al_2O_3 \qquad \text{Reaction 3-10}$$

$$xB + Cr \rightarrow CrB_x \qquad \text{Reaction 3-11}$$

Two Fluoride Salts as Precursors

Figure 3-32c shows the XRD patterns of the in-situ sample using KBF_4 and CrF_3 as B and Cr sources. The phases were identified as Cu and CrB. The underlying reactions are as follows. Al reacts with KBF_4 and CrF_3 at the molten salt/molten metal interface, reducing B and Cr from KBF_4

and CrF_3 to ground states, respectively, according to Reaction 3-12 and 3-13. The high activity Cr and B will immediately react and form CrB_x via Reaction 3-11 at the interface, unlike in the above-mentioned method where CrB_x was formed in the molten metal. The formed CrB_x particles will spontaneously migrate into molten Cu instead of the molten salt to reduce the interfacial energy, as CrB_x has a better wettability with molten Cu than with molten salt **[51,110]**. In this study, although the Cr:B ratio was designed to be 1:2, the final product was CrB due to the more severe evaporation of KBF_4 than CrF_3 at high temperatures. Thus, to produce in-situ CrB_x with an intended stoichiometry, the KBF_4 salt should be more than the theoretical amount.

$$Al + KBF_4 \rightarrow B + KAlF_4 \qquad \text{Reaction 3-12}$$

$$Al + CrF_3 \rightarrow Cr + AlF_3 \qquad \text{Reaction 3-13}$$

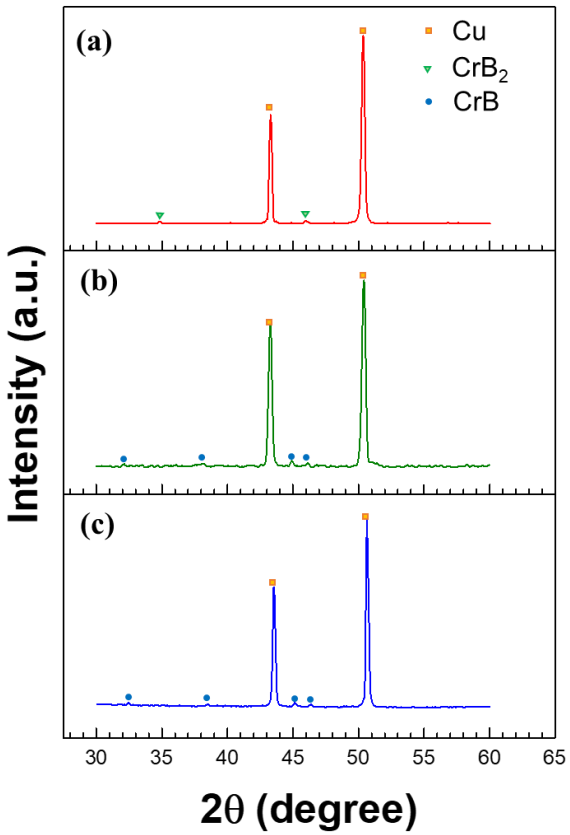

Figure 3-32 XRD patterns of (a) Cu/14 vol.% CrB_2 using borax and CuCr; (b) Cu/11 vol.% CrB using borax and CuCr; (c) Cu/7.6 vol.% CrB using KBF_4 and CrF_3

(2) Microstructures of In-Situ Cu/CrBx

In-Situ Cu/CrB_x by $Na_2B_4O_7$ and CuCr

For in-situ Cu/11 vol.% CrB, as shown in Figure 3-33a, the CrB particles are uniformly distributed in the Cu matrix. Elements that were detected by EDS mapping of Figure 3-33a are shown in Figure 3-33b to 3-33c. Figure 3-33b clearly coincides with the Cu matrix, while Figure 3-33c coincides with the CrB particles. It should be noted that B was not picked up in EDS due to its light-element nature. Additionally, the residual Al formed a solid solution with Cu, as indicated by Figure 3-33d (no CuAl intermetallic phase shown in XRD). No potassium was detected, indicating that salt was not mixed into the metal (or below detection limit). The CrB particles have an average aspect ratio of 2 ± 1.1.

For Cu/14 vol.% CrB_2, similarly, CrB_2 particles are uniformly distributed in the Cu matrix. EDS mappings of Cu, Cr, and Al agree well with the phase analysis. However, the morphology of CrB_2 differs from CrB (Figure 3-33a), with a larger aspect ratio (3 ± 2.7). The magnified image of CrB_2 particles is shown in Fig. 3-34e. One micro-sized CrB_2 particle is comprised of several nanosized particles, which can be attributed to the particle coalescence at the high processing temperature.

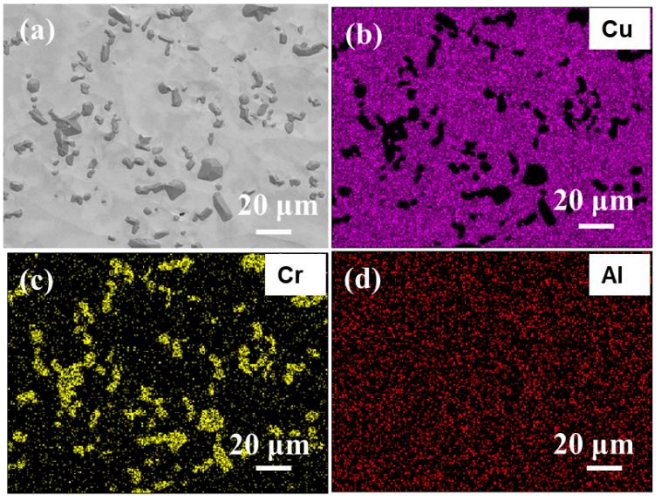

Figure 3-33 SEM and EDS images of in situ Cu/11 vol.% CrB using borax and CuCr: (a) SEM image of Cu/CrB; (b-d) Elemental distribution of Cu, Cr, and Al in (a)

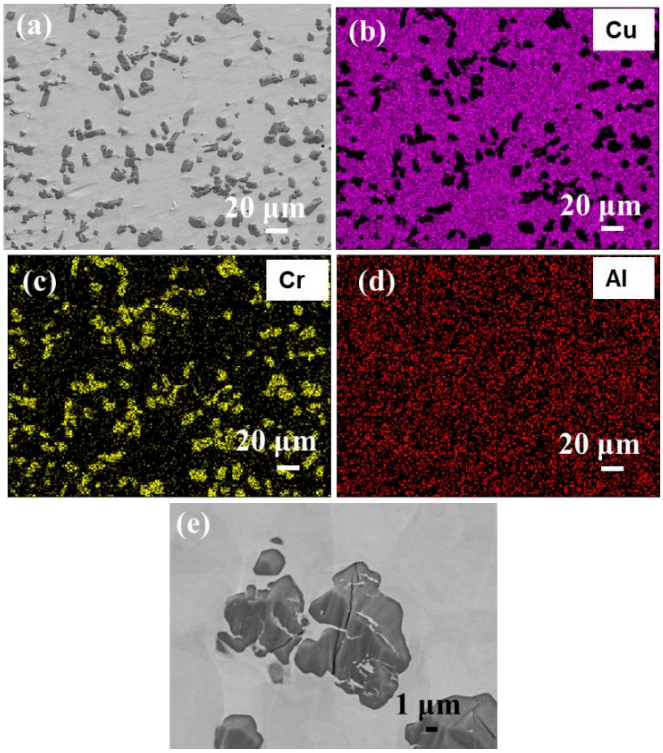

Figure 3-34 SEM and EDS images of Cu/14 vol.% CrB_2 using borax and CuCr: (a) SEM image of Cu/CrB_2; (b-d) Elemental distribution of Cu, Cr, and Al in (a); (e) Magnified image of particles in (a)

In-Situ Cu/CrB by KBF_4 and CrF_3

The microstructure of Cu/7.6 vol.% CrB fabricated through reactions of Al and two fluoride salts is shown in Figure 3-35. The uniformly distributed CrB particles in the Cu matrix exhibit similar appearances with those in Figure 3-33a regardless of the smaller particle sizes in Figure 3-35a. The aspect ratio of particles in Figure 3-35a is 2.1±1.2, which is very close to that in Figure 3-33a (2 ± 1.1). Therefore, it is concluded that, despite size differences, the morphology of the in-situ CrB_x such as aspect ratios in this study depends on the stoichiometry, irrelevant to the precursors and volume fractions. In future work, the morphology of in-situ CrB_x particles in this study will be compared with literature and commercial particles. It is anticipated that the morphology of the CrB_x particles is related to the interfacial energy between the particles and the synthesis media.

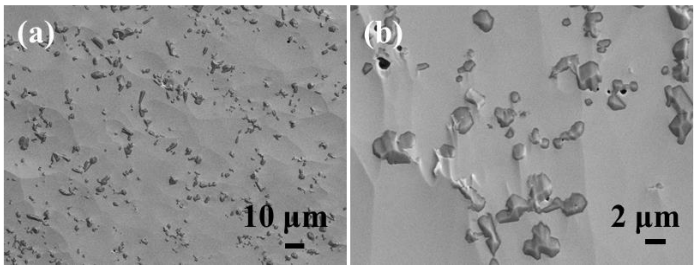

Figure 3-35 SEM image of in-situ Cu/7.6 vol.% CrB using KBF_4 and CrF_3; (b) Magnified image of particles in (a)

(3) Comparison of In-Situ CrB_x Particle Sizes

The statistics of the in-situ CrB_x particles in the Cu matrix fabricated by two sets of precursors are shown in Figure 3-36. CrB and CrB_2 synthesized by $Na_2B_4O_7$ and CuCr show similar sizes, with the average size of CrB particles being 4.3 ± 3.1 μm, and that of the CrB_2 particles being 5.9±4.1 μm. In comparison, the CrB particles, formed by two fluoride salts, have a much smaller particle size (1.7 ± 1.3 μm). The size difference can be partly attributed to the

different synthesis temperatures. Using CuCr alloy as Cr precursor, the synthesis temperature has to be higher than the CuCr liquidus temperature. Otherwise, Cr will be in solid state in molten Cu, greatly restricting the reactions. The CuCr liquidus temperature is much higher than the melting point of Cu (1083°C). Meanwhile, with CrF_3 as Cr source, the reaction temperature can be just over the Cu melting point, which will reduce the degree of particle coalescence.

In addition, the in-situ CrB_x particles in the aforementioned samples exhibit different size distribution patterns. As shown in Figure 3-36. The CrB particles synthesized by two fluoride salts show one peak in the size distribution diagram, with more than 35% of the particles smaller than 1 μm. Meanwhile, the CrB_x particles generated by borax and CuCr both show two peaks in size distribution diagrams. The fractions of particles smaller than 1 μm in Figure 3-36b and 3-36c are also smaller than those in Figure 3-36a. It is thus anticipated that, with borax-CuCr as precursors, the more severe coalescence of particles (smaller than 1 μm) leads to the two-peak pattern, with increased number fractions of particles larger than 5 μm. Therefore, KBF_4-CrF_3 is superior to borax-CuCr as precursors, regarding producing smaller in-situ CrB_x particles. Systematic studies of the effects of temperature, reaction time, precursor type, and reactant concentration on particle sizes will be investigated to optimize the synthesis results and to achieve better properties.

(4) Microhardness of In-Situ Cu/CrB_x

Microhardness of the in-situ Cu/CrB_x is shown in Table 3-2. In-situ Cu/11 vol.% CrB has a microhardness of 128.1±32 HV. For in-situ Cu/14 CrB_2, the microhardness is 138.1±32 HV. Compared to pure Cu (C10100, M20) [58], the hardness of the Cu containing in-situ CrB_x particles is significantly enhanced. The Young's moduli of CrB and CrB_2 are 522 GPa and 442 GPa, respectively [111]. The hardness of CrB is 23-27 GPa, and that of CrB_2 is 15-18 GPa [103]. Thus, CrB is stronger than CrB_2, which is expected to induce higher strengthening effects in Cu. The

residual Al contents in the in-situ samples are also shown in Table 3-2. The strengthening effects in the in-situ Cu/CrB_x arise from the solid solution strengthening of Al, Orowan Strengthening of the CrB_x particles, and Hall-Petch effect due to grain refinement by CrB_x particles [112].

The particle size of CrB in Cu/7.6 vol.% CrB is smaller than that of the Cu/11 vol.% CrB, which will induce higher Orowan strengthening. In the Cu/11 vol.% CrB, the microhardness roughly increased 7.1 HV over Cu per volume percent of CrB incorporated. The strengthening efficiency of CrB in the Cu/7.6 vol.% CrB sample is expected to be higher than 7.1 HV/vol.%. Thus, the hardness of Cu/7.6 vol.% CrB is estimated to be higher than 104 HV.

For future work, the removal of residual Al in the Cu matrix will be investigated to recover the high electrical and thermal conductivity of the composites.

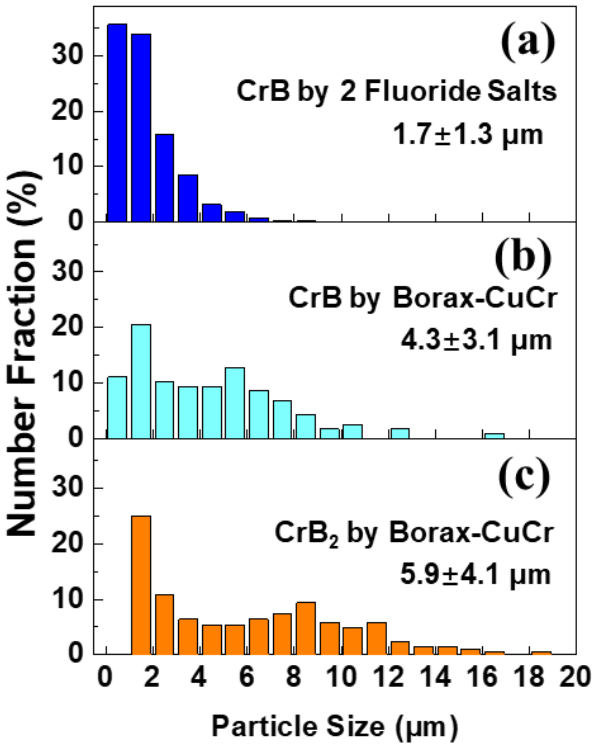

Figure 3-36 Particle size distributions of in-situ Cu/CrB_x samples: (a) CrB fabricated by KBF_4 and CrF_3; (b) CrB fabricated by borax and CuCr; (c) CrB_2 fabricated by borax and CuCr

Table 3-2 Comparison of microhardness in Cu/CrB_x and pure Cu

Sample	**Microhardness (HV)**	**Al Residual in Cu(wt.%)**
Cu/14 vol.% CrB_2	138.1 ± 25	0.22
Cu/11 vol.% CrB	128.1 ± 32	0.40
Cu (C10100, M20)	50 [58]	N/A

3.5.4 Summary

A new scalable manufacturing method was developed to fabricate bulk Cu containing high contents of uniformly distributed in-situ CrB_x particles via casting, assisted by aluminum reductions. Two sets of inexpensive raw materials as B and Cr precursors, i.e., borax-CuCr and KBF_4-CrF_3, were experimented and compared. In-situ CrB and CrB_2 particles displayed different morphologies. It was found that the aspect ratio of the same type of in-situ CrB_x in Cu was irrelevant to the precursor types. However, using KBF_4-CrF_3, smaller boride particle sizes in the Cu matrix were achieved, due to the less severe coalescence of particles. Moreover, the in-situ fabricated Cu/CrB_x samples showed significantly enhanced mechanical property over pure Cu.

3.6 Synthesis of CrB_x Nanoparticles via Magnesiothermic Reduction Assisted by Molten Salts

3.6.1 Introduction

Transition metal borides have been recognized as promising additives to strengthen Cu due to their properties such as high hardness, high melting points, high thermal stability, good wear resistance, and good electrical/thermal conductivity [100,103]. The wettability between nanoparticles and molten metals is vital to the successful incorporation and dispersion of nanoparticles [89,110]. CrB_2 has a contact angle of 25° with molten Cu [113]. CrB and CrB_2 have

the highest melting points and decomposition temperatures among all seven chromium borides with different stoichiometric compositions [103], which will make them more stable in molten Cu (T_m 1083 ℃). Thus, CrB and CrB_2 are of special interest for Cu. While the synthesis of metal borides nanoparticles such as TiB_2, ZrB_2, and MgB_2 have been widely reported, the fabrication of nanosized chromium borides has scarcely been reported [43]. CrB nanorods were synthesized via a reduction–boronation route from chromium trichloride, boron and sodium at 650℃ in molten salt in an autoclave [114]. Although the synthesized CrB has a diameter of 10–30 nm, the length of particles is on the micrometer scale. Nano CrB_2 powder was fabricated in the Mg–B_2O_3–Cr_2O_3 system by ball milling [115], which is difficult to scale up. In addition, it was also reported that CrB_2 nanoparticles were synthesized through reduction of Cr_2O_3 by elemental boron in molten NaCl/KCl salt [116]. Nevertheless, pure boron is too reactive and expensive to be suitable for mass production. Developing a scalable method to prepare nanosized chromium borides is thus of of interest.

3.6.2 Materials and Methods

Chromium borides (CrB_2 and CrB) were synthesized via a magnesiothermic reduction in molten salt under autogenous pressure. B_2O_3 powder (99.98%, #MKCB8911, Sigma-Aldrich) and Cr_2O_3 powder (> 99%, labeled 60 nm APS, US Research Nanomaterials) were used as the boron and chromium precursors, while Mg powder (99.5%, –325 mesh, Sigma-Aldrich) was the reductant. LiCl (99%, –20 mesh, Alfa Aesar) mixed with either KCl (>99%, Fisher Chemical) or $MgCl_2$ (>95%, <200 μm, Sigma-Aldrich) was used to form a liquid medium for reactions. The chemical reaction is shown in Reaction 3-14.

$$2B_2O_3 + Cr_2O_3 + 9Mg \rightarrow 2CrB_2 + 9MgO \qquad \text{Reaction 3-14}$$

B_2O_3 (30% excess), Cr_2O_3, and Mg (33.3% excess) were stoichiometrically mixed (according to Reaction 1) by grinding in an agate mortar, and they were further mixed with either eutectic KCl/LiCl (55:45 wt.%) or $MgCl_2$/LiCl (62.5:37.5 wt.%). The total weight of the salt was kept at 10 times that of Mg. As shown in Fig. S1a, the mixture of raw materials was put in a graphite crucible, covered with a graphite sheet and sealed in an autoclave, which was heated by an induction heater to 1150 °C and held for 4 h under argon protection before cooling in furnace.

To extract the synthesized nanoparticles, the reacted mass was washed repeatedly with DI water to remove the salt, followed by dilute hydrochloric acid (HCl) leaching to remove the by-product, magnesium oxide (MgO). It was further washed with DI water until the pH reached 7. The synthesized nanoparticles were collected by centrifugation at 4000 RPM for 5 min. The final product was dried overnight in a vacuum oven at 80 °C.

Figure 3-37a illustrates the new scalable molten-salt-assisted magnesiothermic reduction synthesis method of CrB_x. Figure 3-37b illustrates the selective incorporation of nanoparticles from the reacted mass into molten Cu.

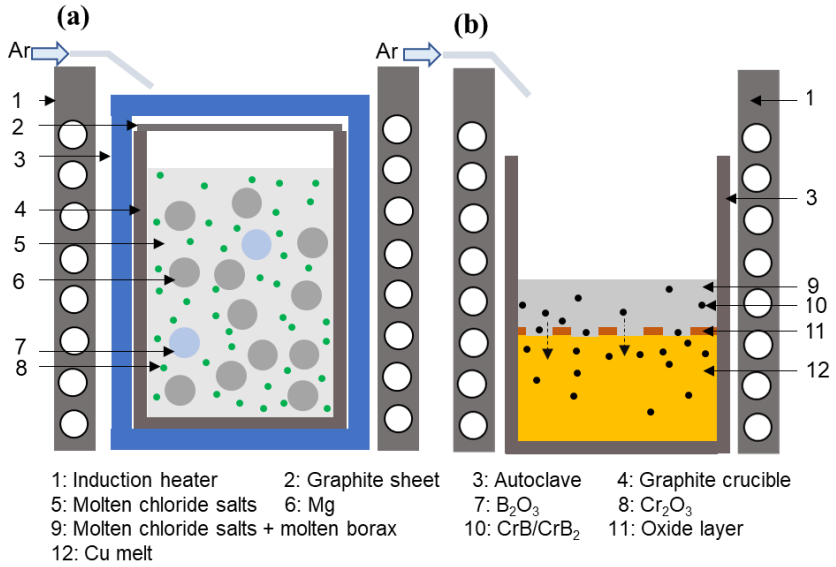

Figure 3-37 Schematic of the synthesis and incorporation process: (a) synthesis of CrB/CrB_2 nanoparticles; (b) selective incorporation of CrB/CrB_2 into Cu

3.6.3 Results and Discussion

Figure 3-38a illustrates the morphology of the initial Cr_2O_3 nanoparticles. The morphology of the washed-out nanoparticles synthesized in the solvent of molten KCl/LiCl is shown in Figure 3-38b. The average particle size of synthesized CrB is ~200 nm. The phase of the nanoparticles is confirmed by XRD to be CrB, as shown in Figure 3-38c.

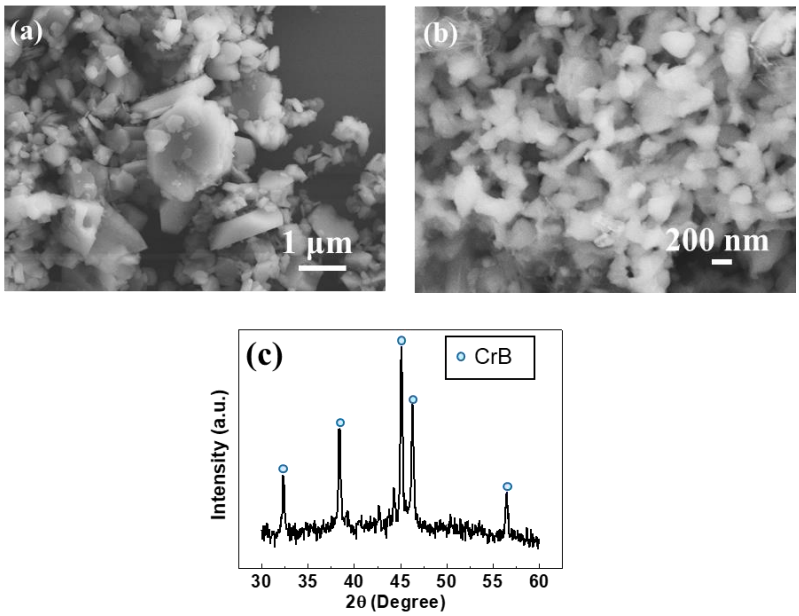

Figure 3-38 Characterization of original Cr_2O_3 and synthesized CrB nanoparticles collected from the reaction product: (a) SEM image of initial Cr_2O_3 particles; (b) SEM image of synthesized CrB nanoparticles; (c) Corresponding XRD pattern of CrB nanoparticles

The formation mechanism of nanosized chromium borides is analyzed. The common belief for the synthesis of metal borides is that metal and boron should be at their ground oxidation state to bind together into boride crystalline framework[43]. According to the DTA thermal analysis of

the B_2O_3-Cr_2O_3-Mg system, Mg reduced B_2O_3 at ~830 ℃ and the subsequent reduction of Cr_2O_3 occurred at ~1100 ℃ [115]. Two mechanisms, i.e., "templated growth" and "dissolution and precipitation", were proposed to explain the nanoparticle synthesis via magnesio-reduction in molten salt [109,117]. It was reported that for the synthesis of TiB_2 in molten chloride salt, both B and Ti resulted from magnesio-reduction partially dissolved in the molten salt, forming TiB_2 via a dissolution-precipitation mechanism [117]. However, for the synthesis of ZrB_2 by a similar method, it was observed that the synthesized ZrB_2 retained the size and shape of the original ZrO_2 nanoparticles, suggesting that the amorphous boron from the magnesio-reduction of B_2O_3 diffused to the surface of ZrO_2, forming ZrB_2 with the initial ZrO_2 as a template [109]. In this study, as shown in Fig. S2, the size and morphology of synthesized CrB nanoparticles are apparently different from the initial Cr_2O_3 particles (a mixture of microparticles and nanoparticles). Hereby, the main reaction mechanism is discussed as follows. Mg is partially dissolved in the molten salt. The dissolved Mg will diffuse rapidly through molten salt to the surface of B_2O_3, generating amorphous boron through Reaction 3-14. Cr is then generated according to Reaction 3-15.

$$B_2O_3 + 3Mg \rightarrow 2B + 3MgO \qquad \text{Reaction 3-14}$$

$$Cr_2O_3 + 3Mg \rightarrow 2Cr + 3MgO \qquad \text{Reaction 3-15}$$

Elemental Cr and B can also be partially dissolved in the molten salt, forming CrB_x and precipitate in molten salt according to Reaction 3-16.

$$Cr\ (dissolved) + xB\ (dissolved) \rightarrow CrB_x \qquad \text{Reaction 3-16}$$

Molten salt, acting as a medium for synthesis, has several advantages for the nanoparticle synthesis compared to solid-state synthesis. In essence, simply heating Cr_2O_3-B_2O_3-Mg system even to 1300 ℃ under Ar protection will not form chromium boride [115]. It is thus anticipated that molten salt lowered the activation energy for the reaction. Besides, the molten salt flux can

lower the reaction temperature and accelerate the reaction due to the faster mass transfer transport by diffusion and convection [118]. Molten salt can also lead to a more homogeneous mixing of raw materials [118]. Besides, molten salt serves as a dilute, preventing the direct contact of crystals, thereby inhibiting the growth of the synthesized crystals [116].

The whole reacted mass in $MgCl_2$/LiCl salt was also directly diluted in borax and placed on molten Cu for the incorporation of nanoparticles. The XRD pattern of the as-solidified sample (Cu/15.1 vol.% CrB_2) is shown in Figure 4-1i with peaks corresponding to Cu and CrB_2 phases. It indicates that the type of the chloride salt as the solvent for the synthesis also controls the stoichiometry of the synthesized chromium borides, which can be attributed to the different intrinsic characteristics of the salt and their interaction with the reactions. As Reaction S1 and S2 proceeds, MgO is generated as a byproduct. It will remain on the surface of reactants as a reaction barrier layer, slowing down the reactions. What's worse, it can combine with unreacted B_2O_3, according to Reaction 3-17, consuming the boron source.

$$B_2O_3 + 3MgO = Mg_3B_2O_6 \qquad \text{Reaction 3-17}$$

Such a barrier layer can be removed more efficiently by molten $MgCl_2$ than KCl due to the higher solubility of MgO in $MgCl_2$. Hence, although the boron/chromium ratio is the same in the raw materials, synthesis in the molten KCl/LiCl yields CrB instead of CrB_2. Bao *et al* also studied the difference of different chloride salts as a medium for the synthesis of TiB_2, reporting $MgCl_2$ as the most effective salt among $MgCl_2$, NaCl, and KCl in accelerating the magnesiothermic reduction and TiB_2 formation due to the higher solubility of Mg in $MgCl_2$ [117].

3.6.4. Conclusions

A scalable method to synthesize nanosized chromium borides via magnesiothermic reduction assisted by molten salt is developed. The formation mechanism of nanosized chromium borides in molten salt bath is discussed. The stoichiometry of the chromium borides can be controlled by the type of molten salt.

Chapter 4 Grain Structure Modification Enabled by Nanoparticles

Grain structure is vital to the properties of metallic crystalline materials. Grain refinement can contribute to increased microstructural homogeneity, enhanced mechanical properties, and improved processability. Ultrafine grained metals can offer superior strength. On the other hand, bimodal grain structure is an effective strategy to achieve strength-ductility synergy. There has been a continuous effort to tune the grain structures of metals. However, the current processing methods to engineer the grain structures suffer from high cost and limited scalability. This chapter will investigate the control of grain nucleation and growth by nanoparticles and present two types of unique grain structures in Cu enabled by nanoparticles via regular casting, i.e., ultrafine grained Cu [54] and bimodal grained Cu [119]. Refining as-solidified grains of metals to the ultrafine and even nanometer scale by nanoparticles via slow cooling has been recently discovered. Here, we report a facile and scalable manufacturing method of bimodal grained Cu by casting followed with hot rolling of metals containing nanoparticles. Besides, microparticles (CrB and CrB_2) with surface nanofeatures due to coalescence of nanoparticles can also enable ultrafine/nano grains via slow cooling. The discovery in this chapter not only advances the fundamental understating of grain nucleation and growth control during solidification but also has great potential to advance the mass production of bimodal and UFG/nanocrystalline metals for widespread applications.

4.1 Thermally Stable Ultrafine Grained Cu Induced by Microparticles with Surface Nanofeatures

4.1.1 Introduction

Grain refinement is an effective method to achieve enhanced properties for metals, including, but not limited to: higher strength/hardness and ductility, better microstructural homogeneity, and

improved processability[90,120,121]. Ultrafine-grained (UFG)/nanocrystalline materials exhibit novel properties[122]. Although the investigation and development of UFG/nanocrystalline metals have been conducted for decades, their applications in industry are still limited. The current fabrication methods of UFG/nanocrystalline metals are very difficult to scale up for mass production. Traditionally, UFG/nanocrystalline materials are prepared by severe plastic deformation (SPD)[123], rapid cooling[124], mechanical alloying[125], electrodeposition[126], crystallization of amorphous solids[127], etc. Mass production of large-scale UFG/nanocrystalline metals with complex geometries via the aforementioned methods is rather challenging.

Recently, a breakthrough was made to fabricate bulk UFG/nanocrystalline metals for the first time via slow-cooling through a continuous nucleation and growth control mechanism enabled by nanoparticles[90]. The dispersed nanoparticles not only effectively modify the solidification behavior, but also significantly enhance material properties. The ex-situ fabrication of metals containing nanoparticles can be expensive due to the high cost of nanoparticles on the market. On the other hand, although microparticles have been proven to show a grain refining effect during metal and alloy solidifications, the achievable grain size fails to reach the ultrafine scale[128]. Various studies have been conducted regarding the transfer of particles into molten metals. A molten-salt-assisted method was employed to incorporate ex-situ TiC nanoparticles into molten aluminum[89]. The transfer of nanoparticles from organic solvent to low-melting-point molten metal was also reported[129]. It is of interest to investigate if microparticles with surface nanofeatures could refine grains down to the ultrafine scale.

In addition, stabilizing the ultrafine/nano grains is crucial, especially in high-temperature applications to maintain their excellent properties. UFG/nanocrystalline metals, especially pure ones, tend to coarsen upon thermal exposure and mechanical loading[130]. Cu grains of 300-400

nm coarsen after annealing at ~0.35T_m (T_m is the melting point) for 30 min[131], while Cu nanograins coarsen even at room temperature[132]. Various fundamental studies[133–135] have been conducted to understand the grain stabilization mechanism and to improve the thermal stability of UFG/nanocrystalline metals. Two pathways, i.e., reducing the grain boundary energy (thermodynamically)[136] or limiting the grain boundary mobility (kinetically), have been proven to effectively inhibit grain growth of ultrafine/nano grains. As-milled W-20 at.% Ti with a grain size of about 20 nm retained the nanostructure even after annealing at 1100 ℃ for 1 week[136]. As-cast UFG Cu stabilized by WC nanoparticles was thermally stable up to 0.75 T_m[90]. However, high thermal stability of as-cast metals containing microparticles has not yet been reported.

Here, we report that microparticles with surface nanofeatures can also effectively refine metal grains to the ultrafine and even nanoscale during slow solidification. The microparticles and surface nanofeatures are formed by the coalescence of nanoparticles. More specifically, CrB/CrB_2 nanoparticles were synthesized by a simple and scalable route: molten-salt-assisted magnesiothermic reduction, with oxides of chromium and boron as sources. The CrB/CrB_2 nanoparticles can then be selectively incorporated into molten Cu while the synthesis by-products remain in the molten salt. The UFG Cu exhibits exceptional thermal stability without grain coarsening even after annealing at 600 ℃ (0.55 Tm) for 1 h. Moreover, mechanical properties of the Cu/CrB and Cu/CrB_2 samples are significantly enhanced over pure Cu.

4.1.2 Materials and Methods

(1) Synthesis of CrB and CrB_2 nanoparticles

See Chapter 3.6.2.

(2) Incorporation of CrB and CrB_2 into Cu

In order to incorporate CrB/CrB_2 into Cu, two methods were employed.

The nanoparticles were washed out from the synthesis product first, and then incorporated into Cu using the molten-salt-assisted self-incorporation method. In detail, CrB nanoparticles, borax ($Na_2B_4O_7$), and CaF_2 were mixed in a volume ratio of 1:49:1.8. Pure Cu was first heated to 1250 °C in a graphite crucible by an induction heater under argon protection. The mixture of nanoparticles and salts was gradually added on top of molten Cu, accompanied by manual mixing with a graphite rod. After holding at 1250 °C for 30 min, the melt was cooled in furnace. Using this method, Cu/4.2 vol.% CrB was fabricated.

To avoid the tedious nanoparticle extraction, the reacted mass was first broken into pieces and then mixed with borax and CaF_2 in the same amount as mentioned above, based on the designed weight of CrB/CrB_2 nanoparticles in the reacted mass. As shown in Figure 3-37b, pure Cu was placed at the bottom of a crucible, and the mixture was placed on top. The crucible was then heated to 1000 °C, where the salt was melted and manually stirred. The temperature was then raised to 1250 °C and held for 30 min to allow nanoparticles to migrate into Cu before cooling to room temperature in a furnace. Cu/16.7 vol.% CrB and Cu/15.1 vol.% CrB_2 were fabricated through this strategy.

(3) Characterization

The CrB nanoparticles extracted from the reaction product were examined by scanning electron microscopy (SEM, ZEISS Supra 40VP) and scanned by x-ray diffraction (XRD, Bruker D8) using Cu Kα radiation with a step size of 0.05° at a speed of 4°/min. To investigate the phases of the Cu/CrB and Cu/CrB_2 samples, XRD analysis was conducted under the same conditions mentioned above. To characterize the microstructure of the Cu/CrB and Cu/CrB_2 samples, specimens were cut from the bulk samples, ground, and polished. The specimens were further

cleaned by low-angle ion milling (Model PIPS 691, Gatan) at 4° and 4.5 kV for 1 h to reveal CrB/CrB_2 particles in the Cu matrix. These samples were examined via SEM equipped with energy dispersive X-ray spectroscopy (EDS). The volume percentage of CrB/CrB_2 particles in Cu was calculated based on the weight percentages of Cu and Cr from EDS mapping data.

Focused ion beaming imaging (FIB) by FEI Nova 600 was utilized to reveal the grain structures of Cu/CrB and Cu/CrB_2 samples, with granular contrast induced by the ion beam due to the channeling contrast[137]. Cu/16.7 vol.% CrB and Cu/15.1 vol.% CrB_2 were further analyzed by electron backscatter diffraction (Oxford EBSD on FEI Quanta 3D SEM). In order to evaluate the thermal stability of the Cu grains in Cu/CrB and Cu/CrB_2, the as-cast Cu/CrB and Cu/CrB_2 samples were annealed at 600 ℃ for 1 h. The as-cast Cu/15.1 vol.% CrB_2 sample was further hot forged at 1000 ℃. The grain structures after the aforementioned heat treatment were also characterized by FIB imaging. The solidification behaviors of Cu/16.7 vol.% CrB and pure Cu samples (both ~15 mg) were analyzed by differential scanning calorimetry (DSC, TA Instrument 600). Samples were heated to 1150 ℃ at 40 ℃/min and cooled at 5 ℃/min in Ar flow. To observe the morphology of the CrB particles, a $FeCl_3$/DI water solution was used to dissolve the Cu matrix of Cu/16.7 vol.% CrB sample, and CrB particles were washed and collected in a centrifuge.

The microhardness of the Cu/CrB and Cu/CrB_2 samples was measured using an LM 800AT microhardness tester with a load of 100 g and a dwell time of 10 s. Young's modulus was determined by an MTS nanoindenter with a Berkovich tip with an indent depth of 2 μm. Each Young's modulus and microhardness data represents ten measurements at random spots at ambient temperature. The as-cast Cu/CrB_2 samples were hot forged at 1000 ℃ into 1.7-mm-thick sheets (85% thickness reduction). Tensile bars with a gauge length of 1.2 cm and a gauge width of 4 mm were machined by electrical discharge machining (EDM) from the Cu/CrB_2 sheets. Tensile tests

of Cu/CrB_2 were conducted on an Instron Universal Testing System equipped with a video extensometer at a constant speed of 0.5 mm/min.

4.1.3 Results and Discussion

(1) Microstructure of Cu containing CrB and CrB_2 microparticles with surface nanofeatures

We synthesized CrB and CrB_2 nanoparticles from B_2O_3 and Cr_2O_3 powders by a new scalable molten-salt-assisted magnesiothermic reduction method (as shown in Figure 3-37a). The average particle size of synthesized CrB is about 200 nm (Figure 3-38). See supplemental text for the reaction mechanism analysis of the synthesis and characterization of the extracted nanoparticles. A novel molten-salt-assisted selective incorporation method was developed to incorporate as-synthesized CrB/CrB_2 nanoparticles into molten Cu (Figure 3-37b). The underlying mechanism of the selective incorporation is ascribed to the reduction of the system's Gibbs energy, which depends on the interfacial energy between nanoparticles and the molten metal. Although the reaction byproduct (MgO) and possible residual reactants were present during the incorporation, they essentially have a higher interfacial energy with molten Cu than with molten salt, so they prefer to remain in the molten salt. Meanwhile, the molten salt partially dissolved the oxide layer on the surface of molten metal, as shown in Figure 3-37b, enabling direct contact between the molten metal and nanoparticles and the subsequent incorporation of nanoparticles that had good wettability with the molten metal. The successful selective incorporation of different nanoparticles by this method was proven by the samples' XRD patterns. The XRD patterns of Cu containing 16.7 vol.% CrB and 15.1 vol.% CrB_2 are shown in Figure 4-1f and Figure 4-1i, respectively, with peaks indexed as Cu, CrB, and CrB_2. XRD analysis also confirms that no phase transformation occurred during the incorporation processing. Cu/4.2 vol.% CrB was fabricated using extracted

pure CrB nanoparticles, with the XRD patterns of this sample shown in Figure 4-1c. The only difference between Figure 4-1c and Figure 4-1f is that CrB peaks are relatively stronger in Figure 4-1f due to the higher volume percentage of CrB. Thus, the molten-salt-assisted selective incorporation method is effective and avoids tedious nanoparticle extraction procedures.

The microstructures of as-cast Cu containing different volume percentages of CrB and CrB_2 are shown in SEM images in Figure 4-1. First, CrB and CrB_2 become microparticles in the Cu matrix, with apparent size larger than as-synthesized nanoparticles. Both CrB and CrB_2 microparticles in the Cu matrix exhibit irregular shapes with various concave and convex faces (as shown in Figure 4-1b, e, h), suggesting that the microparticles were formed by the coalescence of as-synthesized nanoparticles during the high-temperature processing in molten Cu. After all, the processing temperature (1250 °C) is more than half of the melting temperature of CrB (2100 °C) and CrB_2 (2200 °C). Further characterizations reveal that these microparticles in the Cu matrix have surface nanofeatures (described in detail in section 3.2).

The CrB and CrB_2 microparticles are dispersed and uniformly distributed in the Cu matrix. For Cu/4.2 vol.% CrB, as shown in Figure 4-1a, although the CrB microparticles form particle-rich zones, these zones are uniformly distributed in the Cu matrix. When the CrB volume percentage increases to 16.7%, as shown in Figure 4-1d, the entire Cu matrix contains embedded CrB microparticles. The uniform distribution of CrB_2 microparticles in Cu/15.1 vol.% CrB_2 is shown in Figure 4-1g. The uniform distribution of microparticles with surface nanofeatures in the Cu matrix is expected to lead to isotropic properties in the samples. No reaction between the CrB/CrB_2 microparticles and the Cu matrix was observed at the interface.

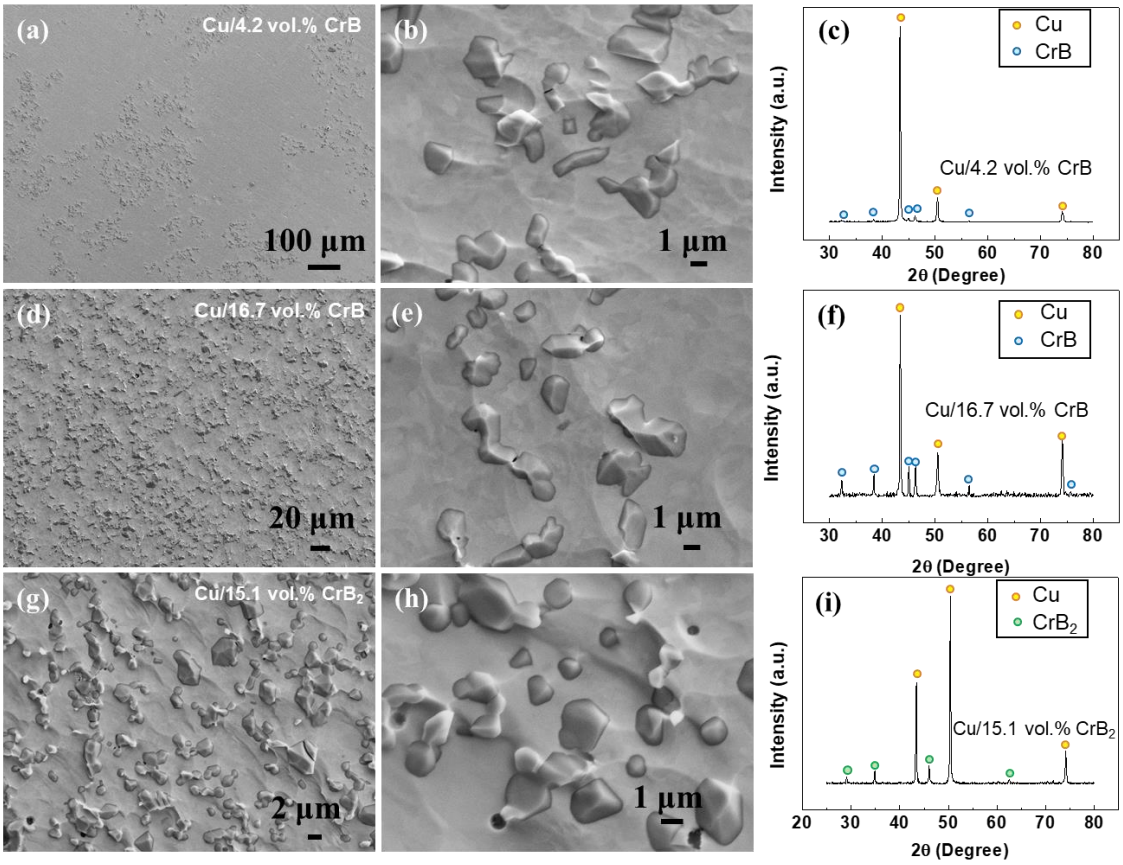

Figure 4-1 Microstructure and phase analysis of Cu containing CrB and CrB_2 microparticles. (a,b) SEM images of Cu/4.2 vol.% CrB. (c) XRD patterns of Cu/4.2 vol.% CrB. (d,e) SEM images of Cu/16.7 vol.% CrB. (f) XRD patterns of Cu/16.7 vol.% CrB. (g,h) SEM image of Cu/15.1 vol.% CrB_2. (i) XRD patterns of Cu/15.1 vol.% CrB_2

(2) Bulk UFG/nanocrystalline Cu induced by microparticles with surface nanofeatures via slow cooling

We characterized the grain structures of the bulk as-cast Cu samples containing different volume percentages of CrB and CrB_2 microparticles. The UFG/nanocrystalline Cu is shown in Figure 4-2, revealed by the channeling contrast of focused ion beam (FIB) imaging. As CrB particles form particle-rich zones in the Cu/4.2 vol.% CrB sample, FIB imaging of a typical area inside the particle-rich zone in Cu/4.2 vol. CrB is shown in Figure 4-2a. It is noteworthy that the

grains nucleated on the CrB microparticles (as indicated by the dashed circle) have a considerably smaller size than other grains, indicating the effective grain refinement effect of CrB microparticles with surface nanofeatures. Although there are still a few grains larger than 1000 nm, the average grain size in the particle-rich zone in Cu/4.2 vol.% CrB is 406.8 ± 239.6 nm, with a grain size distribution shown in Figure 4-2b. It should be noted that Cu grain structure in the Cu/4.2 vol.% CrB sample is heterogeneous due to the particle pseudo-dispersion. The purpose of showing Figure 4-2a here is only to demonstrate the effective nucleation of Cu grains on the CrB particle surfaces. A higher particle content (e.g., Cu/16.7 vol.% CrB and Cu/15.1 vol.% CrB_2) is needed to achieve uniform particle distribution, hereby inducing uniform Cu grains. Figure 4-2c shows the typical grain structures in the Cu/16.7 vol.% CrB. The proportion of Cu grains larger than 1000 nm is lower compared to Cu/4.2 vol.% CrB, with an average grain size of 324.6 ± 184.4 nm (the grain size distribution is shown in Figure 4-2d). The comparison between Figure 4-2a and Figure 4-2b reveals that a higher volume percentage of CrB microparticles with surface nanofeatures can yield a smaller grain size of Cu. Figure 4-2e represents the typical grain structure of Cu/15.1 vol.% CrB_2, which has an average grain size of 375.3 ± 182.9 nm, with the grain size distribution shown in Figure 4-2f. More than 5% of the Cu grains in both Cu/16.7 vol.% CrB and Cu/15.1 vol.% CrB_2 are smaller than 100 nm. Thus, microparticles with surface nanofeatures of different phases have been proven to induce ultrafine/nanocrystalline grains during slow-cooling solidification.

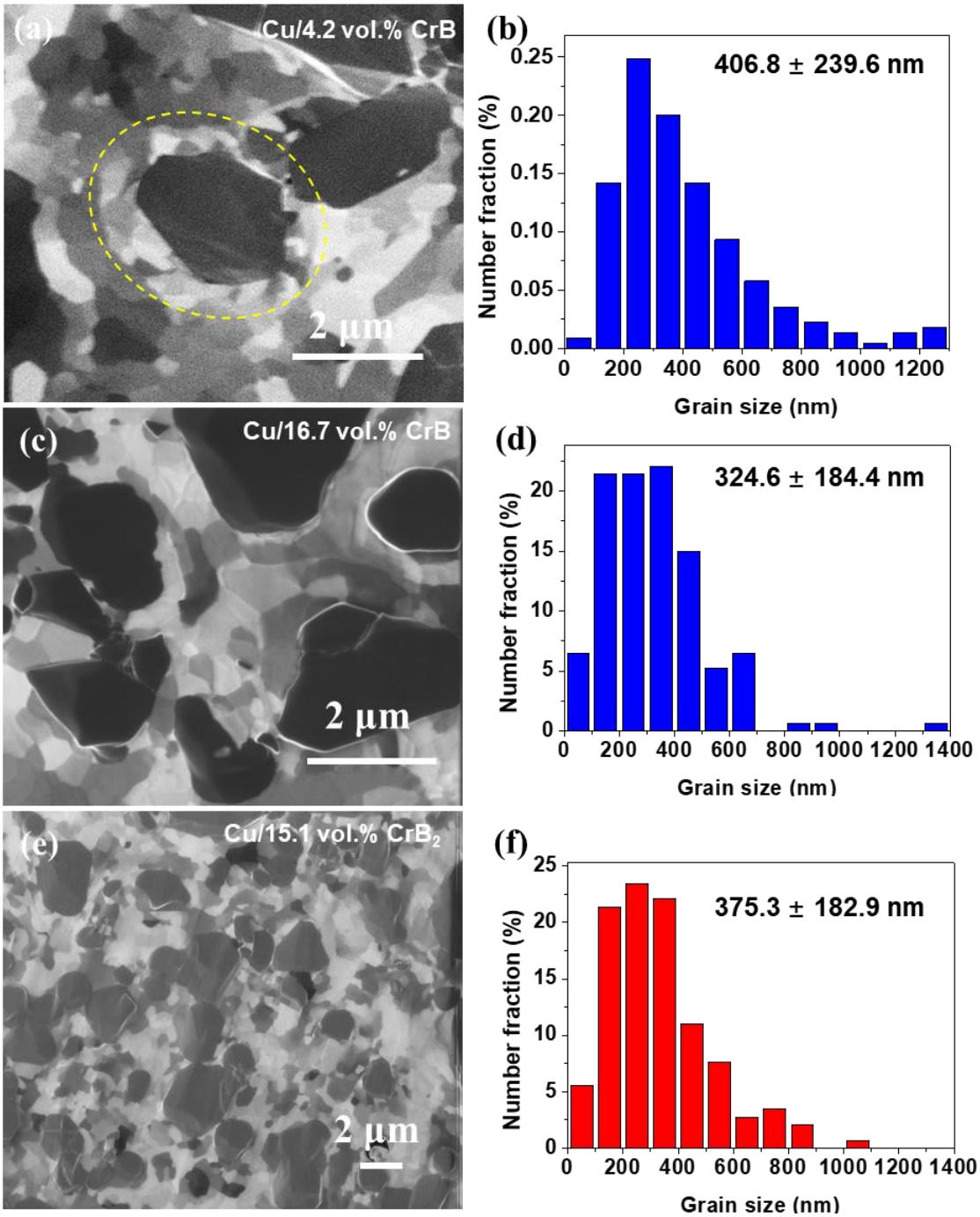

Figure 4-2 As-solidified bulk UFG/nanocrystalline Cu containing CrB and CrB_2 under regular cooling. FIB image of (a) particle-rich zone in Cu/4.2 vol.% CrB, (c) typical Cu/16.7 vol.% CrB, and (d) typical Cu/15.1 vol.% CrB_2 revealing grain structures with grain size distributions in (b), (d), and (f), respectively

EBSD was utilized to further confirm the ultrafine/nanocrystalline grain structure. The EBSD mapping of Cu/16.7 vol.% CrB is shown in Figure 4-3a, with the IPF coloring shown in Figure 4-3b. The black lines correspond to high-angle grain boundaries (GBs) with misorientation larger than 10°, while red lines correspond to low-angle GBs with misorientation between 5° and 10°. CrB microparticles are represented by a grey color, whose orientations were not indexed during EBSD characterization. The EBSD data agrees well with the FIB imaging data. The grain size characterization results confirm that the incorporation of CrB/CrB_2 microparticles with surface nanofeatures substantially refine the grain size of Cu to the ultrafine/nanoscale via slow cooling.

We used DSC to study the solidification behavior of Cu containing microparticles with surface nanofeatures. The cooling curves of molten Cu/16.7 vol.% CrB and pure Cu are shown in Figure 4-3c. The exothermic peak indicating the initiation of solidification started at 1030 °C for pure Cu, corresponding to an undercooling of 53 °C. Meanwhile, the solidification of Cu/16.7 vol.% CrB started at 1070 °C with an undercooling of 13 °C, indicating that CrB microparticles with surface nanofeatures enable easier nucleation of Cu solids. More importantly, the exothermic peak of Cu/16.7 vol.% CrB is 50% wider and less intense than pure Cu, indicating a continuous nucleation of Cu grains induced by the CrB microparticles with surface nanofeatures.

The morphology of extracted CrB microparticles with surface nanofeatures from the as-cast UFG Cu/16.7 vol.% CrB sample is shown in Figure 4-3d and Figure 4-3e. The coalescence of as-synthesized CrB nanoparticles forms CrB microparticles that display surface nanofeatures with large curvatures. In contrast, the morphology of the extracted CrB microparticles in Cu with micro-sized grains is shown in Figure 4-3f. As-solidified Cu shows micro-sized grains and dendrites (shown as the inset in Figure 4-3f) when CrB microparticles grew further, losing surface nanofeatures and exhibiting relatively smooth surfaces with no submicron CrB particles coalesced

to the surface anymore. This comparison suggests that the ability of CrB microparticles to induce ultrafine/nanocrystalline grains is related to the surface morphology of CrB microparticles. The substantial grain refinement effect down to the ultrafine/nanoscale can be attributed to the continuous heterogeneous nucleation and grain growth restriction induced by chromium boride (CrB/CrB_2) microparticles with surface nanofeatures. It should be noted that although we started with synthesized nanoparticles, we prove for the first time that microparticles with surface nanofeatures can effectively refine grains down to ultrafine/nanoscale sizes. It is thus anticipated that manipulating the surface morphology of microparticles for incorporation in metals, such as fabricating surface nanofeatures, can be an effective pathway to enable as-cast UFG/nanocrystalline metals.

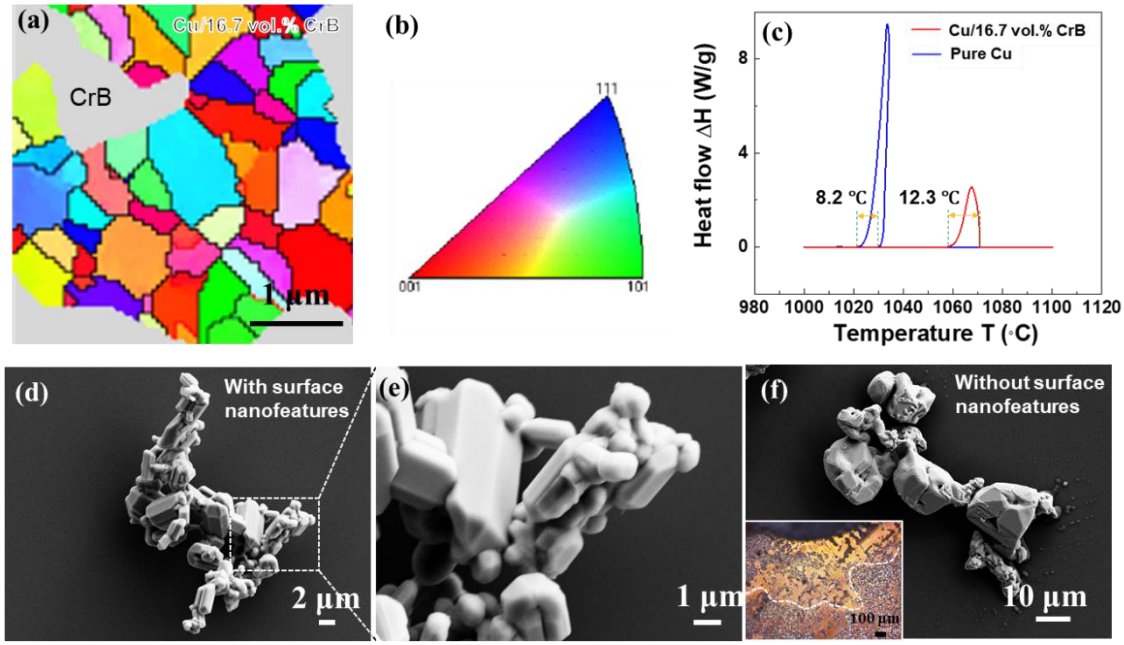

Figure 4-3 UFG/nanocrystalline Cu induced by microparticles with surface nanofeatures. (a) EBSD mapping of Cu/16.7 vol.% CrB, with (b) corresponding IPF coloring. (c) DSC cooling curves of Cu/16.7 vol.% CrB and pure Cu. (d) Morphology of extracted CrB microparticles from Cu/16.7 vol.% CrB. (e) Magnified image of the boxed area in (d) displaying nanofeatures. (f)

Extracted CrB microparticles without surface nanofeatures from Cu with micro-sized grains shown as the inset

(3) Thermal stability of UFG/nanocrystalline Cu

To evaluate the thermal stability of the UFG/nanocrystalline Cu, the Cu/16.7 vol.% CrB and Cu/15.1 vol.% CrB_2 samples were annealed at 600 °C for 1h. The UFG/nanocrystalline Cu in this study is proven to be thermally stable, with grain structures after annealing shown in Figure 4-4. For annealed Cu/16.7 vol.% CrB, the grain size remains ultrafine (335.4 ± 160.1 nm), as shown in Figure 4-4a and 4-4b. The grain structures of the annealed Cu/15.1 vol.% CrB_2 sample are shown in Figure 4-4c. The average grain size is also ultrafine (378.4 ± 225.0 nm), with the corresponding grain size distribution shown in Figure 4-4d. It is noted that the fractions of grains smaller than 100 nm are decreased in both samples after annealing. Compared to the grain sizes of the as-cast samples, there is no grain coarsening even after annealing at 600 °C for 1h. The ultra-high thermal stability of the cast UFG/nanocrystalline Cu grains in Cu/CrB and Cu/CrB_2 is comparable to UFG Cu stabilized by WC nanoparticles[90].

As grain coarsening can occur upon both thermal exposure and mechanical loading, the Cu/15.1 vol.% CrB_2 sample was further subjected to hot forging at 1000 °C. As shown in Figure 4-4e, although the Cu grains grow, a few grains smaller than 1000 nm surprisingly remained intact. The average grain size is measured to be 2.04 ± 1.66 μm, with the grain size distribution shown in Figure 4-4f (more than 25% of grains smaller than 1 μm). Besides, there is a high density of through-grain twins formed. Notably, the thicknesses of the twin lamellae, indicated by blue arrows in Figure 4-4e, are submicron and even nanoscale. From literature, it was challenging to fabricate metals with a high density of twins/nanotwins[138]. A few annealing nanotwins were detected in annealed UFG Cu/TiC samples[134]. It was also reported that twins were observed to

lower grain boundary energy in nanocrystalline Cu with initial grain size smaller than 75 nm during mechanical loading at room temperature[130]. In this study, the formation of twins/nanotwins can originate from both annealing and deformation. Future study, including high-resolution TEM, is needed to study the twinning structure and twin-forming mechanism in metals containing microparticles with surface nanofeatures.

Variations of the grain size in the Cu/CrB and Cu/CrB_2 samples as a function of different conditions are summarized in Figure 4-4g. The CrB/CrB_2 microparticles exert a restriction force on grain boundaries, kinetically restraining grain growth. According to the Zener pinning effect, the maximum grain size (d) after annealing can be predicted by Equation 4-1[90]:

$$d = \frac{4r}{3V_p} \qquad \text{Equation 4-1}$$

where r is the radius of particles and V_p is the volume fraction of particles. Accordingly, the grain size of annealed Cu/15.1 vol.% CrB_2 (particle diameter: 1.8 ± 1.1 μm) is calculated to be 8 μm, which is much larger than the observed grain size. The theoretical interparticle spacing (d_{inter}) can be predicted to be 2.7 μm by Equation 4-2[90].

$$d_{inter} = r(\frac{4\pi}{3V_p})^{1/3} \qquad \text{Equation 4-2}$$

The grain sizes of the as-cast and annealed Cu/15.1 vol.% CrB_2 are much smaller than d_{inter}, but approach d_{inter} after hot forging. It is believed that grain growth during hot forging is impeded by the interparticle spacing, as indicated by the yellow arrow in Figure 4-4e. The high thermal energy and strain energy during hot forging provide a large driving force for grain growth, while it is assumed that the thermal energy during annealing (0.55 Tm) does not provide enough driving force for grain growth due to the restriction by microparticles with surface nanofeatures. Additionally, the twin boundaries are anticipated to play a role in the high thermal stability. Twin boundaries are coherent with relatively low energy, exhibiting much higher thermal and

mechanical stability than traditional high angle grain boundaries[138]. Deformation by twinning can also lead to grain boundary relaxation, which in turn will help stabilize nanograins[130].

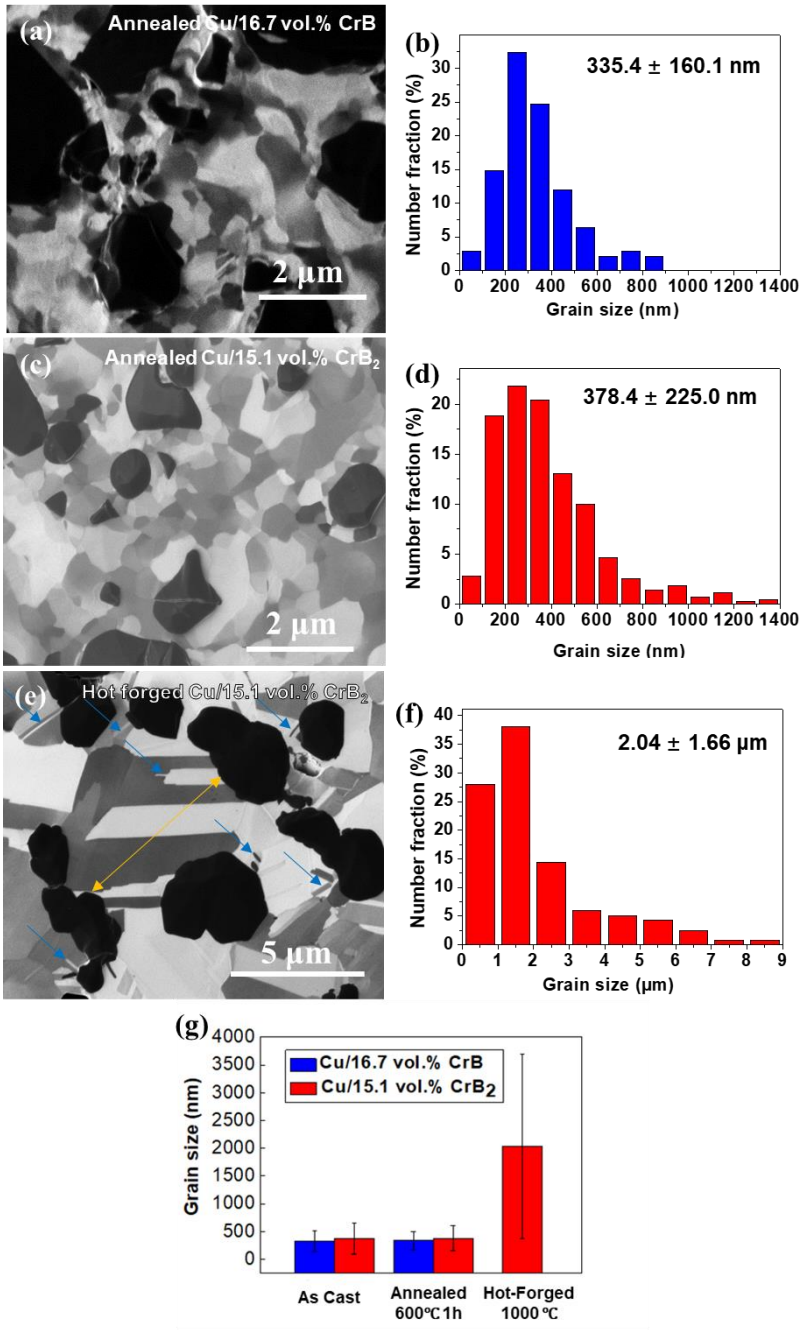

Figure 4-4 Thermal stability of UFG/nanocrystalline Cu/CrB and Cu/CrB_2. FIB image of (a) Cu/16.7 vol.% CrB after annealing at 600 °C for 1 h, (c) Cu/15.1 vol.% CrB_2 after annealing at

600 ℃ for 1 h, (e) Cu/15.1 vol.% CrB_2 after hot forging at 1000 ℃, with (b), (d), and (f) representing grain size distributions, respectively. (g) Summary of Cu matrix grain size as a function of different thermal conditions

(4) Enhanced mechanical properties of Cu/CrB and Cu/CrB_2

Microhardness of the Cu/CrB and Cu/CrB_2 samples versus particle volume percentage is shown in Figure 4-5a. With the addition of CrB (represented by blue squares), the microhardness of the samples increased remarkably compared to pure Cu samples. Average microhardness for the Cu/4.2 vol.% CrB is 93 ± 22.7 HV, and that of Cu/16.7 vol.% CrB is 136 ± 7.8 HV, whereas pure Cu processed by the same conditions is 74 HV. There is a roughly linear correlation between the microhardness of the Cu/CrB samples and the CrB volume percentage, which can be summarized as:

$$H_c = 74 + 3.7V_p \qquad \text{Equation 4-3}$$

where H_c is the microhardness (HV) of the Cu/CrB samples. The microhardness of Cu/15.1 vol.% CrB_2 is 131.6 ± 8.3 HV, which is represented by the red sphere in Figure 4-5a. It also roughly follows the microhardness evolution trend for the Cu/CrB samples. Its yield strength (σ_y) is converted from its Vickers hardness (H_v) by Equation 4-4[139] to be 378.2 MPa.

$$\sigma_y = 2.874H_v \qquad \text{Eq. 4-4}$$

The significant strengthening of Cu/CrB and Cu/CrB_2 compared to pure Cu can be attributed to the Hall-Petch effect of refined grains (σ_{HP}), Orowan strengthening of dispersed particles ($\Delta\sigma_{Orowan}$)[51], load transfer to the particles ($\Delta\sigma_{LT}$)[140], and mismatch in the coefficients of thermal expansion between the particles and the matrix ($\Delta\sigma_{CTE}$)[141], which can be calculated by Equation 4-5 to 4-8.

$$\sigma_{HP} = \sigma_0 + \frac{k}{\sqrt{d}} \qquad \text{Equation 4-5}$$

$$\Delta\sigma_{LT} = 1.5V_p\sigma_i \quad \text{Equation 4-6}$$

$$\Delta\sigma_{Orowan} = \frac{0.13Gb}{d_p[\sqrt[3]{\frac{1}{2V_p}}-1]} ln\frac{d_p}{2b} \quad \text{Equation 4-7}$$

$$\Delta\sigma_{CTE} = \beta Gb(\sqrt{\frac{12\Delta\alpha\Delta T V_p}{bd_p(1-V_p)}}) \quad \text{Equation 4-8}$$

where σ_0 and k are Hall-Petch constants, σ_i is the interfacial bonding strength between matrix and particle, G and b are the shear modulus and Burger's vector of the matrix, d_p is the diameter of particles, $\Delta\alpha$ is the CTE difference, ΔT is the temperature difference between testing and processing, and β is a material constant equal to 1.25. For Cu, σ_0 is 25.5 MPa, and k is 0.12 MPa·m$^{1/2}$[134]. G is 47.7 GPa, and b is 0.265 nm[142]. α_{CrB_2} is $10.5 \times 10^{-6}/K$, α_{Cu} is $16.4 \times 10^{-6}/K$ at 20 °C[143,144], and $\Delta\alpha$ is $5.9 \times 10^{-6}/K$. Taking Cu/15.1 vol.% CrB_2 as an example, d_p of CrB_2 is 1.8 ± 1.1 μm. σ_{HP}, $\Delta\sigma_{Orowan}$, and $\Delta\sigma_{CTE}$ are calculated to be 221.4 MPa, 15.1 MPa, and 83.5 MPa, respectively. $\Delta\sigma_{LT}$ is difficult to estimate as the interfacial bonding strength is difficult to measure. Overall, the predicted value is close to the experimental value. It is noteworthy that since particles are located at the grain boundaries of the ultrafine grains, modifications to the Orowan strengthening mechanism (Eq. 7) may be needed. Alternatively, an enhanced k factor in the Hall-Petch effect (Eq. 5), due to the larger impedance to dislocation motion by the presence of particles at the GBs may apply [145]. Nevertheless, the major contribution to strengthening comes from grain boundary strengthening.

The Young's modulus of the Cu/CrB and Cu/CrB_2 samples versus particle content is shown in Figure 4-5b. The Young's modulus values of Cu/4.2 vol.% CrB and Cu/16.7 vol.% CrB are 138 ± 24.3 GPa and 173.7 ± 59.1 GPa, respectively. The Yong's modulus enhancement is very obvious considering that of pure Cu is only 115 GPa[58], resulting from the high Young's modulus of chromium borides and their strong bonding to the matrix. Besides, the Cu/15.1 vol.% CrB_2 shows

a Young's modulus of 162.1 ± 23 GPa, which falls slightly below the trend for Cu/CrB samples. Average Young's modulus values of CrB and CrB_2 are 522 GPa and 442 GPa, respectively[111]. The upper limit of Young's modulus for the composite can be calculated by Equation 4-9[98],

$$E_c = E_m \times (1 - V_p) + E_p \times V_p \qquad \text{Equation 4-9}$$

where E_c, E_m, and E_p are Young's modulus of the composite, matrix, and reinforcement particles. The predicted Young's moduli of Cu/4.2 vol.% CrB, Cu/16.7 vol.% CrB, and Cu/15.1 CrB_2 are 132.1 GPa, 183.0 GPa, and 164.4 GPa, respectively. The experimental values agree well with the theoretical values. Thus, the lower Young's modulus of the Cu/CrB_2 is due to the lower modulus of the CrB_2 reinforcement particles.

In general, CrB has higher hardness and Young's modulus than CrB_2[103,111]. The mechanical property difference between CrB and CrB_2 is directly linked with the Young's moduli difference between the Cu/CrB_x composite samples due to the rule of mixture. Meanwhile, it is not obvious when comparing microhardness of the Cu/CrB_x samples since other factors such as particle size, matrix-particle interfacial bonding strength, and grain size of the matrix can also affect the microhardness of the composite samples.

The typical tensile stress-strain curve of the hot-forged Cu/15.1 vol.% CrB_2 sample is illustrated in Figure 4-5c. The yield and tensile strengths are determined to be 286.3 MPa and 353.0 MPa, respectively. Compared to M20 pure Cu (C10100, 99.99% Cu, as-hot rolled) with a similar sheet thickness, the yield strength of Cu/15.1 vol.% CrB_2 increased by 217.3 MPa (315%), and the tensile strength increased by 118 MPa (50%)[58]. Assuming other strengthening effects remain constant, the yield strength decrease due to the grain growth (lager d) in hot forging is calculated by Eq. 5 as 111.9 MPa. The yield strength of the as-cast Cu/15.1 vol.% CrB_2 is converted from microhardness (Eq. 4) to be 378.2 MPa. Thus, the yield strength of the hot-forged

sample is estimated to be 266.3 MPa, which is 20 MPa lower than the value shown by the tensile test. Lu *et al.* reported that coherent boundaries, especially nanoscale twin boundaries, can simultaneously increase strength and ductility[138]. Thus, it is anticipated that the extra strengthening of the hot-forged sample results from the high-density twinning, including nanotwinning structures within the grains, as they can partially obstruct dislocation motion.

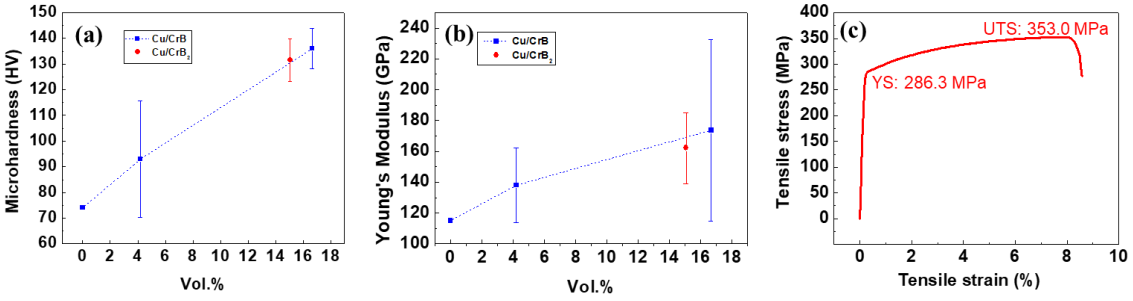

Figure 4-5 Enhanced mechanical properties of UFG/nanocrystalline Cu/CrB and Cu/CrB_2. (a) Microhardness versus volume percentage. (b) Young's modulus versus volume percentage. (c) Tensile stress-strain curve of hot forged Cu/15.1 vol.% CrB_2

4.1.4 Summary

In summary, it was discovered that as-cast bulk UFG Cu can be directly achieved by microparticles with surface nanofeatures under slow cooling. The microparticles with surface nanofeatures, which were formed by the coalescence of nanoparticles, induce substantial grain refinement down to ultrafine/nano scale. Additionally, exceptional thermal stability of the UFG/nanocrystalline Cu was revealed, showing negligible grain growth after annealing at 600 °C (0.55 Tm) for 1 h. Mechanical properties, including microhardness, strength, and Young's modulus of the UFG Cu were remarkably enhanced over pure Cu. This pathway of fabricating bulk UFG metals, assisted by microparticles with surface nanofeatures, has the potential to be

extended to other materials and greatly advance the mass production and application of UFG/nanocrystalline metals, even for high-temperature environments.

4.2 Facile Manufacturing of Bimodal Grained Cu with Nanoparticles

4.2.1. Introduction

Ultrafine grained (UFG)/nanocrystalline metals often exhibit superior strength but limited ductility. Engineering bimodal grain size distributions in UFG/nanocrystalline metals is an effective strategy to achieve strength-ductility synergy [146,147]. Bimodal grained copper (Cu) with micro-sized grains embedded in ultrafine grains displayed a high strength comparable to the UFG Cu counterpart while reaching a high tensile ductility (65% elongation to failure) [147]. Nanocrystalline iron with high strength (ultimate compressive strength: 2.25 GPa) and large plasticity (40%) was achieved due to the bimodal grain size feature [148]. The underlying mechanism is that while the ultrafine/nanoscale grains impart high strength to the material according to the Hall-Petch effect, the heterogeneous grain structure enables pronounced strain hardening to sustain the uniform deformation to large strains [147].

Bimodal grained metals were fabricated by two approaches, *i.e.*, top-down and bottom-up [149]. Initial coarse-grained metals were converted into metals with bimodal grain size distributions by severe plastic deformation often at cryotemperature and subsequent annealing [147]. Consolidating mixture of milled powders and un-milled powders was utilized to fabricate bimodal grained samples from bottom-up [150,151]. In general, these methods are difficult to meet the mass production requirement of parts with large sizes and complex geometries.

Recently, it was discovered that bulk UFG/nanocrystalline metals can be fabricated by casting with slow cooling enabled by nanoparticles [90]. Molten-salt assisted nanoparticle

incorporation has been developed to fabricate various metals containing dispersed nanoparticles via solidification processing [89,90]. Additionally, it was reported that grain boundary migration is subjected to both heat treatment and plastic deformation, while nanoparticles can effectively restrict grain growth [90,130,133]. Hence, it is of interest to investigate fabrication of bimodal grained metals by hot rolling of as-solidified UFG metals enabled by nanoparticles, since casting and hot rolling are commonly used in metal processing industry. Additionally, nanoparticles can further enhance the material properties (*e.g.*, strength, wear resistance) and modify phase morphologies of alloys, to meet the demands of high-performance materials.

Here, we report a facile and scalable manufacturing method of bimodal grained Cu by casting followed with hot rolling of metals containing nanoparticles. As-solidified Cu/WC displayed nanoparticle-rich zones, which were uniformly distributed in the Cu matrix. The Cu matrix exhibit ultrafine/nanoscale grains induced by WC nanoparticles due to the enhanced heterogeneous nucleation and growth restriction induced by WC nanoparticles. After hot rolling, microscale-grain regions and ultrafine-grain regions were formed in the Cu matrix, leading to a bimodal grain structure.

4.2.2. Experimental Procedure

The schematic of the two-step fabrication procedure is shown in Figure 4-6a. First, WC nanoparticles were incorporated into Cu by the molten-salt assisted nanoparticle incorporation method [52,89] with borax ($Na_2B_4O_7$) as the salt flux. WC nanoparticles were selected due to the good wettability with molten Cu, which is essential to the successful incorporation [89,152]. Second, as-cast Cu/8 vol.% WC nanocomposite was hot rolled at approximately 500°C with a total thickness reduction of 85%. Specimens were cut from the bulk samples, ground, polished, and ion

milled (Model PIPS 691, Gatan) at 4° and 4.5 kV for 1 h. Focused ion beaming (FIB) imaging by FEI Nova 600 was utilized to reveal the grain structures of the samples. The granular contrast was induced by the ion beam due to the channeling contrast [137,153]. Grain size analyses were conducted on FIB images using image processing software.

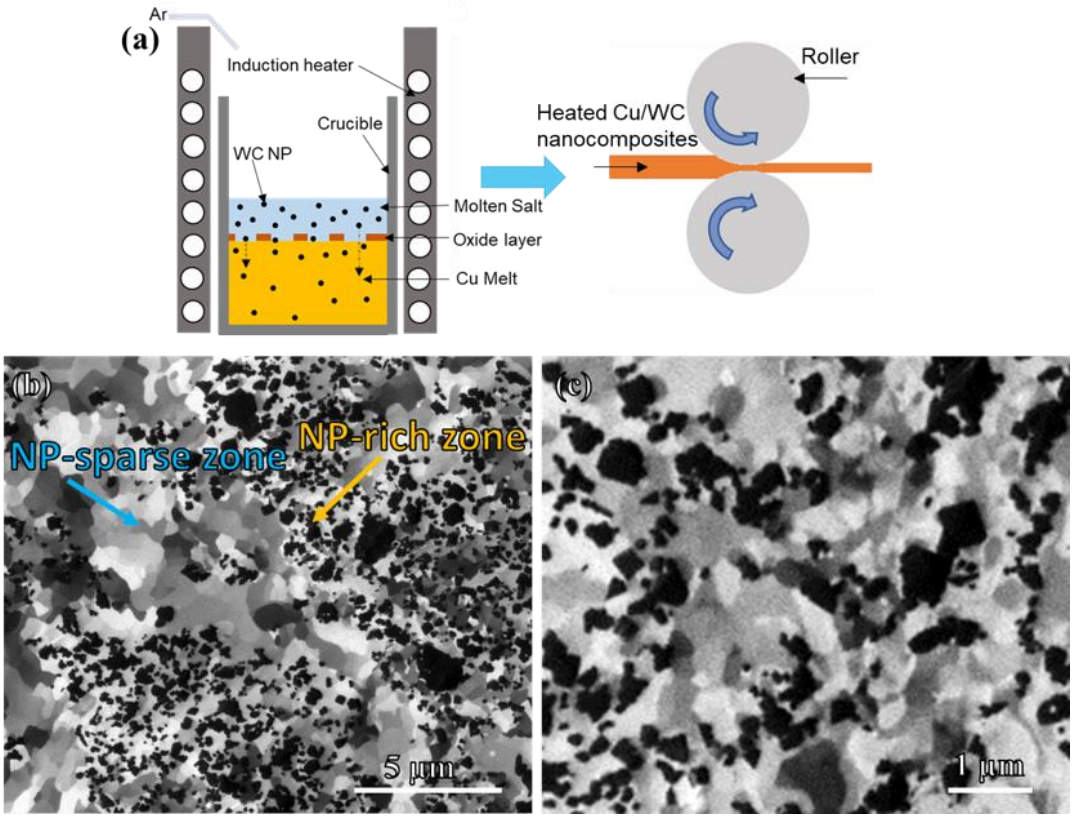

Figure 4-6. (a) Schematic of the two-step fabrication process of bimodal grained Cu. (b) FIB image of as-solidified Cu/8 vol.% WC; (c) FIB image of a nanoparticle-rich zone

4.2.3. Results and Discussion

In this study, to achieve the heterogeneous grain structures, a heterogeneous distribution of dispersed WC nanoparticles in Cu matrix is desired. The microstructure of as-solidified Cu/8 vol.% WC is shown in Figure 4-6b and 4-6c. WC nanoparticles formed nanoparticle-rich zones in the Cu matrix. It was found that the distribution of nanoparticles was affected by the type of salt flux used

in the nanoparticle incorporation processing [52]. $Na_2B_4O_7$ alone as the salt flux resulted in nanoparticle-rich zones distinct from nanoparticle-sparse zones in the Cu matrix compared to $Na_2B_4O_7$ mixed with fluoride salt as the flux [52]. The Cu matrix was comprised of ultrafine/nanoscale grains. The substantial grain refinement is ascribed to the continuous heterogeneous nucleation and growth restriction mechanism by WC nanoparticles [90].

Bimodal grain features were engineered from the UFG Cu after hot rolling, with the grain structures shown in Figure 4-7. As shown in Figure 4-7a, Cu grains grew to microscale in nanoparticle-sparse zones. Meanwhile, grains in the nanoparticle-rich zones remained ultrafine/nanoscale. The average grain size of the coarse-grain regions (Figure 4-7b) and the fine-grain regions (Figure 4-7d) is 6.3±3.5 μm and 230.6±125.8 nm respectively, with the analyzed areas indicated by squares. The corresponding grain size distributions are shown in Figure 4-7c and 4-7e. The stabilization of the ultrafine/nanoscale grains in the nanoparticle-rich zones is attributed to the effective grain growth restriction by WC nanoparticles. Meanwhile, in nanoparticle-sparse zones, due to insufficient restriction, grains grew to microscale to reduce grain boundary energy when subjected to plastic deformation combined with thermal exposure. The nanoparticle percentage determines the area ratio between the coarse-grain and fine-grain regions in a cross-section. Figure 4-7b shows that Cu/8 vol.% WC had a good combination of coarse-grain regions and fine-grain regions. Cao *et al.* reported the high thermal stability of as-solidified UFG Cu enabled by 5 vol.% WC nanoparticles. Grains in nanoparticle-rich zones were stable up to 850°C, and up to 600°C in nanoparticle-sparse zones under annealing [90]. Nevertheless, Cu grains in nanoparticle-sparse zones only grew to 269nm from 134nm even after annealing at 850°C [90]. Hot rolling can facilitate grain coarsening at a lower temperature compared to annealing, which is beneficial to form bimodal grain structures. The grain sizes of the coarse grains can be controlled

by the hot rolling temperature, thickness reduction, and nanoparticle percentage. The grain sizes of the fine grains can be mainly controlled by the nanoparticle percentage.

We demonstrate bimodal grained metals can be directly fabricated by casting followed with hot rolling. Although bimodal grained metals containing nanoparticles were reported before, a complex procedure was needed. Tang *et al.* [154] reported that Al (5083)/SiC nanocomposite samples prepared by the sequence of cryomilling, hot isostatic pressing, and hot rolling displayed coarse grain regions (interparticle) in a fine grain matrix (innerparticle).

It is noteworthy that through-grain twins were observed in the coarse grains after hot rolling, as shown in Figure 4-7a. The microstructure of hot-rolled Cu/WC combining bimodal grains, twins, and nanoparticles is expected to contribute to much-enhanced properties.

The grain size distributions of the matrix after hot-rolling-induced grain growth is strongly affected by the distribution of nanoparticles. With a heterogeneous distribution of nanoparticles, heterogenous grains are achieved, with the schematic shown in Figure 4-8a. On the other hand, it is anticipated that if nanoparticles are homogeneous in the Cu matrix, Cu grains can remain ultrafine after hot rolling due to the homogeneous grain growth restriction by nanoparticles, with the schematic shown in Figure 4-8b. For future work, it is of interest to investigate methods to achieve different types of nanoparticle distributions in metals to enable various heterogeneous grain structures. Besides, tensile tests will be conducted to quantify the mechanical properties. Correlations will be established among grain sizes of both coarse and fine grains, nanoparticle percentage, and processing parameters to potentially control the bimodal grain structures. It is also of interest to identify nanoparticles besides WC for various systems.

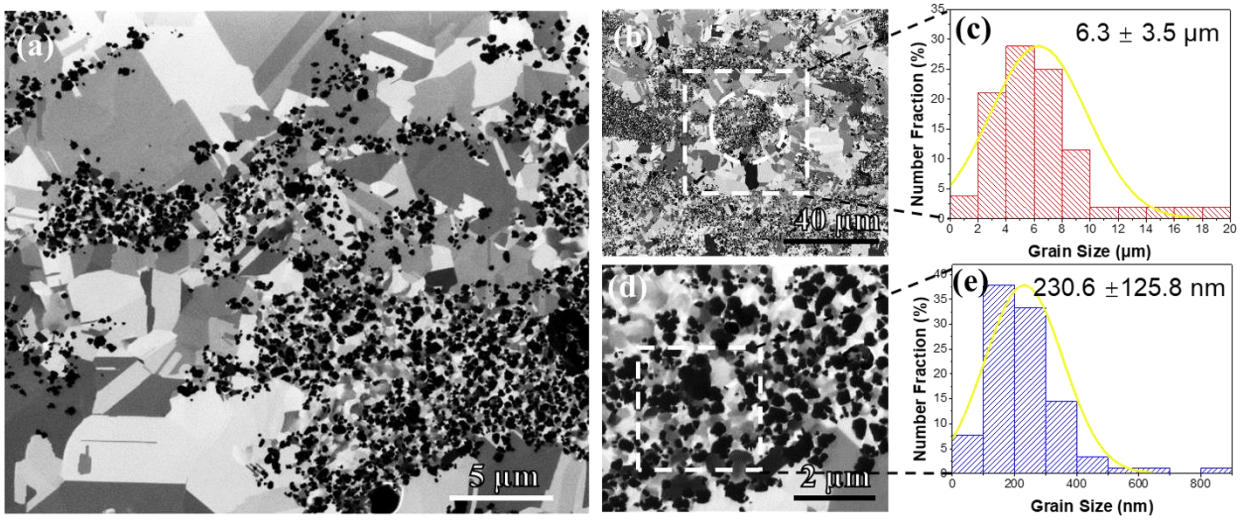

Figure 4-7. (a) Bimodal grain structures of hot-rolled Cu/8 vol.% WC; (b) FIB image at a low magnification to show coarse-grain regions and (c) corresponding grain size distribution; (d) ultrafine-grain region and (e) corresponding grain size distribution

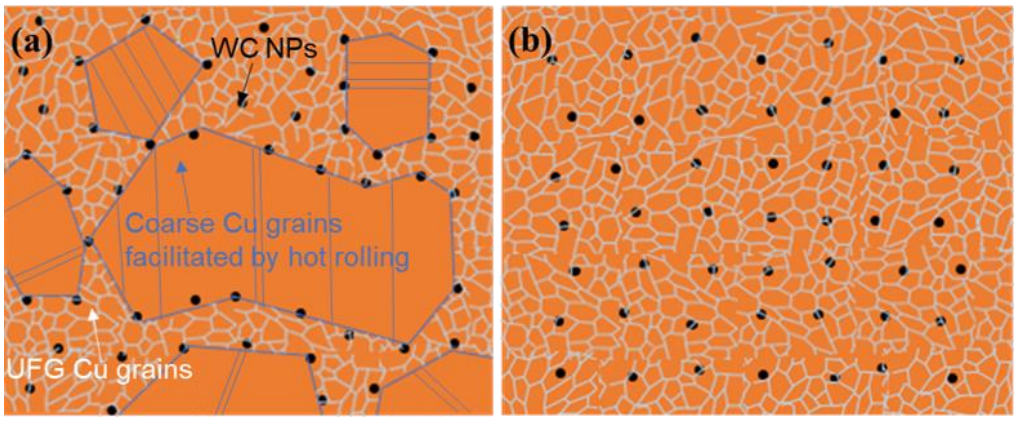

Figure 4-8. Schematics of grain structures of hot-rolled Cu with (a) heterogeneous distribution of nanoparticles; (b) homogeneous distribution of nanoparticles

4.2.4. Conclusions

In summary, bimodal grained Cu was fabricated via casting followed by hot rolling, with the assistance of WC nanoparticles. The heterogeneous grain structure results from the distribution of nanoparticles. As solidified Cu/WC displayed ultrafine/nanoscale Cu grains due to the enhanced

heterogeneous nucleation and restriction of grain growth by nanoparticles. Hot rolling facilitated the growth of the Cu grains in the nanoparticle-sparse zones, while grains in the nanoparticle-rich zones were stable owing to the effective grain growth restriction by nanoparticles. This simple pathway can be potentially extended to other materials to advance the production of bimodal grained metals.

Chapter 5: Phase Modification of Cu Alloys by Nanoparticles

Cu alloys can offer distinct properties based on the alloying elements and heat treatment conditions. However, the properties of traditional Cu alloys have reached certain limits, which can hardly meet the increasing standards for higher system performance and energy efficiency. Nanotechnology enabled metallurgy provides a new pathway to achieve significant performance enhancement of Cu. In this chapter, the nanoparticle enabled phase modification in Cu alloys was studied targeting the intermetallic phases (in high-Al bronze and CuZrSi alloy [155]), the solid solution (in Cu4Al), and the precipitates (in CuCr alloy). We demonstrate that nanoparticles can refine and modify the intermetallic phases, enhance the aging behavior, and mitigate the intergranular corrosion in solid solution in Cu alloys to further improve the properties of the Cu alloys. These findings advance the fundamental understanding of nanoparticle-enabled metallurgy, which can be potentially applied to other alloy systems.

5.1 Enhanced Ductility of Hard Brittle High-Al Bronze

5.1.1 Introduction

Cu-Al alloys (aluminum bronze) are a series of alloys that exhibit distinct microstructures and properties and find various applications depending on the aluminum contents. Among the various Cu-Al alloys, high-aluminum bronze (Cu-14Al), with an aluminum content exceeding its solubility in Cu, shows a microstructure of two intermetallic phases: the γ_2 (Cu_9Al_4) and the β ($AlCu_3$). High-aluminum bronze exhibits high hardness, superior wear resistance, and good sliding properties. However, it suffers from an extremely low ductility due to the brittle nature of the intermetallic phases.

Recently, high-aluminum bronze has drawn attention for tooling and as a mold material for drawing and forming stainless steel. The traditional mold materials for stainless steel drawing are steels such as Cr12 and W18Cr14V [156]. However, the adhesion between the iron-based mold material and the stainless steel due to their miscibility can cause a low life expectancy of the molds and scratch of the parts [156]. High-aluminum bronze is advantageous due to its low miscibility with stainless steel apart from the above-mentioned mechanical properties. Nevertheless, the extremely low ductility of the high-aluminum bronze strongly limits its application.

Adding other alloying elements can modify the microstructure of the high-aluminum bronze and improve its properties. It was reported that iron (Fe) can not only act as a grain refiner but also improve the ultimate tensile strength; nickel (Ni) improves yield strength and corrosion resistance; nickel (Ni) and manganese (Mn) stabilize the microstructure [157]. Nonetheless, the cast high-aluminum bronze (approximately 14 wt.% Al) with Fe and Mn has an elongation of 0.5%.

In addition, solidification control has been reported to tune the microstructure of Cu-Al alloys for enhanced ductility. Cu-12Al single crystal wires were fabricated by the continuous unidirectional solidification method [158]. Due to the high cooling rate, the β phase transformed into β' martensite phase, which avoided the more brittle γ phase [158]. However, this method is difficult to be scaled up for the production of large and complex parts.

Nanoparticle enabled phase modification (nano-treating) has been demonstrated recently. Dispersed nanoparticles in the alloy melt can instill phase nucleation and growth control during solidification. Arc welding of aluminum alloy 7075 was enabled by nanoparticle-enabled phase control: TiC nanoparticles transformed the primary grains from dendrites to equiaxial ones and induced a fine segmented eutectic phase [159]. Besides, nanoparticle-enabled grain refinement of as-solidified pure Cu down to the ultrafine/nanoscale was discovered [90]. However, the phase

modification of materials entirely comprised of intermetallics during solidification by nanoparticles has not been studied.

Here, we report the effective modification of intermetallic phases in Cu-14Al by TiB_2 nanoparticles to achieve improved ductility. Cu-14Al with 5 vol.% TiB_2 nanoparticles was fabricated. Its microstructure was examined and compared with the Cu-14Al counterpart. Microhardness and tensile tests were conducted. Results showed that dispersed TiB_2 nanoparticles preferably stayed in the β phase and effectively modified the morphology and distribution of the γ phase. The mechanical properties of the nano-treated sample including microhardness and especially the ductility were significantly increased over Cu-14Al.

5.1.2 Materials and Methods

Cu-14Al was alloyed by melting Al and Cu at 1200 ℃. Cu-14Al/5 vol.% TiB_2 was fabricated by melting Al, Cu, and in-situ Cu-4Al/10 vol.% TiB_2 at 1200 ℃. $KAlF_4$ was added and Ar was purged to the surface of the melt to prevent oxidation. The melt was manually stirred using a graphite rod and kept at 1200 ℃ for 20 min before cooling to room temperature in air. Specimens cut from the as-solidified bulk samples were ground and polished. The microstructure of the samples was observed by optical microscopy and scanning electron microscopy (SEM, Zeiss Supra 40VP). The phases of the samples were analyzed by X-ray diffraction (XRD, Bruker D8) with Cu Kα radiation. The microhardness of samples was measured using an LM 800AT microhardness tester. Tensile bars with a gauge length of 1 cm were machined by electric discharge machining (EDM). Tensile tests were performed at a strain rate of $5 \times 10^{-3}/\text{min}$.

5.1.3 Results and Discussion

The XRD patterns of the Cu-14Al/5 vol.% TiB_2 and Cu-14Al are shown in Figure 5-1. The phases of Cu-14Al were indexed as $AlCu_3$ (β) and Cu_9Al_4 (γ), while the phases of the nano-treated sample were identified as $AlCu_3$ (β), Cu_9Al_4 (γ), and TiB_2. Thus, TiB_2 nanoparticles were stabilized in the Cu-14Al matrix without reaction between TiB_2 and the Cu-14Al matrix. According to the Cu-Al phase diagram, upon solidification, the equilibrium phase of the alloy is single-phase β. With temperature further decreasing, β phase partially transforms to γ, resulting in a γ + β dual phase microstructure.

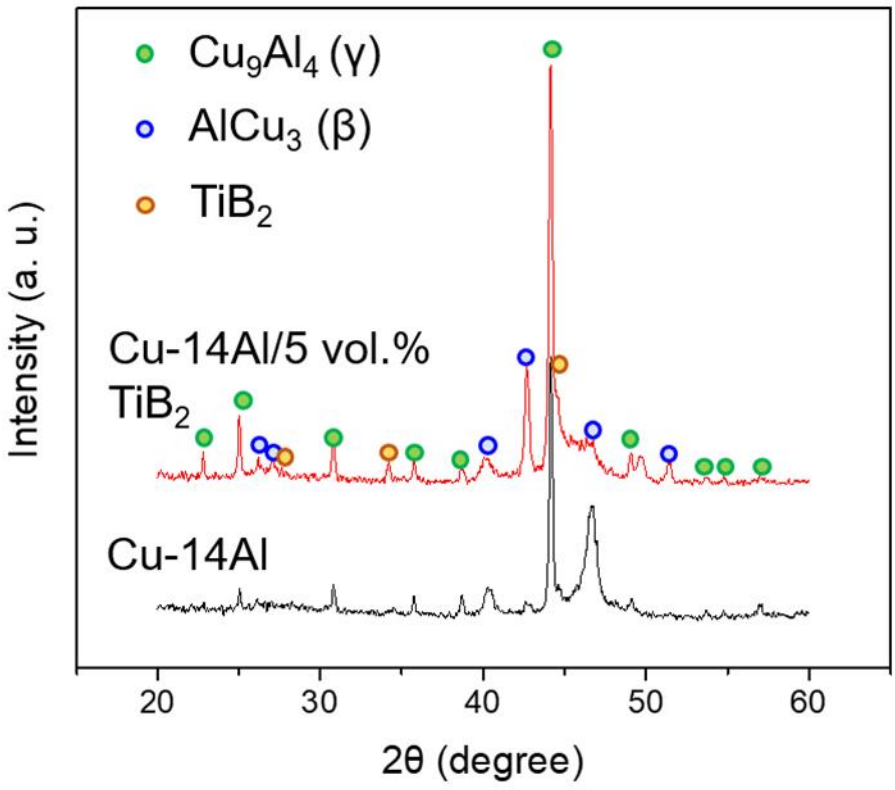

Figure 5-1 XRD patterns of Cu-14Al and Cu-14Al/5 vol.% TiB_2

The microstructures of the nano-treated and pure Cu-14Al samples are shown in Figure 5-2. As shown in Figure 5-2a and 5-2c, the microstructure of Cu-14Al was comprised of the γ phase embedded in the matrix of the β phase. Besides, some dendritic γ were observed. The γ phase also

formed along the grain boundary of the β phase, separating the β grains. It is anticipated that the grain boundaries of the β phase are favorable sites for the phase transformation due to the higher energy state of the grain boundaries than grain interiors. The brittle γ phase at the grain boundary can cause an intergranular fracture. Overall, the unfavorable microstructure of the intermetallic phases in Cu-14Al leads to its extreme brittleness.

On the contrary, the nano-treated sample exhibit a distinct microstructure compared to the Cu-14Al counterpart, as shown in Figure 5-2b and 5-2d. The TiB_2 nanoparticles preferably stayed in the β phase and formed a net-like distribution in the β phase. The morphology and distribution of the γ phase were altered from the Cu-14Al sample. First, the γ phase was significantly refined. Second, no dendritic γ was observed. Instead, the γ phase showed a globular morphology. Moreover, no γ phase was present at the grain boundary.

The mechanism of the modified intermetallic phases of Cu-14Al by TiB_2 nanoparticles is proposed as follows. The net-like distribution of TiB_2 nanoparticles in the β phase roughly separates the β phase into individual β cells, which are surrounded by TiB_2 nanoparticles. TiB_2 nanoparticles act as heterogeneous nucleation sites of the γ phase for the phase transformation to occur. The nanoparticles, as heterogeneous nucleation sites, are more energy favorable than the grain boundaries of the β phase, thereby eliminating the presence of brittle γ phase at the grain boundaries. Besides, phase transformation is confined in such cells surrounded by nanoparticles so the γ phase grows within the interior of the β cells. Thus, the γ phase shows refined and globular morphology. The microstructure in Figure 5-2d also corroborates with this proposed mechanism.

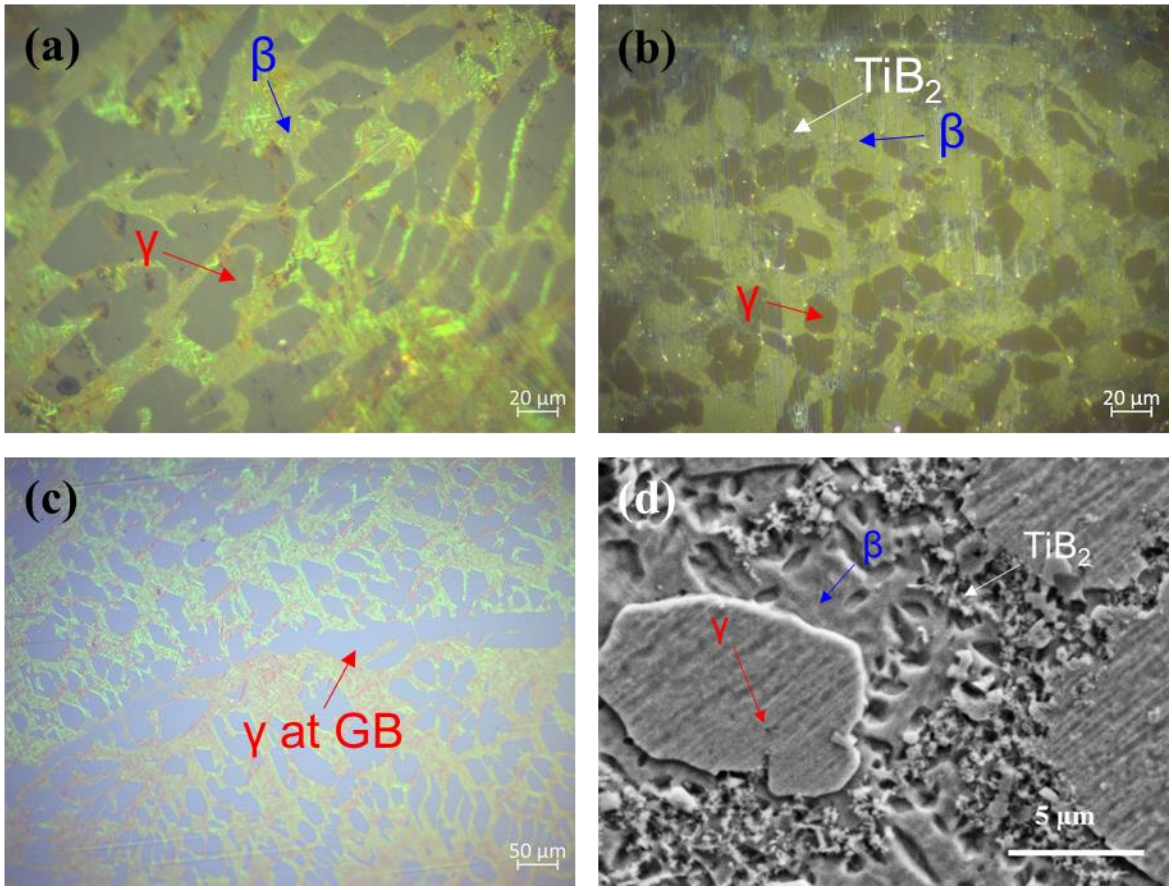

Figure 5-2 Microstructure of (a, c) Cu-14Al and (b, d) Cu-14Al/5 vol.% TiB_2

The mechanical properties of both pure alloy and the nano-treated alloy were evaluated and compared. The microhardness of the nano-treated sample is 397.5 ± 12.0 HV, which is 53.3 HV higher than that of the Cu-14Al (344.2 ± 7.6 HV). The hardness increase comes from the Orowan strengthening by TiB_2 nanoparticles and refined γ phase. It is also anticipated that nanoparticles can potentially further increase the wear resistance of the alloy.

The stress-strain curves of Cu-14Al/5 vol.% TiB_2 and Cu-14Al are shown in Figure 5-3. The failure of Cu-14Al occurred in the very early stage, with extremely low ductility and tensile strength. The elongation and ultimate tensile strength of the nano-treated sample are significantly higher than the pure alloy.

The average ultimate tensile strengths and elongations of the samples are summarized in Table 5-1. The ductility of the nano-treated sample is 1.0±0.02%, 10 times that of the pure alloy (0.1±0.05). The ultimate tensile strength of the nano-treated sample and the control sample is 548.1±8.7 MPa and 138.8±14.2 MPa, respectively. The mechanism for improved ductility is attributed to the modified morphology and distribution of the intermetallics by TiB_2 nanoparticles. In pure Cu-14Al, the brittle and large γ phase, especially those located at the grain boundaries can act as crack initiation sites, leading to rapid failure under tensile conditions. In the nano-treated sample, the refined γ phase, its transition from dendritic to globular, and the elimination of brittle γ at the grain boundary can effectively mitigate crack formation and propagation, thereby increasing ductility. Moreover, it is expected that the TiB_2 nanoparticles in the β phase can possibly deflect crack propagation through β phase, thereby increasing the elongation of the nano-treated sample.

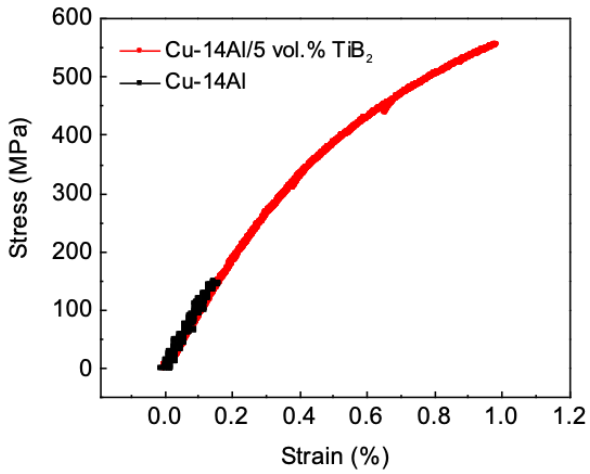

Figure 5-3 Stress-strain curve of (a) Cu-14Al/5 vol.% TiB_2; (b) Cu-14Al

Table 5-1 Summary of ultimate tensile strength and elongation of Cu-14Al and Cu-14Al/5 vol.% TiB_2

Sample	UTS (MPa)	Elongation (%)
Cu14Al/5 vol.% TiB_2	548.1±8.7	1.0±0.02
Cu14Al	138.8±14.2	0.1±0.05

5.1.4 Conclusions

In summary, the effectiveness of nanoparticles to modify the intermetallic phases in the Cu-14Al alloy to alleviate its brittleness is revealed. The TiB_2 nanoparticles in the β phase act as preferable heterogeneous nucleation sites of the γ phase during solid-state phase transformation. Moreover, phase transformation is confined in such cells surrounded by nanoparticles. Thus, the very brittle γ phase is effectively refined, transformed to globular appearances, and eliminated at the grain boundaries. The elongation of the nano-treated sample is significantly improved. It is anticipated that nano-treating of the hard but brittle high-aluminum bronze can expand its applications. Nano-treating has great potential for modifying brittle alloys with only intermetallic phases to achieve enhanced properties.

5.2 High Performance Cu-4Al Alloy Enabled by Nanoparticles

5.2.1 Introduction

Aluminum bronze, with aluminum content lower than its solubility in Cu, shows a microstructure of a single-phase solid solution and has widespread applications in aggressive

environments especially seawater due to the excellent corrosion and biofouling resistance. They also show great resistance to cavitation erosion and impingement attack [157]. The thin but tough self-healing adherent film of alumna on the surface is responsible [157]. Cu-4Al is one of such aluminum bronzes among the varieties.

However, the microhardness/strength and Young's modulus of Cu-4Al can be further improved. Moreover, the intergranular corrosion (IGC) due to dealumination at grain boundaries in Cu-4Al needs to be solved. TiB_2 nanoparticles have attracted much attention as reinforcing elements in metal matrix nanocomposites since they exhibit excellent properties, such as high hardness, modulus, corrosion resistance, and thermal stability. It is expected that dispersed TiB_2 nanoparticles in Cu-4Al can further enhance its properties.

In this study, Cu-4Al with 9.6 vol.% dispersed TiB_2 nanoparticles was fabricated. Distinct grain structures especially grain boundary morphologies of Cu-4Al and Cu-4Al/9.6 vol.% TiB_2 were observed. The Young's modulus and microhardness of the CuAl/TiB_2 nanocomposite were significantly enhanced over the alloy counterpart. Besides, the corrosion rate of the Cu-4Al/TiB_2 nanocomposite was lower than the Cu-4Al counterpart, with the severe intragranular corrosion effectively suppressed.

5.2.2 Materials and Methods

Cu-4Al/9.6 vol.% TiB_2 nanocomposites were fabricated by the in-situ method reported in Chapter 3.2. Cu (99.99%, Rotometals) was heated to 1130 ℃ with argon protection in a graphite crucible by an induction heater. Al shots were added to molten Cu, followed by mixed KBF_4 (Spectrum), K_2TiF_6 (Spectrum), and $KAlF_4$ (AMG Aluminum) powders. After holding for 1.5 h,

the melt was cooled naturally in the furnace. As-synthesized sample was re-melted at 1100 °C for 5 min.

Pure Cu-4Al was alloyed in house for comparison. Al shots were added to Cu melt at 1130 °C, with molten $KAlF_4$ on top of the melt to prevent oxidation. The melt was held for 30 min with manual mixing using a graphite rod before cooling to room temperature in the furnace.

Specimens cut from bulk samples were ground, polished, and ion milled at 4° and 4.5 kV for 1 h by Precision Ion Polishing System (Model PIPS 691, Gatan) to clean the surfaces. The microstructures were observed by optical microscopy and scanning electron microscopy (SEM, ZEISS Supra 40VP). The microhardness of the samples was measured using an LM 800AT microhardness tester with a load of 200 g and a dwell time of 10 s. The Young's modulus of the nanocomposites was measured by the MTS nanoindenter with a Berkovich tip with an indent depth of 2 μm. Each Young's modulus and microhardness data represents 10 measurements at room temperature.

Focused ion beaming imaging (FIB) by FEI Nova 600 was utilized to reveal the grain structures of the nanocomposites, with granular contrast induced by the ion beam due to the channeling contrast [137]. The Cu-4Al was etched using mixed NH_4OH, H_2O_2, and water to reveal the grain boundaries.

The Linear Polarization Resistance measurement was conducted on both Cu-4Al and the Cu-4Al/9.6 vol.% TiB_2 nanocomposite using 3.5 wt.% NaCl solution. The open potential was obtained first. Then, the corrosion rates of the samples were calculated from the potentiodynamic measurement according to ASTM-G102. In addition, immersion tests of Cu-4Al and Cu-4Al/10 vol.% TiB_2 were conducted at room temperature in the 3.5 wt.% NaCl solution for 4 days. After immersion, the corroded surfaces were observed by SEM.

5.2.3 Results and Discussion

The microstructures of Cu-4Al and Cu-4Al/9.6 vol.% TiB_2 are shown in Figure 5-4. TiB_2 nanoparticles are effective grain refiners in Al. Thus, it is of interest to study the grain structures of the as-solidified samples in this study. Cu-4Al and Cu-4Al/9.6 vol.% TiB_2 exhibit distinct grain structures, as shown in Figure 5-4. For pure Cu-4Al (Figure 5-4a), the grains are larger than 1 mm. For Cu-4Al/9.6 vol.% TiB_2 nanocomposite (Figure 5-4b), refined grains compared to Cu-4Al are observed, but they are still in the scale of a few hundred micrometers. The TiB_2 nanoparticles are captured by the grains of the CuAl solid solution matrix, which explains why ultrafine grains of the matrix are not induced. Besides, it is worth mentioning that the morphology of the grain boundaries is modified by the TiB_2 nanoparticles, as shown in Figure 5-4b and 5-41c. Unlike the smooth grain boundaries in Cu-4Al, the grain boundaries in the nanocomposite are serrated. In addition, some TiB_2 nanoparticles are located at the grain boundaries, too. These modified grain boundaries are anticipated to be caused by the impendence of grain boundary advance by nanoparticles [160]. It has been reported that serrated grain boundaries transition can lead to a significant decrease in grain boundary energy [161]. The serration of a random straight grain boundary with high energy results in two segments with lower misorientation angles and lower energies [162]. Moreover, it was reported that serrated grain boundaries can lower crack propagation and impede grain sliding [161].

It is expected that TiB_2 nanoparticles are captured by Cu-4Al matrix via Brownian capture. In the nanoparticle capture theory, when the van der Waals potential is positive, an energy barrier exists resisting the nanoparticle from moving closer to the sonification front [163]. When the

Brownian energy is higher than the energy barrier, the nanoparticle may move toward the solidification front for capture, as shown by Equation 5-1 [163].

$$W_{vwd}(D) = -\frac{(\sqrt{A_{solid}}-\sqrt{A_{liquid}})(\sqrt{A_{nanoparticle}}-\sqrt{A_{liquid}})}{6} \times (\frac{R}{D} + \frac{R}{2R+D} + \ln\frac{D}{2R+D}) \leq \frac{kT}{2} \quad \text{Equation 5-1}$$

where W_{vwd} is van der Waals potential; A is Hamaker constant; R is nanoparticle radius; D is the distance between the nanoparticle and the solidification front; k is Boltzmann's constant; T is the absolute temperature. For Brownian capture to occur, a small nanoparticle radius and/or a small absolute value of the system's Hamaker constant is desired [163]. In our study, it is anticipated that alloying Cu with Al reduces the system's absolute Hamaker constant since Al has a lower Hamaker constant than Cu. Moreover, the small TiB_2 nanoparticle size is also beneficial for capturing. The size effect of TiB_2 nanoparticles on Brownian capture is indicated in the sample after removal of Al (Cu/9.6 vol.% TiB_2). The FIB image revealing the grain structures of Cu/9.6 vol.% TiB_2 is shown in Figure 5-5. As discussed in Chapter 3.2, the size of TiB_2 nanoparticles increases after the removal of Al. Ultrafine grains are observed in the Cu/9.6 vol.% TiB_2 sample, as shown in Figure 5-5a. Notably, the TiB_2 are located both inside and outside the Cu grains, which is related to the sizes of the TiB_2 particles. As indicated by white arrows, small TiB_2 nanoparticles are captured by Cu grains. On the other hand, larger TiB_2 particles are not captured, which locate at the grain boundaries of Cu grains and restrict the grain growth. The observation agrees well with the Brownian capture theory. The average grain size of Cu/9.6 vol.% TiB_2 is 449.2 nm, with the grain size distributions shown in Figure 5-5b.

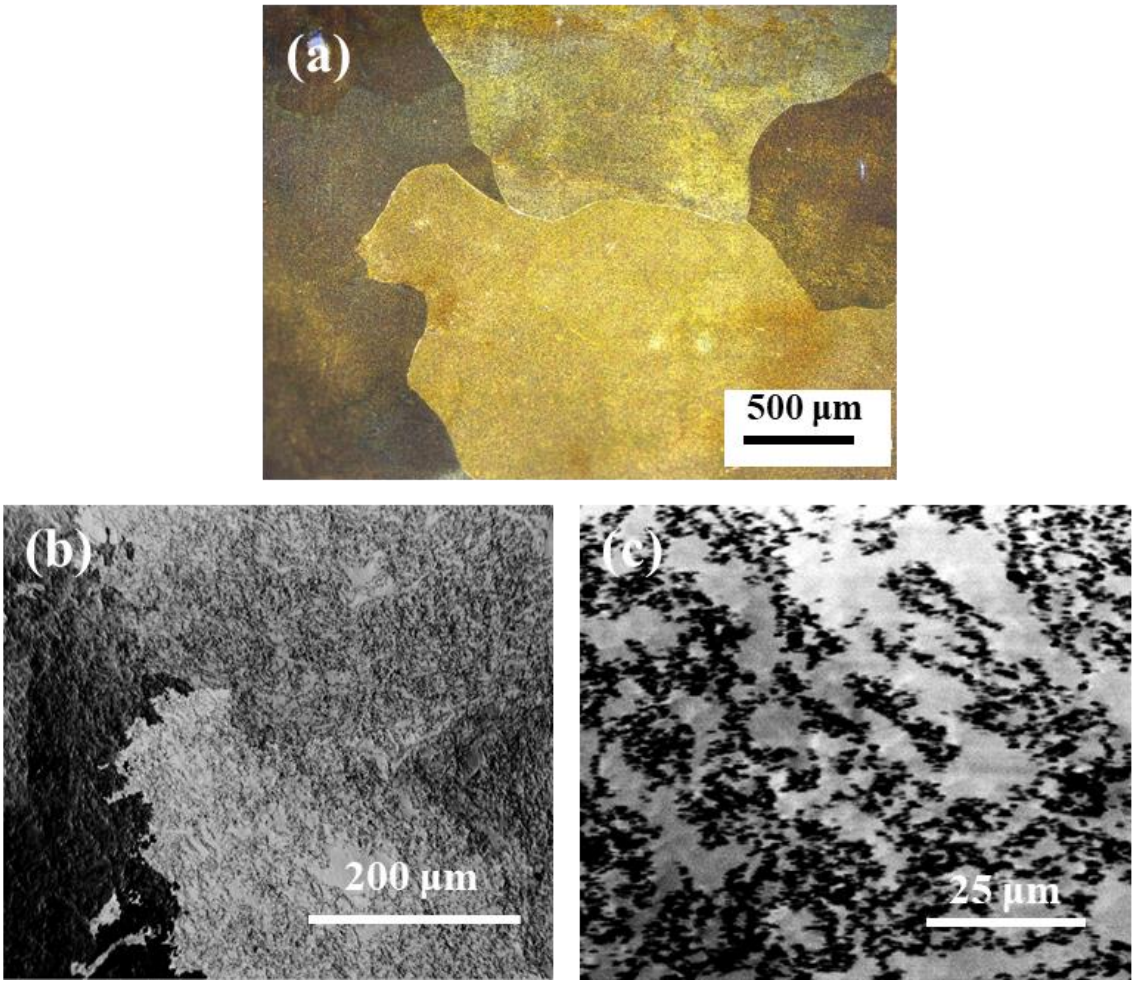

Figure 5-4 Microstructures of (a) Cu-4Al and (b, c) Cu-4Al/9.6 vol.% TiB_2

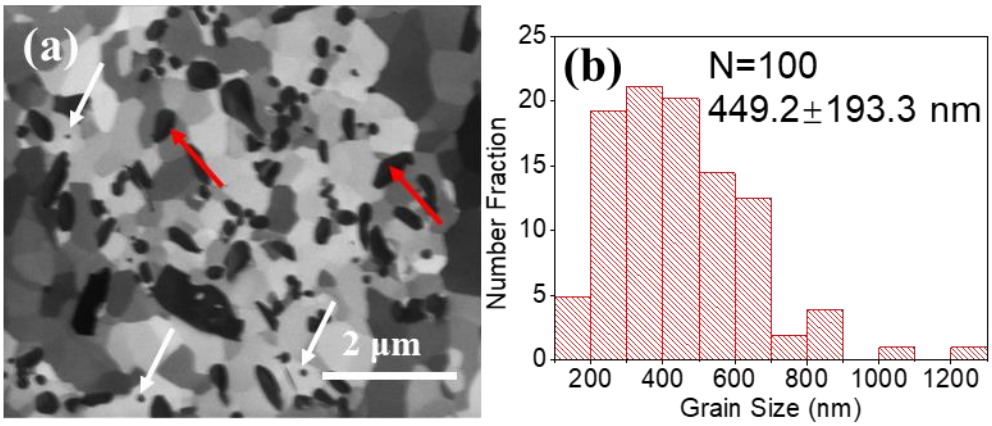

Figure 5-5 Grain structures of Cu/9.6 vol.% TiB_2

The comparison of the microhardness and Young's modulus of the as-solidified Cu-4Al/9.6 vol.% TiB_2 nanocomposite and pure Cu-4Al is shown in Figure 5-6. Significant strengthening of the CuAl alloy by TiB_2 nanoparticles was achieved. The Young's modulus the Cu4Al/9.6 vol.% TiB_2 is 167.6 ± 26.5 GPa, which is 30% higher than Cu4Al (129.2 ± 6.3 GPa). The microhardness of the Cu4Al and Cu4Al/9.6 vol.% TiB_2 is 95.3 ± 2.5 HV and 203.3 ± 52.3 HV. It is estimated that the strengthening efficiency of TiB_2 nanoparticles is 11.3 HV/vol.%, much higher than commercial WC nanoparticles. The microhardness increase arises mainly from the Orowan strengthening effect of TiB_2 nanoparticles. TiB_2 nanoparticles are captured, which can contribute to Orowan strengthening. The TiB_2 nanoparticles reduce the grain size, leading to a stronger Hall-Petch effect.

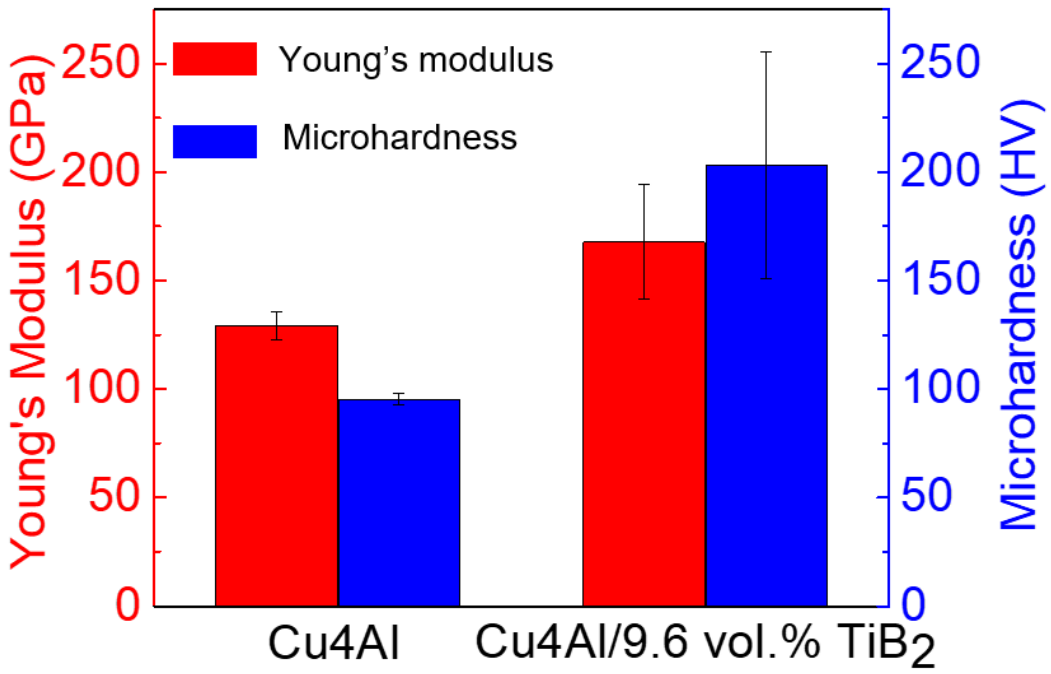

Figure 5-6 Mechanical properties of Cu-4Al and Cu-4Al/9.6 vol.% TiB_2

It was reported that ZrB_2 and TiB_2 particulates can increase the corrosion resistance of Al-Cu alloy [164,165]. Thus, the corrosion resistance of the Cu-4Al/9.6 vol.% TiB_2 nanocomposite

and the Cu-4Al counterpart was studied. The electrochemical characterization data are shown in Figure 5-7. From the electrochemical measurements, it was found that in in-situ TiB_2 nanoparticles can further increase its corrosion resistance. The open circuit potential of nano-treated sample in 3.5 wt.% NaCl solution is higher than pure Cu-4Al, as shown in Figure 5-7a. Besides, the corrosion rate estimated from the potentiodynamic measurement (Figure 5-7b) shows that nano-treated sample has a lower corrosion rate. The corrosion rate of Cu-4Al/9.6 vol.% TiB_2 nanocomposite is calculated to be 0.018 mm/year, while that of Cu-4Al is 0.026 mm/year.

The microstructures of the samples after the immersion tests are shown in Figure 5-8. Noticeable intergranular corrosion (IGC) was observed in Cu-4Al, as shown in Figure 5-8a. Deep trenches approximately 2.5 μm wide along grain boundaries were observed, as shown in Figure 5-8b. On the other hand, more uniform corrosion occurred in the nanocomposite, as shown in Fig. 8c and 8d, with no intergranular corrosion observed. It was reported that the corrosion resistance of grain boundaries was affected by grain orientation relationships. Results show that low-angle boundaries and boundaries with a sigma-3 or sigma-7 coincident site lattice relationship in 2124 Al tend to have a higher corrosion resistance than other random boundaries [166]. In this study, we suspect that the mitigated IGC arises from the modified grain boundary structures by TiB_2 nanoparticles. It is expected that the serrated grain boundaries with lower grain boundary energy and the partially blocked dealumination at grain boundaries blocked by nanoparticles lead to the mitigated IGC behavior.

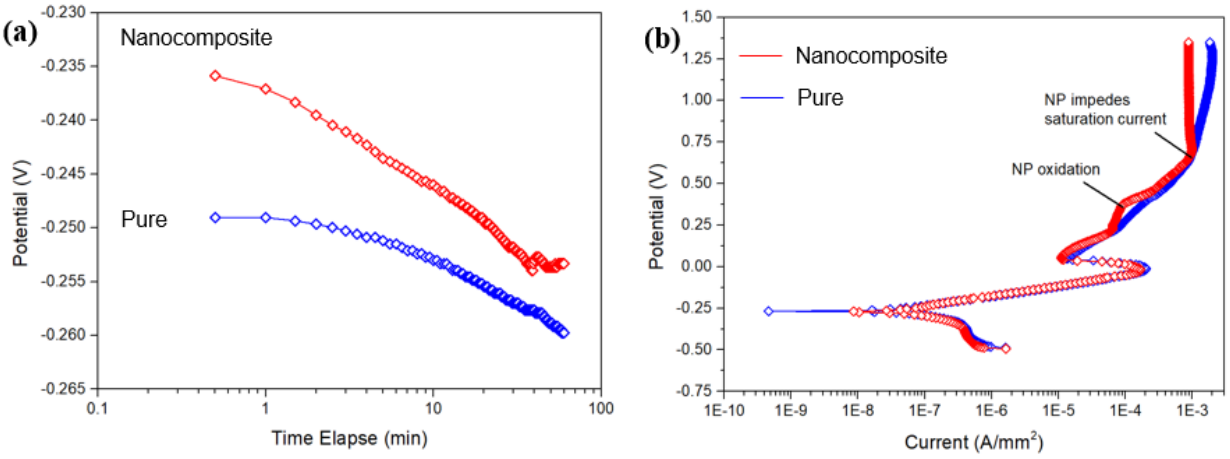

Figure 5-7 (a) The open potential; (b) potentiodynamic curves of Cu-4Al and Cu-4Al/9.6 vol.% TiB_2

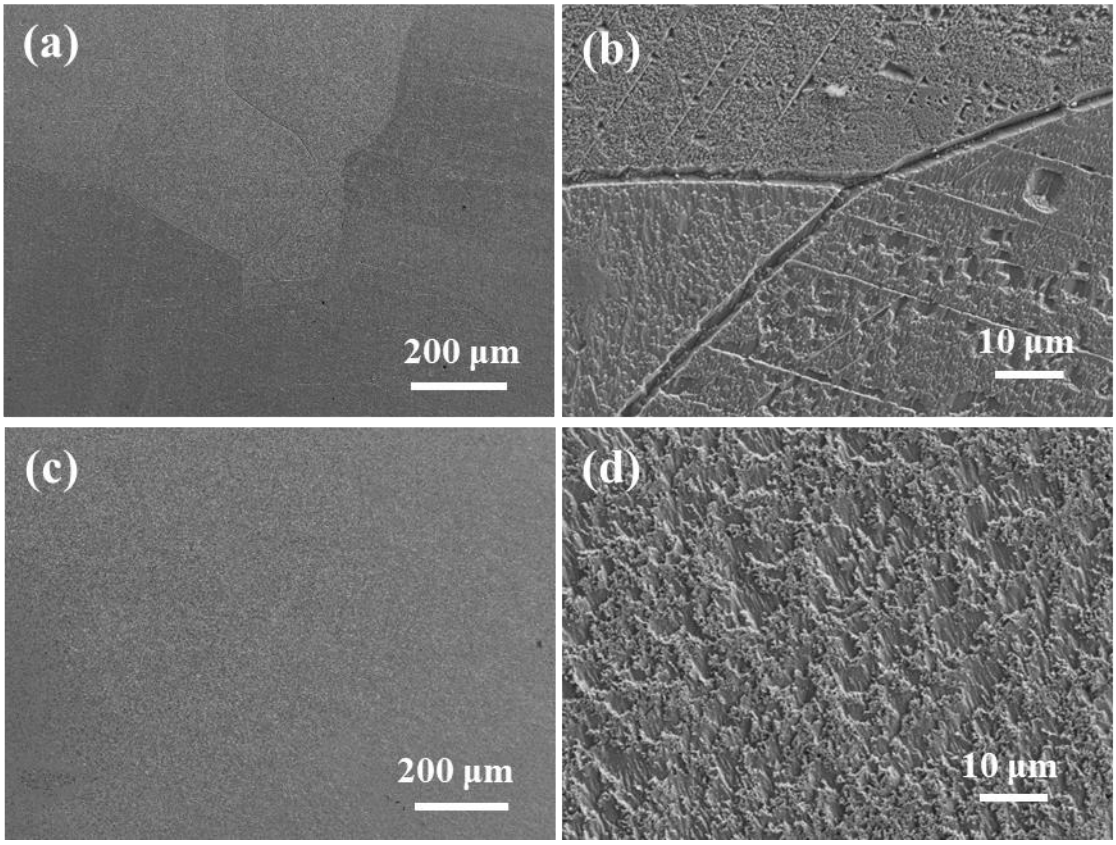

Figure 5-8 Microstructure of samples after immersion test.(a,b) Cu-4Al; (c,d) Cu-4Al/9.6 vol.% TiB_2

5.2.4 Conclusions

In summary, TiB_2 nanoparticles are dispersed in Cu-4Al to modify the microstructure and enhance its properties. The TiB_2 nanoparticles are captured in the CuAl solid solution grains possibly by Brownian capture. The TiB_2 nanoparticles induce serrated grain boundaries in the nanocomposite. The Cu-4Al/9.6 vol.% TiB_2 exhibits significantly enhanced microhardness and Young's modulus over the Cu-4Al counterpart. In addition, the severe intergranular corrosion of Cu-4Al is mitigated by the TiB_2 nanoparticles, which is anticipated to arise from the reduced grain boundary energy of serrated grain boundaries and the partially blocked dealumination by nanoparticles at the grain boundaries.

5.3 Nanoparticle-Enabled Phase Modification (Nano-Treating) of CuZrSi Pseudo-Binary Alloy

5.3.1 Introduction

There is a strong correlation between properties and microstructure in every material. For alloys that exhibit microstructures with intermetallic phases in forms of massive faceted flakes, rods, needles, *etc.*, growing directly from the melt, properties such as strength and ductility often suffer significantly. Thus, tailoring the phase morphology of as-solidified alloys to improve material properties has drawn much interest [167–171].

Traditional methods to alter the as-cast phase morphology include minor additions of chemical modifiers and solidification control [26]. One of the most well-known cases of phase modification is the transition of graphite flakes in gray cast iron to graphite spheres in nodular cast iron through the addition of Mg and Ce, which significantly increases tensile strength and ductility

[172]. By adding Eu and Yb in small amounts, the transition of eutectic Si in Al-Si alloys from plate-like to coral-like morphologies was reported to improve toughness [173]. However, modification through chemical modifiers only showed limited success towards particular alloys. On the other hand, phase modification through solidification control such as rapid cooling and application of a magnetic field or ultrasonic vibration during solidification was reported [174,175]. The size of M_7C_3 carbides was refined via fast-cooling of a hypereutectic Fe-Cr-C alloy to improve wear resistance [176,177]. High costs and limited productivity hinder the application of these solidification control processes for the mass production of engineering materials.

Incorporating nanoparticles (NPs) into molten alloys is expected to modify the alloy's phases, as the presence of nanoscale solids with large surface areas in molten alloys can change the alloy's solidification behavior. However, in literature, the volume fraction of nanoparticles that can be incorporated into molten alloys was very low, resulting in very limited modification at the micrometer scale. The addition of 1.5 vol.% $TiC_{0.5}N_{0.5}$ nanoparticles into Al-10Si by ultrasonic processing reduced the eutectic grain size and changed the aspect ratio of the Si particles within eutectic cells [27]. A nanoparticle-induced nucleation mechanism was proposed to explain the refinement due to the favorable crystallographic matching of $TiC_{0.5}N_{0.5}$ and Si [27]. The microstructural modification effect of SiC nanoparticles (0.7 wt.%) on Sn-3.0Ag-0.5Cu solder alloy was studied [30]. Primary β-Sn dendrites were refined, and the fraction of fine eutectic in the as-solidified alloy was increased. Evident morphology change and especially refinement of the intermetallic phases down to the ultrafine/nanoscale by nanoparticles during solidification has not been reported. Recently, an effective and scalable molten-salt-assisted nanoparticle incorporation method via solidification processing was developed [89]. Based on that, arc welding of aluminum alloy 7075 was enabled by nanoparticle-enabled phase control: TiC nanoparticles transformed the

primary grains from dendrites to equiaxial ones and induced fine segmented eutectic phase [159]. Besides, nanoparticle-enabled grain refinement of as-solidified pure Cu down to the ultrafine/nanoscale was discovered [90]. Thus, it is expected that more significant phase modification of the intermetallic phases can be achieved by effectively incorporating suitable nanoparticles into molten alloys.

The CuZrSi alloy is of interest because it can potentially exhibit high strength, ductility, and conductivity if its intermetallic phase is modified. The CuZrSi alloy exhibits a pseudo-binary phase diagram section between pure Cu and ZrCuSi phases as shown in Figure 5-9, with a microstructure of large rod-like ZrCuSi in the Cu matrix [178]. The eutectic Cu/ZrCuSi alloy (Cu-3.43Zr-1.05Si) contains 9.5 vol.% ZrCuSi rods, providing sufficient strong intermetallic compounds as potential reinforcements in the Cu matrix if modified [178,179]. The lattice misfit between (110) Cu and $(1\bar{1}0)$ ZrCuSi is less than 10% [178]. Directional solidification was utilized to align ZrCuSi rods in an attempt to enhance the material's properties [178]. Apart from the high cost of directional solidification, the resultant property was highly anisotropic, with a reduction in the strength transverse to the solidification direction.

Here we report the effective nano-treating to modify and refine the intermetallic phase of the cast CuZrSi alloy to the ultrafine/nanoscale. Nanocomposite masters with stabilized nanoparticles were fabricated first, which can be readily diluted to treat alloys with desired percentages of nanoparticles. Different percentages of WC nanoparticles were successfully diluted into a CuZrSi alloy. While 1 vol.% WC partially transformed the ZrCuSi phase with sizes reduced to approximately 1 μm. Morphology change of the entire ZrCuSi phase and refinement down to the ultrafine/nanoscale was achieved by 4 vol.% WC.

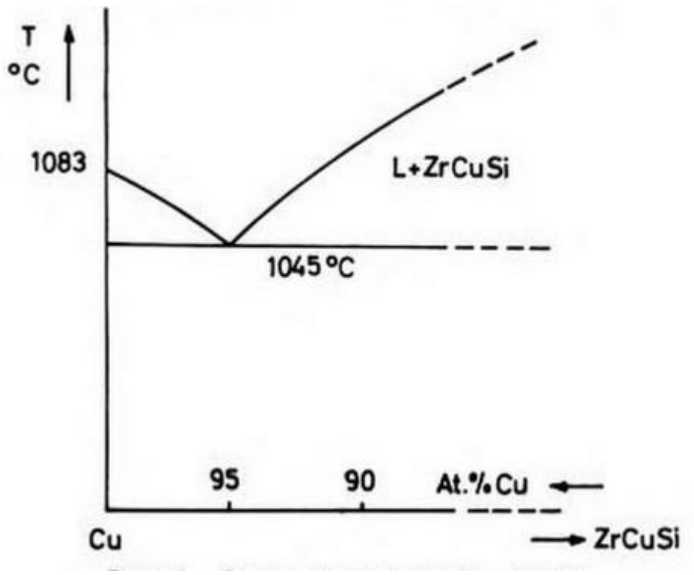

Figure 5-9 Cu-ZrCuSi pseudo-binary phase diagram

5.3.2. Materials and Methods

A Cu/5 vol.% WC nanocomposite master was fabricated by the molten-salt-assisted self-incorporation method [52,89]. Pure Cu was heated to 1230 °C in a graphite crucible by induction heating, with the surface of the melt purged with Ar gas to prevent oxidation. WC nanoparticles (US Research Nanomaterials) premixed with $KAlF_4$ powder by a mechanical shaker (SK-O330-Pro) with a volume ratio of 1:9 were loaded slowly on the surface of the melt. The molten metal/molten salt interface was disturbed by manual mixing with a graphite rod. After loading the salt-nanoparticle mixture, the melt was held for 30 min before cooling in air.

A eutectic pseudo-binary alloy (Cu-3.43Zr-1.05Si) was fabricated by melting Cu-33Zr master (Belmont Metals), Cu-10Si master (Belmont Metals), and Cu in a graphite crucible at 1200 °C using induction heating with Ar protection. Two such samples were made for comparison purposes: one was cooled in air, while the other was cooled in a Cu wedge mold. The cooling rate (R) at different positions of the copper wedge mold can be calculated by $R = \frac{4000}{d^2}\frac{Kmm^2}{s}$, where d is the

mold's thickness [180]. To nano-treat the Cu-3.43Zr-1.05Si alloy with 1 vol.% WC, pieces of the Cu/5 vol.% WC master were submerged in the melt of Cu, CuZr, and CuSi masters at 1200 ℃. The melt was then mechanically mixed with a graphite blade for 15 min and cooled to room temperature in air. To nano-treat the Cu-3.43Zr-1.05Si alloy with approximately 4 vol.% WC, a similar procedure was conducted except that no mechanical mixing was applied to avoid air entrapment, as the viscosity of the melt increased. The CuZrSi alloy composition is nominal composition in wt.%.

Specimens cut from the as-solidified bulk samples were ground, polished, and then ion milled (Gatan PIPS) at 4° and 4.5 kV for 1 h to expose the nanoparticles. The microstructure of the samples was observed by scanning electron microscopy (SEM, Zeiss Supra 40VP) equipped with energy-dispersive X-ray spectroscopy (EDS). The phase compositions of the samples were analyzed by X-ray diffraction (XRD, Bruker D8) with Cu Kα radiation and a step size of 0.02°. The microhardness of samples was measured using an LM 800AT microhardness tester with a load of 200 g and a dwell time of 10 s. Micropillars with an average size of 4.1 ± 0.1 μm in diameter and 10.7 ± 1.0 μm in height were machined by focused ion beam (FIB, FEI Nova 600) from the bulk samples. Pillar compression tests were performed at a strain rate of $5 \times 10^{-2}\ s^{-1}$ and a compression depth limit of 3 μm at room temperature by an MTS nanoindenter with a flat punch tip.

5.3.3 Results and Discussion

The microstructure of the air-cooled CuZrSi alloy is shown in Figure 5-10a. It is comprised of a rod-like intermetallic ZrCuSi phase embedded in the Cu matrix. The length of the ZrCuSi rods is 8 ± 7 μm (distribution shown in Figure 5-10b). The large size of the ZrCuSi rods can be attributed

to their rapid growth rate, as they grew directly from the melt. Meanwhile, the thickness of the sample cooled in the Cu wedge mold was measured to be 0.15 mm, with a cooling rate calculated to be $1.7 \times 10^5 K/s$. The rapidly cooled CuZrSi alloy counterpart shows a significantly refined intermetallic ZrCuSi phase, with lengths of approximately 50-400 nm (Figure 5-11, SEM in-lens image). This observation can be attributed to an increased nucleation rate and reduced growth rate due to rapid cooling.

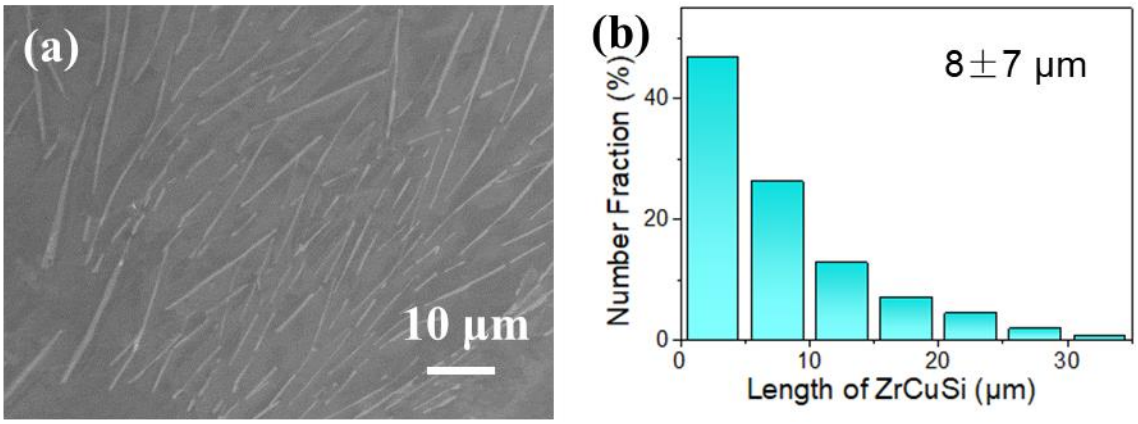

Figure 5-10 (a) Microstructure of air-cooled Cu-3.43Zr-1.05Si alloy; (b) distributions of lengths of ZrCuSi rods in (a)

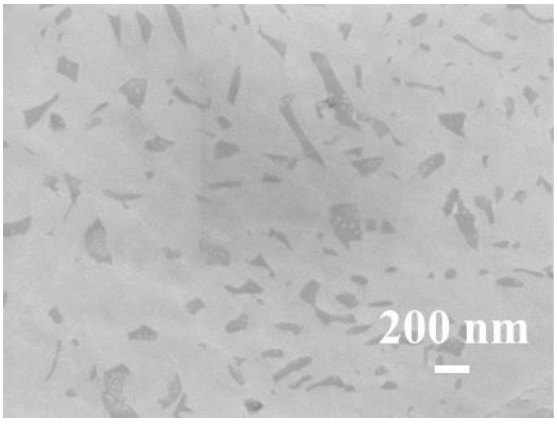

Figure 5-11 Microstructure of rapid-cooled Cu-3.43Zr-1.05Si by a Cu wedge mold

The SEM image of WC nanoparticles in the Cu matrix of the Cu/5 vol.% WC nanocomposite master is shown in Figure 5-12. While some agglomeration of nanoparticles is

observed in this sample, true clustering of nanoparticles forming microparticles did not occur. Better dispersion of WC nanoparticles in the Cu matrix by tuning the nanoparticle incorporation processing parameters has been reported [52]. The incorporation of WC nanoparticles from the molten salt into molten Cu is to reduce the system's Gibbs energy since there is lower interfacial energy between WC/molten Cu than WC/molten salt [51].

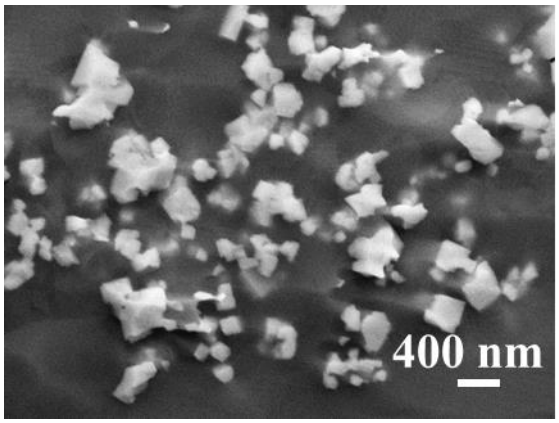

Figure 5-12 SEM image of the Cu/5 vol.% WC master

The XRD patterns of air-cooled CuZrSi samples (both the pure sample and nano-treated samples that contain 1 and 4 vol.% WC nanoparticles) are shown in Figure 5-13. For the pure CuZrSi alloy, the peaks correspond to the Cu phase and the ZrCuSi intermetallic phase, which agree well with the literature [178]. An unindexed peak at around 40.5° appears in all samples, and the possible reasons include background noise or minor phase reactions. For CuZrSi/1 vol.% WC, the XRD pattern is indexed as Cu and ZrCuSi, while WC peaks are weak due to its low volume fraction. Meanwhile, the phase composition of the CuZrSi/4 vol.% WC sample is clearly identified as Cu, ZrCuSi, and WC. Therefore, the successful incorporation of WC into the CuZrSi alloy is confirmed.

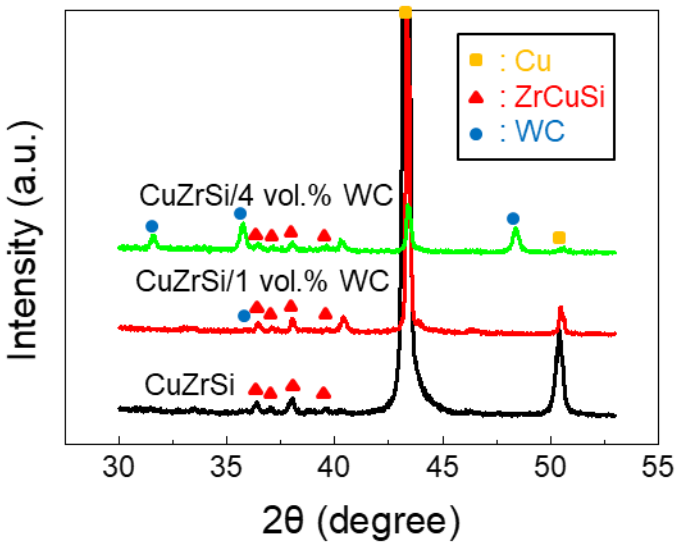

Figure 5-13 XRD patterns of original CuZrSi alloy and nano-treated CuZrSi alloy with 1 vol.% and 4 vol.% WC nanoparticles

The ZrCuSi intermetallic phase was partially modified by 1 vol.% WC nanoparticles at the micrometer scale. Figure 5-14a illustrates the microstructure of CuZrSi/1 vol.% WC, with the magnified image of the boxed area shown in Figure 5-14b. The spatial distributions of Cu, Zr, and W in Figure 5-14b are revealed by EDS mappings shown in Figure 5-14c to 5-14e. It is worth mentioning that Si is not indexed, as its characteristic peaks in EDS are too close to W. While some of the ZrCuSi rods (about 5-20 μm in length) remain, as indicated by dotted lines in Figure 5-14a, the rest is transformed into a refined and irregularly shaped microstructure growing on the surfaces of nanoparticles shown in the white circled area, forming intermetallic/nanoparticles complexes with sizes of approximately 1 μm, as indicated by the orange dotted circle in Figure 5-14b. Similar findings were reported in aluminum alloy 7075 nano-treated by 1 vol.% TiC nanoparticles. The eutectic phase and nanoparticles formed encapsulation attachment structure, and nanoparticles induced finer eutectic features at the micrometer scale [181]. It is thus believed

that, while effective, 1 vol.% WC is not enough to modify the entirety of the intermetallic phase and refine it to the ultrafine/nanoscale.

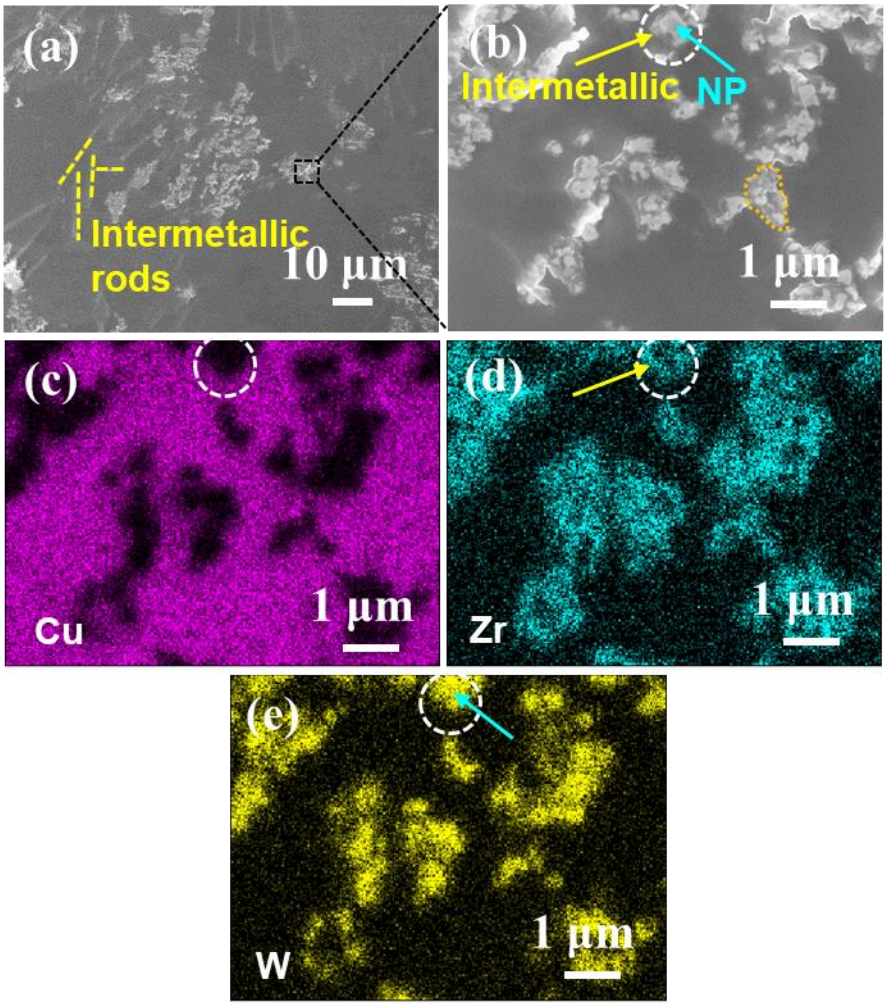

Figure 5-14 (a) Microstructure of CuZrSi alloy nano-treated by 1 vol.% WC; (b) magnified image of the boxed area in (a); (c)-(e) spatial distribution of Cu, Zr, and W in (b) by EDS mapping

Significant morphology transformation and refinement of the entire intermetallic phase (originally 8 ± 7 µm) down to the ultrafine/nanoscale was achieved upon the addition of 4 vol.% WC nanoparticles. Figure 5-15a and 5-15b illustrate the microstructure of the CuZrSi alloy nano-treated by 4 vol.% WC. No rod-shaped ZrCuSi intermetallic is observed. Instead, there is a

homogeneous distribution of irregularly shaped intermetallic/nanoparticle complexes in the Cu matrix, indicated by EDS mappings of Cu, W, and Zr (Figure 5-15c to 5-15e). Besides, the circled area in Figure 5-15b and the corresponding EDS mappings show that nanoparticles pin the growth of the intermetallic phase.

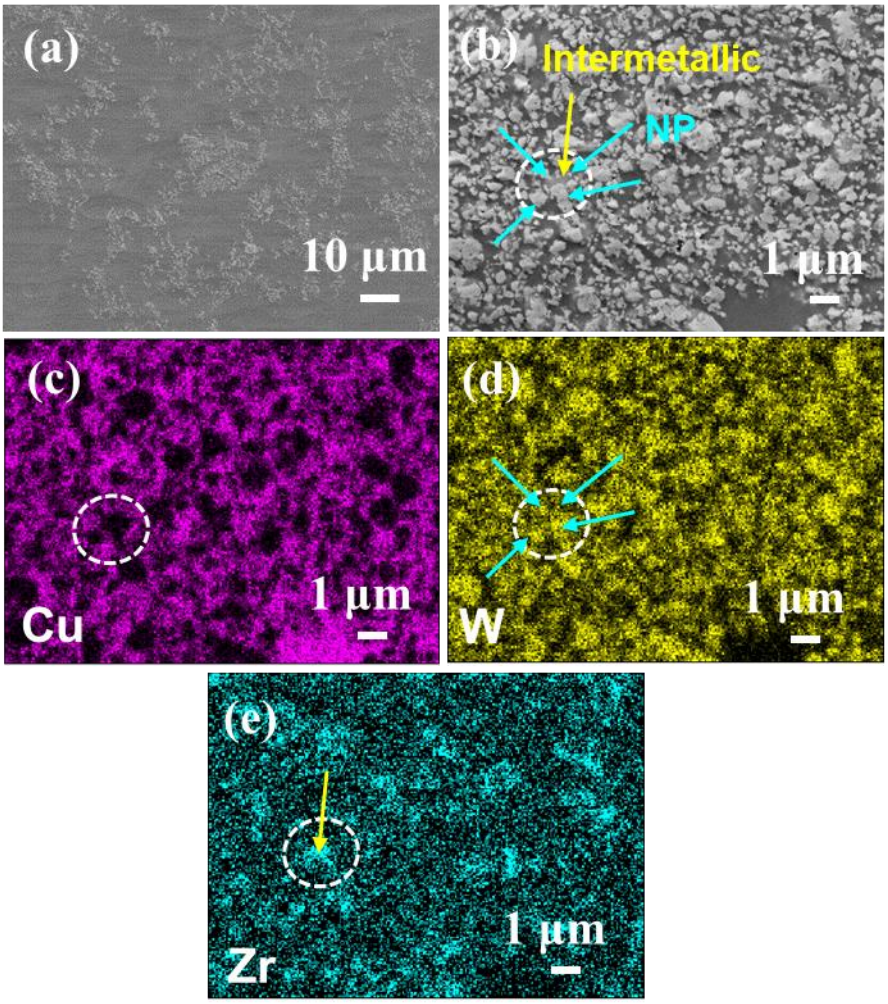

Figure 5-15 (a) Microstructure of CuZrSi alloy nano-treated by 4 vol.% WC; (b) magnified image of (a); (c)-(e) spatial distributions of Cu, W, and Zr in (b) by EDS mapping

The pseudo-dispersion of WC nanoparticles in the CuZrSi/WC samples as shown in Figure 5-15 still needs to be solved despite the effective phase modification. Here, a uniform distribution of dispersed nanoparticles in the alloy matrix is desired. The strategy to potentially alleviate the

nanoparticle agglomeration is discussed as follows. First, it is of interest to identify nanoparticles (in terms of sizes, types, *etc.*) that can form a uniform dispersion in the molten alloy based on the thermally activated nanoparticle dispersion mechanism [17]. The uniform dispersion of SiC nanoparticles in molten Mg2Zn owing to the synergy of reduced Van der Waals forces, high energy barrier preventing sintering, and thermal energy to disperse nanoparticles has been reported [17]. Second, applying ultrasonic processing to the molten alloy can further help disperse the nanoparticles.

Figure 5-16 shows a magnified image of the modified ZrCuSi intermetallic phase in CuZrSi/4 vol.% WC. The intermetallic phase is refined to the ultrafine/nanoscale, with sizes comparable to the rapidly cooled counterpart (Figure 5-11). The enhanced nucleation of ZrCuSi intermetallics is indicated by the numerous ultrafine/nanoscale intermetallics on the edges of the nanoparticles. Examples are shown in white circled areas in Figure 5-16. The confinement of ZrCuSi intermetallics by neighboring nanoparticles is revealed in red circled areas in Figure 5-16. Based on the above-mentioned microstructural observations, the hypothesis of the nanoparticle-enabled phase modification mechanism in the CuZrSi alloy is proposed as follows. WC nanoparticles act as heterogeneous nucleation sites for the intermetallic phase, enhancing the nucleation of the intermetallic phase. Moreover, the growth control of the intermetallic with a decreased growth rate is enabled by nanoparticles, which can be attributed to the following reasons. First, the decreased growth rate of eutectic grains induced by $TiC_{0.5}N_{0.5}$ nanoparticles in Sr-modified Al-Si alloy melt was reported, which arose from the increased solid-liquid surface area for the same fraction solid as the number of nucleated grains increased [27]. By the same token, the growth rate of the intermetallic phase in this study is anticipated to be decreased. Second, it was reported that the grain growth restriction factor by nanoparticles is much higher than the

chemical restriction from solute atoms [90]. Nanoparticles-enabled continuous nucleation and especially growth restriction led to the grain refinement of pure metals (Cu, Al, Zn, etc.) to the ultrafine/nanoscale [90]. Cu with 10 vol.% WC nanoparticles took an 83% longer time than pure Cu to complete solidification derived from a wider and less intense exothermic solidification peak in differential scanning calorimetry (DSC) curves, indicating a decreased growth rate enabled by nanoparticles [90]. In this study, the growth of the intermetallic phase is also effectively restricted by adjacent nanoparticles. Third, nanoparticles are inferred to partially block the transport of atoms to the growth front and hinder the transport of latent heat, thereby slowing down the phase growth.

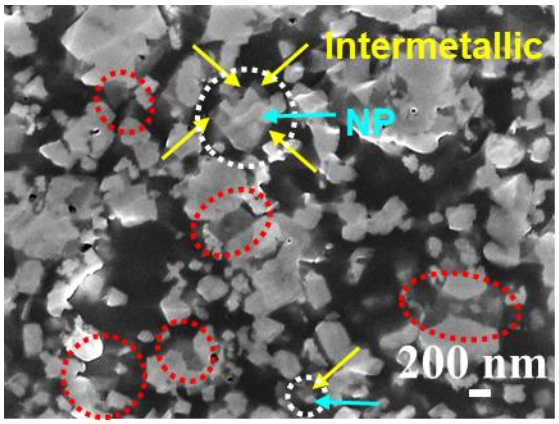

Figure 5-16 Magnified image of the nano-treated CuZrSi alloy by 4 vol.% WC

In addition to the larger number of WC nanoparticles as nucleation sites, the much more evident phase modification in the CuZrSi/4 vol.% WC sample may arise from the significantly reduced interparticle spacing. Assuming that nanoparticles are spherical and homogeneously distributed, the theoretical interparticle spacing (d) can be estimated by Equation 5-2 [90], where r is the radius of nanoparticles, and V_m is the volume fraction of the nanoparticles. For 4 vol.% WC, d is 507.6 nm while d of 1 vol.% WC is 805.8 nm. Thus, the intermetallic phase is more severely confined by the nanoparticles, leading to ultrafine/nanoscale intermetallics in CuZrSi/4 vol.% WC.

$$d = \sqrt[3]{\frac{4\pi r}{3V_m}}$$ Equation 5-2

Future work will focus on revealing more evidence for theoretical interpretations. Transmission electron microscopy (TEM) study will be conducted to provide high-resolution pictures of the intermetallic/nanoparticle nanostructures especially the interfaces and show the crystallographic orientation relationships for the lattice misfit calculation, which can indicate the potency of WC nanoparticles as heterogeneous nucleation sites for the intermetallic phase. DSC study will be conducted to compare the undercooling and the exothermic peak intensity and width of the nano-treated alloy and pure alloy for indications of the nanoparticle-induced intermetallic phase nucleation and growth. A Scheil diagram will be produced from DSC or simulation to provide insight into the modified intermetallic phase formation during solidification. It was reported that aluminum alloy 7075/1.7 vol.% TiC nanoparticles and pure 7075 showed distinct solid fraction versus temperature curves during solidification derived from DSC results [159].

The microhardness of CuZrSi/4 vol.% WC is 112.5 ± 17.5 HV, which is 43.5% higher than that of the CuZrSi counterpart (78.4 ± 5.6 HV). More importantly, it is expected that the plasticity of this nano-treated material is enhanced due to the absence of a large and sharp intermetallic phase [182]. Figure 5-17 shows the typical micropillar compression test results of pure CuZrSi alloy and CuZrSi/4 vol.% WC. Micropillars with an average size of 4.1 ± 0.1 μm in diameter and 10.7 ± 1.0 μm in height were machined to avoid obvious size effect. Figure 5-17a to 5-17c show the different phase distributions of the initial micropillars. For pure CuZrSi, since its mechanical properties depend on the orientation of the strengthening intermetallic rods, micropillars with two types of ZrCuSi distributions were machined, i.e., ZrCuSi intermetallics roughly parallel (as indicated by arrows in Figure 5-17a, denoted as ∥) and perpendicular (as indicated by arrows in Figure 5-17b, denoted as ⊥) to the compression direction. CuZrSi (∥) was expected to exhibit higher strength

than CuZrSi (⊥). Figure 5-17c shows the micropillar from the CuZrSi/4 vol.% WC, with no large rod-like intermetallics observed. The typical stress-strain curves are shown in Figure 5-17g. The strains of CuZrSi pillars increase discontinuously at an early stage, while the pillar of the nano-treated sample can sustain the load gradually to a strain over 30% without catastrophic failure. The uniform plasticity of CuZrSi (⊥), CuZrSi (∥), and nano-treated CuZrSi is 3%, 13%, and 31%, respectively, as indicated by the arrows in Figure 5-17g. Besides, the yield strength of CuZrSi (⊥), CuZrSi (∥), and nano-treated CuZrSi is 106, 128, and 530 MPa, respectively. It should be noted that the yield strength of CuZrSi/4 vol.% WC obtained from the micropillar is higher than that of the bulk sample due to the higher nanoparticle content in the micropillar.

The low plasticity of the pillars from pure CuZrSi is also indicated in the morphology of the pillars after compression, as shown by arrows in Figure 5-17d and 5-17e, where catastrophic failure and multiple slip traces are observed. For CuZrSi (∥), the main failure mode is cracking, which originated from the unmodified intermetallic phase. For CuZrSi (⊥), the main failure mode is severe slips of the Cu matrix as intermetallics induced little strengthening to the matrix when they are roughly perpendicular to the compression direction. On the contrary, as shown in Figure 5-17f and 5-17h, the pillar of CuZrSi/4 vol.% WC after compression shows no catastrophic failure with significantly fewer slip traces observed. The micropillar compression results confirm that phase modification by nanoparticles can simultaneously enhance the plasticity and strength of the CuZrSi alloy. Large and sharp intermetallics in the matrix can act as origins of cracks, induce fast crack propagation, and show limited strengthening to the matrix during deformation. Modifying and refining intermetallics by nanoparticles can effectively mitigate crack formation/propagation and impede dislocation motion to improve plasticity and strength. Tensile testing will be conducted in future work to validate the improved ductility and strength of CuZrSi/4 vol.% WC.

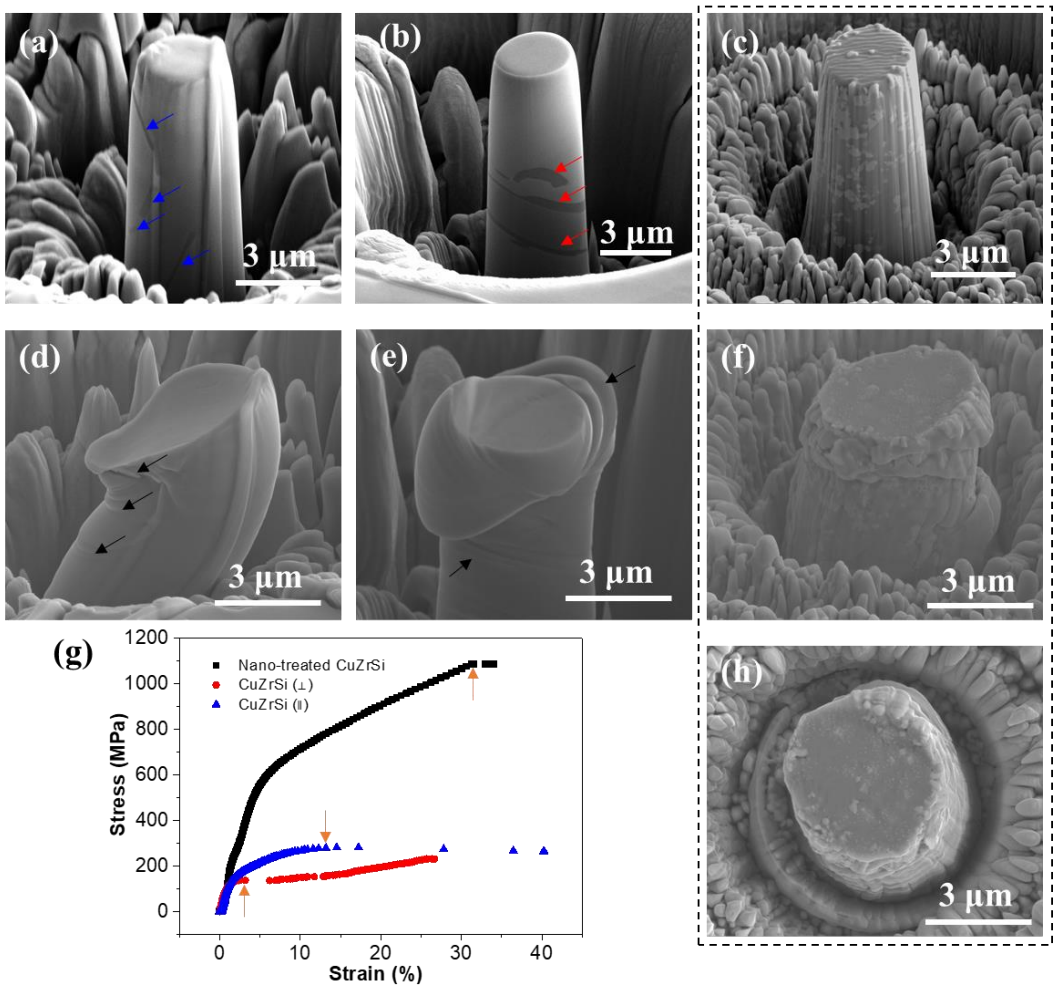

Figure 5-17 Micropillar compression of CuZrSi and CuZrSi/4 vol.% WC. SEM image taken at a tilt angle of 52° showing initial micropillar of CuZrSi with intermetallics approximately (a) parallel (denoted as ∥), (b) perpendicular (denoted as ⊥) to the compression direction, and (c) nano-treated CuZrSi; (d-f) SEM image of micropillars after compression acquired at a tilt angle of 52° of a-c; (g) stress-strain curves; (h) top view of (f)

5.3.4 Conclusions

In summary, the effectiveness of nanoparticles to modify and refine the intermetallic phase in as-cast CuZrSi alloy to the ultrafine/nanoscale is demonstrated. While 1 vol.% of WC partially transformed the ZrCuSi phase morphology at the micrometer scale, significant morphological transition and refinement of the entire ZrCuSi phase down to the ultrafine/nanoscale was observed upon addition of 4 vol.% WC nanoparticles, which may arise from increased heterogeneous nucleation sites and the enhanced growth restriction from a significantly decreased interparticle spacing. The hardness, strength, and plasticity of the CuZrSi alloy were simultaneously improved by nano-treating with 4 vol.% WC due to the effective intermetallic modification by nanoparticles. Nano-treating has great potential for modifying various alloys to achieve materials with enhanced properties.

5.4 Enhanced Aging Behavior of a CuCr Alloy by W Nanoparticles

5.4.1 Introduction

Age-hardenable copper-chromium (Cu-Cr) alloys are a class copper (Cu) alloys finding widespread applications where high strength and high conductivity are required, such as spot welding electrodes, heat exchangers, and railway contact wires [183]. Their high strength arises from the formation of nanoscale chromium (Cr) precipitates in the matrix by the aging process, while the high conductivity is attributed to the extremely low solubility of chromium (Cr) in copper (Cu) at temperatures below 500 °C [184–186]. Limited by the copper-chromium (Cu-Cr) phase diagram, the hardness/strength of the copper-chromium (Cu-Cr) alloys by precipitation-hardening have reached a certain limit. Besides, the softening of copper-chromium (Cu-Cr) alloys at elevated

temperatures due to the coarsening of precipitates and grains prevents them from being used in high-temperature environments [187].

Dispersing nanoparticles into the alloys is promising to further enhance the properties by multiple mechanisms including modifying aging behavior, refining microstructures, and inducing Orowan strengthening. Thus, incorporating suitable nanoparticles into copper-chromium (Cu-Cr) alloys is expected to modify the aging behavior and further enhance their properties. Positive results of nanoparticle effects on precipitation formation have been reported for aluminum (Al) alloys [188,189]. Incorporating titanium carbide (TiC) nanoparticles into a high-zinc Al–Zn–Mg–Cu alloy enhanced the dissolution of the secondary phase by solution heat treatment and increased the aging speed [190]. Besides, titanium carbide (TiC) nanoparticles led to the higher hardness via natural aging and better machinability of Al-Zn-Mg-Cu alloy [191].

Tungsten (W) has excellent mechanical properties (high hardness, strength, and Young's modulus) and thermal properties (high melting point, thermal stability, thermal conductivity, and a low thermal expansion coefficient) [75]. Tungsten (W) and copper (Cu) do not form a solid solution or intermetallic compounds at room temperature, which otherwise would deteriorate the electrical conductivity or ductility of copper [73]. In fact, copper (Cu) strengthened by nano-tungsten (W) dispersions also exhibits a good combination of high strength and high conductivity [192]. Moreover, tungsten (W) has a much higher electrical conductivity than common ceramic reinforcements for metals such as titanium carbide (TiC) and titanium diboride (TiB_2). Thus, tungsten (W) nanoparticles are considered a promising candidate to modify copper-chromium (Cu-Cr) alloys.

Fabrication of copper-chromium (Cu-Cr) matrix nanocomposites and the resultant property improvement by nanoparticles have been reported in literature. Cu-2 at.% Cr-1 wt.% W

nanocomposite was fabricated by high energy ball milling and spark plasma sintering, with the hardness and wear resistance increased by 5% and 44% from nanoscale tungsten (W) in the matrix [193]. Dispersed aluminum oxide (Al_2O_3) nanoparticles in Cu-4.5 weight percent chromium (Cr) was achieved by mechanical alloying and high-pressure sintering, leading to increased microhardness [194]. Adding titanium diboride (TiB_2) to copper-chromium (Cu-Cr) during mechanical alloying led to decreased grain sizes of copper (Cu) and chromium (Cr) that were less than 50 nm [195]. However, little work was reported on the aging behavior of copper-chromium (Cu-Cr) matrix nanocomposites.

In this study, Cu-1.2Cr alloy nano-treated by 2 volume percent tungsten (W) nanoparticles was fabricated. The microstructure and the improved aging behavior of Cu-Cr/W nanocomposite were studied. The underlying mechanism of the enhanced precipitation strengthening by tungsten (W) nanoparticles was discussed. This study provides new insights into the design of high-strength high-conductivity copper-chromium (Cu-Cr) alloys.

5.4.2 Materials and Methods

Copper (Cu) containing 2 volume percent tungsten (W) nanoparticles was provided by MetaLi LLC. Alloying was conducted to fabricate Cu-1.2Cr with approximately 2 volume percent tungsten (W) samples. The copper/tungsten (Cu/W) nanocomposite was heated to 1250 °C in a graphite crucible by induction heating, with the surface of the melt purged by argon (Ar) gas to prevent oxidation. Chromium (Cr) powders wrapped in copper (Cu) foil were submerged in the melt, which was then held at 1250 °C for 30 min with manual mixing before cooling to room temperature. The samples were then subjected to solution heat treatment at 1000 °C for 1 h, followed by water quenching and aging at 460 °C for different durations ranging from 0.25 h to

48 h. Cold rolling with various thickness reductions up to approximately 50% was conducted on the Cu-1.2Cr/2 vol.% W nanocomposite (aged for 0.75 h) sample and the Cu-1.2Cr (aged for 3 h) sample.

Specimens cut from the bulk samples were ground, polished, and then ion milled (Gatan PIPS) at 4° and 4.5 kV for 1 h to clean the surfaces. The microstructure of the samples was observed by scanning electron microscopy (SEM, Zeiss Supra 40VP) equipped with energy-dispersive X-ray spectroscopy (EDS). The microhardness of samples was measured using an LM 800AT microhardness tester with a load of 200 grams and a dwell time of 10 seconds.

5.4.3 Results and Discussion

The microstructure of the Cu-1.2Cr/2 volume percent tungsten (W) after solution heat treatment is shown in Figure 1. As shown in Figure 1a, the tungsten (W) nanoparticles form nanoparticle-rich zones in the matrix. The magnified images of a nanoparticle-rich zone and the alloy matrix are shown in Figure 1b and Figure 1c, respectively. Some partial sintering between adjacent tungsten (W) nanoparticles is observed, which likely occurred in the melt during alloying. The melting point of the copper-chromium (Cu-Cr) alloy increases significantly with the increment of the chromium (Cr) content. To mitigate the sintering of tungsten (W) nanoparticles, a proposed solution is to design a lower chromium (Cr) content so that the alloying temperature and time can be decreased. Besides, since approximately 0.4 wt.% chromium (Cr) can be solutionized in copper (Cu) at 1000 °C theoretically according to the Cu-Cr phase diagram as shown in Figure 5-18 [184], undissolved chromium (Cr) can be observed in the sample indicated by arrows in Figure 5-19b and Figure 5-19c. As shown in Figure 5-19d, minor spinodal decomposition between chromium (Cr) and tungsten (W) occurred, which can be attributed to the locally high concentration of

chromium (Cr) at the start of the alloying process. Chromium (Cr) and tungsten (W) do not form intermetallic compounds according to the Cr-W phase diagram, which otherwise would hurt the mechanical properties of the nanocomposites. Instead, they can only form tungsten-rich and chromium-rich solid solutions [196].

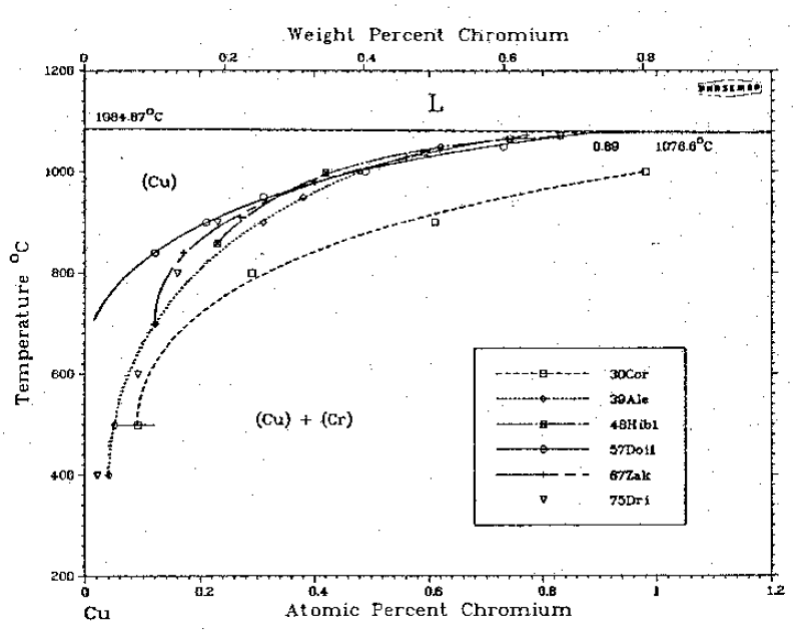

Figure 5-18 Cu-rich side of Cu-Cr phase diagram

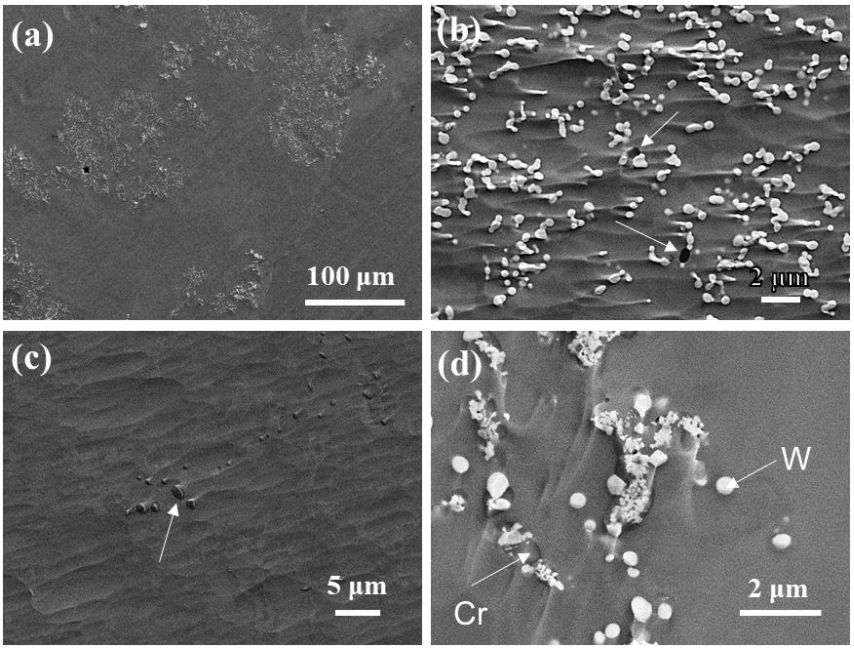

Figure 5-19 Microstructure of Cu-1.2Cr/2 volume percent W nanoparticles after solution heat treatment: (a) SEM image at low magnification; (b) SEM image of the nanoparticle-rich zone; (c) SEM image of the matrix; (d) SEM showing the locally spinodal decomposition between chromium and tungsten

The microhardness evolution with the aging time of the Cu-1.2Cr/2 vol. W sample and the Cu-1.2Cr control sample is shown in Figure 5-20. First, the pure Cu-Cr sample requires 3 h of aging to reach the peak microhardness. The Cu-1.2Cr/2 vol.% W sample reaches peak aging condition after 45-60 minutes, suggesting that tungsten (W) nanoparticles can facilitate the aging process. Second, the nanoparticle-rich zones and metal zones of the Cu-1.2Cr/2 vol.% W sample exhibit distinct aging behaviors. The nanoparticle-rich zones reach the peak condition 15 minutes earlier than the metal zones in Cu-1.2Cr/2 vol.% W, further confirming that tungsten nanoparticles accelerate aging. The facilitated aging possibly results from the enhanced heterogeneous nucleation and growth of chromium precipitates induced by the nanoparticle/matrix interfaces and the dislocations generated by nanoparticles. Atomic-scale investigation of Al-Zn-Mg-Cu matrix nanocomposite with uniformly distributed titanium diboride (TiB_2) nanoparticles revealed that the semi-coherent TiB_2/Al interfaces reduced precipitate nucleation energy barrier and acted as short-circuit diffusion paths for transporting solute atoms and vacancies to accelerate the growth rate of precipitates [197]. Despite the distinct microhardness evolution, the nanoparticle-rich zones and metal zones of the nanocomposite sample reach similar hardness at the aging time of 45 min, which will ensure the homogeneous mechanical properties of the nanocomposite sample. Thus, the optimal aging time of the Cu-1.2Cr/2 vol.% W is 45 min. The average microhardness of the Cu-Cr/W nanocomposite sample aged for 45 min and the peak-aged Cu-Cr control sample is 160.74 ± 8.22 HV and 150. 46 ± 4.34 HV, respectively. Thus, an increase of 10.28 HV in microhardness

after aging is achieved by the addition of tungsten (W) nanoparticles. The enhanced strengthening possibly results from the modified chromium (Cr) precipitate formation induced by the tungsten (W) nanoparticles, the Orowan strengthening by the tungsten (W) nanoparticles, and the Hall-Petch effect from grain refinement by W nanoparticles.

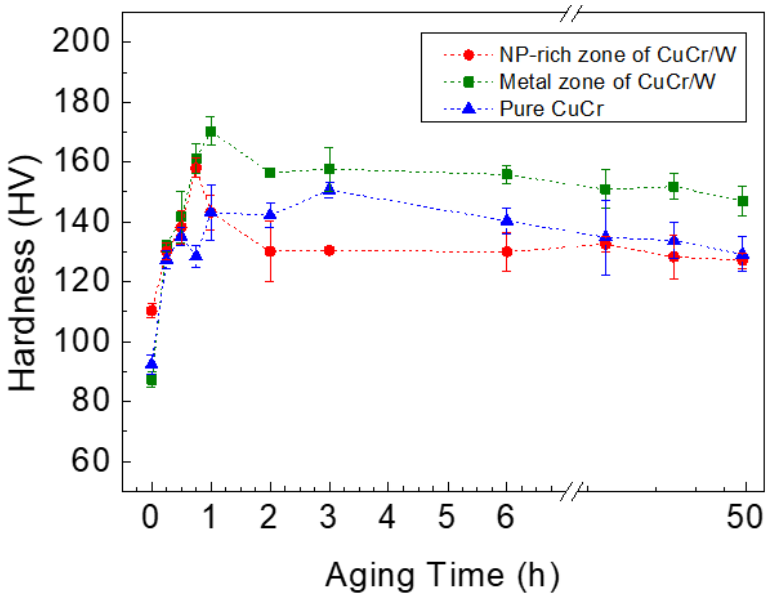

Figure 5-20 Variations of the microhardness with the aging time of the nanoparticle-rich zones and the matrix of the copper-chromium/tungsten (Cu-Cr/W) and pure copper-chromium (Cu-Cr)

The microhardness of the metal zones in Cu-Cr/W becomes notably higher than that of the nanoparticle-rich zones when the sample is over-aged starting from 1 h despite the lower hardness of the metal zones before aging. More study is still needed to explain this novel phenomenon. It is proposed that the modified chromium precipitation thermodynamics and kinetics induced by tungsten nanoparticle is responsible. The microhardness of the aged sample is related to the concentration, size, and type of the precipitates [190], which can be modified by the addition of the tungsten nanoparticles. The shape, size, orientation relationship, and phase transportation of the chromium precipitates in copper-chromium (Cu-Cr) alloys are still under discussion [185,186].

The equilibrium crystallographic structure of chromium is body-centered cubic (bcc), but it could have metastable structures in the early stage of precipitation [186]. The sequence of precipitate formation in Cu-0.71 wt% Cr aged at 450 ℃ was reported to be super-saturation solid solution, GP zones (face-centered cubic (fcc) Cr-rich phase), fcc chromium (Cr) phase, order fcc chromium (Cr) phase, and bcc chromium (Cr) phase [185]. The addition of other alloying elements, such as zirconium (Zr), magnesium (Mg), and iron (Fe) can modify the chromium (Cr) precipitation kinetics. It was reported that additional magnesium in Cu-Cr alloy accelerated the process of precipitates nucleation with enriched magnesium areas as nucleation centers and restrained the precipitate growth by magnesium segregation along the precipitate surface, which reduced the precipitate size and improved the mechanical properties [187]. For this study, the hypothesis is as follows. Chromium precipitates in nanoparticle-rich zones grew to larger sizes than those outside the nanoparticle-rich zones when overaged, due to the higher growth rate induced by the high diffusivity paths such as copper/tungsten interfaces, leading to the lower hardness in the nanoparticle-rich zones. Meanwhile, it is hypothesized that chromium precipitates with a higher number density formed in the metal zones arising from a higher chromium (Cr) solute concentration, due to possibly enhanced chromium (Cr) dissolution in solution heat treatment or changed thermodynamics by tungsten (W) nanoparticles, leading to the higher hardness.

The Cu-Cr/W nanocomposite exhibits higher thermal stability than pure Cu-Cr. Poor softening resistance of Cu-Cr alloys at elevated temperatures has been reported [187]. Extended aging of the samples leads to over-aging and decreased microhardness. In this study, the microhardness of the nano-treated Cu-Cr during prolonged aging roughly plateaus from 2 h up to 48 h. Meanwhile, the microhardness of the pure Cu-Cr shows a continuously decreasing trend when aging time extends from 3 h to 48 h. After aging at 460 ℃ for 48 h, the overall hardness of

nano-treated Cu-Cr is still higher than the control sample. The high thermal stability of nanocomposites has been reported [198]. Unlike chromium (Cr) precipitates, tungsten (W) nanoparticles are thermally stable and continuously induce strengthening in the sample even at high temperatures, which leads to the improved thermal stability of the nano-treated sample.

To indicate the evolution of chromium distribution during aging, detailed microstructural characterizations of the nano-treated Cu-Cr are shown in Figure 5-21. EDS line scan was conducted in the solutionized sample across a tungsten nanoparticle, as shown in Figure 5-21a. The corresponding counts of chromium and tungsten signals along the line are shown in Figure 5-21b. The peak of the tungsten signal coincides with the tungsten nanoparticle with only background noise in the matrix, which verifies the immiscibility of tungsten in copper. Chromium signal is detected in the alloy matrix, indicating that chromium is solutionized in the matrix. Besides, relatively high counts of chromium are detected inside the tungsten nanoparticle, indicating that some chromium is also solutionized in the tungsten nanoparticle. On the other hand, different chromium distribution is observed in the over-aged sample. The EDS line scan results across a tungsten nanoparticle in Figure 5-21c in the 48-h-aged nanocomposite sample are shown in Figure 5-21d. A chromium signal peak appears at the copper/tungsten interface, as indicated by the square in Figure 5-21c and Figure 5-21d. Although more evidence is needed especially transmission electron microscopy (TEM) analysis, it indicates that copper/tungsten interfaces can act as heterogeneous nucleation sites for chromium.

Cold rolling was applied to the optimally aged samples to further increase the microhardness. The microhardness of the Cu-Cr/W (aged for 45 min) and the pure Cu-Cr (aged for 3 h) with different thickness reductions by cold rolling is shown in Figure 5-22. Although effective hardness increase is achieved for both samples due to strain hardening, the nano-treated

Cu-Cr consistently shows a higher hardness than the pure Cu-Cr. The microhardness of both samples saturates after a thickness reduction of approximately 40%. After an approximately 40% thickness reduction, the microhardness of the nano-treated sample reaches around 194 HV. For future work, TEM study will be conducted for a fundamental understanding of the nanoparticle-induced precipitation formation and enhanced strengthening in the Cu-Cr alloy. Besides, the electrical conductivity evolution during aging will be investigated, which in turn indicates the precipitation kinetics [187]. The tensile properties of the nano-treated Cu-Cr will also be evaluated.

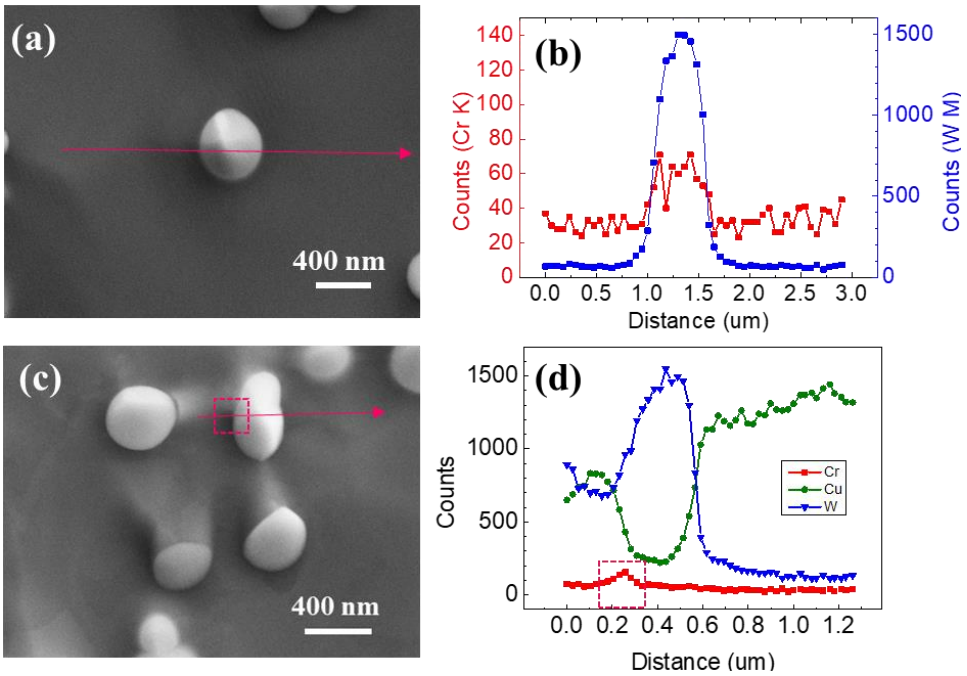

Figure 5-21 The microstructure and EDS line scan results of: (a, b) solutionized copper-chromium/tungsten (Cu-Cr/W) sample; (c, d) copper-chromium/tungsten (Cu-Cr/W) sample aged for 48 h

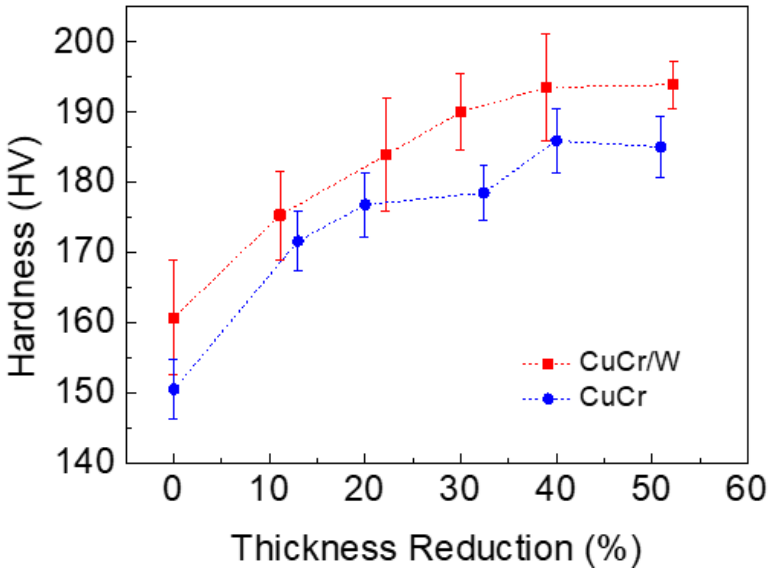

Figure 5-22 The microhardness evolution during cold rolling of copper-chromium/tungsten (Cu-Cr/W) and pure copper-chromium (Cu-Cr)

5.4.4 Conclusions

In summary, tungsten (W) nanoparticles effectively enhanced the aging behavior of Cu-1.2Cr. Incorporating 2 volume percent tungsten (W) nanoparticles to Cu-1.2Cr reduced the peak aging time significantly from 3 h to 45-60 min. Besides, a microhardness increase of 10.28 HV was achieved for the nano-treated copper-chromium (Cu-Cr) aged for 45 minutes over the peak-aged pure copper-chromium (Cu-Cr). By cold rolling, a microhardness of as high as 194 HV was obtained for the nano-treated copper-chromium (Cu-Cr). The nano-treated sample showed improved thermal stability than pure copper-chromium (Cu-Cr). This work provides a new pathway to design age-hardenable copper-chromium (Cu-Cr) alloys with improved properties beyond current limits.

Chapter 6 Conclusions

High performance (hardness, strength, electrical/thermal conductivity, Young's modulus, and corrosion resistance, etc.) copper (Cu) based materials are in strong demand in industry for numerous applications. However, it has been a long-standing challenge to achieve high performance Cu by scalable and cost-effective fabrication due to the limits of traditional metallurgy. Pure Cu is very soft and improving the mechanical properties of Cu comes at great expense of electrical and thermal conductivity. The properties of Cu alloys have reached certain limits. There are also other inherent issues of alloying: Young's modulus barely improved; softening at elevated temperatures; brittleness caused by intermetallics. Nanotechnology enabled metallurgy provides a new pathway to achieve significant performance enhancement of Cu that cannot be achieved by conventional methods. The overarching goal of this dissertation is to advance the fundamental understanding of nanoparticle effects on micro/nano-structures and properties of Cu/Cu alloys, thereby overcoming the existing limits of Cu/Cu alloys. The specific research objectives are to develop effective processing methods to synthesize and disperse nanoparticles in Cu/Cu alloys; understand nanoparticle effects and break the limits of grain refinement, phase modification, and property enhancement in Cu/Cu alloys by nanoparticles.

Effective nanoparticle synthesis and dispersion into Cu/Cu alloys was achieved by novel molten-salt assisted ex-situ and in-situ fabrication. Two ex-situ processing methods were developed to fabricate Cu matrix nanocomposites containing a wide volume fraction range of well dispersed nanoparticles. Cu/WC nanocomposites with a series of WC volume fractions were fabricated. Nanoparticles can effectively increase the hardness/strength and Young's modulus of the Cu/WC nanocomposites without significantly affecting electrical and thermal conductivity. By

tuning the WC volume percentage, different combinations of properties can be achieved for specific applications.

To enable the size control of the nanoparticles, novel in-situ synthesis of nanoparticles and Cu matrix nanocomposites were also developed. In-situ Cu/TiB_2 and Cu/W nanocomposites were fabricated. The in-situ synthesis method can enable fabrication of metals reinforced by uniformly distributed nanoparticles through conventional casting using inexpensive raw materials, which also decreases the nanoparticle size and expand the choices of nanoparticles for Cu/Cu alloys.

In-situ TiB_2 nanoparticles with an average size of 65 nm in the Cu matrix were synthesized using two fluoride salts as Ti and B precursors and Al as the reduction agent. It was also discovered that Al in molten Cu can stabilize TiB_2 nanoparticles, which otherwise do not have good wetting with molten Cu. This finding overcomes the challenge of incorporating TiB_2 nanoparticles into molten Cu. Further, a Cu-0.1Al-0.1Mg/3 vol.% TiB_2 nanocomposite was designed and fabricated by diluting CuAl/TiB_2 master and alloying. Results showed that TiB_2 nanoparticles effectively increase the hardness while causing less deterioration of the electrical conductivity compared to alloying with Al and Mg.

In addition, a novel and scalable method to fabricate Cu/W nanocomposites by casting using inexpensive WO_3 microparticles as the W precursor with salt-melt assisted in-situ reactions was developed. The size of the in-situ W nanoparticles in Cu was reduced by decreasing the reaction time and the concentration of WO_3 dissolved in the molten salt. An average size of the in-situ W nanoparticles as small as 132.7 nm was achieved. Roughly linear relationships between the Young's modulus and the microhardness of the in-situ Cu/W nanocomposites with the content of W nanoparticles were discovered.

A scalable manufacturing method was developed to fabricate bulk Cu containing high contents of uniformly distributed in-situ CrB_x particles via casting, assisted by aluminum reductions. Two sets of inexpensive raw materials as B and Cr precursors, i.e., borax-CuCr and KBF_4-CrF_3, were experimented with and compared. In-situ CrB and CrB_2 particles displayed different morphologies. It was found that the aspect ratio of the same type of in-situ CrB_x in Cu was irrelevant to the precursor types. However, using KBF_4-CrF_3, smaller boride particle sizes in the Cu matrix were achieved, due to the less severe coalescence of particles. Moreover, the in-situ fabricated Cu/CrB_x samples showed significantly enhanced mechanical property over pure Cu.

The effective grain modification in Cu was achieved. Bimodal grained Cu was fabricated via casting followed by hot rolling, with the assistance of WC nanoparticles. The heterogeneous grain structure results from the distribution of nanoparticles. As solidified Cu/WC displayed ultrafine/nanoscale Cu grains due to the enhanced heterogeneous nucleation and restriction of grain growth by nanoparticles. Hot rolling facilitated the growth of the Cu grains in the nanoparticle-sparse zones, while grains in the nanoparticle-rich zones were stable owing to the effective grain growth restriction by nanoparticles. This simple pathway can be potentially extended to other materials to advance the production of bimodal grained metals.

Moreover, it was discovered that as-cast bulk UFG Cu can be achieved by microparticles with surface nanofeatures under slow cooling. The microparticles with surface nanofeatures, which were formed by the coalescence of nanoparticles, induce substantial grain refinement down to ultrafine/nano scale. Additionally, exceptional thermal stability of the UFG/nanocrystalline Cu was revealed, showing negligible grain growth after annealing at 600 °C (0.55 T_m) for 1 h. Mechanical properties, including microhardness, strength, and Young's modulus of the UFG Cu were remarkably enhanced over pure Cu. This pathway of fabricating bulk UFG metals, assisted

by microparticles with surface nanofeatures, has the potential to be extended to other materials and greatly advance the mass production and application of UFG/nanocrystalline metals, even for high-temperature environments.

The significant phase modification of different Cu alloys (nano-treating) targeting the intermetallic phase, the solid solution, and the precipitates was achieved.

High-Al bronze (Cu-14Al) with improved ductility is enabled by dispersed TiB_2 nanoparticles. TiB_2 nanoparticles are mainly located in β phase ($AlCu_3$) and roughly separate the β phase into individual cells, surrounded by nanoparticles. The TiB_2 nanoparticles in the β phase act as preferable heterogeneous nucleation sites of the γ phase (Cu_9Al_4) during solid-state phase transformation. Moreover, phase transformation is confined in such cells surrounded by nanoparticles. Thus, the very brittle γ phase is eliminated at the grain boundaries, transformed to globular appearances, and effectively refined. The elongation of the nano-treated sample is effectively improved. It is anticipated that nano-treating of the hard but brittle high-Al bronze can expand its applications. Nano-treating has great potential for modifying brittle alloys with intermetallic phases to achieve enhanced properties.

Strong and corrosion-resistant Cu-4Al alloy is enabled by dispersed TiB_2 nanoparticles. The TiB_2 nanoparticles are captured in the CuAl solid solution grains possibly by Brownian capture. The TiB_2 nanoparticles induce serrated grain boundaries in the nanocomposite. The Cu-4Al/9.6 vol.% TiB_2 exhibits significantly enhanced microhardness and Young's modulus over the Cu-4Al counterpart. In addition, the severe intergranular corrosion of Cu-4Al is mitigated by the TiB_2 nanoparticles, which is anticipated to arise from the reduced grain boundary energy of serrated grain boundaries and the partially blocked dealumination by nanoparticles at the grain

boundaries. Thus, Cu4Al with dispersed TiB_2 nanoparticles shows much enhanced properties over the CuAl counterpart.

The effectiveness of nanoparticles to modify and refine the intermetallic phase in as-cast CuZrSi alloy to the ultrafine/nanoscale is demonstrated. While 1 vol.% of WC partially transformed the ZrCuSi phase morphology at the micrometer scale, significant morphological transition and refinement of the entire ZrCuSi phase down to the ultrafine/nanoscale was observed upon addition of 4 vol.% WC nanoparticles, which may arise from increased heterogeneous nucleation sites and the enhanced growth restriction from a significantly decreased interparticle spacing. The hardness, strength, and plasticity of the CuZrSi alloy were simultaneously improved by nano-treating with 4 vol.% WC due to the effective intermetallic modification by nanoparticles. Nano-treating has great potential for modifying various alloys to achieve materials with enhanced properties.

Tungsten (W) nanoparticles effectively enhanced the aging behavior of Cu-1.2Cr. Incorporating 2 volume percent tungsten (W) nanoparticles to Cu-1.2Cr reduced the peak aging time significantly from 3 h to 45-60 min. Besides, a microhardness increase of 10.28 HV was achieved for the nano-treated Cu-Cr aged for 45 minutes over the peak-aged pure Cu-Cr. By cold rolling, a microhardness of as high as 194 HV was obtained for the nano-treated Cu-Cr. The nano-treated sample showed improved thermal stability than pure Cu-Cr. This work provides a new pathway to design age-hardenable Cu-Cr alloys with improved properties beyond current limits.

In summary, this dissertation presents the experimental study and the fundamental understanding of nanoparticle effects on micro/nano-structures and properties of Cu/Cu alloys. The nanotechnology enabled metallurgy in Cu/Cu alloys is considerably advanced. This pathway has proven effective to break the limits of the traditional liquid metallurgy to enable high

performance Cu. It can also be readily applied to other alloy systems for the rational design of high performance materials.

Chapter 7 Recommendations for Future Work

This dissertation has advanced the fundamental understanding of nanotechnology enabled metallurgy in Cu/Cu alloys. The experimental study presented in this study has demonstrated the high performance Cu by dispersing nanoparticles into Cu/Cu alloys. Nanoparticles can strengthen the matrix, modify the grains and phases, which leads to unusual mechanical, electrical, thermal, and electrochemical properties. To further utilize nanoparticles to solve metallurgy and material processing problems, the recommended future work is as follows.

7.1 In-situ Study of Nanoparticles Enabled Grain and Phase Control

Direct observation of the grain/phase nucleation and growth modified by nanoparticles would be of great significance to verify the nanoparticles-enabled grain and phase control mechanism. Here we propose two approaches. First, the dynamic transmission electron microscope (DTEM) at LLNL is a powerful tool to investigate nucleation with nanoparticles. DTEM is a powerful tool to study transient, non-equilibrium behavior and microstructure evolution with unprecedented spatial and temporal resolutions. The DTEM uses two pulsed laser systems: one laser directed toward the specimen to initiate laser heating and one directed to a photocathode that replaces the standard thermionic emission source in the electron gun. Second, in-situ synchrotron X-ray imaging is another powerful tool to directly observe the nucleation/growth process. The time-evolved radiographs of the solidification process can be taken, which will indicate the nucleation rate and growth velocity [199]. In addition, the fraction of active nanoparticles during solidification can also be calculated.

7.2 High-strength High-conductivity Cu

High-strength high-conductivity Cu based materials exceeding the currently achieved properties are of interest to investigate. The possible route is to disperse nanoelements with different types, morphologies, distributions, and volume fractions in Cu as well as properly tuning the compositions of the matrix.

The microstructure/processing/property relationships should be established first, which will guide the rational design of high-strength high-conductivity Cu by selecting the suitable parameters.

Last but not least, theoretical models simulating the electron and phonon behavior in the Cu matrix nanocomposites should be built, which in turn can predict the electrical/thermal properties of the nanocomposites.

7.3 Laser Additive Manufacturing of Hard-to-Process Cu Assisted by Nanoparticles

To deposit dense Cu parts with desired properties has been a great challenge because of the extremely high laser reflection and thermal conductivity of Cu. The property tuning of metals by nanoparticles has proven effective in this study. Facing similar challenges, Al has been successfully deposited by laser additive manufacturing enabled by dispersed nanoparticles [198]. Thus, it is promising that the dispersed nanoparticles can also enhance the laser beam absorption of Cu during SLM. The fabrication of Cu matrix nanocomposite micropowders assisted by molten salt has been successfully developed in this study. Besides, it has been demonstrated that dispersed nanoparticles can significantly enhance mechanical performance while maintaining good thermal

and electrical properties of Cu. Thus, high-performance and complex Cu parts are expected to be built by laser additive manufacturing.

7.4 Nanoparticle-Enabled Ductility Improvement in Brittle Materials (Intermetallics and High Entropy Alloys)

There can be a trade-off between strength and ductility. Materials such as intermetallics and high-entropy alloys are strong but have limited ductility. It has been of great interest to improve the ductility of such materials. The ductility enhancement in Cu alloys by refining/modifying the intermetallic phase has been demonstrated in this study. Nanoparticles can tune the micro/nano-structures such as grains, grain boundaries, and phases in such materials. Besides, nanoparticles can also interact with dislocation during deformation. Thus, the potential ductility enhancement of intermetallics and high-entropy alloys by suitable nanoparticles will be another exciting research direction that is worth exploring.

References

[1] S.G. Jia, P. Liu, F.Z. Ren, B.H. Tian, M.S. Zheng, G.S. Zhou, Sliding wear behavior of copper alloy contact wire against copper-based strip for high-speed electrified railways, Wear. 262 (2007) 772–777. https://doi.org/10.1016/j.wear.2006.08.020.

[2] D.-P. Lu, J. Wang, W.-J. Zeng, Y. Liu, L. Lu, B.-D. Sun, Study on high-strength and high-conductivity Cu–Fe–P alloys, Mater. Sci. Eng. A. 421 (2006) 254–259. https://doi.org/10.1016/j.msea.2006.01.068.

[3] F. Huang, J. Ma, H. Ning, Y. Cao, Z. Geng, Precipitation in Cu–Ni–Si–Zn alloy for lead frame, Mater. Lett. 57 (2003) 2135–2139. https://doi.org/10.1016/S0167-577X(02)01212-0.

[4] Copper Facts, (n.d.). https://www.copper.org/education/c-facts/ (accessed March 6, 2018).

[5] J.R. Davis, Copper and copper alloys, ASM international, 2001.

[6] C. McHenry, The New Encyclopaedia Britannica, Chicago, Encyclopaedia Britannica, Inc 1150pp. (1992).

[7] C.W. D Jr, Materials science and engineering: an introduction, John Wiley Sons Inc–New York USA. (2007).

[8] N.Y. Tang, D.M.R. Taplin, G.L. Dunlop, Precipitation and aging in high-conductivity Cu–Cr alloys with additions of zirconium and magnesium, Mater. Sci. Technol. 1 (1985) 270–275.

[9] J. Ma, F. Huang, L. Huang, Z. GENG, H. NING, Z. HAN, Trends and development of copper alloys for lead frame, J. Funct. Mater. 33 (2002) 1–4.

[10] N. Takata, S.-H. Lee, N. Tsuji, Ultrafine grained copper alloy sheets having both high strength and high electric conductivity, Mater. Lett. 63 (2009) 1757–1760. https://doi.org/10.1016/j.matlet.2009.05.021.

[11] M. Liang, Y. Lu, Z. Chen, C. Li, G. Yan, C. Li, P. Zhang, Characteristics of High Strength and High Conductivity Cu-Nb Micro-Composites, IEEE Trans. Appl. Supercond. 20 (2010) 1619–1621. https://doi.org/10.1109/TASC.2009.2039703.

[12] I.J. Beyerlein, N.A. Mara, J.S. Carpenter, T. Nizolek, W.M. Mook, T.A. Wynn, R.J. McCabe, J.R. Mayeur, K. Kang, S. Zheng, J. Wang, T.M. Pollock, Interface-driven microstructure development and ultra high strength of bulk nanostructured Cu-Nb multilayers fabricated by severe plastic deformation, J. Mater. Res. 28 (2013) 1799–1812. https://doi.org/10.1557/jmr.2013.21.

[13] Y. Sakai, K. Inoue, T. Asano, H. Maeda, Development of a high strength, high conductivity copper-silver alloy for pulsed magnets, IEEE Trans. Magn. 28 (1992) 888–891. https://doi.org/10.1109/20.120021.

[14] J.H. Kim, J.H. Yun, Y.H. Park, K.M. Cho, I.D. Choi, I.M. Park, Manufacturing of Cu-TiB2 composites by turbulent in situ mixing process, Mater. Sci. Eng. A. 449–451 (2007) 1018–1021. https://doi.org/10.1016/j.msea.2006.02.302.

[15] X.J. Liu, Z.P. Jiang, C.P. Wang, K. Ishida, Experimental determination and thermodynamic calculation of the phase equilibria in the Cu–Cr–Nb and Cu–Cr–Co systems, J. Alloys Compd. 478 (2009) 287–296.

[16] L. Lu, Y. Shen, X. Chen, L. Qian, K. Lu, Ultrahigh Strength and High Electrical Conductivity in Copper, Science. 304 (2004) 422–426. https://doi.org/10.1126/science.1092905.

[17] L.-Y. Chen, J.-Q. Xu, H. Choi, M. Pozuelo, X. Ma, S. Bhowmick, J.-M. Yang, S. Mathaudhu, X.-C. Li, Processing and properties of magnesium containing a dense uniform dispersion of nanoparticles, Nat. Lond. 528 (2015) 539-543E. http://dx.doi.org/10.1038/nature16445.
[18] V.C. Nardone, K.M. Prewo, On the strength of discontinuous silicon carbide reinforced aluminum composites, Scr. Metall. 20 (1986) 43–48.
[19] D. Hull, D.J. Bacon, Introduction to dislocations, Butterworth-Heinemann, 2001.
[20] R. Casati, M. Vedani, Metal matrix composites reinforced by nano-particles—a review, Metals. 4 (2014) 65–83.
[21] J. Wang, A. Horsfield, U. Schwingenschlögl, P.D. Lee, Heterogeneous nucleation of solid Al from the melt by ${\text{TiB}}_{2}$ and ${\text{Al}}_{3}\text{Ti}$: An ab initio molecular dynamics study, Phys. Rev. B. 82 (2010) 184203. https://doi.org/10.1103/PhysRevB.82.184203.
[22] B. Cantor, Heterogeneous nucleation and adsorption, Philos. Trans. R. Soc. Lond. Math. Phys. Eng. Sci. 361 (2003) 409–417. https://doi.org/10.1098/rsta.2002.1137.
[23] A.L. Greer, Overview: Application of heterogeneous nucleation in grain-refining of metals, J. Chem. Phys. 145 (2016) 211704. https://doi.org/10.1063/1.4968846.
[24] J.A. Patchett, G.J. Abbaschian, Grain refinement of copper by the addition of iron and by electromagnetic stirring, Metall. Trans. B. 16 (1985) 505–511. https://doi.org/10.1007/BF02654849.
[25] Z. Yan, M. Chen, J. Yang, L. Yang, H. Gao, Grain Refinement of CuNi10Fe1Mn Alloy by SiC Nanoparticles and Electromagnetic Stirring, Mater. Manuf. Process. 28 (2013) 957–961. https://doi.org/10.1080/10426914.2013.763971.
[26] S.-Z. Lu, A. Hellawell, The mechanism of silicon modification in aluminum-silicon alloys: Impurity induced twinning, Metall. Trans. A. 18 (1987) 1721–1733. https://doi.org/10.1007/BF02646204.
[27] K. Wang, H.Y. Jiang, Q.D. Wang, B. Ye, W.J. Ding, Nanoparticle-induced nucleation of eutectic silicon in hypoeutectic Al-Si alloy, Mater. Charact. 117 (2016) 41–46. https://doi.org/10.1016/j.matchar.2016.04.016.
[28] J. Li, F.S. Hage, X. Liu, Q. Ramasse, P. Schumacher, Revealing heterogeneous nucleation of primary Si and eutectic Si by AlP in hypereutectic Al-Si alloys, Sci. Rep. 6 (2016) 25244. https://doi.org/10.1038/srep25244.
[29] J. Zhang, Z. Fan, Y.Q. Wang, B.L. Zhou, Microstructural development of Al–15wt.%Mg2Si in situ composite with mischmetal addition, Mater. Sci. Eng. A. 281 (2000) 104–112. https://doi.org/10.1016/S0921-5093(99)00732-7.
[30] A.A. El-Daly, W.M. Desoky, T.A. Elmosalami, M.G. El-Shaarawy, A.M. Abdraboh, Microstructural modifications and properties of SiC nanoparticles-reinforced Sn–3.0Ag–0.5Cu solder alloy, Mater. Des. 1980-2015. 65 (2015) 1196–1204. https://doi.org/10.1016/j.matdes.2014.08.058.
[31] Y.L. Yang, Y.D. Wang, Y. Ren, C.S. He, J.N. Deng, J. Nan, J.G. Chen, L. Zuo, Single-walled carbon nanotube-reinforced copper composite coatings prepared by electrodeposition under ultrasonic field, Mater. Lett. 62 (2008) 47–50.
[32] D.W. Lee, B.K. Kim, Nanostructured Cu–Al2O3 composite produced by thermochemical process for electrode application, Mater. Lett. 58 (2004) 378–383.

[33] X.-H. Zhang, X.-X. Li, H. Chen, T.-B. Li, W. Su, S.-D. Guo, Investigation on microstructure and properties of Cu–Al2O3 composites fabricated by a novel in-situ reactive synthesis, Mater. Des. 92 (2016) 58–63.
[34] M. Zebarjadi, G. Joshi, G. Zhu, B. Yu, A. Minnich, Y. Lan, X. Wang, M. Dresselhaus, Z. Ren, G. Chen, Power factor enhancement by modulation doping in bulk nanocomposites, Nano Lett. 11 (2011) 2225–2230.
[35] M. Liu, Y. Ma, H. Wu, R.Y. Wang, Metal Matrix–Metal Nanoparticle Composites with Tunable Melting Temperature and High Thermal Conductivity for Phase-Change Thermal Storage, ACS Nano. 9 (2015) 1341–1351. https://doi.org/10.1021/nn505328j.
[36] L.-Y. Chen, H. Konishi, A. Fehrenbacher, C. Ma, J.-Q. Xu, H. Choi, H.-F. Xu, F.E. Pfefferkorn, X.-C. Li, Novel nanoprocessing route for bulk graphene nanoplatelets reinforced metal matrix nanocomposites, Scr. Mater. 67 (2012) 29–32.
[37] P.K. Rohatgi, B. Schultz, Lightweight metal matrix nanocomposites–stretching the boundaries of metals, Mater. Matters. 2 (2007) 16–20.
[38] M.-J. Wang, L.-Y. Zhang, X.-Y. Liu, Study on WC dispersion-strengthened copper, Rare Met. 23 (2004) 120–125.
[39] J. Khosravi, M.K.B. Givi, M. Barmouz, A. Rahi, Microstructural, mechanical, and thermophysical characterization of Cu/WC composite layers fabricated via friction stir processing, Int. J. Adv. Manuf. Technol. 74 (2014) 1087–1096.
[40] X. Yang, S. Liang, X. Wang, P. Xiao, Z. Fan, Effect of WC and CeO 2 on microstructure and properties of W–Cu electrical contact material, Int. J. Refract. Met. Hard Mater. 28 (2010) 305–311.
[41] D. Gu, Y. Shen, Influence of reinforcement weight fraction on microstructure and properties of submicron WC–Co p/Cu bulk MMCs prepared by direct laser sintering, J. Alloys Compd. 431 (2007) 112–120.
[42] C. Portesi, S. Borini, G. Amato, E. Monticone, Fabrication of superconducting MgB2 nanostructures by an electron beam lithography-based technique, J. Appl. Phys. 99 (2006) 066115. https://doi.org/10.1063/1.2183392.
[43] S. Carenco, D. Portehault, C. Boissière, N. Mézailles, C. Sanchez, Nanoscaled Metal Borides and Phosphides: Recent Developments and Perspectives, Chem. Rev. 113 (2013) 7981–8065. https://doi.org/10.1021/cr400020d.
[44] M.X. Guo, M.P. Wang, K. Shen, L.F. Cao, Z. Li, Z. Zhang, Synthesis of nano TiB2 particles in copper matrix by in situ reaction of double-beam melts, J. Alloys Compd. 460 (2008) 585–589.
[45] G. Kaptay, S.A. Kuznetsov, Electrochemical synthesis of refractory borides from molten salts, Plasmas Ions. 2 (1999) 45–56. https://doi.org/10.1016/S1288-3255(00)87686-8.
[46] J. Ma, Y. Du, M. Wu, G. Li, Z. Feng, M. Guo, Y. Sun, W. Song, M. Lin, X. Guo, A simple inorganic-solvent-thermal route to nanocrystalline niobium diboride, J. Alloys Compd. 468 (2009) 473–476. https://doi.org/10.1016/j.jallcom.2008.01.021.
[47] Y. Gu, Y. Qian, L. Chen, F. Zhou, A mild solvothermal route to nanocrystalline titanium diboride, J. Alloys Compd. 352 (2003) 325–327. https://doi.org/10.1016/S0925-8388(02)01173-8.
[48] S.E. Kravchenko, V.I. Torbov, S.P. Shilkin, Preparation of titanium diboride nanopowder, Inorg. Mater. 46 (2010) 614–616. https://doi.org/10.1134/S0020168510060105.
[49] H.-C. Eun, H.-C. Yang, Y.-Z. Cho, H.-S. Lee, I.-T. Kim, Study on a vacuum distillation of LiCl-KCl eutectic salts containing rare earth oxidative precipitates, (2008).

[50] D. Portehault, S. Devi, P. Beaunier, C. Gervais, C. Giordano, C. Sanchez, M. Antonietti, A General Solution Route toward Metal Boride Nanocrystals, Angew. Chem. Int. Ed. 50 (2011) 3262–3265. https://doi.org/10.1002/anie.201006810.
[51] G. Yao, C. Cao, S. Pan, T.-C. Lin, M. Sokoluk, X. Li, High-performance copper reinforced with dispersed nanoparticles, J. Mater. Sci. 54 (2019) 4423–4432. https://doi.org/10.1007/s10853-018-3152-0.
[52] C. Cao, G. Yao, M. Sokoluk, X. Li, Molten salt-assisted processing of nanoparticle-reinforced Cu, Mater. Sci. Eng. A. (2020) 139345. https://doi.org/10.1016/j.msea.2020.139345.
[53] G. Yao, J. Yuan, S. Pan, Z. Guan, C. Cao, X. Li, Casting In-Situ Cu/CrBx Composites via Aluminum-Assisted Reduction, Procedia Manuf. 48 (2020) 320–324. https://doi.org/10.1016/j.promfg.2020.05.053.
[54] G. Yao, C. Cao, S. Pan, J. Yuan, I. De Rosa, X. Li, Thermally stable ultrafine grained copper induced by CrB/CrB2 microparticles with surface nanofeatures via regular casting, J. Mater. Sci. Technol. 58 (2020) 55–62. https://doi.org/10.1016/j.jmst.2020.03.052.
[55] L.-Y. Chen, H. Konishi, A. Fehrenbacher, C. Ma, J.-Q. Xu, H. Choi, H.-F. Xu, F.E. Pfefferkorn, X.-C. Li, Novel nanoprocessing route for bulk graphene nanoplatelets reinforced metal matrix nanocomposites, Scr. Mater. 67 (2012) 29–32. https://doi.org/10.1016/j.scriptamat.2012.03.013.
[56] G.C. Yao, Q.S. Mei, J.Y. Li, C.L. Li, Y. Ma, F. Chen, M. Liu, Cu/C composites with a good combination of hardness and electrical conductivity fabricated from Cu and graphite by accumulative roll-bonding, Mater. Des. 110 (2016) 124–129. https://doi.org/10.1016/j.matdes.2016.07.129.
[57] H.O. Pierson, Handbook of Refractory Carbides & Nitrides: Properties, Characteristics, Processing and Apps., William Andrew, 1996.
[58] J.R. Davis, Copper and copper alloys, ASM international, 2001.
[59] S. Pan, J. Yuan, P. Zhang, M. Sokoluk, G. Yao, X. Li, Effect of electron concentration on electrical conductivity in in situ Al-TiB2 nanocomposites, Appl. Phys. Lett. 116 (2020) 014102. https://doi.org/10.1063/1.5129817.
[60] S. Pan, Z. Guan, G. Yao, C. Cao, X. Li, Study on electrical behavior of copper and its alloys containing dispersed nanoparticles, Curr. Appl. Phys. (2019).
[61] Z. Yu, H. Zhu, J. Huang, J. Li, Z. Xie, Processing and characterization of in-situ ultrafine TiB2-Cu composites from Ti-B-Cu system, Powder Technol. 320 (2017) 66–72. https://doi.org/10.1016/j.powtec.2017.07.036.
[62] Y.-S. Kwon, D.V. Dudina, M.A. Korchagin, O.I. Lomovsky, Microstructure changes in TiB2-Cu nanocomposite under sintering, J. Mater. Sci. 39 (2004) 5325–5331. https://doi.org/10.1023/B:JMSC.0000039238.31362.93.
[63] D.V. Dudina, O.I. Lomovsky, Ì.À. Korchagin, Reactions in a Metal Matrix: Synthesis and Properties of TiB2 – Cu Nanocomposites, (n.d.) 7.
[64] N. El-Mahallawy, M.A. Taha, A.E.W. Jarfors, H. Fredriksson, On the reaction between aluminium, K2TiF6 and KBF4, J. Alloys Compd. 292 (1999) 221–229. https://doi.org/10.1016/S0925-8388(99)00294-7.
[65] J. Fjellstedt, A.E.W. Jarfors, On the precipitation of TiB2 in aluminum melts from the reaction with KBF4 and K2TiF6, Mater. Sci. Eng. A. 413–414 (2005) 527–532. https://doi.org/10.1016/j.msea.2005.09.054.

[66] J. Nie, Y. Wu, P. Li, H. Li, X. Liu, Morphological evolution of TiC from octahedron to cube induced by elemental nickel, CrystEngComm. 14 (2012) 2213–2221. https://doi.org/10.1039/C1CE06205K.
[67] T. Zhang, Z. Li, K. Feng, H. Kokawa, Y. Wu, Microstructure evolution and properties of in situ synthesized TiB2-reinforced aluminum alloy by laser surface alloying, J. Mater. Res. 33 (2018) 4307–4316. https://doi.org/10.1557/jmr.2018.413.
[68] J. Sun, X. Wang, L. Guo, X. Zhang, H. Wang, Synthesis of nanoscale spherical TiB2 particles in Al matrix by regulating Sc contents, J. Mater. Res. 34 (2019) 1258–1265. https://doi.org/10.1557/jmr.2018.469.
[69] N. Eustathopoulos, M.G. Nicholas, B. Drevet, Wettability at high temperatures, Elsevier, 1999.
[70] N. Eustathopoulos, Wetting by Liquid Metals—Application in Materials Processing: The Contribution of the Grenoble Group, Metals. 5 (2015) 350–370. https://doi.org/10.3390/met5010350.
[71] CuMg0,2, (n.d.). http://www.conductivity-app.org/alloy-sheet/12 (accessed December 3, 2020).
[72] T. Raghu, R. Sundaresan, P. Ramakrishnan, T.R. Rama Mohan, Synthesis of nanocrystalline copper–tungsten alloys by mechanical alloying, Mater. Sci. Eng. A. 304–306 (2001) 438–441. https://doi.org/10.1016/S0921-5093(00)01444-1.
[73] T. Xie, J. Zhu, L. Fu, R. Zhang, N. Li, M. Yang, J. Wang, W. Qin, W. Yang, D. Li, L. Zhou, The evolution of hardness in Cu-W alloy thin films, Mater. Sci. Eng. A. 729 (2018) 170–177. https://doi.org/10.1016/j.msea.2018.05.035.
[74] J. Zhang, Y. Huang, Y. Liu, Z. Wang, Direct diffusion bonding of immiscible tungsten and copper at temperature close to Copper's melting point, Mater. Des. 137 (2018) 473–480. https://doi.org/10.1016/j.matdes.2017.10.052.
[75] C. Hou, X. Song, F. Tang, Y. Li, L. Cao, J. Wang, Z. Nie, W–Cu composites with submicron- and nanostructures: progress and challenges, NPG Asia Mater. 11 (2019) 1–20. https://doi.org/10.1038/s41427-019-0179-x.
[76] L.L. Dong, M. Ahangarkani, W.G. Chen, Y.S. Zhang, Recent progress in development of tungsten-copper composites: Fabrication, modification and applications, Int. J. Refract. Met. Hard Mater. 75 (2018) 30–42. https://doi.org/10.1016/j.ijrmhm.2018.03.014.
[77] Y.X. Zhou, Y.L. Xue, K. Zhou, Failure analysis of arc ablated tungsten-copper electrical contacts, Vacuum. 164 (2019) 390–395. https://doi.org/10.1016/j.vacuum.2019.03.052.
[78] B. Li, Z. Sun, G. Hou, P. Hu, F. Yuan, Fabrication of fine-grained W-Cu composites with high hardness, J. Alloys Compd. 766 (2018) 204–214. https://doi.org/10.1016/j.jallcom.2018.06.338.
[79] N. Selvakumar, S.C. Vettivel, Thermal, electrical and wear behavior of sintered Cu–W nanocomposite, Mater. Des. 46 (2013) 16–25. https://doi.org/10.1016/j.matdes.2012.09.055.
[80] T. Venugopal, K.P. Rao, B.S. Murty, Synthesis of Cu-W Nanocomposite by High-Energy Ball Milling, (2007). https://doi.org/info:doi/10.1166/jnn.2007.418.
[81] S.V. Aydinyan, H.V. Kirakosyan, M.K. Zakaryan, L.S. Abovyan, S.L. Kharatyan, A. Peikrishvili, G. Mamniashvili, B. Godibadze, E.Sh. Chagelishvili, D.R. Lesuer, M. Gutierrez, Fabrication of Cu-W Nanocomposites by Integration of Self-Propagating High-Temperature Synthesis and Hot Explosive Consolidation Technologies, Eurasian Chem.-Technol. J. 20 (2018) 301–309.

[82] A. Elsayed, W. Li, O.A. El Kady, W.M. Daoush, E.A. Olevsky, R.M. German, Experimental investigations on the synthesis of W–Cu nanocomposite through spark plasma sintering, J. Alloys Compd. 639 (2015) 373–380. https://doi.org/10.1016/j.jallcom.2015.03.183.
[83] Z. Wang, X. Li, J. Zhu, F. Mo, C. Zhao, L. Wang, Dynamic consolidation of W–Cu nanocomposites from W–CuO powder mixture, Mater. Sci. Eng. A. 527 (2010) 6098–6101. https://doi.org/10.1016/j.msea.2010.05.077.
[84] W.M. Daoush, J. Yao, M. Shamma, K. Morsi, Ultra-rapid processing of high-hardness tungsten–copper nanocomposites, Scr. Mater. 113 (2016) 246–249. https://doi.org/10.1016/j.scriptamat.2015.11.012.
[85] A.V. Druzhinin, D. Ariosa, S. Siol, N. Ott, B.B. Straumal, J. Janczak-Rusch, L.P.H. Jeurgens, C. Cancellieri, Effect of the individual layer thickness on the transformation of Cu/W nano-multilayers into nanocomposites, Materialia. 7 (2019) 100400. https://doi.org/10.1016/j.mtla.2019.100400.
[86] A. Chu, Z. Wang, Rafi-ud-din, Y. Dong, C. Guo, W. Liu, H. Xu, L. Wang, Citric acid-assisted combustion-nitridation-denitridation synthesis of well-distributed W-Cu nanocomposite powders, Int. J. Refract. Met. Hard Mater. 70 (2018) 232–238. https://doi.org/10.1016/j.ijrmhm.2017.10.016.
[87] X. Wang, S. Wei, L. Xu, J. Li, X. Li, K. Shan, Preparation of w–cu nano-composite powders with high copper content using a chemical co-deposition technique, Adv. Powder Technol. 29 (2018) 1323–1330. https://doi.org/10.1016/j.apt.2018.02.027.
[88] T. Lu, C. Chen, Z. Guo, P. Li, M. Guo, Tungsten nanoparticle-strengthened copper composite prepared by a sol-gel method and in-situ reaction, Int. J. Miner. Metall. Mater. 26 (2019) 1477–1483. https://doi.org/10.1007/s12613-019-1889-3.
[89] W. Liu, C. Cao, J. Xu, X. Wang, X. Li, Molten salt assisted solidification nanoprocessing of Al-TiC nanocomposites, Mater. Lett. 185 (2016) 392–395. https://doi.org/10.1016/j.matlet.2016.09.023.
[90] C. Cao, G. Yao, L. Jiang, M. Sokoluk, X. Wang, J. Ciston, A. Javadi, Z. Guan, I.D. Rosa, W. Xie, E.J. Lavernia, J.M. Schoenung, X. Li, Bulk ultrafine grained/nanocrystalline metals via slow cooling, Sci. Adv. 5 (2019) eaaw2398. https://doi.org/10.1126/sciadv.aaw2398.
[91] S. Pan, G. Yao, M. Sokoluk, Z. Guan, X. Li, Enhanced thermal stability in Cu-40 wt% Zn/WC nanocomposite, Mater. Des. 180 (2019) 107964. https://doi.org/10.1016/j.matdes.2019.107964.
[92] T. Ishitsuka, K. Nose, Solubility study on protective oxide films in molten chlorides created by refuse incineration environment, Mater. Corros. 51 (2000) 177–181. https://doi.org/10.1002/(SICI)1521-4176(200003)51:3<177::AID-MACO177>3.0.CO;2-O.
[93] X. Wang, S. Wei, L. Xu, F. Fang, J. Li, K. Pan, B. Peng, Effect of sintering temperature on fine-grained Cu W composites with high copper, Mater. Charact. 153 (2019) 121–127. https://doi.org/10.1016/j.matchar.2019.04.017.
[94] X. Liu, N. Fechler, M. Antonietti, Salt melt synthesis of ceramics, semiconductors and carbon nanostructures, Chem. Soc. Rev. 42 (2013) 8237–8265. https://doi.org/10.1039/C3CS60159E.
[95] T. Amietszajew, S. Seetharaman, R. Bhagat, The Solubility of Specific Metal Oxides in Molten Borate Glass, J. Am. Ceram. Soc. 98 (2015) 2984–2987. https://doi.org/10.1111/jace.13801.
[96] L.-Y. Chen, J.-Q. Xu, H. Choi, H. Konishi, S. Jin, X.-C. Li, Rapid control of phase growth by nanoparticles, Nat. Commun. 5 (2014) 3879. https://doi.org/10.1038/ncomms4879.

[97] M.A. Atwater, D. Roy, K.A. Darling, B.G. Butler, R.O. Scattergood, C.C. Koch, The thermal stability of nanocrystalline copper cryogenically milled with tungsten, Mater. Sci. Eng. A. 558 (2012) 226–233. https://doi.org/10.1016/j.msea.2012.07.117.
[98] Z. Fan, P. Tsakiropoulos, A.P. Miodownik, Prediction of Young's modulus of particulate two phase composites, Mater. Sci. Technol. 8 (1992) 922–929. https://doi.org/10.1179/mst.1992.8.10.922.
[99] Y. Gao, T. Yang, J. Xue, S. Yan, S. Zhou, Y. Wang, D.T.K. Kwok, P.K. Chu, Y. Zhang, Radiation tolerance of Cu/W multilayered nanocomposites, J. Nucl. Mater. 413 (2011) 11–15. https://doi.org/10.1016/j.jnucmat.2011.03.030.
[100] A. Javadi, S. Pan, C. Cao, G. Yao, X. Li, Facile synthesis of 10 nm surface clean TiB2 nanoparticles, Mater. Lett. 229 (2018) 107–110. https://doi.org/10.1016/j.matlet.2018.06.054.
[101] P.R. Jothi, K. Yubuta, B.P.T. Fokwa, A Simple, General Synthetic Route toward Nanoscale Transition Metal Borides, Adv. Mater. 30 (2018) 1704181. https://doi.org/10.1002/adma.201704181.
[102] A. Piasecki, M. Kotkowiak, N. Makuch, M. Kulka, Wear behavior of self-lubricating boride layers produced on Inconel 600-alloy by laser alloying, Wear. 426–427 (2019) 919–933. https://doi.org/10.1016/j.wear.2018.12.026.
[103] B. Wang, D.Y. Wang, Z. Cheng, X. Wang, Y.X. Wang, Phase Stability and Elastic Properties of Chromium Borides with Various Stoichiometries, ChemPhysChem. 14 (2013) 1245–1255. https://doi.org/10.1002/cphc.201201009.
[104] P.M. Kumar, K. Sivakumar, N. Jayakumar, Surface Modification on OHNS Steel Using Cu-CrB2 Green Compact Electrode in EDM, Mater. Today Proc. 5 (2018) 17389–17395. https://doi.org/10.1016/j.matpr.2018.04.152.
[105] M.A. Morris, D.G. Morris, Microstructural refinement and associated strength of copper alloys obtained by mechanical alloying, Mater. Sci. Eng. A. 111 (1989) 115–127. https://doi.org/10.1016/0921-5093(89)90204-9.
[106] J.S. Lee, C.M. Wayman, Grain refinement of Cu Zn Al shape memory alloys, Metallography. 19 (1986) 401–419. https://doi.org/10.1016/0026-0800(86)90074-1.
[107] G.V. Samsonov, A.D. Panasyuk, M.S. Borovikova, Contact reaction between refractory compounds and liquid metals, Sov. Powder Metall. Met. Ceram. 12 (1973) 403–407. https://doi.org/10.1007/BF00791269.
[108] Q. Lin, P. Shen, L. Yang, F. Qiu, Q. Jiang, Warping of triple line in the wetting of B4C by a Cu-1 at.% Cr alloy, Surf. Interface Anal. 43 (2011) 1360–1364. https://doi.org/10.1002/sia.3713.
[109] S. Zhang, M. Khangkhamano, H. Zhang, H.A. Yeprem, Novel Synthesis of ZrB2 Powder Via Molten-Salt-Mediated Magnesiothermic Reduction, J. Am. Ceram. Soc. 97 (2014) 1686–1688. https://doi.org/10.1111/jace.12945.
[110] J. Xu, L. Chen, H. Choi, H. Konish, X. Li, Assembly of metals and nanoparticles into novel nanocomposite superstructures, Sci. Rep. 3 (2013). https://doi.org/10.1038/srep01730.
[111] R. Gaillac, P. Pullumbi, F.-X. Coudert, ELATE: an open-source online application for analysis and visualization of elastic tensors, J. Phys. Condens. Matter. 28 (2016) 275201. https://doi.org/10.1088/0953-8984/28/27/275201.
[112] C. Cao, G. Yao, L. Jiang, M. Sokoluk, X. Wang, J. Ciston, A. Javadi, Z. Guan, I. De Rosa, W. Xie, E.J. Lavernia, J.M. Schoenung, X. Li, Bulk ultrafine grained/nanocrystalline metals via slow cooling, Sci. Adv. 5 (2019) eaaw2398. https://doi.org/10.1126/sciadv.aaw2398.

[113] G.A. Yasinskaya, The wetting of refractory carbides, borides, and nitrides by molten metals, Sov. Powder Metall. Met. Ceram. 5 (1966) 557–559. https://doi.org/10.1007/BF00780116.
[114] J. Ma, Y. Gu, L. Shi, L. Chen, Z. Yang, Y. Qian, Reduction–boronation route to chromium boride (CrB) nanorods, Chem. Phys. Lett. 381 (2003) 194–198. https://doi.org/10.1016/j.cplett.2003.09.128.
[115] O. Torabi, M.H. Golabgir, H. Tajizadegan, An investigation on the formation mechanism of nano CrB2 powder in the Mg–B2O3–Cr2O3 system, Int. J. Refract. Met. Hard Mater. 51 (2015) 50–55. https://doi.org/10.1016/j.ijrmhm.2015.02.015.
[116] Z. Liu, Y. Wei, X. Meng, T. Wei, S. Ran, Synthesis of CrB2 powders at 800°C under ambient pressure, Ceram. Int. 43 (2017) 1628–1631. https://doi.org/10.1016/j.ceramint.2016.10.108.
[117] K. Bao, Y. Wen, M. Khangkhamano, S. Zhang, Low-temperature preparation of titanium diboride fine powder via magnesiothermic reduction in molten salt, J. Am. Ceram. Soc. 100 (2017) 2266–2272. https://doi.org/10.1111/jace.14649.
[118] X. Liu, N. Fechler, M. Antonietti, Salt melt synthesis of ceramics, semiconductors and carbon nanostructures, Chem. Soc. Rev. 42 (2013) 8237–8265.
[119] G. Yao, C. Cao, S. Pan, X. Li, Facile manufacturing of bimodal grained copper with nanoparticles, Mater. Lett. 281 (2020) 128606. https://doi.org/10.1016/j.matlet.2020.128606.
[120] J. Hou, X. Shi, J. Qiao, Y. Zhang, P.K. Liaw, Y. Wu, Ultrafine-grained dual phase Al0.45CoCrFeNi high-entropy alloys, Mater. Des. 180 (2019) 107910. https://doi.org/10.1016/j.matdes.2019.107910.
[121] L. Wang, E. Mostaed, X. Cao, G. Huang, A. Fabrizi, F. Bonollo, C. Chi, M. Vedani, Effects of texture and grain size on mechanical properties of AZ80 magnesium alloys at lower temperatures, Mater. Des. 89 (2016) 1–8. https://doi.org/10.1016/j.matdes.2015.09.153.
[122] K. Lu, Novel Properties of Nanostructured Metals, Mater. Sci. Forum. (2005). https://doi.org/10.4028/www.scientific.net/MSF.475-479.21.
[123] W. Xu, X.C. Liu, K. Lu, Strain-induced microstructure refinement in pure Al below 100 nm in size, Acta Mater. 152 (2018) 138–147. https://doi.org/10.1016/j.actamat.2018.04.014.
[124] M. Brochu, G. Portillo, Grain Refinement during Rapid Solidification of Aluminum–Zirconium Alloys Using Electrospark Deposition, Mater. Trans. 54 (2013) 934–939. https://doi.org/10.2320/matertrans.MD201228.
[125] J. Jeon, S. Nam, S. Kang, J. Shin, H. Choi, Mechanical behavior of ultrafine-grained high-Mn steels containing nanoscale oxides produced by powder technology, Mater. Des. 92 (2016) 73–78. https://doi.org/10.1016/j.matdes.2015.12.028.
[126] L. Lu, M.L. Sui, K. Lu, Superplastic Extensibility of Nanocrystalline Copper at Room Temperature, Science. 287 (2000) 1463–1466. https://doi.org/10.1126/science.287.5457.1463.
[127] K. Lu, Nanocrystalline metals crystallized from amorphous solids: nanocrystallization, structure, and properties, Mater. Sci. Eng. R Rep. 16 (1996) 161–221. https://doi.org/10.1016/0927-796X(95)00187-5.
[128] S. Nimityongskul, M. Jones, H. Choi, R. Lakes, S. Kou, X. Li, Grain refining mechanisms in Mg–Al alloys with Al4C3 microparticles, Mater. Sci. Eng. A. 527 (2010) 2104–2111. https://doi.org/10.1016/j.msea.2009.12.030.

[129] H. Zhang, K. Dasbiswas, N.B. Ludwig, G. Han, B. Lee, S. Vaikuntanathan, D.V. Talapin, Stable colloids in molten inorganic salts, Nature. 542 (2017) 328–331. https://doi.org/10.1038/nature21041.
[130] X. Zhou, X. Li, K. Lu, Size Dependence of Grain Boundary Migration in Metals under Mechanical Loading, Phys. Rev. Lett. 122 (2019) 126101. https://doi.org/10.1103/PhysRevLett.122.126101.
[131] X. Zhou, X.Y. Li, K. Lu, Enhanced thermal stability of nanograined metals below a critical grain size, Science. 360 (2018) 526–530. https://doi.org/10.1126/science.aar6941.
[132] Y. Huang, S. Sabbaghianrad, A.I. Almazrouee, K.J. Al-Fadhalah, S.N. Alhajeri, T.G. Langdon, The significance of self-annealing at room temperature in high purity copper processed by high-pressure torsion, Mater. Sci. Eng. A. 656 (2016) 55–66. https://doi.org/10.1016/j.msea.2016.01.027.
[133] X. Zhou, X.Y. Li, K. Lu, Enhanced thermal stability of nanograined metals below a critical grain size, Science. 360 (2018) 526–530. https://doi.org/10.1126/science.aar6941.
[134] F. Wang, Y. Li, X. Xu, Y. Koizumi, K. Yamanaka, H. Bian, A. Chiba, Superthermostability of nanoscale TIC-reinforced copper alloys manufactured by a two-step ball-milling process, Philos. Mag. 95 (2015) 4035–4053. https://doi.org/10.1080/14786435.2015.1112442.
[135] K. Sikdar, A. Mahata, B. Roy, D. Roy, Hybrid thermal stabilization of Zr doped nanocrystalline Cu, Mater. Des. 164 (2019) 107564. https://doi.org/10.1016/j.matdes.2018.107564.
[136] T. Chookajorn, H.A. Murdoch, C.A. Schuh, Design of stable nanocrystalline alloys, Science. 337 (2012) 951–954.
[137] S. Canovic, T. Jonsson, M. Halvarsson, Grain contrast imaging in FIB and SEM, J. Phys. Conf. Ser. 126 (2008) 012054. https://doi.org/10.1088/1742-6596/126/1/012054.
[138] K. Lu, L. Lu, S. Suresh, Strengthening Materials by Engineering Coherent Internal Boundaries at the Nanoscale, Science. 324 (2009) 349–352. https://doi.org/10.1126/science.1159610.
[139] S.C. Krishna, N.K. Gangwar, A.K. Jha, B. Pant, On the Prediction of Strength from Hardness for Copper Alloys, J. Mater. (2013). https://doi.org/10.1155/2013/352578.
[140] L.-Y. Chen, J.-Q. Xu, H. Choi, M. Pozuelo, X. Ma, S. Bhowmick, J.-M. Yang, S. Mathaudhu, X.-C. Li, Processing and properties of magnesium containing a dense uniform dispersion of nanoparticles, Nature. 528 (2015) 539–543.
[141] Z. Liu, N. Cheng, Q. Zheng, J. Wu, Q. Han, Z. Huang, J. Xing, Y. Li, Y. Gao, Processing and tensile properties of A356 composites containing in situ small-sized Al3Ti particulates, Mater. Sci. Eng. A. 710 (2018) 392–399. https://doi.org/10.1016/j.msea.2017.11.005.
[142] D. Zhou, H. Geng, W. Zeng, G. Sha, C. Kong, Z. Quadir, P. Munroe, R. Torrens, P. Trimby, D. Zhang, Effect of extrusion temperature on microstructure and properties of an ultrafine-grained Cu matrix nanocomposite fabricated by powder compact extrusion, J. Mater. Sci. 53 (2018) 5389–5401. https://doi.org/10.1007/s10853-017-1952-2.
[143] H.O. Pierson, Handbook of refractory carbides and nitrides: properties, characteristics, processing and applications, William Andrew, 1996.
[144] K. Yoshida, H. Morigami, Thermal properties of diamond/copper composite material, Microelectron. Reliab. 44 (2004) 303–308. https://doi.org/10.1016/S0026-2714(03)00215-4.

[145] C.L. Li, Q.S. Mei, J.Y. Li, F. Chen, Y. Ma, X.M. Mei, Hall-Petch relations and strengthening of Al-ZnO composites in view of grain size relative to interparticle spacing, Scr. Mater. 153 (2018) 27–30. https://doi.org/10.1016/j.scriptamat.2018.04.042.
[146] E. Ma, T. Zhu, Towards strength–ductility synergy through the design of heterogeneous nanostructures in metals, Mater. Today. 20 (2017) 323–331. https://doi.org/10.1016/j.mattod.2017.02.003.
[147] Y. Wang, M. Chen, F. Zhou, E. Ma, High tensile ductility in a nanostructured metal, Nature. 419 (2002) 912–915. https://doi.org/10.1038/nature01133.
[148] B. Srinivasarao, K. Oh-ishi, T. Ohkubo, T. Mukai, K. Hono, Synthesis of high-strength bimodally grained iron by mechanical alloying and spark plasma sintering, Scr. Mater. 58 (2008) 759–762. https://doi.org/10.1016/j.scriptamat.2007.12.016.
[149] M. Zha, H.-M. Zhang, Z.-Y. Yu, X.-H. Zhang, X.-T. Meng, H.-Y. Wang, Q.-C. Jiang, Bimodal microstructure – A feasible strategy for high-strength and ductile metallic materials, J. Mater. Sci. Technol. 34 (2018) 257–264. https://doi.org/10.1016/j.jmst.2017.11.018.
[150] D. Witkin, Z. Lee, R. Rodriguez, S. Nutt, E. Lavernia, Al–Mg alloy engineered with bimodal grain size for high strength and increased ductility, Scr. Mater. 49 (2003) 297–302. https://doi.org/10.1016/S1359-6462(03)00283-5.
[151] Z. Dapeng, L. Yong, L. Feng, W. Yuren, Z. Liujie, D. Yuhai, ODS ferritic steel engineered with bimodal grain size for high strength and ductility, Mater. Lett. 65 (2011) 1672–1674. https://doi.org/10.1016/j.matlet.2011.02.064.
[152] N. Eustathopoulos, M.G. Nicholas, B. Drevet, Wettability at high temperatures, Elsevier, 1999.
[153] J. Gupta, J.M.E. Harper, J.L.M. Iv, P.G. Blauner, D.A. Smith, Focused ion beam imaging of grain growth in copper thin films, Appl. Phys. Lett. 61 (1992) 663–665. https://doi.org/10.1063/1.107815.
[154] F. Tang, M. Hagiwara, J.M. Schoenung, Formation of coarse-grained inter-particle regions during hot isostatic pressing of nanocrystalline powder, Scr. Mater. 53 (2005) 619–624. https://doi.org/10.1016/j.scriptamat.2005.05.034.
[155] G. Yao, S. Pan, C. Cao, M. Sokoluk, X. Li, Nanoparticle-enabled phase modification (nano-treating) of CuZrSi pseudo-binary alloy, Materialia. 14 (2020) 100897. https://doi.org/10.1016/j.mtla.2020.100897.
[156] L.U. Yang, J.I.N. Woxin, L.I. Wensheng, Z. He, L.I. Zheng, W. Yaqing, Effect of Fe on Wear-Friction Properties of High Aluminum Bronze [J], Mater. Rev. 2 (2008).
[157] aluminum_bronze.pdf, (n.d.). https://www.copper.org/publications/newsletters/innovations/2002/08/aluminum_bronze.pdf (accessed November 18, 2020).
[158] J.P. Liu, X.F. Liu, H.Y. Huang, J.X. Xie, Martensite structure of Cu-12% Al alloy and its effect on mechanical properties, Chin J Nonferr Met. 21 (2011) 1052–9.
[159] M. Sokoluk, C. Cao, S. Pan, X. Li, Nanoparticle-enabled phase control for arc welding of unweldable aluminum alloy 7075, Nat. Commun. 10 (2019) 98. https://doi.org/10.1038/s41467-018-07989-y.
[160] A.K. Koul, R. Thamburaj, Serrated grain boundary formation potential of Ni-based superalloys and its implications, Metall. Trans. A. 16 (1985) 17–26. https://doi.org/10.1007/BF02656707.

[161] H.U. Hong, H.W. Jeong, I.S. Kim, B.G. Choi, Y.S. Yoo, C.Y. Jo, Significant decrease in interfacial energy of grain boundary through serrated grain boundary transition, Philos. Mag. 92 (2012) 2809–2825. https://doi.org/10.1080/14786435.2012.676212.
[162] K.J. Kim, H.U. Hong, S.W. Nam, Investigation on the formation of serrated grain boundaries with grain boundary characteristics in an AISI 316 stainless steel, J. Nucl. Mater. 393 (2009) 249–253. https://doi.org/10.1016/j.jnucmat.2009.06.011.
[163] J.Q. Xu, L.Y. Chen, H. Choi, X.C. Li, Theoretical study and pathways for nanoparticle capture during solidification of metal melt, J. Phys. Condens. Matter. 24 (2012) 255304. https://doi.org/10.1088/0953-8984/24/25/255304.
[164] N.H. Mustafa, M.M. Mahat, S.M. Yahaya, R. Rosmamuhamadani, Corrosion behaviour of *in-situ* Zirconium Diboride (ZrB_2) reinforced by Aluminium-Copper (Al-Cu) alloy metal matrix composite, J. Phys. Conf. Ser. 1349 (2019) 012083. https://doi.org/10.1088/1742-6596/1349/1/012083.
[165] R. Rosmamuhamadani, M.K. Talari, S.M. Yahaya, S. Sulaiman, M.I.S. Ismail, M.A.A. Hanim, Corrosion characterization of in-situ titanium diboride (TiB2) reinforced aluminium-copper (Al-Cu) alloy by two methods: Salts spray fog and linear polarization resistance (LPR), in: Selangor, Malaysia, 2018: p. 020021. https://doi.org/10.1063/1.5036867.
[166] L.H. Chan, H. Weiland, S. Cheong, G.S. Rohrer, A.D. Rollett, The Correlation Between Grain Boundary Character and Intergranular Corrosion Susceptibility of 2124 Aluminum Alloy, (n.d.) 7.
[167] T. Wang, X. Chen, X. Luo, H. Jiang, M. Chen, Z. Wang, Formation of Si nanoparticle in Al matrix for Al-7wt.%Si alloy during complex shear flow casting, J. Alloys Compd. 739 (2018) 30–34. https://doi.org/10.1016/j.jallcom.2017.12.243.
[168] C. Cao, L. Chen, J. Xu, J. Zhao, M. Pozuelo, X. Li, Phase control in immiscible Zn-Bi alloy by tungsten nanoparticles, Mater. Lett. 174 (2016) 213–216.
[169] S. Moniri, X. Xiao, A.J. Shahani, The mechanism of eutectic modification by trace impurities, Sci. Rep. 9 (2019) 1–13. https://doi.org/10.1038/s41598-019-40455-3.
[170] Z.H. Li, Y. Tang, Q.W. Guo, G.Y. Li, Effects of CeO2 nanoparticles addition on shear properties of low-silver Sn–0.3Ag–0.7Cu-xCeO2 solder alloys, J. Alloys Compd. 789 (2019) 150–162. https://doi.org/10.1016/j.jallcom.2019.03.013.
[171] B. Zhao, Q. Cai, J. Cheng, S. Yang, F. Chen, Investigation on recrystallization and precipitation behaviors of Al-4.5Cu-1.5 Mg alloy refined by Ti-supported TiC nanoparticles, J. Alloys Compd. 800 (2019) 392–402. https://doi.org/10.1016/j.jallcom.2019.05.323.
[172] D.M. Stefanescu, Solidification and modeling of cast iron—A short history of the defining moments, Mater. Sci. Eng. A. 413–414 (2005) 322–333. https://doi.org/10.1016/j.msea.2005.08.180.
[173] J. Barrirero, C. Pauly, M. Engstler, J. Ghanbaja, N. Ghafoor, J. Li, P. Schumacher, M. Odén, F. Mücklich, Eutectic modification by ternary compound cluster formation in Al-Si alloys, Sci. Rep. 9 (2019) 1–10. https://doi.org/10.1038/s41598-019-41919-2.
[174] J. Wang, Z. Guo, J.L. Song, W.X. Hu, J.C. Li, S.M. Xiong, Morphology transition of the primary silicon particles in a hypereutectic A390 alloy in high pressure die casting, Sci. Rep. 7 (2017) 1–11. https://doi.org/10.1038/s41598-017-15223-w.
[175] J. Wang, S. Yue, Y. Fautrelle, P.D. Lee, X. Li, Y. Zhong, Z. Ren, Refinement and growth enhancement of Al_2Cu phase during magnetic field assisting directional solidification of hypereutectic Al-Cu alloy, Sci. Rep. 6 (2016) 24585. https://doi.org/10.1038/srep24585.

[176] S. Liu, Y. Zhou, X. Xing, J. Wang, X. Ren, Q. Yang, Growth characteristics of primary M_7C_3 carbide in hypereutectic Fe-Cr-C alloy, Sci. Rep. 6 (2016) 32941. https://doi.org/10.1038/srep32941.
[177] S. Buytoz, M.M. Yildirim, H. Eren, Microstructural and microhardness characteristics of gas tungsten are synthesized Fe–Cr–C coating on AISI 4340, Mater. Lett. 59 (2005) 607–614. https://doi.org/10.1016/j.matlet.2004.08.038.
[178] H. Sprenger, J.J. Nickl, F. fur FestkBrperchemie, UNIDIRECTIONAL SOLIDIFICATION OF A PSEUDO-BINARY EUTECTIC COPPER/E PHASE, in: Proc. Conf. N T U Compos. Sept. 5-8 1972 Lakeville Conn., National Academies, 1973: p. 111.
[179] A.J. Perry, Directionally solidified copper CuZrSi pseudo-binary eutectic alloys, Mater. Sci. Eng. 11 (1973) 203–209. https://doi.org/10.1016/0025-5416(73)90079-7.
[180] C. Cao, W. Liu, Z. Liu, J. Xu, I. Hwang, I. De Rosa, X. Li, Scalable manufacturing of immiscible AlBi alloy by self-assembled nanoparticles, Mater. Des. 146 (2018) 163–171. https://doi.org/10.1016/j.matdes.2018.03.008.
[181] M. Zuo, M. Sokoluk, C. Cao, J. Yuan, S. Zheng, X. Li, Microstructure Control and Performance Evolution of Aluminum Alloy 7075 by Nano-Treating, Sci. Rep. 9 (2019) 1–11. https://doi.org/10.1038/s41598-019-47182-9.
[182] S.-H. Kim, H. Kim, N.J. Kim, Brittle intermetallic compound makes ultrastrong low-density steel with large ductility, Nature. 518 (2015) 77–79. https://doi.org/10.1038/nature14144.
[183] R.K. Islamgaliev, K.M. Nesterov, J. Bourgon, Y. Champion, R.Z. Valiev, Nanostructured Cu-Cr alloy with high strength and electrical conductivity, J. Appl. Phys. 115 (2014) 194301. https://doi.org/10.1063/1.4874655.
[184] D. J. Chakrabarti, D. Laughlin, The Cr-Cu (Chromium-Copper) system, Bull. Alloy Phase Diagr. 5 (1984) 59–68. https://doi.org/10.1007/BF02868727.
[185] L. Peng, H. Xie, G. Huang, G. Xu, X. Yin, X. Feng, X. Mi, Z. Yang, The phase transformation and strengthening of a Cu-0.71 wt% Cr alloy, J. Alloys Compd. 708 (2017) 1096–1102. https://doi.org/10.1016/j.jallcom.2017.03.069.
[186] A. Chbihi, X. Sauvage, D. Blavette, Atomic scale investigation of Cr precipitation in copper, Acta Mater. 60 (2012) 4575–4585. https://doi.org/10.1016/j.actamat.2012.01.038.
[187] Z. Zhao, Z. Xiao, Z. Li, M. Ma, J. Dai, Effect of magnesium on microstructure and properties of Cu-Cr alloy, J. Alloys Compd. 752 (2018) 191–197. https://doi.org/10.1016/j.jallcom.2018.04.159.
[188] X. Liu, Q. Zhao, Q. Jiang, Effects of cooling rate and TiC nanoparticles on the microstructure and tensile properties of an Al–Cu cast alloy, Mater. Sci. Eng. A. 790 (2020) 139737. https://doi.org/10.1016/j.msea.2020.139737.
[189] B. Pu, X. Lin, B. Li, X. Chen, C. He, N. Zhao, Effect of SiC nanoparticles on the precipitation behavior and mechanical properties of 7075Al alloy, J. Mater. Sci. 55 (2020) 6145–6160. https://doi.org/10.1007/s10853-020-04381-4.
[190] J. Yuan, M. Zuo, M. Sokoluk, G. Yao, S. Pan, X. Li, Nanotreating High-Zinc Al–Zn–Mg–Cu Alloy by TiC Nanoparticles, in: A. Tomsett (Ed.), Light Met. 2020, Springer International Publishing, Cham, 2020: pp. 318–323. https://doi.org/10.1007/978-3-030-36408-3_46.
[191] S. Pan, G. Yao, J. Yuan, M. Sokoluk, X. Li, Manufacturing of Bulk Al-12Zn-3.7Mg-1Cu Alloy with TiC Nanoparticles, Procedia Manuf. 48 (2020) 325–331. https://doi.org/10.1016/j.promfg.2020.05.054.

[192] T. Lu, C. Chen, P. Li, C. Zhang, W. Han, Y. Zhou, C. Suryanarayana, Z. Guo, Enhanced mechanical and electrical properties of in situ synthesized nano-tungsten dispersion-strengthened copper alloy, Mater. Sci. Eng. A. 799 (2021) 140161. https://doi.org/10.1016/j.msea.2020.140161.
[193] S. Chakraborty, R. Bagala, K. Sikdar, D. Roy, A. Basumallick, Structure property relationship in a bulk Cu–Cr–W composite synthesized by high-energy ball milling and spark plasma sintering, Mater. Chem. Phys. 256 (2020) 123708. https://doi.org/10.1016/j.matchemphys.2020.123708.
[194] S. Bera, I. Manna, Synthesis of CuCr and CuCrAg alloy with nano-ceramic dispersion by mechanical alloying and consolidation by laser assisted sintering, Mater. Chem. Phys. 132 (2012) 109–118. https://doi.org/10.1016/j.matchemphys.2011.11.005.
[195] Z. Li, W. Wang, J. lin Wang, Effects of TiB2 on microstructure of nano-grained Cu–Cr–TiB2 composite powders prepared by mechanical alloying, Adv. Powder Technol. 25 (2014) 415–422. https://doi.org/10.1016/j.apt.2013.07.001.
[196] A. Calvo, C. García-Rosales, F. Koch, N. Ordás, I. Iturriza, H. Greuner, G. Pintsuk, C. Sarbu, Manufacturing and testing of self-passivating tungsten alloys of different composition, Nucl. Mater. Energy. 9 (2016) 422–429. https://doi.org/10.1016/j.nme.2016.06.002.
[197] Y. Ma, A. Addad, G. Ji, M.-X. Zhang, W. Lefebvre, Z. Chen, V. Ji, Atomic-scale investigation of the interface precipitation in a TiB2 nanoparticles reinforced Al–Zn–Mg–Cu matrix composite, Acta Mater. 185 (2020) 287–299. https://doi.org/10.1016/j.actamat.2019.11.068.
[198] T.-C. Lin, C. Cao, M. Sokoluk, L. Jiang, X. Wang, J.M. Schoenung, E.J. Lavernia, X. Li, Aluminum with dispersed nanoparticles by laser additive manufacturing, Nat. Commun. 10 (2019) 4124. https://doi.org/10.1038/s41467-019-12047-2.
[199] J. Xu, Y. Li, K. Ma, Y. Fu, E. Guo, Z. Chen, Q. Gu, Y. Han, T. Wang, Q. Li, In-situ observation of grain refinement dynamics of hypoeutectic Al-Si alloy inoculated by Al-Ti-Nb-B alloy, Scr. Mater. 187 (2020) 142–147. https://doi.org/10.1016/j.scriptamat.2020.06.020.